

INFORMATION TO USERS

This manuscript has been reproduced from the microfilm master. UMI films the text directly from the original or copy submitted. Thus, some thesis and dissertation copies are in typewriter face, while others may be from any type of computer printer.

The quality of this reproduction is dependent upon the quality of the copy submitted. Broken or indistinct print, colored or poor quality illustrations and photographs, print bleedthrough, substandard margins, and improper alignment can adversely affect reproduction.

In the unlikely event that the author did not send UMI a complete manuscript and there are missing pages, these will be noted. Also, if unauthorized copyright material had to be removed, a note will indicate the deletion.

Oversize materials (e.g., maps, drawings, charts) are reproduced by sectioning the original, beginning at the upper left-hand corner and continuing from left to right in equal sections with small overlaps. Each original is also photographed in one exposure and is included in reduced form at the back of the book.

Photographs included in the original manuscript have been reproduced xerographically in this copy. Higher quality 6" x 9" black and white photographic prints are available for any photographs or illustrations appearing in this copy for an additional charge. Contact UMI directly to order.

U·M·I

University Microfilms International
A Bell & Howell Information Company
300 North Zeeb Road, Ann Arbor, MI 48106-1346 USA
313/761-4700 800/521-0600

Order Number 9317195

**Electron transport in $\text{Al}_x\text{Ga}_{1-x}\text{As}/\text{GaAs}$ semiconductors with
intense far-infrared perturbations**

Plombon, John Joseph, Ph.D.

University of California, Santa Barbara, 1992

U·M·I
300 N. Zeeb Rd.
Ann Arbor, MI 48106

UNIVERSITY OF CALIFORNIA

Santa Barbara

Electron Transport in $\text{Al}_x\text{Ga}_{1-x}\text{As}/\text{GaAs}$ Semiconductors with Intense Far-
infrared Perturbations

A Dissertation submitted in partial satisfaction of the requirements for the degree

of

Doctor of Philosophy

in

Physics

by

John Joseph Plombon

Committee in charge:

Professor Mark S. Sherwin, Chairperson

Professor S. James Allen

Professor Philip Pincus

November 1992

The dissertation of John Joseph Plombon
is approved:

Mark Shwin for Philip Pincus

R + Sawyer for J. Allen

Mark Shwin

Committee Chairperson

November 1992

ACKNOWLEDGMENTS

I am indebted to Bill Bewley and Chris Felix for discovering the effect this thesis tries to explain and for their help along the rocky road it took us along. I would like to thank my advisor Mark Sherwin for all his devoted effort in trying to train me as a physicist even though at times he met strong opposition. All the time and effort Mark spent reading this thesis and providing comments is greatly appreciated. I owe a special thanks to the brilliant technical staff, past and present, of the Center for Free-Electron Laser Studies (CFELS). A very special thanks goes out to David Enyeart for teaching me how to operate the free-electron laser (FEL) and for his help on technical details involved in performing an FEL experiment.

The early stages of this research was done in collaboration with Michael Warden and I thank him for his encouraging words and support during the days of the mysterious photovoltaic data.

I am very grateful to CFELS for providing me with the opportunity to work with Bob Austin and Mi Hong of Princeton University. This was a very unique opportunity and the experience can be described as down right fun! They are two very special people.

I would like to acknowledge the state of California and all her beauty. The Higher Cathedral Spire and East Buttress of the Middle Cathedral Rocks of Yosemite Valley deserve special mention here for putting all of this work in perspective.

Finally I would like to thank my family for their love and support.

VITA

May 14, 1964—Born—St. Paul, Minnesota.

1986—B.S., University of Minnesota.

1986-87—Teaching Assistant, Department of Physics, University of California, Santa Barbara.

1987-1991—Research Assistant, Department of Physics, University of California, Santa Barbara.

1991-1992—Teaching Assistant, Department of Physics, University of California, Santa Barbara.

PUBLICATIONS

“Far-infrared Perturbation of Electron Tunneling in Reaction Centers?”, Robert H. Austin, Mi K. Hong, Chris Moser, and John Plombon, *Chemical Physics* **158**, 473 (1991).

“Far-infrared Capture of Electrons by DX Centers”, J. J. Plombon, W. W. Bewley, C. L. Felix, M. S. Sherwin, P. Hopkins, M. Sundaram, A. C. Gossard. *Appl. Phys. Lett.* **60**, 1972 (1992).

“Far-infrared Harmonic Generation in an $\text{Al}_x\text{Ga}_{1-x}\text{As}$ Heterostructure”, W. W. Bewley, C. L. Felix, J. J. Plombon, B. Galrikian, M. S. Sherwin, M. Sundaram, A. C. Gossard, and B. Birnir. To be submitted to *Physical Review B*.

ABSTRACT

Electron Transport in $\text{Al}_x\text{Ga}_{1-x}\text{As}/\text{GaAs}$ Semiconductors with Intense Far-infrared Perturbations

by

John Joseph Plombon

Hall electron transport measurements were done in an $\text{Al}_{0.3}\text{Ga}_{0.7}\text{As}:\text{Si}$ epilayer with intense far-infrared radiation (FIR) perturbations. Intense FIR of a few meV was found to induce hot electron capture by DX centers. Transport measurements were also done in an $\text{Al}_{0.3}\text{Ga}_{0.7}\text{As}/\text{GaAs}$ heterostructure (2DEG) and the intense FIR is believed to induce hot electron real-space transfer from the 2DEG to the $\text{Al}_{0.3}\text{Ga}_{0.7}\text{As}:\text{Si}$ region of the heterostructure.

TABLE OF CONTENTS

Introduction.....	1
Chapter 1: Electronic Impurity Levels of Silicon in $Al_xGa_{1-x}As$ Semiconductors.....	5
Chapter 2: Samples, Equipment, and Experimental Technique.....	51
Chapter 3: Hall Electron Transport Data for an $Al_{0.3}Ga_{0.7}As:Si$ Epilayer.....	101
Chapter 4: Hot Electron Capture of Electrons by DX Centers.....	141
Chapter 5: FIR Induced Hot Electron Real-Space Transfer in an $Al_{0.3}Ga_{0.7}As/GaAs$ Heterostructure.....	163
Chapter 6: Photovoltaic Responses of $Al_xGa_{1-x}As/GaAs$ Semiconductors to Intense FIR.....	187
Chapter 7: Conclusions and Future Experiments.....	213

LIST OF FIGURES

Chapter 1

1.1	Cubic cell of the zinc-blende structure.....	7
1.2	First Brillouin zone for the zinc-blende structure.....	8
1.3	Band structure of GaAs.....	10
1.4	Pressure dependence of the shallow hydrogenic Si donor in GaAs.....	12
1.5	Dependence of Γ , L, and X bands on aluminum mole fraction.....	13
1.6	Effective mass Si impurity levels for the 3 conduction band minima, Γ , L, and X.....	21
1.7	Structural substitutional interstitial Si atom in an AlGaAs alloy.....	25
1.8	Phonon density of states in GaAs.....	27
1.9	Ns versus $1000/T$ for an Al _{0.29} Ga _{0.71} As epilayer.....	29
1.10	DX center photoionization cross section versus photon energy.....	31
1.11	DX center emission and capture energy versus Al mole fraction.....	32
1.12	Basic configuration coordinate diagram for a small lattice relaxation.....	36
1.13	Configuration coordinate diagram for a small lattice relaxation.....	38
1.14	Chadi and Chang configuration coordinate diagram for the DX center and its intermediate state.....	41

Chapter 2

2.1	Cleavage planes for a GaAs substrate.....	52
-----	---	----

2.2	MBE growth schematic for a digitally alloyed parabolic well.....	56
2.3	MBE growth schematic of an AlGaAs:Si epilayer without a buffer.....	58
2.4	MBE growth schematic of an AlGaAs:Si epilayer with a buffer.....	60
2.5	MBE growth schematic of a heterostructure.....	62
2.6	MBE growth schematic of half parabolic quantum well.....	63
2.7	Mesa and contact geometries for transport measurements.....	70
2.8	I-V curves for Hall bar contacts.....	71
2.9	I-V curves for Hall bar contacts.....	72
2.10	Effect of nonlinearity of Hall contacts on N_H and μ_H	73
2.11	Permanent magnetic assembly used for Hall measurements.....	78
2.12	Magnetic field lines for permanent magnet assembly.....	80
2.13	Typical optics layout and FIR coupling to sample.....	82
2.14	Band structure with the population of an unintentional 2DEG.....	91
2.15	Orientation of the magnetic field for Hall transport measurements.....	92

Chapter 3

3.1	N_H versus $1000/T$ for an $Al_{0.3}Ga_{0.7}As:Si$ epilayer.....	102
3.2	Hall mobility versus temperature for an $Al_{0.3}Ga_{0.7}As:Si$ epilayer.....	105
3.3	IR LED flash effect on N_H and μ_H in the epilayer.....	109
3.4	Non-exponential resistance relaxation and stretched exponential fit.....	111
3.5	Resistance relaxations for four different temperatures.....	112
3.6	Arrhenius plot of IR LED induced resistance relaxations.....	113
3.7	FIR effect on dark cooled $Al_{0.3}Ga_{0.7}As:Si$ epilayer.....	115

3.8	FIR effect on epilayer at 11K after an IR LED flash.....	119
3.9	Unusual FIR effects on epilayer at low temperature.....	121
3.10	FIR effect at 1/2Hz on epilayer at 9K.....	122
3.11	FIR effect on epilayer with large N_H	123
3.12	Effect of LED flashes on persistent photoconductivity.....	125
3.13	FIR effect on $Al_{0.3}Ga_{0.7}As:Si$ epilayer at 150K.....	126
3.14	Stretched exponential fit to FIR induced resistance relaxation.....	127
3.15	Power dependence of resistance changes in the epilayer at 11K.....	131
3.16	Histogram of resistance changes at $29.5cm^{-1}$	134
3.17	Histogram of resistance changes at $43.3cm^{-1}$	135

Chapter 4

4.1	Temperature dependent FIR induced resistance relaxations.....	144
4.2	Arrhenius plot of FIR induced resistance relaxations.....	145

Chapter 5

5.1	FIR effect on a 10 half-parabolic quantum well sample.....	169
5.2	FIR effect on a heterostructure (2DEG).....	171
5.3	Power dependence of FIR effect on the heterostructure.....	175
5.4	FIR effect on epilayer with unintentional 2DEG populated.....	179
5.5	Power dependence of FIR effect on epilayer/2DEG.....	180
5.6	FEL FIR induced effect on epilayer/2DEG.....	182

Chapter 6

6.1	The Schottky barrier and rectification due to thermionic emission.....	191
6.2	Contact geometries from which photovoltages were observed.....	196
6.3	Typical photovoltaic response from an AlGaAs semiconductor.....	197
6.4	Photovoltaic responses from an n ⁺ -GaAs substrate.....	199
6.5	Correlation of the photovoltaic response to 2DEG mobility.....	201
6.6	Positional dependence of the photovoltaic response.....	202
6.7	Resolution of mode beating in an FEL pulse from a 2DEG.....	204
6.8	Mode beating in an FEL pulse from n ⁺ -GaAs substrate.....	205
6.9	Photovoltaic response from a semi-insulating GaAs substrate.....	207
6.10	Power dependence of a photovoltage from an epilayer/2DEG.....	208

Introduction

The silicon donor in GaAs and $\text{Al}_x\text{Ga}_{1-x}\text{As}$ determines the electrical properties of these technologically important semiconductors. For $\text{Al}_x\text{Ga}_{1-x}\text{As}$ with $x < 0.22$, the Si donor acts as a shallow hydrogenic impurity, familiar from elementary solid state physics courses. However, for $x > 0.22$, the Si donor can act as a deep donor, and its behavior becomes much more complicated. Perhaps most remarkable is the phenomenon of "persistent photoconductivity". For $T < 50\text{K}$, photoconductivity persists even after the light source ($\hbar\omega > 0.8\text{eV}$) is removed. At these low temperatures, the ionized state of the deep Si level, or DX center, is metastable. Capture is prevented by a barrier associated with a "large lattice relaxation" necessary to fill and empty the DX center. Most deep semiconductor levels are not associated with such a capture barrier, and the electrons are easily recaptured once they have been ionized from the deep level.

Because of the technological importance of GaAs/ $\text{Al}_x\text{Ga}_{1-x}\text{As}$ based semiconductors for making very fast transistors, the DX center has received much attention in the last 15 years. For example, physical properties of the DX center play a large role in determining the switching times of these devices.

We discovered that the large electric fields of intense far-infrared radiation (FIR) can induce electron capture by DX centers (deep silicon impurity levels) in $\text{Al}_x\text{Ga}_{1-x}\text{As}$ ($x > 0.22$) semiconductors. The capture was observed in the regime of persistent photoconductivity ($T < 50\text{K}$) where the electrons trapped by the silicon

atoms take hours to days to equilibrate with the conduction band electrons by emitting and absorbing thermal phonons.

Chapter 1 discusses the electronic states of the Si impurity atom in $\text{Al}_x\text{Ga}_{1-x}\text{As}$ ($x > 0.22$) semiconductors. When the silicon impurity is located at a lattice site (replaces a Ga or Al atom) it is referred to as a substitutional donor and donates an electron to the crystal. In this substitutional configuration, the electron is weakly bound to the Si atom. The Si impurity level can become deep, the DX level, when the Si atom moves between lattice sites to what is called an interstitial position. This movement to an interstitial position takes place with the rupturing of Si - As chemical bond. The discussion of substitutional electronic impurity levels of Si leads to the development of the interstitial model for the DX center.

Chapter 2 discusses samples and experimental techniques. The electron capture was observed by monitoring the electron Hall concentration of a silicon doped $\text{Al}_{0.3}\text{Ga}_{0.7}\text{As}$ epilayer as the sample was exposed to short (50psec) pulses of intense FIR from a CO_2 pumped Raman shifted molecular gas laser (TEA laser). The importance of doing photo-Hall measurements to determine the electron concentration is discussed in detail.

Chapter 3 discusses the transport or photo-Hall data which clearly shows that intense FIR reduces the electron concentration in a Si doped $\text{Al}_{0.3}\text{Ga}_{0.7}\text{As}$ epilayer for temperatures below 200K. This reduction in electron concentration is interpreted as electron capture by DX centers.

Chapter 4 discusses the analysis of the photo-Hall data and it is suggested that the observed capture is the result of heating of electrons by intense electric fields from FIR laser pulses. A simple calculation of electron heating is presented in terms

of energy and momentum relaxation times to estimate the amount the electrons are heated by the intense FIR.

Chapter 5 discusses and analyzes photoconductivity data of an $\text{Al}_{0.3}\text{Ga}_{0.7}\text{As}/\text{GaAs}$ heterostructure two dimensional electron gas (2DEG). The electrons of the 2DEG are heated by the intense electric field of the FIR and transferred (in real space) to the $\text{Al}_{0.3}\text{Ga}_{0.7}\text{As}$ barrier of the heterostructure. This transfer of electrons is called real-space transfer. A threshold FIR electric field for real-space transfer is found that is consistent with intense microwave induced (35GHz) real-space transfer in a 2DEG.

Chapter 6 discusses photovoltaic signals believed to arise from both the metal contacts to the $\text{Al}_x\text{Ga}_{1-x}\text{As}/\text{GaAs}$ semiconductor and electrons in the $\text{Al}_x\text{Ga}_{1-x}\text{As}/\text{GaAs}$ quantum wells.

Chapter 7 summarizes the thesis, discusses the circumstances necessary to observe the FIR induced capture, and discusses possible future experiments.

Chapter 1

Electronic Impurity Levels of Silicon in $\text{Al}_x\text{Ga}_{1-x}\text{As}$ Semiconductors

§A Introduction

The electronic impurity levels of a silicon atom in an $\text{Al}_x\text{Ga}_{1-x}\text{As}$ semiconductor are quite complex. The levels can be shallow or deep bound states in the forbidden gap of the semiconductor depending on the position of the silicon atom in the lattice and the lattice temperature. The impurity levels can also be resonant with the conduction band states and not bound within the gap. The purpose of this chapter is to provide background information about the different Si impurity levels and discuss how they are related. Much time is spent developing this background information because an understanding of both the shallow and deep level are necessary to interpret the photo-Hall transport measurements discussed within this thesis.

We assume throughout that the silicon atoms are far enough apart (150\AA apart for Si concentration $\rho_{\text{Si}} = 3 \times 10^{17} \text{cm}^{-3}$, compared with 3\AA for the "Bohr radius" of the deep level) that they do not interact with each other. We will then consider only a single Si impurity in the GaAs or $\text{Al}_x\text{Ga}_{1-x}\text{As}$ lattice. The discussion begins by studying the GaAs lattice and is generalized to the $\text{Al}_x\text{Ga}_{1-x}\text{As}$ lattice as the subject

is developed.

The chapter is organized so that all the background information about the $\text{Al}_x\text{Ga}_{1-x}\text{As}$ band structure and substitutional Si impurity levels needed to understand the deep interstitial level (DX center) are presented first so the model for the DX center can be developed as clearly as possible. The chapter starts off with a discussion of the band structure of GaAs and $\text{Al}_x\text{Ga}_{1-x}\text{As}$. The substitutional Si level is then discussed with an emphasis on the fact that the substitutional Si impurity level can exist as a deep level called the D^0 level. The most important feature of this D^0 level is that it can exist as a resonant state in the conduction band and is believed to be the intermediate state for hot electron capture by the DX center. It is very important to understand the details of the substitutional donor before attempting to understand the interstitial level or DX center since the DX center is formed when the Si atom moves from its substitutional position to an interstitial position. With all this background information presented, the DX center is discussed and the chapter is concluded with a discussion of the different possible capture mechanisms of electrons by the DX centers.

§B The band structure and symmetry properties of GaAs and $\text{Al}_x\text{Ga}_{1-x}\text{As}$

Introduction

In order to pursue discussions of Si impurity levels in GaAs and $\text{Al}_x\text{Ga}_{1-x}\text{As}$, a knowledge of the band structure and symmetry properties of the GaAs ($\text{Al}_x\text{Ga}_{1-x}$

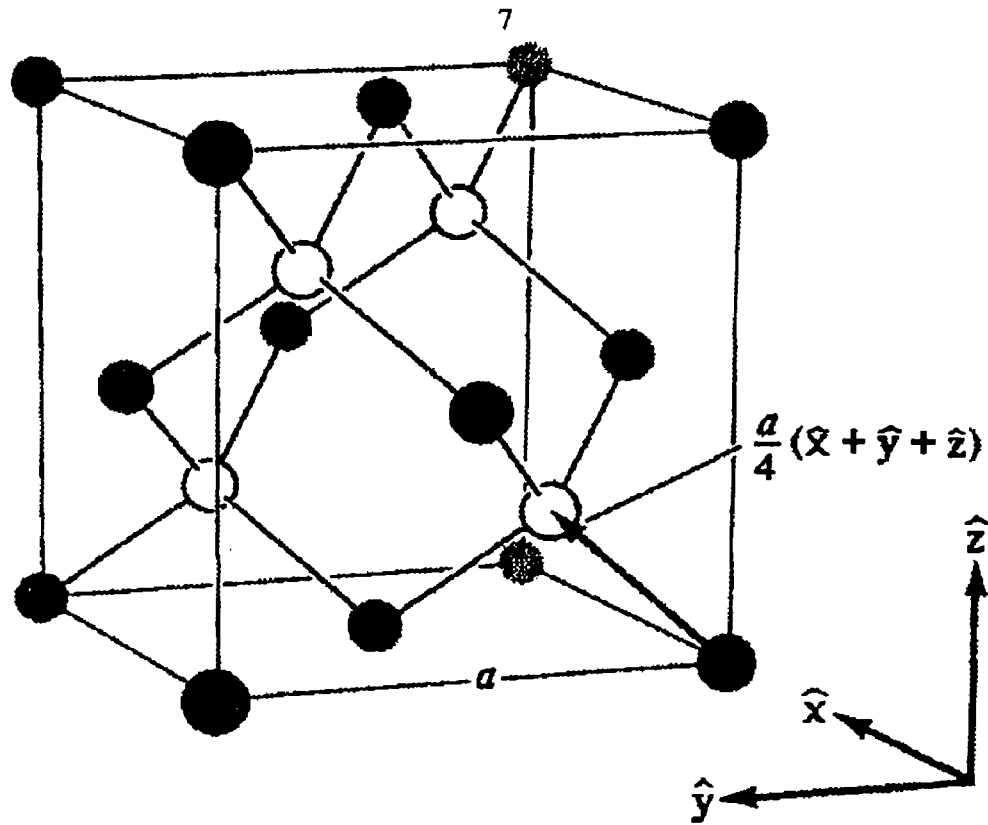


Fig.(1.1) Conventional cubic cell of the zinc-blende structure where the shaded sites are occupied by one kind of atom and the unshaded by another [1.1]. For GaAs $a = 5.6533\text{\AA}$ [1.2].

$x\text{As}$) lattice is needed. This section provides the necessary background information needed for understanding deep Si impurity levels in $\text{Al}_x\text{Ga}_{1-x}\text{As}$. The most important information about the GaAs band structure is the existence of three main conduction band minima (Γ , L, and X) along with their degeneracies.

The GaAs crystal lattice

The GaAs lattice is a zinc-blende lattice which has an equal number of gallium and arsenic atoms distributed on a diamond lattice. Each atom has four of the opposite kind as nearest neighbors, as shown in Fig.(1.1). The zinc-blende

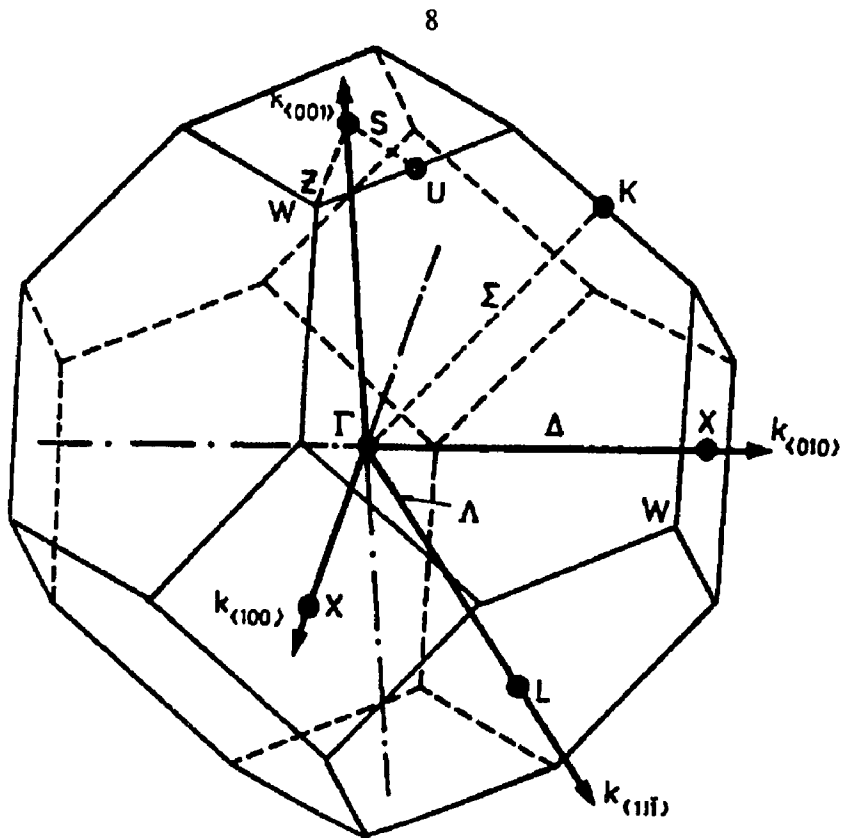


Fig.(1.2) First Brillouin zone for the zinc-blende lattice including important symmetry points and lines[1.3].

structure consists of two interpenetrating face-centered cubic (fcc) Bravais lattices (i.e. a Ga fcc and an As fcc), displaced along the body diagonal of the cubic cell by one quarter of the length of the body diagonal. In summary, the GaAs lattice can be regarded as a face-centered cubic lattice with a two-atom basis at $\mathbf{0}$ and $(a/2)(x + y + z)$ with a lattice constant $a = 5.65\text{\AA}$ as illustrated in Fig.(1.1).

Important symmetry points Γ , L , and X of the reciprocal lattice

Many of the important symmetry properties of GaAs are described in terms of the reciprocal lattice. The first Brillouin zone for GaAs is a body-centered cubic

(bcc) primitive unit cell in reciprocal space. Shown in Fig.(1.2) is the first Brillouin zone with its boundary and high symmetry points and lines. The two points labeled L and X correspond to points on the first Brillouin zone boundary in the $\langle 111 \rangle$ and $\langle 100 \rangle$ directions respectively. The Γ point is at the center of the Brillouin zone with $\mathbf{k} = (0,0,0)$. The other two high symmetry points are given by

$$\text{X-points: } \mathbf{k} = \pm(2\pi/a)\mathbf{x}, \pm(2\pi/a)\mathbf{y}, \pm(2\pi/a)\mathbf{z}$$

$$\text{L-points: } \mathbf{k} = \pm(\pi/a)(\mathbf{x}+\mathbf{y}+\mathbf{z}), \pm(\pi/a)(-\mathbf{x}+\mathbf{y}+\mathbf{z})$$

$$\pm(\pi/a)(\mathbf{x}-\mathbf{y}+\mathbf{z}), \pm(\pi/a)(\mathbf{x}+\mathbf{y}-\mathbf{z})$$

where \mathbf{x} , \mathbf{y} , and \mathbf{z} are unit vectors in the x , y , and z directions respectively.

The conduction band minima Γ , L, and X of GaAs

These high symmetry points Γ , L, and X correspond to local conduction band minima as shown in Fig.(1.3). The energy bands for GaAs shown in Fig.(1.3) are the results of an empirical pseudopotential calculation [1.4] that neglects spin-orbit effects and agrees well with experiments. The absolute minimum of the conduction band and the absolute maximum of the valence band occur at the same \mathbf{k} point of the Brillouin zone, namely $\mathbf{k} = (0,0,0)$, the Γ point, as can be seen from Fig.(1.3). This means that GaAs is a direct band gap semiconductor.

The degeneracy of Γ , L, and X, is important for constructing effective mass states associated with each of the degenerate local minima. The Γ point, $\mathbf{k}=(0,0,0)$, at the center of the first Brillouin zone, is nondegenerate. The eight equivalent points of the L minima at the zone boundary are shared by two Brillouin zones, so the L minima are 4-fold degenerate. Similarly the X minima at the zone boundary are three fold degenerate.

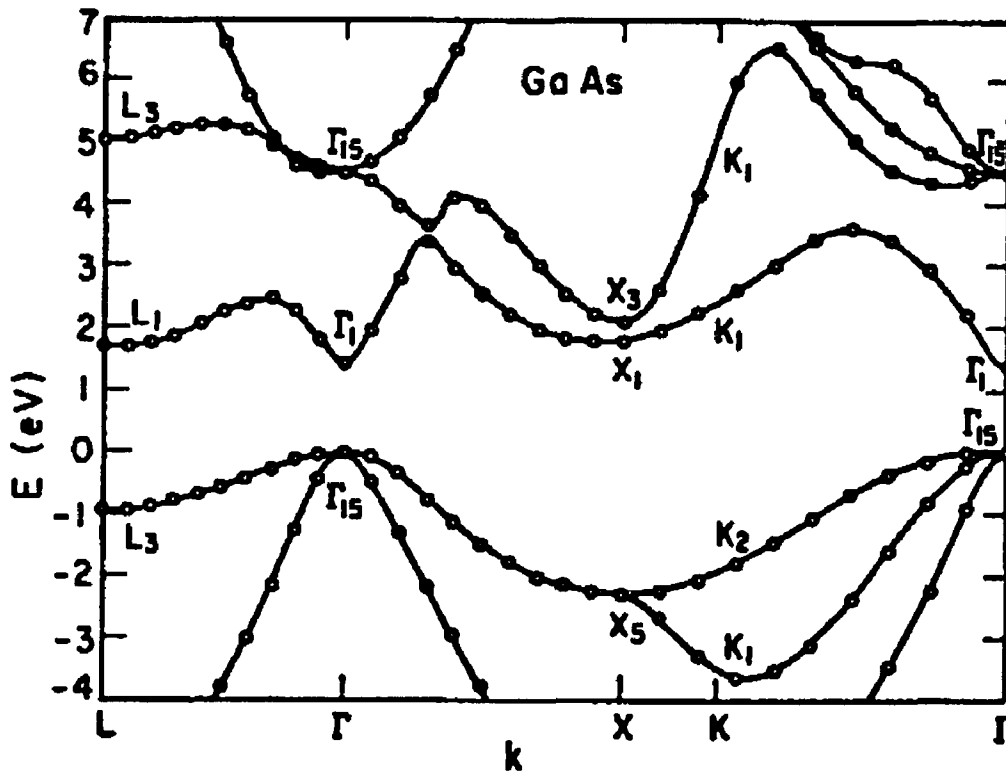


Fig.(1.3) Band structure of GaAs [1.4].

The conduction band minima at Γ , L, and X have further important distinctions in the fact that the electron mobility, effective mass, and density of states is different for each of the minima. When the electrons are transferred from the Γ band minimum to either the X or L band minima, their effective masses are heavier because of the smaller band curvature ($m^* = \hbar^2(d^2E/dk^2)^{-1}$). The electrons in the X or L band minima also have a reduced momentum relaxation time (lower electron mobility) because of the scattering between these minima and the higher density of states at these minima (larger effective masses, m^* , $\rho_{DOS} \propto (m^*)^{3/2}(E-E_c)^{1/2}$).

The effective masses in the various conduction band minima of GaAs are as follows: for the Γ band minimum,

$$m^*(\Gamma) = 0.067m_e, \quad m_e \text{ is the electron mass,}$$

for the L band minima

$$m^*(L) = 0.22m_e$$

and for the X band minima

$$m^*(X) = 0.41m_e.$$

The effective masses are density of states effective masses without the degeneracy factor included [1.5]. The degeneracy factor was left out (effective masses taken from [1.6]) since each degenerate minimum will be considered to have a shallow effective mass state associated with it as discussed in Chapter 1, §D below.

Pressure dependence of the Γ , L, and X minima of GaAs

Applying hydrostatic pressure to GaAs changes the relative positions of the Γ , L, and X minima as shown in Fig.(1.4). For pressures below 41.3kbar, GaAs is a direct band gap semiconductor with the Γ minimum the absolute conduction band minimum. For pressures above 41.3kbar, GaAs becomes an indirect band gap semiconductor with the X minimum as the absolute conduction band minimum. The effect of hydrostatic pressure on GaAs band structure is very similar to adding aluminum to GaAs to form $\text{Al}_x\text{Ga}_{1-x}\text{As}$ (compare Fig(1.4) with Fig.(1.5)). The conduction band minima change qualitatively in the same way with 1kbar of pressure equivalent to about 1% Al content in $\text{Al}_x\text{Ga}_{1-x}\text{As}$.

The Γ , L, and X bands in $\text{Al}_x\text{Ga}_{1-x}\text{As}$

When aluminum is added to the GaAs lattice, it substitutes with the Ga atom

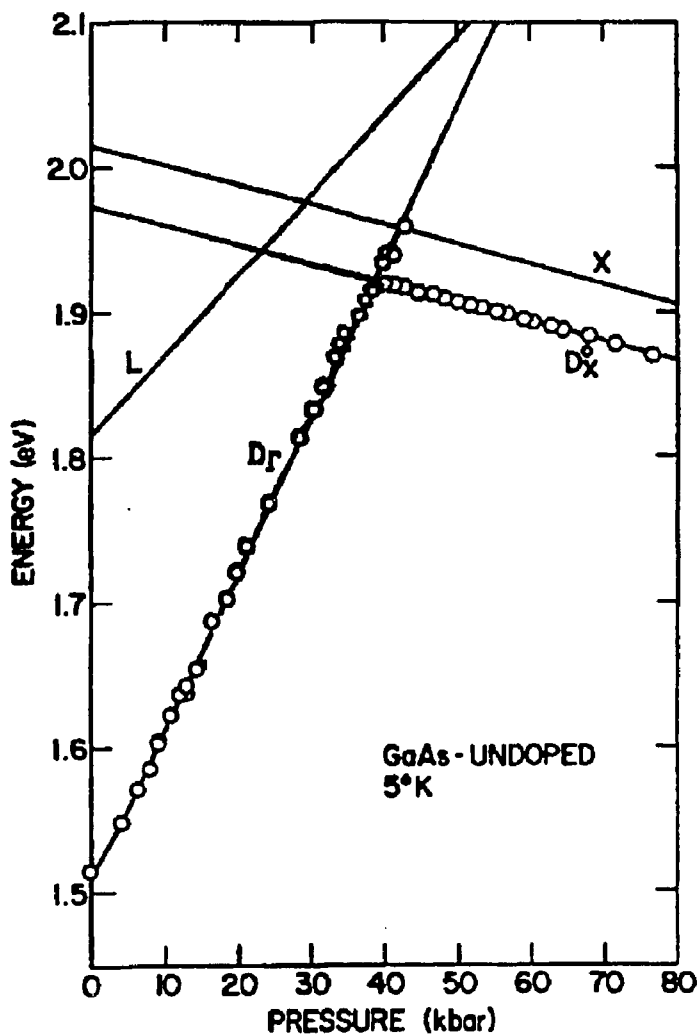


Fig.(1.4) Pressure dependence of the shallow hydrogenic Si donor in GaAs. For pressures less than 41.3kbar, the donor, D_{Γ} , is associated with the Γ band (not shown) and D_{Γ} lies about 6meV below it. For pressures greater than 41.3kbar, the donor is associated with the X band and D_X lies about 40meV below the X band [1.7].

(Group III element) and forms the ternary compound $Al_xGa_{1-x}As$ where the mole fraction x represents the fraction of Al replacing Ga in the GaAs lattice. With the addition of Al in GaAs, the energy band minima Γ , L, and X change in response to the changing atomic environment of the $Al_xGa_{1-x}As$ crystal as is shown in Fig.(1.5).

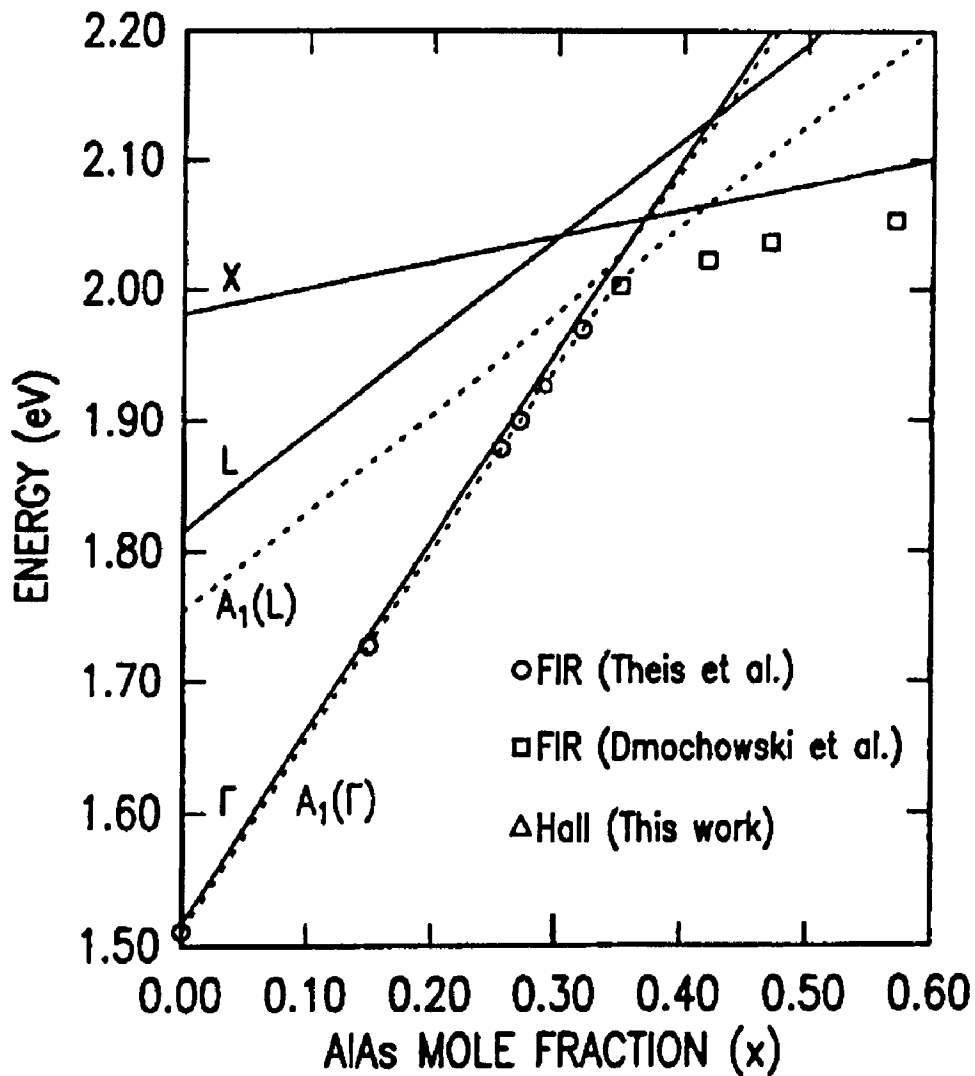


Fig.(1.5) The three band minima, Γ , L, and X dependence on aluminum mole fraction, x . Also shown is the dependence of the shallow hydrogenic Si impurity level, $A_1(\Gamma)$ or d^0 , and the deep substitutional Si impurity, $A_1(L)$ or D^0 , on aluminum mole fraction, x [1.8].

The rate at which the Γ minimum changes is faster than the rate at which the X and L minima change. Thus, with a sufficient percent of aluminum the Γ minimum crosses the X minimum and then the $A_1(\Gamma)$ minimum crosses the L minimum and then the $A_1(L)$ minimum crosses the L minimum. This direct to indirect band crossing occurs at a value of Al mole

fraction, x_c , around 0.40. The value of x_c is somewhat uncertain and has been reported to be anywhere from $x=0.37$ [1.9] to $x=0.45$ [1.10]. Recently T. N. Theis [1.8] argued in favor of the smaller value of $x_c=0.37$ which is much lower than the commonly accepted value of $x_c=0.43$.

A parameterization of how E_Γ , E_L , and E_X depends on Al mole fraction can be found in [1.8]. All of the $Al_xGa_{1-x}As$ epilayer studied in this thesis had $x=0.30$. Using the parameterization found in [1.8], $\Delta E_{\Gamma L}(x=0.3)$ and $\Delta E_{\Gamma X}(x=0.3)$ are estimated to be

$$\Delta E_{\Gamma L}(x=0.3) = E_L(0.3) - E_\Gamma(0.3) = 0.087\text{eV} \quad (x_c=0.37)$$

$$\Delta E_{\Gamma X}(x=0.3) = E_X(0.3) - E_\Gamma(0.3) = 0.087\text{eV}.$$

There are quadratic corrections to the above parameterization and slightly different parameterization for $x_c=0.45$ [1.11]. For comparison purposes, these parameterizations give

$$\Delta E_{\Gamma L}(x=0.3) = E_L(0.3) - E_\Gamma(0.3) = 0.103\text{ eV} \quad (x_c=0.45)$$

$$\Delta E_{\Gamma X}(x=0.3) = E_X(0.3) - E_\Gamma(0.3) = 0.152\text{eV}.$$

The important information to draw from all this is that $\Delta E_{\Gamma L}(x=0.3)\approx 0.1\text{eV}$.

§C The Shallow Hydrogenic Silicon donor, d^0

Introduction

The Si atom (a column IV element of the periodic table) is a substitutional impurity when it sits at the site of a gallium (Ga) atom (a column III element) in a GaAs lattice. In this substitutional configuration, the extra valence electron of the Si atom (compared with Ga) is weakly bound to the silicon impurity, resulting in a bound shallow level within the gap. Other deep substitutional Si impurity states exist. These deep states are not bound states but resonant with the conduction band states (see Chapter 1, §E).

The spectrum of bound electronic states of the Si substitutional donor in GaAs is well described by hydrogenic levels of the effective mass approximation (EMA) [1.12] because the electron bound by the Si impurity sees the Si nucleus screened by the large dielectric constant of the GaAs crystal. Furthermore, the small effective mass of the electron in GaAs increases the electron orbital radius around the Si impurity (reducing the binding energy even more). For a semiconductor with dielectric constant ϵ and effective mass m^* , the electronic substitutional impurity levels are given by

$$E_n = -e^4 m^* / (2\hbar^2 \epsilon^2 n^2) = -(m^* / m \epsilon^2) R / (n^2) = -R^* / n^2 \quad \text{Eq.(1.1)}$$

with $Z = 1$ and $R = 13.6\text{eV}$ where $-R/n^2$ is the electron energy spectrum of the free hydrogen atom. The substitutional Si impurity in the GaAs lattice can be thought of in terms of a screened hydrogen atom with an effective Rydberg of

$$R^* = (m^* / m \epsilon^2) R = (4.29 \times 10^{-4})(13.6\text{eV}) = 5.83\text{meV}$$

where $m^* = 0.067m_e$ and $\epsilon = \epsilon(0) = 12.5$ for GaAs. For a hydrogenic impurity in GaAs, the Rydberg is reduced by about a factor of 1000 from that of a free hydrogen atom. Similarly the effective Bohr radius for the electron around the impurity in a semiconductor is given within EMA by

$$a_n^* = (\hbar^2 \epsilon n^2) / (e^2 m^*) = 0.53 (m/m^*) n^2 \epsilon \text{ \AA}. \quad \text{Eq.(1.2)}$$

For GaAs, $a_o^* \approx 100 \text{ \AA}$ corresponding to about 18 lattice constants (the lattice constant for GaAs is 5.65 \AA which is the length of a unit cell side).

Optical and thermal ionization energies of the shallow donor

At very low temperatures ($T < 5\text{K}$) where the shallow Si donor is not ionized, the donor may be ionized with a photon of energy equal to or greater than the binding energy of 5.8meV . The minimum photon energy needed to ionize the donor is referred to as the optical ionization energy, E_o . The donor may be ionized by phonons and this thermal ionization has a threshold energy called E_d . For shallow hydrogenic donors, E_o is equal to or very close to E_d . This means that when the impurity is ionized there is little or no rearrangement of the neighboring atoms (lattice relaxation) around the impurity. The case of a deep donor can be quite different and sometimes there is a large rearrangement of the impurity atom and its neighboring atoms which is referred to as a large lattice relaxation (LLR). This will be discussed in more detail in §F and §G of this chapter and is mentioned here to provide a context for the lack of a lattice relaxation associated with the shallow hydrogenic donors.

The central cell correction

Shown in table 1.1 [1.13] is how well the effect mass approximation describes the experimentally measured energy levels for a variety of hydrogenic like impurities in GaAs. The effective Rydberg in GaAs is 5.83meV which is equal to the EMA's prediction of the energy eigenvalue for the ground state, E_{1s} level, for a hydrogenic donor in GaAs. Table 1.1 shows that there is a slight dependence of E_{1s} on donor chemical species, referred to as the chemical shift. EMA does not predict a dependence of the ground state energy on impurity chemical species.

Table 1.1 GaAs Donor Levels

Donor	E_{1s} (meV), Exp.	E_{2s} (meV), Exp.	E_{2s} (meV), EMA
Si	5.854	1.42	1.44
Ge	5.908		
Sn	5.817		
S	5.890		
Se	5.808		
Te	5.892		

Also given in table 1.1 is the energy eigenvalue for the first excited state, E_{2s} level. The EMA value agrees well with experiment since the screening of the donor atom's nucleus is more effective for the excited states than the ground state. Whereas with the donor in the 1s ground state (spherically symmetric) with the smallest Bohr radius, a^*_0 , it will spend more time in the unit cell containing the impurity and be more affected by impurity differences. A correction for the ground state energy

taking into account the effect of the interaction of the ground state electron with the donor nucleus can be estimated with a pseudopotential calculation [1.14] and is referred to as the central cell correction. The chemical shifts of the E_{1s} level observed in GaAs for different impurity atoms can be thought of qualitatively in terms of the differences in electronegativity between the substitutional impurity and the atom it replaces [1.13].

The energy level at which the central cell correction can be neglected depends on the semiconductor system studied. For impurities in GaAs, it suffices to consider a central cell correction only for the ground state whereas for impurities in Si the deviations from the EMA are more significant and central cell corrections for some of the excited states are discussed within the literature [1.14].

The limit where EMA is applicable

The effective mass approximation works well for substitutional impurities in GaAs since the dielectric constant is large and the effective mass is small which leads to a very delocalized electron wave function. Then the predicted EMA binding energy of the electron to the impurity atom is about 5.8meV which is more than 2 orders of magnitude smaller than the GaAs band gap ($E_{\text{gap}}^{\Gamma} = 1.42\text{eV}$). Within the limit that $E_{1s} \ll E_{\text{gap}}^{\Gamma}$, the effective mass theory works well.

§D Shallow donors associated with the L and X conduction band minima

The effective mass approximation predicts the existence of shallow donor levels associated with the conduction band minima other than the absolute minimum of the conduction band (Γ minimum for $\text{Al}_x\text{Ga}_{1-x}\text{As}$ $x < 0.37$ and X minimum for $x > 0.37$) [Bassani's theorem Ref(1.15)]. These states are only weakly coupled by the coulomb potential so that their energies depend mostly on the band masses. This means that there is a series of hydrogenic effective mass states (1s, 2s, 2p, etc.) associated with each of the degenerate conduction band minima - one at Γ , three at X, and four at L.

The effective mass associated with the X minimum is $m^*(X) \approx 0.41m_e$ so the 1s state associated with the X minimum is then $E_{1s}(X) \approx 36\text{meV}$ (Eq.(1.1) with $n=1$ and $m^*=m^*(X)$) [1.16] which is of moderate depth. The central cell potential does not mix and split the three degenerate 1s states of the X minimum because it is of opposite symmetry to the effective mass state. The three fold degenerate shallow level associated with the X minimum is labeled as a T_2 crystal symmetry state [1.12] (a triplet hybridized state of the crystal host atom's (Ga atom) wavefunction and a p like impurity (Si atom) wavefunction).

The 1s state derived from the L minimum ($m^*(L) \approx 0.21m_e$) is also of moderate depth, $E_{1s}(L) \approx 18\text{meV}$. The impurity potential of the group III Si substitutional donor does mix the four degenerate L minima [1.19] so that the crystal symmetry state A_1 [1.12] (a singlet hybridized state of the crystal host atom's wavefunction and

the $1s$ like impurity wave function) is pulled down by about an additional 25meV or so [1.19] by the attractive central cell potential. The triplet T_2 state is not affected and is left near its one-minimum value.

Pressure dependence of donors associated with Γ and X

Applying hydrostatic pressure to a sample of GaAs:Si, the E_{1s} level follows the Γ band of the conduction band and not the L or X band (or a combination of all three minima) for pressures below 41.3kbar as shown in Fig.(1.4). Above 41.3kbar , GaAs becomes an indirect band gap semiconductor and then E_{1s} follows the X band which is the point that corresponds to the absolute minimum band gap energy for these pressures. The conclusion drawn from these measurements is that the ground-state wave function for the donor electron in GaAs is made up of low lying Bloch states (with small wavevector) from a single conduction band minimum. This is an important property of effective mass states (shallow donors). This is not the case for deeply bound donors which are constructed from high and low lying Bloch states (with large and small wavevector, k) from many conduction band minima.

The E_{1s} level in $\text{Al}_x\text{Ga}_{1-x}\text{As}$

A similar tracking of E_{1s} to the Γ band is seen for $\text{Al}_x\text{Ga}_{1-x}\text{As}$ when the aluminum mole fraction, x , increases from 0 to 0.35 as is shown in Fig.(1.5). For $x > 0.37$, $\text{Al}_x\text{Ga}_{1-x}\text{As}$ crosses over from a direct band gap to an indirect band gap semiconductor and then E_{1s} tracks the X band as discussed above.

The levels discussed above are schematically (not to scale) represented in

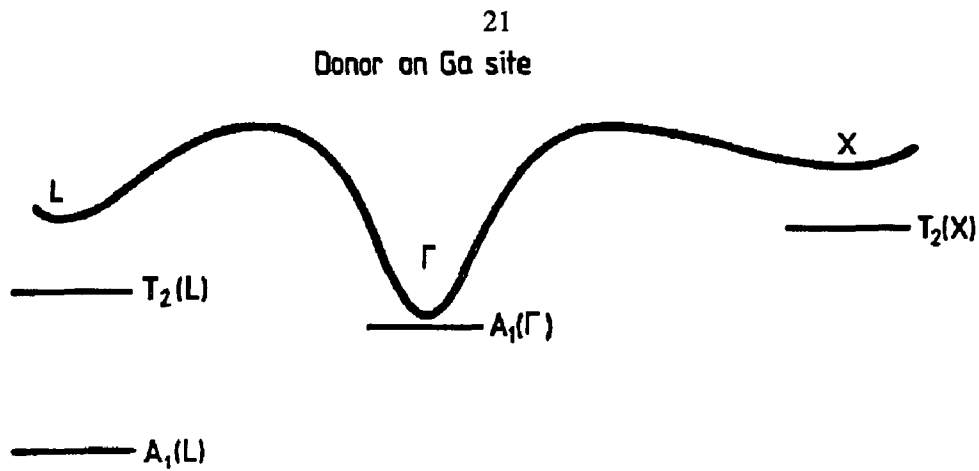


Fig.(1.6) The Si impurity donor levels associated with the three conduction band minima Γ , L, and X in GaAs (not to scale) [1.20].

Fig.(1.6). An important feature of the A_1 and T_2 states associated with the L and X minima in $Al_xGa_{1-x}As$ is that there are regions of aluminum mole fraction, x , where the states are resonant with the conduction band (i.e., above the conduction-band minimum) and regions where A_1 is a bound state. Both $T_2(L)$ and $T_2(X)$ are resonant conduction band states for all values of Al mole fraction. Whether $A_1(L)$ is resonant or bound depends on the Al mole fraction in $Al_xGa_{1-x}As$ as shown in Fig.(1.5) and is a bound state near $x=0.35$.

§E Deep substitutional Si impurity level, D^0

Introduction

If an external perturbation causes the neighboring As atoms around the Si substitutional impurity to move slightly, then the shallow substitutional Si levels, d^0 , can become deep while the Si atom still sits at its substitutional location. This more deeply bound state is referred to as a D^0 level. Hydrostatic pressure on GaAs is an example of such an external perturbation along with the strain field that occurs on the As atoms in $Al_xGa_{1-x}As$ from the mixture of neighboring Al and Ga atoms (nearest neighbor atoms of As).

The effective mass approximation (EMA) predicts the existence of shallow hydrogenic states for substitutional impurities in semiconductors. The EMA fails when the impurity levels become deep (i.e. E_{1s} is no longer much smaller than the band gap, E_{gap}). As discussed above, effective mass states from degenerate conduction band minima can be mixed by the impurity central cell potential and become deeper than what EMA predicts them to be. There is theoretical support for the existence of deep substitutional impurity levels of A_1 symmetry when the central cell potential of the impurity is taken into account. There are a number of different ways to calculate the effect of the central cell potential that either consider a position dependent dielectric constant of the impurity, $\epsilon(r)$, [1.21, 1.22, 1.23] or an interaction of the impurity with the nearest neighbor atoms [1.24, 1.25, 1.26]. In one case, Ref(1.25), the effect of the central cell potential is to produce a distortion or shift of the nearest neighbor atoms of the impurity with the impurity remaining in its

substitutional position.

Experimental evidence for D^0

There is experimental evidence for this deep substitutional A_1 state (D^0 level) [1.27, 1.28]. It has been observed by photoluminescence (PL) studies of Si, S, and Ge impurities in GaAs under hydrostatic pressure. All three impurities are resonant with the conduction band at zero pressure and become bound states with applied pressure (9kbar for Ge, 20kbar for S, and 29kbar for Si). Below these pressures, the donors are shallow and above these pressures the donors are deep bound substitutional levels. These donors do not exhibit evidence of moving from there substitutional position and becoming interstitial (between lattice sites) - i.e. are distinct from the deep interstitial impurities (DX centers) in that they do not exhibit persistent photoconductivity (PPC) (see Chapter 1, §F).

Deep donors which move to interstitial positions are quite complicated and are very distinct from substitutional donors. These interstitial donors are the subject of the next section and are critically important to this thesis. All that has been said so far about substitutional donors was intended as important background information leading up to the interstitial donor.

§F Deep interstitial Si donor in $\text{Al}_x\text{Ga}_{1-x}\text{As}$, the DX center

Introduction

When an impurity in a substitutional configuration shifts to a position between lattice sites (interstitial position) the physical, electronic, and equilibrium properties of the impurity donor drastically change. Shown in Fig.(1.7) is an example of a silicon impurity in GaAs moving from a substitutional position (Fig.(1.7a)) to an interstitial position (Fig.(1.7b)). The motion is along the cubic crystal [111] direction and the Si-As bond ruptures when the Si impurity moves to an interstitial configuration.

Although the substitutional Si impurity donor can be deeply bound, the interstitial Si donor is much more deeply bound. This is discussed quantitatively in terms of the amount of lattice relaxation associated with the deeply bound state. For the deep substitutional case of $\text{GaAs:Si}_{\text{Ga}}$ (Si substituting a Ga), the neighboring As atoms are calculated to shift by about 3% (0.07\AA) [1.30] in creating the deep A_1 substitutional impurity state, D^0 donor. Whereas for the interstitial configuration, the calculated distortion introduces a 1.17\AA shift of the Si atom away from one of its nearest neighbor (n.n.) As atoms along the [111] bond axis [1.29]. In addition to the Si atom shift, the bond length between the Ga and As atoms near the Si impurity are calculated to change by about 2.4% (0.06\AA). The large movement of the silicon and neighboring atomic rearrangement is referred to as a large lattice relaxation (LLR). When the silicon impurity is in the interstitial configuration with electrons bound to the impurity, it is referred to in the literature as a DX center [1.31]. The neighboring

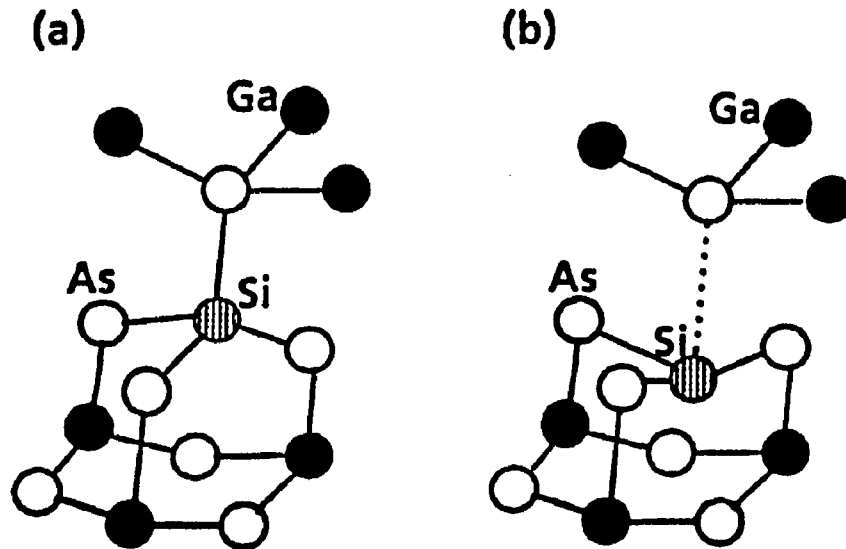


Fig.(1.7) The structural states of a Si donor atom in an AlGaAs alloy are shown. The structure shown in (a) is stable when the donor is in a positive or neutral state. The configuration in (b) occurs only for a negatively charged state (two electrons localized at the Si atom, see Chapter 1, §G, the charge state of the DX center). The relative stabilities of the two geometries is alloy dependent [1.29].

atomic movement of the deep substitutional donor, D^0 , is referred to as a small lattice relaxation (SLR).

The degree of lattice relaxation can be regarded as a measure of how strongly the lattice is coupled to the bound electron of the donor impurity. The deeply bound electrons extend only over a few lattice constants (say 10\AA). Because of this high degree of localization in space, they are superpositions of high and low lying (large and small wavevector, k) Bloch states from many different conduction band minima (i.e. Γ , L, X). This is in sharp contrast to shallow effective mass hydrogenic bound states that are spread out in space (Bohr radius of about 100\AA) and are superpositions of only a few low-lying (small wavevector, k) Bloch states from a single conduction band minimum.

Electron capture cross section

When the electron is deeply bound to an impurity, the impurity is referred to as a deep trap, since it traps the electron deep within the band gap and prevents it from moving freely within the semiconductor. The large lattice coupling suggests that phonons play a large role in the electron capture and emission process from the deep trap. This implies that the equilibration of electrons trapped at these deep levels with electrons in the conduction band occurs via multiphonon capture and emission processes (nonradiative processes). This leads to a highly temperature dependent electron capture cross section for electrons within the conduction band [1.32].

The high temperature limit of the electron capture cross section [1.33] has the form

$$\sigma_c^e = \sigma_\infty \exp(-E_c/kT) \quad \text{Eq.(1.3)}$$

where σ_∞ is between 10^{-14} and 10^{-15} cm^2 and E_c is the thermal capture barrier which depends on the aluminum mole fraction x in $\text{Al}_x\text{Ga}_{1-x}\text{As}$, $x > 0.22$ [1.34], and is between 0.15 and 0.45 eV with a minimum of 0.21 eV at $x = 0.35$ near the crossover from direct to indirect band gap material (see Fig.(1.11b)). The capture cross section is well described by Eq.(1.3) for $\text{Al}_x\text{Ga}_{1-x}\text{As}$, $x > 0.22$, with temperature above about 150K ($kT \approx 10 \text{ meV}$) where capture by a multiphonon process is dominant. Below this temperature, the cross section for capture by multiphonon process becomes sufficiently small that an optical capture process is dominant. The value of the critical temperature depends on the energy of the phonon mode involved in the multiphonon capture process. With the critical temperature being around 150K, this implies that the phonons involved in the capture process have an energy of about 10 meV or less. Shown in Fig.(1.8) is the phonon density of states in GaAs and it has a local

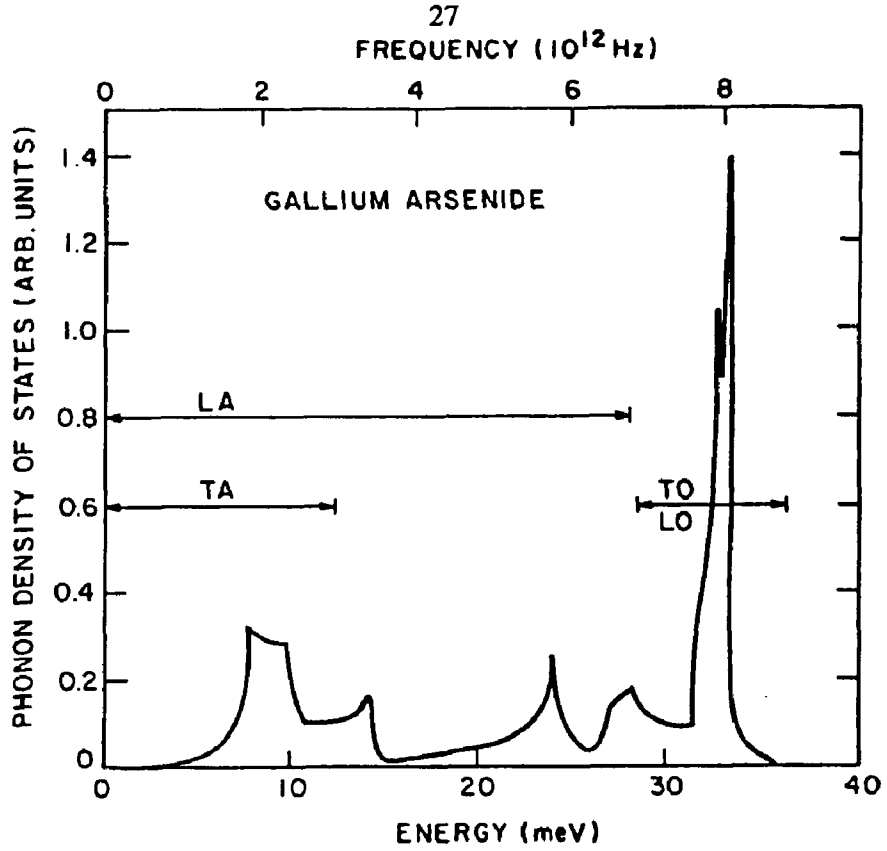


Fig.(1.8) Phonon density of states in GaAs [1.32].

maximum around 10meV (TA phonons) which makes the above phonon mode assignment plausible (a phonon density of states for $Al_xGa_{1-x}As$, $x > 0.22$, would be more relevant).

In the intermediate to low temperature regime ($T < 150K$), the electron capture cross section takes the form

$$\sigma = Af(0) = A(4\pi E_R kT^*)^{1/2} \exp(-E_c/kT^*),$$

$$kT^* = (\hbar\omega/2) \coth(\hbar\omega/2kT) \quad \text{Eq.(1.4)}$$

where A is a term involving only the electronic matrix element of the electron transition, $\hbar\omega$ is the average energy of the phonons to which the impurity is coupled, $E_R = S\hbar\omega$ is the lowering of the energy of the bound state due to lattice relaxation,

T^* is an effective temperature defined above in Eq.(1.4) [1.32]. At high temperature, $T^* = T$ and Eq.(1.4) shows the classical thermally activated capture first predicted by Mott [1.35]. At low temperature, $kT^* = \hbar\omega/2$ and the zero-point vibrations of the lattice play the role of temperature in promoting multiphonon emission (MPE) transitions. In the definition of E_R ($E_R = S\hbar\omega$) S can be regarded as the number of phonons needed to induce capture and hence is a qualitative measure of how strongly the impurity is coupled to the lattice.

Persistent photoconductivity (PPC)

At low temperatures ($T < 50\text{K}$) the electron capture cross section becomes very small and is less than 10^{-30}cm^2 [1.32]. This very small capture cross section leads to very long times for photoexcited carriers to remain in the conduction band before they are recaptured by the deep level or DX center. This effect leads to a large photoconductivity that persists for hours, or even days after the optical excitation is removed and is referred to as persistent photoconductivity (PPC). Shown in Fig.(1.9) is the effect of PPC on electron carrier concentration, N_s , for a Si doped $\text{Al}_x\text{Ga}_{1-x}\text{As}$ ($x=0.29$) epilayer sample (see Chapter 2 §B and §C for a discussion of samples). While warming the sample from cold temperatures, $T=10\text{K}$, N_s is seen to depend on whether or not the sample is illuminated or kept in the dark. The persistent ionization is evident by the difference of 2 orders of magnitude in the electron carrier concentration of the illuminated sample compared to the dark warmed case. When the sample is at a temperature ($T \approx 150\text{K}$ or higher) where the DX centers can equilibrate with the conduction band states on the time scale of the measurements, the carrier concentration for each case of illumination are the same, $T > 150\text{K}$ (warming at a rate

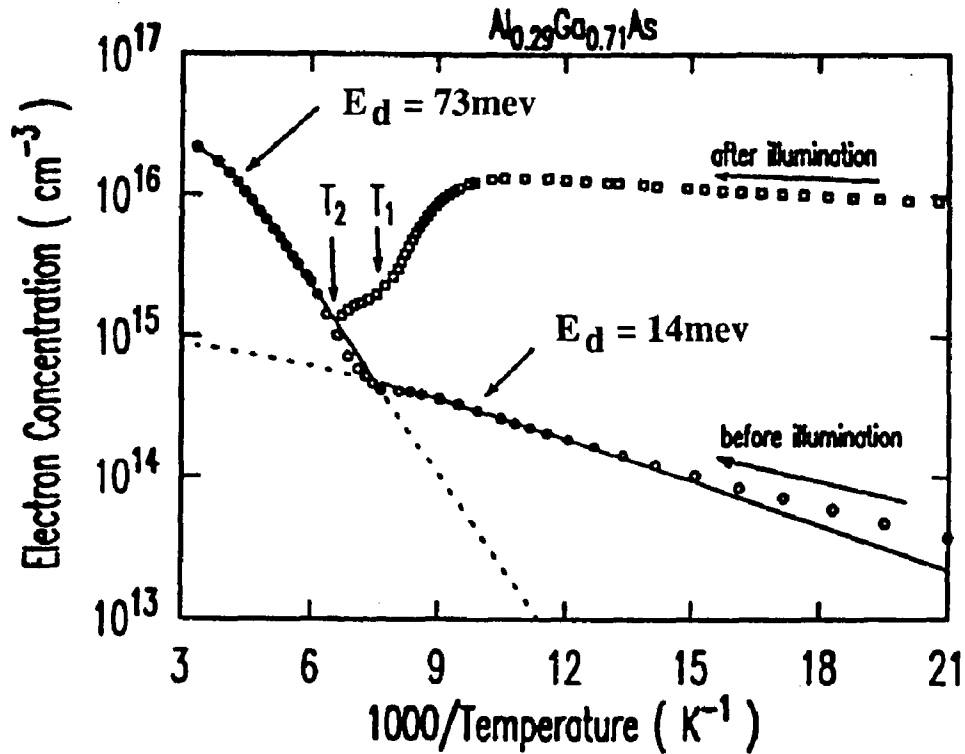


Fig.(1.9) Hall measurements of the free electron concentration as a function of reciprocal temperature in lightly doped $\text{Al}_{0.29}\text{Ga}_{0.71}\text{As}:\text{Si}$ [1.36].

of 2K/min.). The fits to the data in Fig.(1.9) show that freeze out (electron capture) in the low temperature region is to a shallow hydrogenic state with a thermal ionization energy of 14meV and the high temperature region shows that the electron is deeply trapped with a thermal ionization of about 73meV (ionization from the DX center) [1.36]. This is referred to within the literature as the *bistability of the silicon donor* in $\text{Al}_x\text{Ga}_{1-x}\text{As}:\text{Si}$, $x>0.22$.

Photoionization energy, E_0 , of the DX center

The electrons are trapped at low temperatures when the silicon impurity is in the interstitial configuration (DX center) and can be ionized by either warming up

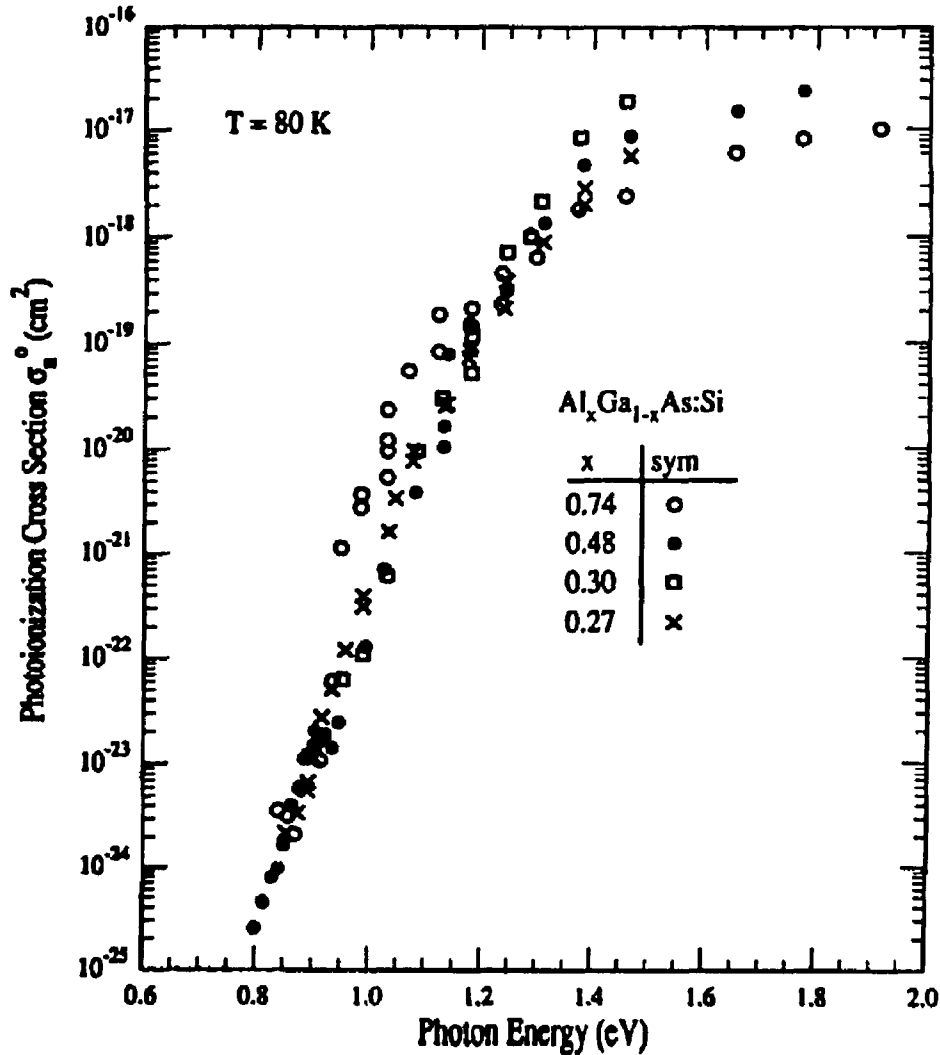


Fig.(1.10) Composite plot of photoionization cross sections for samples with four different Al mole fractions for $\text{Al}_x\text{Ga}_{1-x}\text{As:Si}$ doped epilayers. The vertical axis is logarithmic covering 9 orders of magnitude. The data are normalized at 1.3eV [1.37].

the sample to about 150K or shining light onto the sample. There is a photoionization threshold, E_0 , of about 0.8eV as shown in Fig.(1.10). This means that, in order to ionize the electrons from the DX centers in $\text{Al}_x\text{Ga}_{1-x}\text{As:Si}$ (Si doped) $x > 0.22$, the photon energy must be greater than about 0.8eV (wavelength of $1\mu\text{m}$).

From the temperature dependence of the photoionization cross section curve, a value for the dominant phonon mode for MPE can be estimated. Mooney et al. [1.38] did such a fit for an $\text{Al}_{0.33}\text{Ga}_{0.67}\text{As}:\text{Si}$ epilayer and found $\hbar\omega = 5.53\text{meV}$ which is consistent with the statement made earlier that the dominant phonon mode is around 10meV or less [1.32].

Thermal capture, E_c , and emission, E_e , energies of the DX center

Along with the thermal capture barrier, E_c , for electrons getting captured by DX centers, there is a thermal emission barrier, E_e , for electrons emitted from the DX centers. These are called thermal barriers since they involve the absorbing or emitting of many phonons by the electrons to overcome the barrier. Shown in Fig.(1.11) is how E_e and E_c depend on aluminum mole fraction in $\text{Al}_x\text{Ga}_{1-x}\text{As}$. The thermal emission barrier, E_e , is essentially independent of x indicating that it does not depend on the conduction band edge (Γ band for $x < x_c$ and X band for $x > x_c$). The thermal capture barrier has an x dependence since the energy of an electron in the conduction band depends on the position of the conduction band edge with respect to the valence band edge - i.e. the Γ and X band depend on Al mole fraction, x . The dependence of E_c on electron carrier concentration or Fermi level has been subtracted out so it is not a factor for the data in Fig.(1.11b). The minimum in E_c occurs at about $x = 0.35$ with $E_c = 210\text{meV}$ which is near the direct to indirect band gap cross-over at $x_c = 0.37$ (see Chapter 1, §B). These barriers can be measured by monitoring electrical capacitance transients while the temperature is varied around a value of about 180K . The emission or capture barrier is measured depending on whether or not the sample had been prepared with the traps filled or empty respectively. This

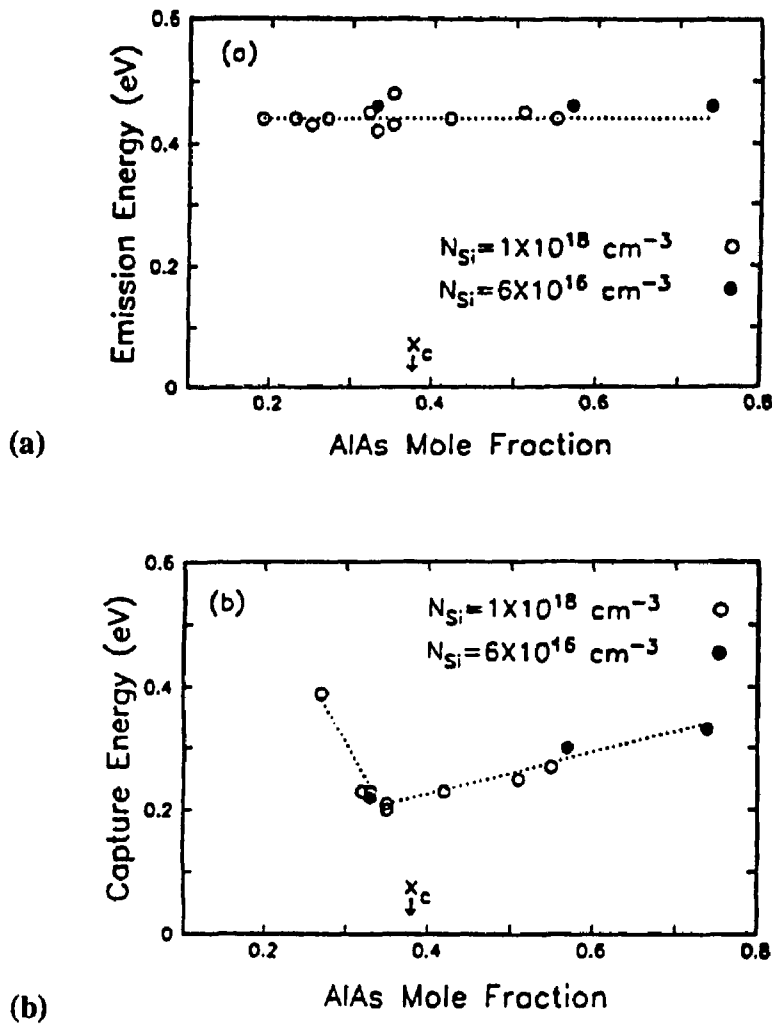


Fig.(1.11) (a) Emission energy of the DX center in Si-doped $\text{Al}_x\text{Ga}_{1-x}\text{As}$. (b) Capture barrier of the DX center in $\text{Al}_x\text{Ga}_{1-x}\text{As}$ measured with respect to the conduction band. The diodes have $6 \times 10^{16} \text{ Si/cm}^3$ and the MODFETs have $1 \times 10^{18} \text{ Si/cm}^3$ [1.39]. E_c and E_e are measured by DLTS [1.40].

technique briefly described above is referred to as deep level transient spectroscopy (DLTS) [1.40].

Thermal binding energy, E_d , of the DX center

The thermal ionization (or binding) energy, E_d , of the DX center in $Al_xGa_{1-x}As:Si$ $x > 0.22$ can be obtained by measuring the temperature dependence of the Hall electron concentration for temperatures above about 150K. For this temperature range, the electrons trapped by DX centers can equilibrate with the electrons in the conduction band on the order of a few minutes.

The electron concentration for this temperature range ($T > 150K$) is given approximately by

$$N_s = N_0 \exp(-E_d/kT) \quad \text{Eq.(1.5)}$$

so E_d maybe measured by finding the slope of an Arrhenius plot of the electron concentration versus temperature (see Ref(1.41) for a more accurate analysis). This has been done for the data shown in Fig.(1.9) and the DX center thermal ionization energy E_d is found to be $E_d=73\text{meV}$ for $x = 0.29$ in $Al_xGa_{1-x}As:Si$.

§G Lattice relaxations and the configuration coordinate diagram (CCD)

Introduction

A configuration coordinate diagram (CCD) is a qualitative way to help picture the lattice relaxation associated with a deep or shallow impurity level. The CCD is often confused with E versus k dispersion relations describing the semiconductor band structure, but is not related to it. The CCD shows how the total energy of the electronic energy and elastic lattice energy depend on how much the lattice is distorted. Most CCDs consider a distortion only in one dimension of a single impurity and therefore are simplified versions of the three dimensional case of the actual crystal.

Large lattice relaxation (LLR) of the interstitial silicon impurity in $\text{Al}_x\text{Ga}_{1-x}\text{As}:\text{Si}$ ($x > 0.22$)

A distinguishing feature of the DX center is the fact that the optical ionization energy barrier, $E_0 \approx 1.0\text{eV}$, is much greater than the thermal ionization barrier, $E_d \approx 0.1\text{eV}$ whereas for a shallow donor the two are equal ($E_0 \approx E_d$). In addition, the large barrier for electron capture, $0.2\text{eV} < E_c < 0.5\text{eV}$, is unusual for a deep trap and leads to a very small electron capture cross sections at low temperature ($T < 50\text{K}$) and the phenomenon of persistent photoconductivity (see Fig.(1.12b) for a schematic picture of the barrier between the conduction band and the DX center). The large atomic rearrangement that goes on when the silicon impurity moves to an interstitial

position in $\text{Al}_x\text{Ga}_{1-x}\text{As}:\text{Si}$ ($x > 0.22$) is responsible for the size of the barriers discussed above.

A qualitative semi-classical model of this interaction of the electron with the lattice relaxation (electron-phonon interaction) can be developed by considering the balance of a one-dimensional lattice energy $E_l(Q) = (\alpha/2)Q^2$ with a one-dimensional electronic energy $E_e(Q) = E_e^0 - \beta Q$. In these equations, Q represents the lattice distortion coordinate, Q_0 is the equilibrium position of the lattice, $E_l(Q)$ is the energy gained by distorting the lattice by Q , α is the lattice force or spring constant, $E_e(Q)$ is the electronic energy gained by a lattice distortion Q . The term E_e^0 of $E_e(Q)$ is the contribution to the energy from the purely electronic part of the Hamiltonian, $p^2/2m^* + V(r)$, where p is the momentum of the electron, m^* is the effective mass of the electron, and $V(r)$ is the electronic potential. Distorting the lattice by Q causes the depth of the electronic potential well $V(r)$ to change by $BQV(r)$. The term $BQV(r)$ in the Hamiltonian gives rise to the term $-\beta Q$ in the expression for $E_e(Q)$.

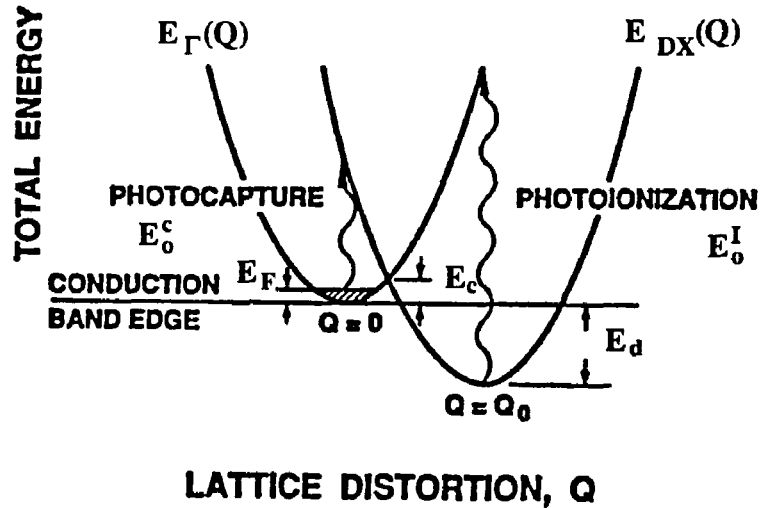
For electrons in the conduction band, vibrations of the lattice coordinate Q have no effect on the delocalized electrons but increase the energy of the lattice electron system so the total energy of the conduction band electrons, E_Γ , can be written as

$$E_\Gamma(Q) = (\alpha/2)Q^2. \quad \text{Eq.(1.6)}$$

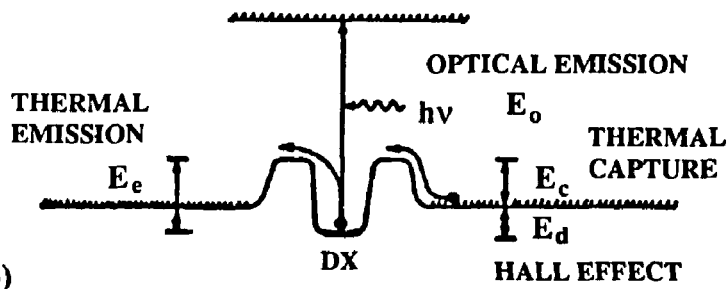
For electrons bound at the DX center, the total energy, E_{DX} , is written as a sum of lattice energy, $(\alpha/2)Q^2$, and the electronic contribution from the electron bound in a potential, $E_e^0 - \beta Q$, so then E_{DX} is

$$E_{DX}(Q) = (\alpha/2)Q^2 + E_e^0 - \beta Q. \quad \text{Eq.(1.7)}$$

Shown in Fig.(1.12a) is a sketch of Eq.(1.6) and Eq.(1.7) which are parabolas



(a)



(b)

Fig.(1.12) (a) The basic configuration coordinate model illustrating both photoionization and photocapture in the case of large lattice relaxation (LLR) [1.42]. (b) Summary of the measured quantities going into the LLR model [1.33].

with one centered at the origin and one centered at $Q_0 = \beta/\alpha$, which is the minimum of the DX state. The DX center equilibrium energy at Q_0 is $E_{DX}(Q_0) = E_e^0 - E_s$ with E_s the Stokes energy $E_s = \beta^2/2\alpha$, i.e. the lattice relaxation energy. The distorted DX state lies at an energy $E_d = E_s - E_e^0$ below the conduction band edge. For $Al_{0.3}Ga_{0.7}As:Si$ [1.8], $E_d = 0.073\text{eV}$ and $E_s = 1.0\text{eV}$ [1.33].

The DX center can be photoionized and the photoionization energy is given

by the difference in the total conduction band energy E_c at Q_0 and total DX center energy at the lattice coordinate Q_0

$$E_0^I = E_c(Q_0) - E_{DX}(Q_0) = E_s + E_d.$$

By examining Fig.(1.12a), it can be seen that no transitions, from the conduction band to the DX center, involving emission of photons can occur (compare with Fig.(1.13), an example of a small lattice relaxation where it can occur). This lack of radiative capture explains why photoconductivity persists (PPC) for a long time in these systems at low temperature.

The two parabolas sketched in Fig.(1.12) are referred collectively to as a configuration coordinate diagram in the literature and is a useful way to qualitatively discuss the interaction of electrons with the lattice. Configuration coordinate diagrams are used in most fields that are concerned with the electron phonon interaction - for example, electronic transitions in large molecules, i.e. proteins or polymers.

Photocapture is possible within this model and the transition takes place at $Q=0$ and crosses over to the distorted configuration at the undistorted resonant state of energy E_0^c . The threshold for this transition is

$$E_0^c = E_s - E_d.$$

Comparing E_0^I and E_0^c , E_0^c lies $2E_d$ below E_0^I . To date photocapture has not been observed. Hjalmarson et al. [1.42] did not detect this photocapture in a measurement where it should have been readily detected.

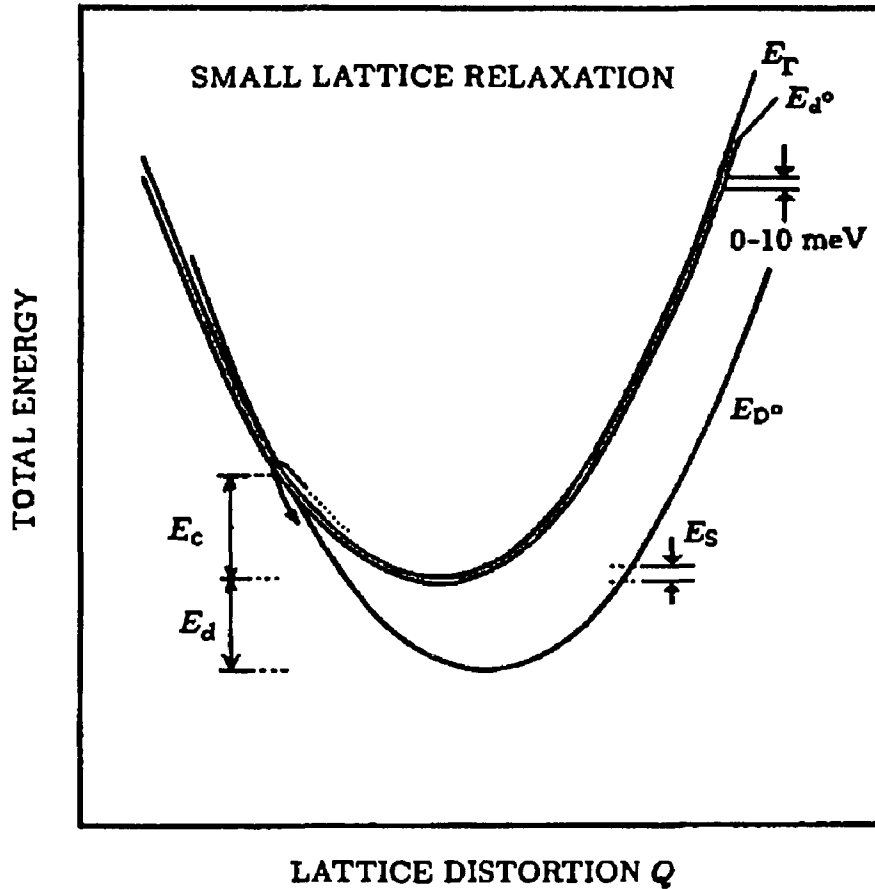


Fig.(1.13) Schematic configuration coordinate diagram for the small lattice relaxation [1.43]. This configuration corresponds to a bound D^0 level within the band gap. See Fig.(1.14) for an example of a resonant D^0 level (the parabola labeled $U_{\Gamma}+U_{D^0}$).

Small lattice relaxation associated with the deep substitutional silicon impurity in $Al_xGa_{1-x}As$

The A_1 symmetry state, D^0 , of the deep substitutional Si impurity has a lattice (Chapter 1, §E) distortion associated with it. The nearest neighbor As atoms shift by a few percent and lead to a difference in optical and thermal ionization energies ($E_0 \approx 40 \text{ meV}$, $E_d \approx 30 \text{ meV}$ [1.25]) that is much smaller than the case of the interstitial donor. Because the lattice distortion for the substitutional impurity is much smaller

than the distortion for the interstitial impurity, the parabolas making up the configuration coordinate diagram for the substitutional deep A_1 symmetry state, D^0 , are not shifted as much as for the deep interstitial DX state. The situation shown in Fig.(1.13) corresponds to a bound D^0 state since the minimum of the D^0 parabola is below the minimum of the Γ band parabola. If the D^0 minimum were above the Γ band minimum then the D^0 state would be a resonant state (as shown in Fig.(1.14), the parabola labeled as $U_{\Gamma}+U_{D^0}$). From Fig.(1.5), D^0 or $A_1(L)$ is a resonant state in $Al_xGa_{1-x}As$ for $x < 0.35$ and $x > 0.41$, it becomes a bound state around $x \approx 0.35$.

Since there is only a small lattice distortion associated with the D^0 state, an electron in the conduction band can make a transition to D^0 by emitting photons (if D^0 is a bound state). So radiative capture from the conduction band to the D^0 state can occur for the case of a small lattice relaxation. This is not possible for the DX center which exhibits a large lattice relaxation as illustrated in Fig.(1.12).

The charge state of the DX center, DX^- ground state

The substitutional Si impurity in $Al_xGa_{1-x}As$ ($x > 0.22$) can move into an interstitial location with the neighboring atoms and impurity atom going through a large nuclear rearrangement as discussed above (large lattice relaxation (LLR)). This bond-rupturing distortion is energetically favorable (stable) if the Si impurity binds two electrons in its interstitial position. This means that the charge state of the interstitial Si impurity is negative, i.e. the DX center has a negatively charged ground state, DX^- . This model of the microscopic structure for the DX center was proposed by Chadi and Chang [1.44] and is supported by a large body of experimental evidence [1.45].

The calculation of Chadi and Chang was based on a pseudopotential total-energy method. An eighteen atom hexagonal cell was used with its axis oriented along the Si-As bond rupturing direction [111]. Optimal atomic coordinates were determined by minimizing the total energy. The atomic coordinates were further optimized by tight-binding calculations on 144 atom cells. Physically this calculation involves moving the impurity atom and its neighboring atoms and then calculating the total energy of the distorted configuration. While this is done, one looks for a configuration of electrons and lattice distortion that is stable (minimizes the total energy). The major result of Chadi and Chang's calculation is that the large bond-rupturing lattice distortion of the Si impurity moving to an interstitial site (along the [111] crystal direction) is possible (stable) for the negatively charged Si impurity center (two electrons trapped at the DX center).

The neutral interstitial Si impurity state, DX^0 , is thought to be thermodynamically unstable but should play a role in all carrier capture and emission processes as an intermediate state of the distorted configuration. There is experimental evidence for the existence of this neutral DX^0 state and has a lifetime of a few seconds at low temperature ($T < 50K$). The DX^0 has a very weakly temperature dependent electron capture cross section ($DX^0 + e^- \rightarrow DX^-$) which means that even at low temperature ($T < 50K$, i.e. the PPC regime) the photogenerated DX^0 state captures the second electron. It also means that the barrier between DX^0 and DX^- cannot be high but a barrier must exist between DX^0 and the conduction band [1.46]. Dabrowski et al. [1.47] have calculated the neutral DX level, DX^0 , to be metastable lying about 1.0eV above the DX^- level with a thermal barrier on the order of 100meV.

The configuration coordinate diagram of Fig.(1.12) (LLR model of Lang and

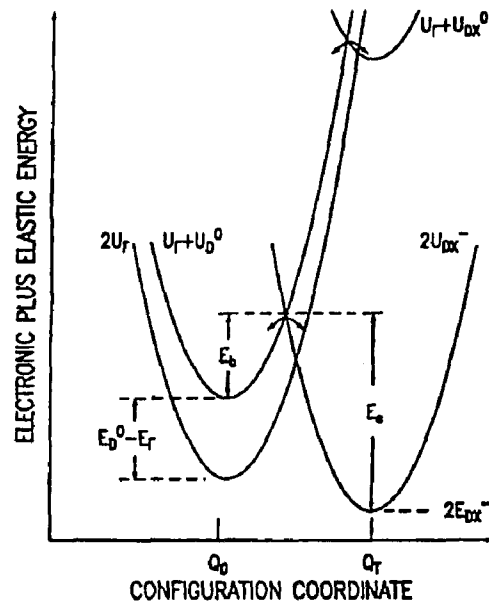


Fig.(1.14) Configuration coordinate diagram for the model of Chadi and Chang in direct-gap $\text{Al}_x\text{Ga}_{1-x}\text{As}$ ($0.22 < x < 0.37$) [1.48].

Logan) needs to be modified to incorporate the model of the DX center presented by Chadi and Chang and the two step ionization process ($\text{DX}^- \longleftrightarrow \text{DX}^0 + e^- \longleftrightarrow \text{d}^{0+} + 2e^-$). Illustrated in Fig.(1.14) is the modified configuration coordinate diagram of Chadi and Chang. The lower parabola on the left, centered at Q_0 , has two electrons in the conduction band. The upper left parabola, offset by a small amount to the right by a small lattice relaxation, has one electron in an A_1 symmetry deep substitutional donor, D^0 , and one in the conduction band. Hot electron capture transitions (Chapter 1, §H) from the conduction band to the DX^- state are assumed to occur via the D^0 level and it is thought to be an intermediate state for hot electron capture by the DX center (Chapter 1, §H). The two parabolas with minima near Q_T represent the distorted configuration of the DX center. The one-electron state of the distorted neutral

configuration, DX^0 , is the intermediate state of the two-step photoionization process described in Ref(1.49). The first step in this process ionizes one electron from the DX^- state to the conduction band, Γ , leaving the donor in the metastable DX^0 level. The neutral DX^0 can be ionized by another photon or return to the DX^- level by capturing an electron from the conduction band.

§H Electron Capture by the DX Center

Introduction

Electron capture by the DX center is of primary importance for electron transport in $Al_xGa_{1-x}As:Si$ epilayers at temperatures below around 200K. Hot electron capture by DX centers at these temperatures is of central importance to this thesis since this is the dominant process occurring in the far-infrared radiation (FIR) photo-Hall transport measurements described within this thesis [1.50].

Electron capture

In general, an electron can be captured by a trap via photocapture, thermal capture, (phonons) and hot electron capture from large electric fields. Photocapture has not been observed as discussed above [1.42]. Phonon assisted photocapture is possible within the CCD of Fig.(1.14) if photons induce a transition to the D^0 level and then a multiphonon capture process takes the electron from the D^0 level to the DX^- . The photon energy required for the phonon assisted photon capture is around 100meV but this resonant A_1 state, D^0 level, has not been directly observed (as an

intermediate state for electron capture) in spectroscopic studies. There is only indirect evidence for the A_1 state to be an intermediate state of the DX center for hot electron capture [1.51, 1.52].

Hot electrons

A hot electron is an electron within the conduction band that has an energy greater than all the electrons filling the lowest lying conduction band states. An electron attains energies greater than the conduction band minimum with the application of an electric field. In crystalline semiconductors with drift mobilities, μ_d , greater than about $50\text{cm}^2/\text{Vsec}$ [1.53], an electron will gain a drift velocity given by $v_d = \mu_d E$ (hence gain kinetic energy) and be heated to energies above the conduction band minimum. See Chapter 4, §C for a more detailed discussion of hot electrons in $\text{Al}_x\text{Ga}_{1-x}\text{As}$ semiconductors.

Experimental observations of hot electron capture

Electron capture by DX centers has been observed with the application of short DC voltage pulses across an $\text{Al}_x\text{Ga}_{1-x}\text{As}:\text{Si}$ $x > 0.22$ epilayer [1.52] with $\mu_d \approx 1000\text{cm}^2/\text{Vsec}$ at temperatures below 200K. The hot electron capture was observed to be phonon assisted for temperature above about 75K and to be athermal for temperatures below 75K which is believed illustrates the metastability of the resonant D^0 trap state [1.52]. This D^0 level is metastable in the sense that for sufficiently low temperatures electrons remain trapped at the D^0 level (the intermediate state, for hot electron capture, of the DX center).

Virtually identical temperature dependent hot electron capture was observed

in $\text{Al}_{0.3}\text{Ga}_{0.7}\text{As:Si}$ with the application of intense far-infrared radiation (FIR) ($E \approx 10\text{kV/cm}$ at 50cm^{-1} or 10^{12}Hz) instead of DC voltage pulses [1.50]. We propose the same hot electron capture mechanism as Theis et al. [1.52, 1.51] does for heating from DC voltage pulses, for the observed effect in FIR photo-Hall transport measurements presented here. See Chapter 3 for the photo-Hall transport data and Chapter 4 for a discussion of these data in terms of hot electron capture mechanism described above.

Chapter 1 references

1. N. W. Ashcroft and N. D. Mermin, **Solid State Physics** (Saunders College, Philadelphia, 1978) p. 76.
2. S. M. Sze, **Physics of Semiconductors**, 2nd Ed. (John Wiley & Sons, New York, 1981) p. 850.
3. K. Seeger, **Semiconductor Physics**, 4th Ed. (Springer-Verlag, New York, Berlin, Heidelberg, 1989) p. 25.
4. M. L. Cohen and J. K. Bergstresser, *Phys. Rev.* **141**, 789 (1966).
5. Since the L and X minima are elliptical energy surfaces, they have two distinct band curvatures which implies they are characterized by two effective masses; one for the two transverse directions, m_t , and one for the longitudinal direction, m_l . There are two ways to “average” these two effective masses to form either an effective conduction band effective mass or density of states effective mass for all the degenerate minima of a given symmetry point L or X. The conduction band effective mass is given by $m_c^\alpha = (2/m_{l\alpha} + 1/m_{t\alpha})^{-1}$, $\alpha=L$ or X , and the density of states effective mass is given by $m_{DOS}^\alpha = \gamma^{2/3} m_{l\alpha}^{2/3} m_{t\alpha}^{1/3}$, $\alpha=L$ or X , where γ is the number of equivalent minima. For values of $m_{l\alpha}$ and $m_{t\alpha}$ see S. Adachi, *J. Appl. Phys.* **58**, R1 (1985) and J. S. Blakemore, **Semiconductor Statistics** (Pergamon, New York, 1962) p. 76.
6. T. N. Morgan, *J. Elec. Mat.* **20**, 63 (1991).
7. D. J. Wolford and J. A. Bradley, *Solid State Comm.* **53**, 1069 (1985).
8. T. N. Theis, P. M. Mooney, B. D. Parker, *J. Elec. Mat.* **20**, 35 (1991).

9. H. C. Casey, Jr., and M. B. Panish, *J. Appl. Phys.* **40**, 4910 (1969).
10. T. F. Kuech, D. J. Wolford, R. Potemski, J. A. Bradley, K. H. Kelleher, D. Yan, J. P. Farrell, P. M. S. Lesser, and F. H. Pollack, *Appl. Phys. Lett.* **51**, 505 (1987); G. Oelgart, R. Schwabe, M. Heider and B. Jacobs, *Semicond. Sci. Technol.* **2**, 468 (1987).
11. H. C. Casey, Jr. and M. B. Panish, **Heterostructure Lasers** (Academic, New York, 1978), Part A, Table 4.2-1, p. 192.
12. W. Kohn, in **Solid State Physics**, editors F. Seitz and D. Turnbull (Academic Press, New York) **5**, 257 (1957).
13. C. M. Wolfe, N. Holonyak, G. E. Stillman, **Physical Properties of Semiconductors** (Prentice Hall, New Jersey) p. 89.
14. F. Bassani, G. Iadonisi, and B. Preziosi, *Rep. Prog. Phys.* **37**, 1099 (1974).
15. F. Bassani, G. Indonisis, and B. Preziosi, *Phys. Rev.* **B1**, 4673 (1970).
16. The caption of Fig.(1.4) says that $E_{1s}(X)$ is about 40meV. This is taken from a figure caption in Ref.(1.7) and nothing more is said about it within that reference. We will consider this value of 40meV to be in agreement with 36meV estimated above which is taken from Ref.(1.19).
17. The central cell potential can be regarded as that part of the impurity potential that produces the observed chemical shift discussed in table 1.1. Pseudopotential calculations are done to estimate the central cell potential [1.14]. There is not a simple analytic expression for the central cell potential.

18. T. N. Morgan, Phys. Rev. Lett. **21**, 819 (1968).
19. T. N. Morgan, Phys. Rev. **B34**, 2664 (1986).
20. J. C. M. Henning, J. P. M. Ansems, and P. J. Roksnoer, Semicond. Sci. Technol. **3**, 361 (1988).
21. L. Resca, R. Resta, Phys. Rev. Letts. **44**, 1340 (1980).
22. R. Resta, Phys. Rev. **B16**, 2717 (1977).
23. I. Resca and R. Resta, Sol. Stat. Comm. **29**, 275 (1979).
24. H. P. Hjalmarson, P. Vogl, D. J. Wolford, J. D. Dow, Phys. Rev. Letts. **44**, 810 (1980).
25. A. Oshiyam and S. Ohnishi, Phys. Rev. **B33**, 4320 (1986).
26. J. Dabrowski, M. Scheffler, and R. Strehlow, in **20th International Conference on Physics of Semiconductors**, Vol. 1, Editors E. M. Anastassalis and J. D. Joannopoulos (World Scientific, Singapore, 1990) p.489.
27. J. E. Dmochowski, P. D. Wang, and R. A. Stradling in **20th International Conference on Physics of Semiconductors**, Vol. 1, Editors E. M. Anastassalis and J. D. Joannopoulos (World Scientific, Singapore, 1990) p. 658.
28. X. Lin, L. Samuelson, M. E. Pistol, M. Gerling, and S. Nilsson, Phys. Rev. **B42**, 11791 (1990).
29. D. J. Chadi and K. J. Chang, Phys. Rev. **B39**, 10063 (1989).
30. A. Oshiyama and S. Ohnishi, Phys. Rev. **B33**, 4320 (1986).

31. Why the name DX center? Before the microscopic structure of the DX center was known (before 1990), it was thought to consist of a simple donor, D, near a defect complex, X, and so the name DX center. This historical name has remained to this day even though the DX center is now believed not to be associated with a defect, X.
32. D. V. Lang, **Deep Levels in Semiconductors**, edited by S. T. Pantelides (London and Breach, New York, 1986) p.489.
33. D. V. Lang, R. A. Logan, and M. Jaros, *Phys. Rev. B* **19**, 1015 (1979).
34. The DX center is a resonant state with the conduction band states for aluminum mole fraction x less than 0.22 and becomes a bound state when $x > 0.22$.
35. N. F. Mott, *Proc. Roy. Soc. London A* **167**, 384 (1938).
36. T. N. Theis, P. M. Mooney, and B. D. Parker, *J. Elec. Mat.* **20**, 35 (1991).
37. G. A. Northrop and P. M. Mooney, *J. Elec. Mat.* **20**, 13 (1991).
38. P. M. Mooney, G. A. Northrop, T. N. Morgan, and H. G. Grimmeiss, *Phys. Rev. B* **37**, 8298 (1988).
39. P. M. Mooney, *J. Appl. Phys.* **67**, R1 (1990).
40. G. L. Miller, D. V. Lang, and L. C. Kimerling, *Ann. Rev. Mat. Sci.*, 377 (1977).
41. J. E. Dmochowski, L. Dobaczawski, J. M. Langer, and W. Jantsch, *Phys. Rev. B* **40**, 9671 (1989).

42. H. P. Hjalmarson, S. R. Kurtz, and T. M. Brennan (submitted).
43. E. Yamaguchi, *J. Phys. Soc. Japan* **56**, 2835 (1987).
44. D. J. Chadi and K. J. Chang, *Phys. Rev. Letts.* **61**, 873 (1988); D. J. Chadi and K. J. Chang, *Phys. Rev.* **B39**, 10063 (1989); D. J. Chadi and K. J. Chang, *Phys. Rev. Letts.* **60**, 2187 (1988).
45. P. M. Mooney, **Semiconductor Science and Technology** (Symposium on DX centers and other metastable Defects, Austin, February 1991).
46. P. M. Mooney, G. A. Northrop, T. N. Morgan, and H. G. Grimmeiss, *Phys. Rev.* **B37**, 8298 (1988); M. F. Li, P. Y. Yu, E. R. Weber, and W. Hansen, *Phys. Rev.* **B36**, 4531 (1987); R. Legros, P. M. Mooney, and S. L. Wright, *Phys. Rev.* **E35**, 7505 (1987).
47. J. Dabrowski, M. Scheffler, and R. Strehlow, **20th Int. Conf. on the Physics of Semiconductors**, edited by E. M. Anastassakis and J. D. Joannopoulos (World Scientific, Singapore, 1990) p. 489.
48. T. N. Theis, *Proc. of the Mat. Res. Soc.* (Boston, December 1990) (to be published).
49. L. Dobaczewski and P. Kaczor, *Phys. Rev. Letts.* **66**, 68 (1991).
50. J. J. Plombon, W. W. Bewley, C. L. Felix, M. S. Sherwin, P. F. Hopkins, M. Sundarum, and A. C. Gossard, *Appl. Phys. Letts.* **60**, 1972 (1992).
51. Private communication with T. N. Theis.
52. T. N. Theis and B. D. Parker, *Appl. Sur. Sci.* **30**, 52 (1987); T. N. Theis, B.

D.Parker, P. M. Solomon, and S. L. Wright, *Appl. Phys. Lett.* **49**, 1542 (1986);
T. N. Theis, *Inst. Phys. Conf. Ser.* **91**, 927 (1988); T. N. Theis, B. Parker, P.
M. Solomon and S. L. Wright, **Proc. 18th Intern. Conf. on the Physics of
Semiconductors**, Ed. O. Engstrom (World Scientific Publishing, Singapore,
1987) p. 927.

53. Amorphous (noncrystalline) semiconductors have such low mobility $\mu_d < 10 \text{ cm}^2/\text{Vs}$ that the notion of a drift mobility no longer physically makes sense (see R. A. Smith, *Semiconductors*, 2nd ed. (Cambridge University Press 1978) p.483).

Chapter 2

Samples, Equipment, and Experimental Technique

Introduction

This chapter is divided into three parts. Part I discusses the samples studied and details about molecular beam epitaxy (MBE) which was used to grow the samples. Part II covers the equipment that was used to make the measurements discussed in this thesis. Part III discusses the details of making the measurements and the importance of doing photo-Hall transport measurements for determining the electron carrier concentration of the samples studied

Part I, Sample details

The purpose of part I is to discuss the samples and a few of the important details of the molecular beam epitaxial [2.1] growth (MBE) useful to the researcher studying MBE grown samples. All the GaAs/Al_xGa_{1-x}As samples studied in this thesis were grown by using the technique of MBE. M. Sundaram and P. F. Hopkins of the U.C.S.B. Material Science Department grew the samples.

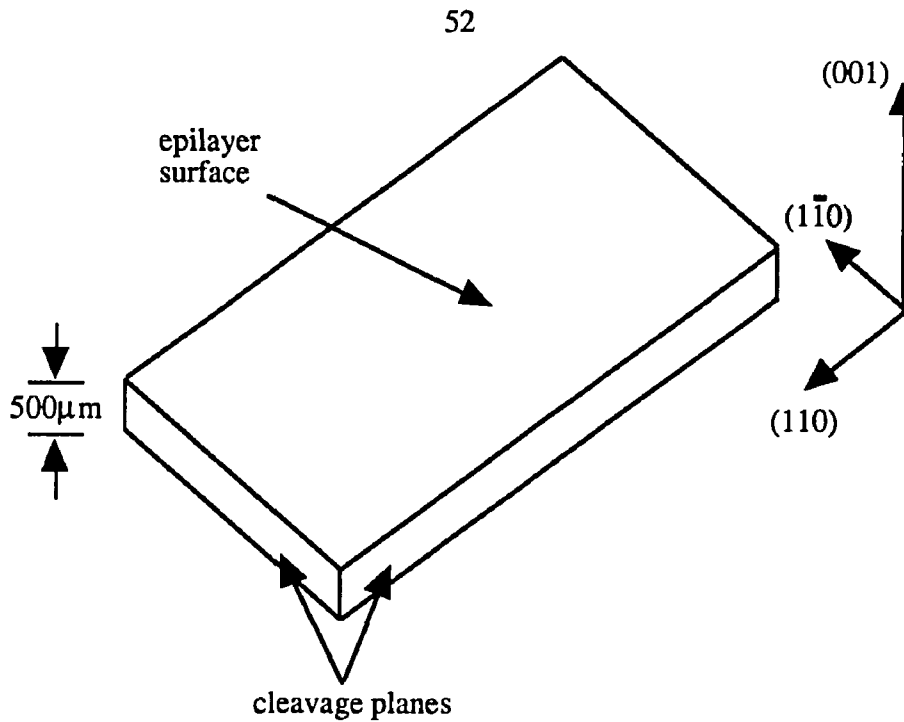


Fig.(2.1) Cleavage planes (110) and (1-10) and growth direction (001) for GaAs substrates used for samples studied in this thesis.

§A MBE grown $\text{Al}_x\text{Ga}_{1-x}\text{As}/\text{GaAs}:\text{Si}$ semiconductors

Introduction

The MBE epilayers are grown on either semi-insulating (SI) GaAs or n^+ -GaAs substrates. The SI-GaAs substrates have impurity concentrations of around 10^{14} to 10^{15}cm^{-3} with the primary impurity atom being carbon. The n^+ -GaAs substrates have been doped with about $5 \times 10^{18}\text{cm}^{-3}$ silicon donors. All the samples studied in this thesis have been grown on SI-GaAs substrates. The n^+ -GaAs substrates are useful when the substrate itself is used as an ohmic contact. All the substrates used for samples in this thesis have cleavage planes in the (110) or (1-10) directions with the epilayers being grown in the (001) direction as shown in Fig.(2.1). All of the

substrates were 500 μm thick.

MBE growth

Atomic layers can be grown by MBE. Layers 50 \AA thick are quite common with a limiting thickness of around 3 \AA (1/2 a lattice constant) corresponding to a layer one atom thick. Such atomic or monolayers are grown within an ultra high vacuum of 10^{-10} to 10^{-11} torr. A molecular beam of Gallium (Ga) and Arsenic (As) is created by heating up crucibles of Ga and As to temperatures above their heat of vaporization and heat of sublimation respectively. Typically this corresponds to about 800 $^{\circ}\text{C}$ for Ga and 360 $^{\circ}\text{C}$ for As. These temperatures give a growth rate for Ga of about 1 $\mu\text{m/hr}$ and a flux of about 5 μtorr for As. The group III element determines the growth rate. The As is kept at a high flux to ensure plenty is around as the group III element growth takes place. A molecular beam of aluminum (Al), Ga, As, and Si dopant atoms can be made with the addition of Al and Si crucibles operated at about 1000 $^{\circ}\text{C}$ and 1300 $^{\circ}\text{C}$ respectively.

Monolayers are grown on the substrates by keeping the substrates at a temperature around 600 $^{\circ}\text{C}$. This allows the atoms to move around a small amount as the monolayers are grown hence facilitating the crystalline growth of the epilayer (many monolayers). The temperature the crucibles are operated at determine the rate at which the monolayers grow to form an epilayer. The temperatures quoted above produce a growth rate of about 1 μm per hour and will vary from MBE machine to MBE machine (This assumes that the crucibles are not too depleted of material, if they are then they need to be operated at a higher temperature as is common with the As crucible.). For more details of the science of MBE growth see [2.2].

The GaAs substrates are not smooth on the monolayer scale so before any sample layers are grown a series of about 20 Al_{0.3}Ga_{0.7}As/GaAs quantum wells (periods of 20Å Al_{0.3}Ga_{0.7}As followed by 20Å of GaAs) are grown. Growing this series of 20 wells (superlattice), produces an epilayer on the surface of the substrate that is smooth on the monolayer scale [2.3].

With the growth of the superlattice, the epilayer of the substrate is smooth enough to allow the growth of a quantum well. A heterostructure is grown by growing 1000Å to 1µm of GaAs then abruptly changing to growing Al_{0.3}Ga_{0.7}As for about 200Å and then adding Si to the Al_{0.3}Ga_{0.7}As layer for about another 200Å. Then a GaAs cap layer of about 200Å is grown on top of the Al_{0.3}Ga_{0.7}As layer to prevent the aluminum in the Al_{0.3}Ga_{0.7}As layer from oxidizing.

Graded structures

One way of controlling the aluminum mole fraction, x , in an Al _{x} Ga_{1- x} As layer is by controlling the temperature of the aluminum and gallium crucibles. The higher the temperature of the crucible the larger the aluminum mole fraction, x , in the Al _{x} Ga_{1- x} As epilayer. So growing an Al_{0.3}Ga_{0.7}As layer requires that the growth rate for Al be 0.3µm/hr and Ga be 0.7µm/hr. This translates to temperatures of 960°C for the Al and 840°C for the Ga. An important point to realize is that an increase of 50 to 60°C in the crucible temperature will result in changing the growth rate from 0.1µm/hr to 1.0µm/hr. If the temperature of the crucible is varied with time as the Al _{x} Ga_{1- x} As layers are grown, the aluminum mole fraction will vary spatially in the growth direction. The energy gap varies with mole fraction as [2.4]

$$E_{\text{gap}}^{\Gamma}(x) = 1.424 + 1.247x \quad (0 < x < 0.45).$$

A spatially varying Al mole fraction leads to a spatial variation in the conduction and valence band. This spatial variation of the conduction and valence band produces potential wells on the length scale of 10\AA to 100\AA . The conduction band discontinuity $\Delta E_c(\text{eV})$ between GaAs and $\text{Al}_x\text{Ga}_{1-x}\text{As}$ layers is predicted [2.5] to be

$$\Delta E_c(x) = (1.1x)\text{eV}.$$

For a typical quantum well, the maximum aluminum mole fraction is 0.3 and the minimum is 0.0. This gives a quantum well depth of about 300meV . With the potential wells on the order of a 100\AA in width, quantum mechanical effects arise for an electron confined in the well [2.6]. This is why such GaAs/ $\text{Al}_x\text{Ga}_{1-x}\text{As}$ wells are referred to as quantum wells.

Digital alloying

The technique of digital alloying to grow a quantum well is significantly different from that of smoothly varying the aluminum mole fraction. With digital alloying the mole fraction is either a maximum, typically 0.3, or a minimum, typically for parabolic wells 0.02. A GaAs/ $\text{Al}_x\text{Ga}_{1-x}\text{As}$ superlattice is grown with a 20\AA period of the GaAs/ $\text{Al}_x\text{Ga}_{1-x}\text{As}$ wells having a spatially varying duty cycle. An example of such a structure with its effective conduction band potential is shown in Fig.(2.2). The duty cycle of the GaAs and $\text{Al}_{0.3}\text{Ga}_{0.7}\text{As}$ 20\AA period superlattice is varied quadratically which produces a parabolic potential well in the conduction and valence band. It is not obvious that this digital alloying will produce a parabolic well for an electron confined in the digital alloy superlattice. Self-consistent quantum mechanical calculations [2.7, 2.9] and experiments [2.8, 2.10] have shown that the digital alloying shown in Fig.(2.2) does indeed produce a parabolic potential

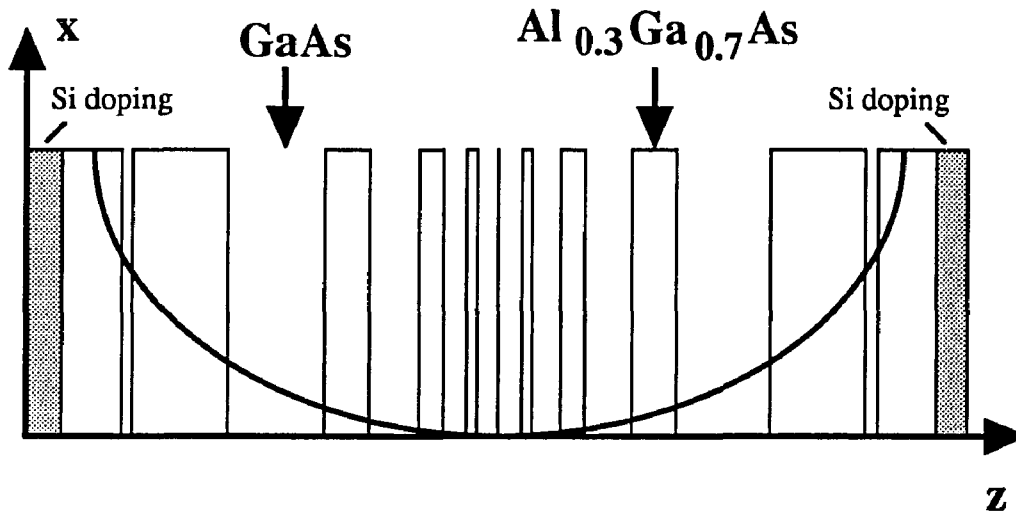


Fig.(2.2) Schematic of a digitally alloyed parabolic well. A 20\AA period superlattice is grown with each period consisting of one layer of GaAs and one layer of $\text{Al}_{0.3}\text{Ga}_{0.7}\text{As}$. The duty cycle of these two layers is varied quadratically during the growth, such that the average Al content if integrated over the superlattice approaches the solid parabola shown in the figure.

well for an electron confined within it. The technique of digital alloying [2.7,2.8] has been used for all the parabolic and half-parabolic quantum wells studied in this thesis.

Silicon doping

Silicon doping of the GaAs/ $\text{Al}_x\text{Ga}_{1-x}\text{As}$ quantum well (Si is substitutional with Ga) donates electrons to the quantum well. The electrons have very high mobilities on the order of a $100,000\text{cm}^2/\text{Vs}$ at liquid helium temperatures when the Si atoms are placed in the $\text{Al}_x\text{Ga}_{1-x}\text{As}$ epilayer outside the quantum well. The Si doping outside of the quantum well is referred to as modulation doping [2.11]. The reason the mobility is so high is that the electrons are removed from their donor Si

atoms and hence the ionized impurity scattering is greatly reduced. The distance between the Si atom doping in the $\text{Al}_x\text{Ga}_{1-x}\text{As}$ epilayer and the edge of the quantum well is on the order of 100\AA .

Typical Si atom concentrations in the $\text{Al}_x\text{Ga}_{1-x}\text{As}:\text{Si}$ epilayer is between 10^{17} to 10^{18}cm^{-3} . The back ground impurity concentration in a GaAs epilayer is around 10^{14} to 10^{15}cm^{-3} . This back ground impurity is primarily a carbon acceptor. The presence of the carbon acceptor in GaAs epilayers produces p-type doping for the GaAs layer in an $\text{Al}_x\text{Ga}_{1-x}\text{As}/\text{GaAs}$ heterostructure (2DEG).

The $\text{Al}_x\text{Ga}_{1-x}\text{As}$ barrier layer of the heterostructure is doped with silicon which makes it an n-type material. The modulation doping of the $\text{Al}_x\text{Ga}_{1-x}\text{As}$ layer gives the $\text{Al}_x\text{Ga}_{1-x}\text{As}/\text{GaAs}$ interface a negative charge of electrons from the Si atoms. The electrons are attracted to the interface because of the Coulomb attraction to the positive Si ions in the $\text{Al}_x\text{Ga}_{1-x}\text{As}$ region. The electrons at the interface are localized within a region on the order of 100\AA wide which produces a two dimensional electron gas (2DEG) at the interface of the heterostructure.

§B Band structures for samples studied

The three basic $\text{Al}_x\text{Ga}_{1-x}\text{As}/\text{GaAs}$ structures studied in this thesis were an $\text{Al}_{0.3}\text{Ga}_{0.7}\text{As}:\text{Si}$ $2\mu\text{m}$ thick Si doped epilayer, an $\text{Al}_{0.3}\text{Ga}_{0.7}\text{As}/\text{GaAs}$ heterostructure (2DEG) and a digital alloyed half-parabolic well. The $\text{Al}_{0.3}\text{Ga}_{0.7}\text{As}:\text{Si}$ epilayer was used to study the effect of FIR on electron capture and emission by and from DX centers. The half-parabolic well and heterostructure were used to investigate ionization or real-space transfer of electrons from the well or 2DEG to the $\text{Al}_x\text{Ga}_{1-x}$.

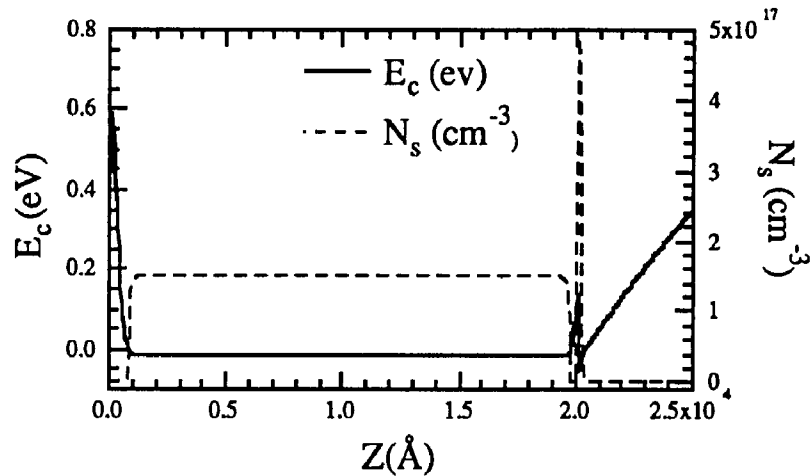
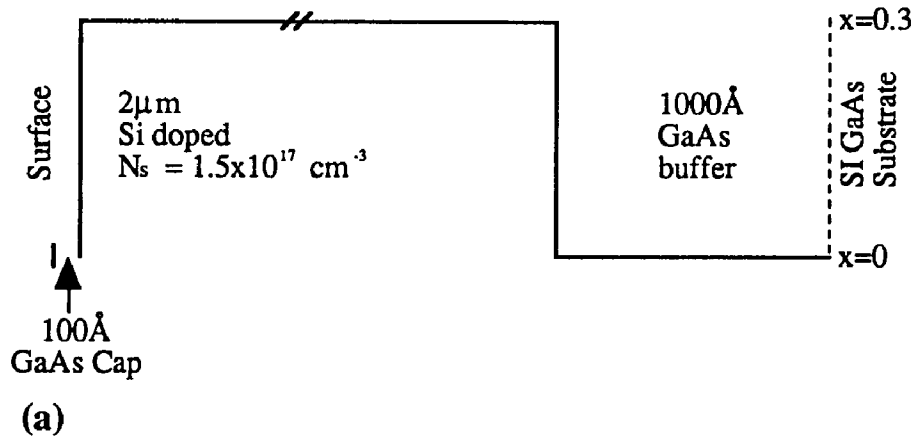


Fig.(2.3) (a) Schematic diagram of the MBE growth of an $\text{Al}_{0.3}\text{Ga}_{0.7}\text{As}:\text{Si}$ $2\mu\text{m}$ thick epilayer without an undoped $\text{Al}_{0.3}\text{Ga}_{0.7}\text{As}$ buffer layer. (b) The band diagram and electron distribution for the $\text{Al}_{0.3}\text{Ga}_{0.7}\text{As}:\text{Si}$ epilayer. Note the population of the unintentional 2DEG at the GaAs substrate interface.

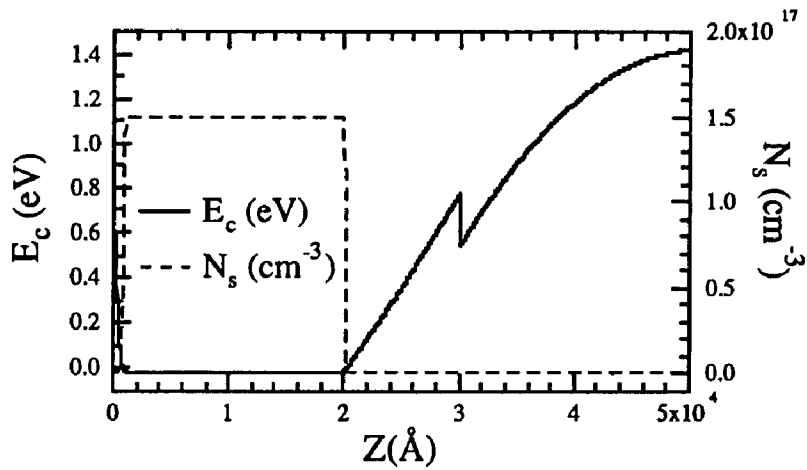
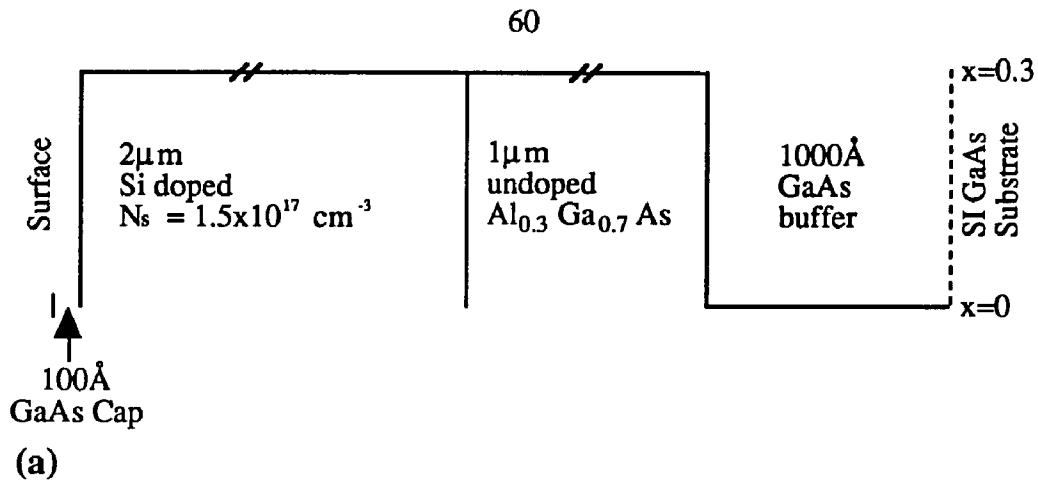
x As barrier layer.

$\text{Al}_x\text{Ga}_{1-x}\text{As}:\text{Si}$ epilayer

Two $\text{Al}_{0.3}\text{Ga}_{0.7}\text{As}:\text{Si}$ epilayers were studied in connection with the effect of FIR on electron transport in the presence of the DX center. The first one studied did

not have an undoped $\text{Al}_{0.3}\text{Ga}_{0.7}\text{As}$ buffer layer between the GaAs substrate and the Si doped $\text{Al}_{0.3}\text{Ga}_{0.7}\text{As}$ epilayer. The schematic diagram of the MBE growth, band structure, and electron charge distribution are shown in Fig.(2.3). The important aspect of Fig.(2.3b) is that the GaAs substrate interface is populated with a large amount of electrons. The band structure and electron charge distribution were the results of a self-consistent quantum mechanical calculation [2.12]. No superlattice was grown between the GaAs substrate and the 1000\AA GaAs buffer layer. The $2\mu\text{m}$ thick $\text{Al}_{0.3}\text{Ga}_{0.7}\text{As}$ epilayer was doped with a silicon atom concentration of $1.5 \times 10^{17}\text{cm}^{-3}$. The surface layer depletion depth for this carrier concentration (200\AA) is much less than the $2\mu\text{m}$ thickness of the epilayer [2.32]. The 100\AA GaAs cap layer is always grown to prevent the oxidation of the Aluminum in the $\text{Al}_{0.3}\text{Ga}_{0.7}\text{As}:\text{Si}$ epilayer. The presence of the unintentional 2DEG shown in Fig.(2.3b) is very troublesome and complicates transport measurements done on samples that have this 2DEG populated (see Chapter 2, §J). An undoped $\text{Al}_{0.3}\text{Ga}_{0.7}\text{As}$ buffer layer between the GaAs and the Si doped $\text{Al}_{0.3}\text{Ga}_{0.7}\text{As}:\text{Si}$ epilayer helps prevent the population of the substrate interface 2DEG if it is sufficiently thick.

The conduction band and electron distribution for an $\text{Al}_{0.3}\text{Ga}_{0.7}\text{As}:\text{Si}$ epilayer identical to Fig.(2.3) except for the presence of an undoped $\text{Al}_{0.3}\text{Ga}_{0.7}\text{As}$ epilayer is shown in Fig.(2.4). As can be seen from Fig.(2.4b), the effect of having an undoped $\text{Al}_{0.3}\text{Ga}_{0.7}\text{As}$ epilayer is to raise the substrate interface 2DEG about 0.8eV above the Fermi level at low temperatures. This greatly simplifies transport measurements since the electron concentration in the substrate interface 2DEG is very small compared with the electron concentration within the doped $\text{Al}_{0.3}\text{Ga}_{0.7}\text{As}:\text{Si}$ epilayer. A self-consistent calculation predicts that there will be no electrons populating the



(b)

Fig.(2.4) (a) Schematic diagram of the MBE growth of an $\text{Al}_{0.3}\text{Ga}_{0.7}\text{As}:\text{Si}$ epilayer with an undoped $\text{Al}_{0.3}\text{Ga}_{0.7}\text{As}$ buffer layer between the doped epilayer and substrate. (b) The conduction band and electron distribution corresponding to the epilayer structure in (a). Note that the 2DEG at the substrate interface is not populated with electrons.

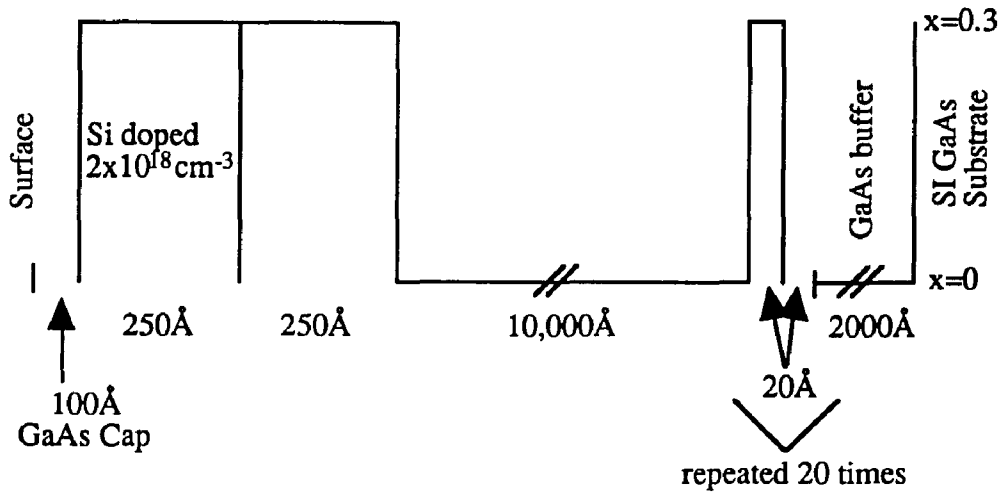
substrate interface 2DEG. There will probably be a very small concentration of electrons in the substrate interface 2DEG. Measurements of the Hall mobility provide a crude measure of whether or not the unintentional 2DEG is populated (see Chapter 2, §J).

Al_xGa_{1-x}As/GaAs heterostructure

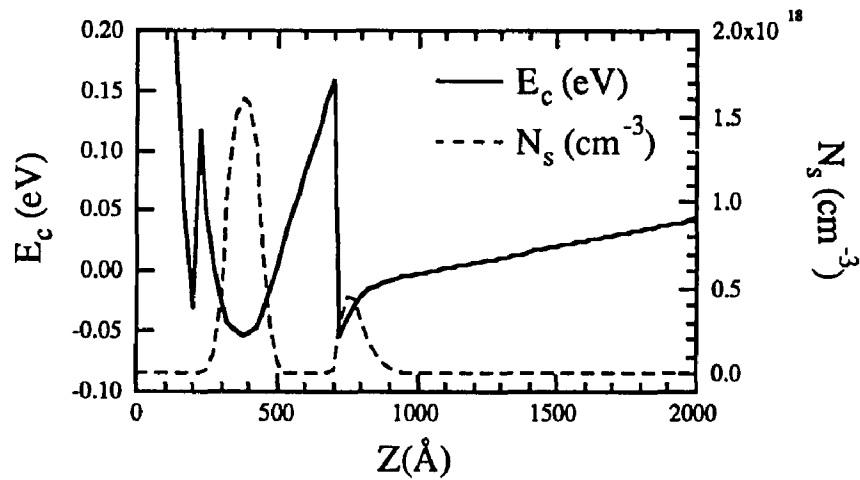
Two Al_{0.3}Ga_{0.7}As/GaAs heterostructure were studied in this thesis and are referred to as 2D-12c and 2D-2a. One of the 2DEGs (2D-12c) was used to investigate real-space transfer of electrons by intense FIR (Chapter 5) and the other (2D-2a) was used to investigate photovoltaic responses to intense FIR (Chapter 6). There is not anything significantly different between the two 2DEGs. The reason the two different samples were studied is that the measurements done with them were about one year apart which means that different samples were available at the time of the measurements. Only the details of heterostructure 2D-12c are presented.

The MBE growth and band structure shown in Fig.(2.5) are typical of Al_xGa_{1-x}As/GaAs heterostructures. The GaAs semi-insulating substrate has a 2000Å GaAs buffer layer followed by the substrate smoothing superlattice of 20 periods. Immediately after the superlattice the actual heterostructure growth is begun with 1µm of GaAs and then 250Å of undoped Al_{0.3}Ga_{0.7}As and another 250Å of Si doped Al_{0.3}Ga_{0.7}As. This completes the actual heterostructure growth. The last layer is a 200Å GaAs cap layer.

Hall mobility and electron concentration were measured and found to be $\mu_H = 125,000 \text{cm}^2/\text{Vs}$ and $N_H = 3 \times 10^{11} \text{cm}^{-2}$ at 8K in the dark. The Hall mobility and electron concentration measured while the sample was saturated with light from a LED were $\mu_H = 320,000 \text{cm}^2/\text{Vs}$ and $N_H = 5 \times 10^{11} \text{cm}^{-2}$. The areal density of $N_H = 3 \times 10^{11} \text{cm}^{-2}$ corresponds to a bulk dopant density of $6 \times 10^{18} \text{cm}^{-3}$ (The sample was delta doped at $2 \times 10^{18} \text{cm}^{-3}$ in 10Å in increments within the Si doped Al_{0.3}Ga_{0.7}As layer which corresponds to $2 \times 10^{11} \text{cm}^{-2}$ since $10 \text{Å} = 10^{-7} \text{cm}$ then $N_{2D} = (N_{3D}) 10^{-7} \text{cm}$).



(a)



(b)

Fig.(2.5) (a) Schematic diagram of the MBE growth of an $\text{Al}_{0.3}\text{Ga}_{0.7}\text{As}/\text{GaAs}$ heterostructure. (b) The conduction band and the electron distribution corresponding to the heterostructure shown in (a).

Assuming that half of the dopants go to surface depletion the measured areal density is within a factor of 3 of the growth parameters.

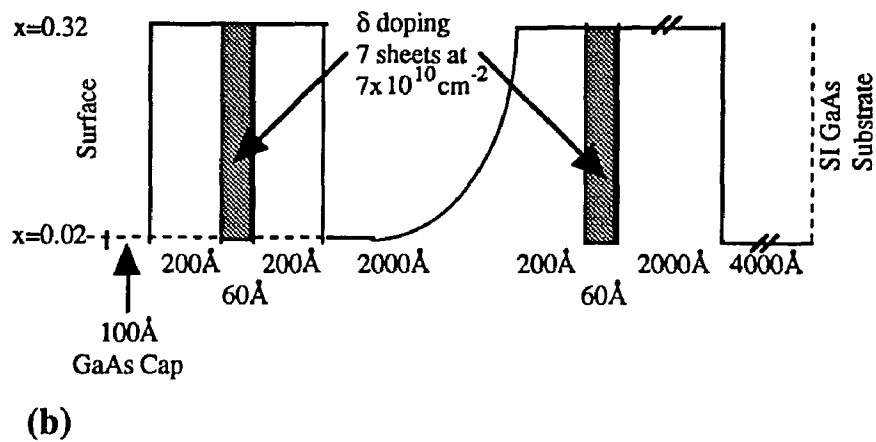
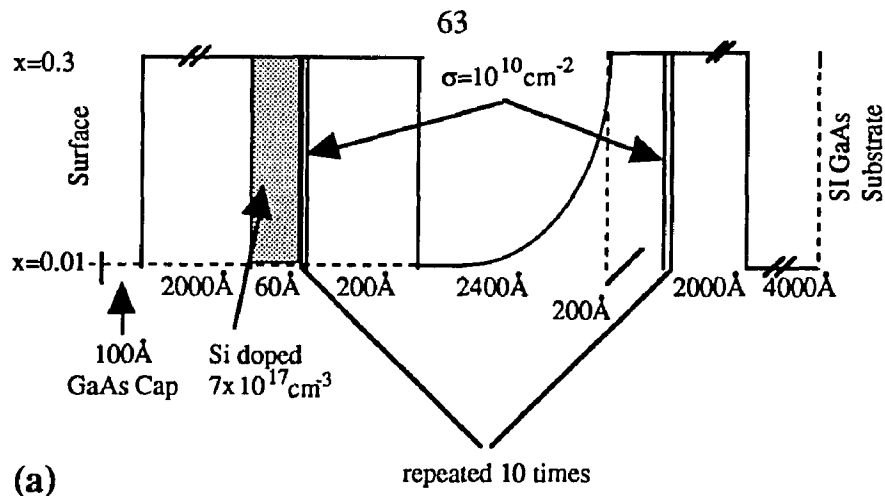


Fig.(2.6) (a) MBE growth schematic for the 10 half-parabolic well sample HPB-2. (b) MBE growth schematic for the single half-parabolic well sample HPB-3.

Half-parabolic $\text{Al}_x\text{Ga}_{1-x}\text{As}/\text{GaAs}$ quantum wells

Two half-parabolic quantum wells were studied in the context of real-space transfer, or ionization of electrons from the well (see Chapter 5). Real-space transfer is the transfer of electrons from the high mobility well region to the low mobility $\text{Al}_x\text{Ga}_{1-x}\text{As}:\text{Si}$ region of the quantum well structure. They are referred to as HPB-2 and HPB-3.

One of the half-parabolic wells, HPB-2, was grown for studying 2nd harmonic generation in the FIR. It was made up of a superlattice of 10-half parabolic wells grown by digital alloying as shown in Fig.(2.6a). The structure was doped so as to have 10^{10}cm^{-2} electrons per well. It seems that most of the charge was in the first well closest to the surface. A serious problem with this structure was the uncertainty of where the charge was through the course of an experiment. Diode flashing, illuminating with visible or IR light, seemed to help distribute the charge throughout the wells but this was never for certain.

A sample with a single half-parabolic well was also studied in the context of real-space transfer. A schematic of the MBE growth is shown in Fig.(2.6b). The digital alloyed half-parabolic well was grown to be 2000\AA wide with 7 sheets of delta doping of $0.7 \times 10^{11}\text{cm}^{-2}$ of Si on both sides of the well. The Hall mobility and electron concentration were measured, after a short period of illumination from an LED at 8K, to be $\mu_{\text{H}} = 40,000\text{cm}^2/\text{Vs}$ and $N_{\text{H}} = 1.5 \times 10^{11}\text{cm}^{-2}$. After saturating the sample with illumination, the Hall mobility and electron concentration were found to be $\mu_{\text{H}} = 100,000\text{cm}^2/\text{Vs}$ and $N_{\text{H}} = 5.1 \times 10^{11}\text{cm}^{-2}$. With the sample saturated with illumination the well was over-filled and parallel conduction (electron conduction in the $\text{Al}_{0.3}\text{Ga}_{0.7}\text{As}:\text{Si}$ layer) was taking place.

§C Sample processing and contact geometry

Introduction

Most of the samples studied in this thesis required only very simple sample processing. The photo-Hall measurements only required a mesa etch and annealing

of ohmic contacts. Some of the samples used to study photovoltaic responses required a Schottky gate along with ohmic contacts. Attempts were made to try and control the depths of the annealed ohmic AuGe/Ni/Au contacts but were not successful and the experiment was subsequently redesigned.

Processing procedures

The very first step in processing the sample is to clean the sample. Some sample cleaving may precede cleaning but the final cleaving may not take place until all the processing is completed. A standard cleaning processes was followed: acetone to clean off organic matter, isopropyl alcohol to clean off the acetone, and then deionized water (D.I. water) to clean off the isopropyl alcohol. The sample is then blow dried with high purity nitrogen gas.

If a mesa (an elevated table top portion of the sample) etch is required, it should be done next. This step usually involves photolithography. First a thin ($\approx 1\mu\text{m}$ thick) photoresist layer is spun on the surface of the sample. The thickness of photoresist films depends on the spin speed and the viscosity of the photoresist. The samples processed for the photo-Hall measurements needed to have a mesa $4\mu\text{m}$ thick in order to get down to the SI GaAs substrate. A photoresist (Shipley AZ4330) that was about $3\mu\text{m}$ thick after spinning at 6000 rpm was used. (When a $4\mu\text{m}$ thick mesa is etched any feature $8\mu\text{m}$ or less wide will be etched away since the etcher not only chemically dissolves material beneath it but also material at the sides of the edges of the mesa so make sure the features are larger than $10\mu\text{m}$ or resort to a dry etch procedure.) After the photoresist is spun, the mesa geometry is transferred to the photoresist via exposure to UV light through an emulsion or metal mask. The mask

is aligned with the edges of the sample using a mask aligner. After the exposure, the photoresist is developed and the mesa pattern remains on the sample with the rest of the photoresist developed away. The developer used was a solution of 50% D.I. water and 50% Shipley developer.

Now the sample is ready to be wet etched with a solution that chemically dissolves GaAs and $\text{Al}_x\text{Ga}_{1-x}\text{As}$ without dissolving the photoresist. The etch solution is 14 parts D.I. water (42ml), 5 parts phosphoric acid (15ml), 1 part hydrogen peroxide (3ml) and will etch at a rate of about $7,000\text{\AA}/\text{min}$. The thickness of the mesa is periodically checked with a Dektak II profiler (an instrument used to measure films on a substrate as thin as 50 to 100\AA and up to about $100,000\text{\AA}$). The Dektak can also be used to calibrate the etch rate of the etcher solution. The etch is stopped by rinsing the sample in D.I. water. Once the mesa is the correct height, the photoresist layer over the mesa is removed with acetone and the sample is again cleaned as described above.

The next step is evaporating ohmic contacts onto selected areas of the mesa. The contact geometry is specified using photolithography similar to how the mesa geometry was photographically transferred onto the photoresist. Once again, a mask aligner is used to align the contact pattern with the mesa geometry. The metalization used for all ohmic contacts in this thesis was 1000\AA of AuGe then 200\AA of Ni followed by 1000\AA of Au as a wire bonding cap layer. The gold cap layer is only necessary if a mechanical wire bonder is going to be used. In that case, the thickness of the gold layer should be at least 1500\AA if not 2000\AA . The photoresist layer covers all of the sample except those areas that will be ohmic contacts. After evaporation, the sample is placed in an acetone solution which dissolves the acetone and hence

lifts off all of the metal that was deposited on the photoresist. It seemed that most every time liftoff was done some specks of gold were left behind on regions originally covered with photoresist. So it is important that any region that will eventually be covered with a metal gate be covered with a copper shadow mask. This assumes that the sample and gate surface are relatively large (at least a few millimeter square). The reason for this added precaution is that an ohmic contact speck left behind from a poor lift off will act like a short from the gate to the 2DEG if the speck lies on the gate region. After lift off, the contacts are annealed at about 400 to 420°C for about 3 to 5 minutes. After annealing the contacts, the contacts should be checked to make sure they are ohmic (i.e. that they have a linear I-V curve). If they are not ohmic, more annealing is necessary.

If the contacts are not ohmic after more annealing, then there is a problem with the sample and or contacts and a new sample should be processed. It is important to check if the contacts are ohmic at low temperature because many times contacts that are linear at room temperature become nonlinear (Schottky) at low temperature ($T < 50\text{K}$).

Once the ohmic contacts have been successfully annealed and the gate region is clear of metal flakes from liftoff (determined from examination of the gate region with a microscope), it is worth while to attempt to evaporate a Schottky gate onto the gate region of the sample. Once again the contact region is specified using photoresist as was done for the ohmic contacts. If large samples are being used, use copper shadow masks to prevent unwanted metalization of selected surfaces. The metalization for the Schottky contacts is 400Å of Ti (to help the gold stick to the semiconductor) followed by at least 1000Å of Au. The author has been told that the

better the vacuum in the evaporator used make the contact the better the gate will be. A good vacuum in the e-beam evaporator in the Engineering II cleanroom is about 5×10^{-7} torr. Many times the Au on the gate is used to help confine the FIR within the quantum well and it is important that the gold layer is thicker than the FIR skin depth into the gold (At least 1000 \AA of Au if not 1500 \AA , since the FIR skin depth is about 300 \AA for gold). If a photoresist was used to specify the Schottky contact, then lift off should be done and the sample cleaned one last time.

The next step is to test to see if the gate is Schottky. This is done by measuring an I-V curve between an ohmic contact and the gate. A good Schottky gate will have a nonlinear (diode like) I-V curve with a forward turn on voltage of about 1.0 Volt corresponding to the height of the Schottky barrier at the metal-GaAs surface (see Chapter 6, §B).

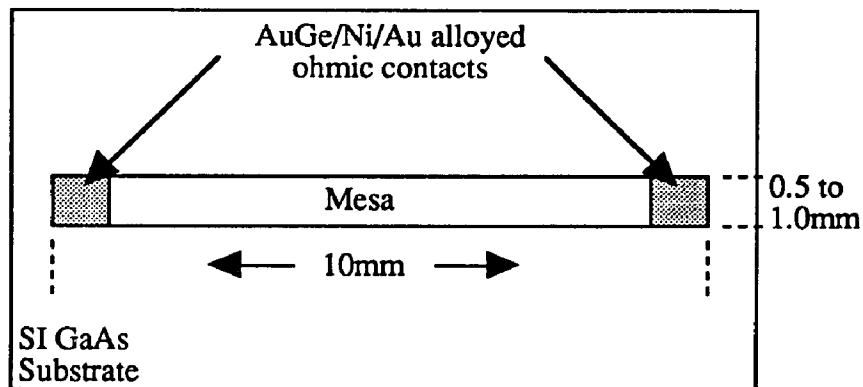
As a final step for preparing an experiment, the sample should be mounted and wires bonded to the contact pads. The sample is usually G. E. varnished (General Electric no. 7031) to a copper sample holder that bolts onto a cold finger of a cryostat. Wires from the cryostat are connected to a small PC board which acts as a strain relief for fine gold wires which run from the sample to the PC board. The fine gold wires are silver painted to the contact pads on the sample and to solder lugs on the PC board. The wires may fail (pop off) upon cooling the sample in the cryostat if they have not been allowed to dry thoroughly. For best results, let them dry overnight but if pressed do the wire bonding first then continue with the rest of the experimental setup by the time you are ready to cool the sample a few hours will have passed and the silver paint should have dried sufficiently well.

If the sample is larger than 5mm square, do not G. E. varnish the entire sample

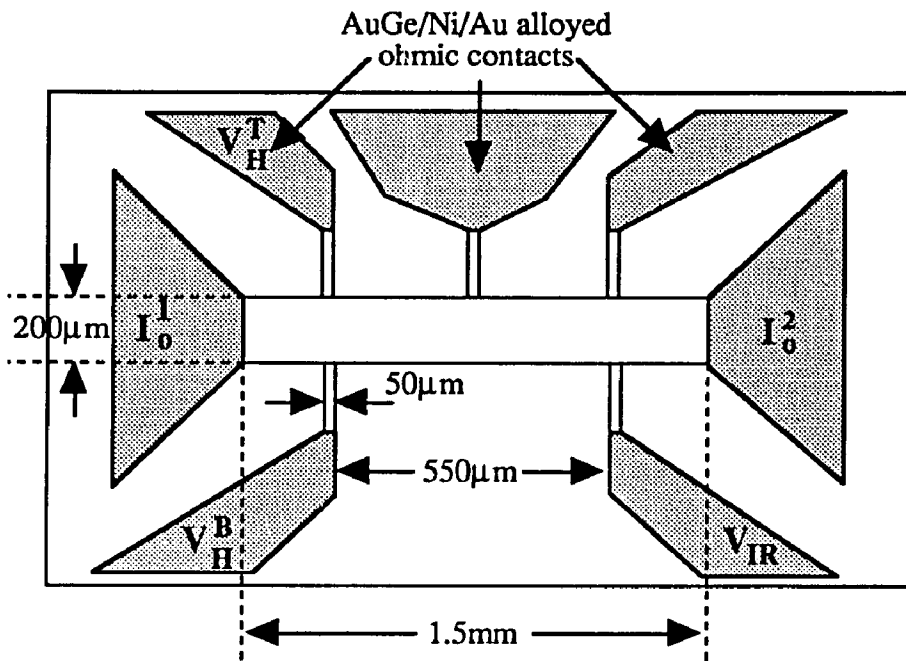
to the sample holder. The author has repeatedly cracked samples 12mm by 6mm by G. E. varnishing the entire sample to the sample holder. Since the entire cold finger contacts by about 2mm when cooling to 10K from 300K. This large sample was successfully cooled when only a small dot (about 2mm in diameter) of G. E. varnish was used to hold the sample in place.

Contact and mesa geometries

The contact and mesa geometries used for investigating photovoltaic response to intense FIR in $\text{Al}_x\text{Ga}_{1-x}\text{As}/\text{GaAs}$ systems are shown in Fig.(6.2) of Chapter 6, §D. We were attempting to measure ionization of electrons from a quantum well by measuring the photoconductivity of the sample in the presence of intense FIR. The evolution of the contact and mesa geometries used to investigate photovoltaic responses is discussed in Chapter 6. A valuable lesson can be learned from the contact geometry of Fig.(6.2a). This was the first attempt made at an eventually abandoned scheme of trying to contact to the quantum well and a shallow ohmic contact to the first $\text{Al}_{0.3}\text{Ga}_{0.7}\text{As}$ epilayer not shorting to the quantum well in the process. The contact to the quantum well is simple enough if you etch the correct depth. The shallow ohmic contact proved to be so difficult we simply gave up trying. Talking with A. Kastalsky [2.13] about the problem after we had given up made us realize that obtaining a shallow contact with AuGe/Ni/Au metalization is a hopeless task. If the reader needs shallow ohmic contacts, collaborate with A. Kastalsky and have his colleagues process the samples for you. The valuable lesson to be learned here is to never trust anybody you might think is painting a rosier picture than you might think possible especially if it is a field that is new to you. One final important



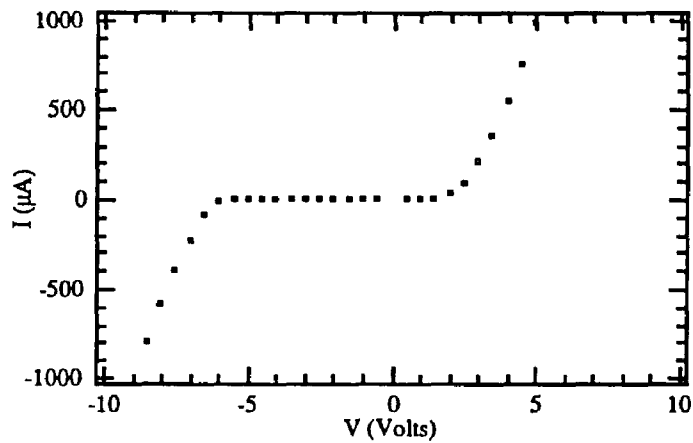
(a)



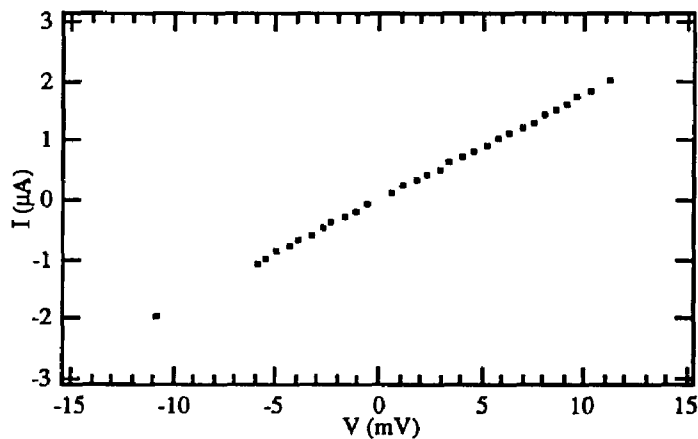
(b)

Fig.(2.7) Top view of the mesa and contact geometry for the (a) photoconductivity measurements and (b) Photo-Hall measurements. The rectangle surrounding the mesa and contact geometry is the edge of the sample.

lesson: do your own processing if it is simple enough and give up the project if the processing is too complicated (this assumes you are with the physics department,



(a)

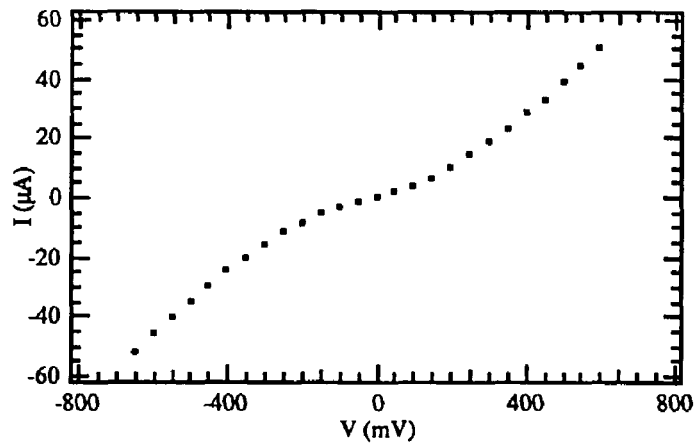


(b)

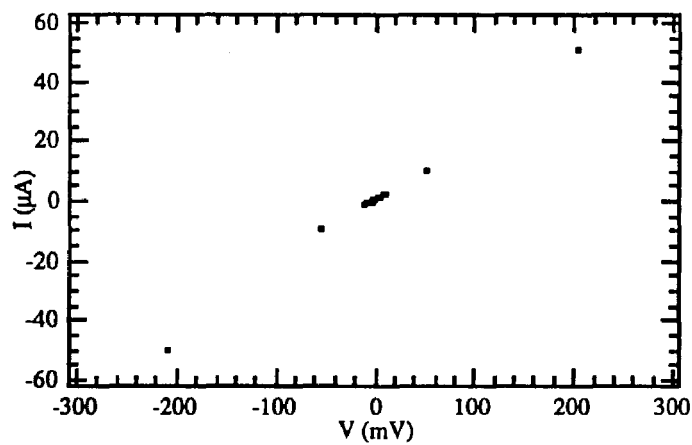
Fig.(2.8) (a) I-V curve for the contacts, I_0^1 and I_0^2 , at the end of the Hall bar shown in Fig.(2.7b). (b) I-V curve for the two Hall contacts V_H^B and V_H^T shown in Fig.(2.7b).

leave the heroic processing for the engineers).

The contact and mesa geometry used to study photoconductivity in an $Al_xGa_{1-x}As/GaAs$ systems is shown in Fig.(2.7a). Two mesa widths were studied 0.5mm and 1.0mm. The mesas were chosen to be narrower than the diameter of the focused FIR beam which was typically 1.5 to 3 mm in diameter for both the TEA laser



(a)



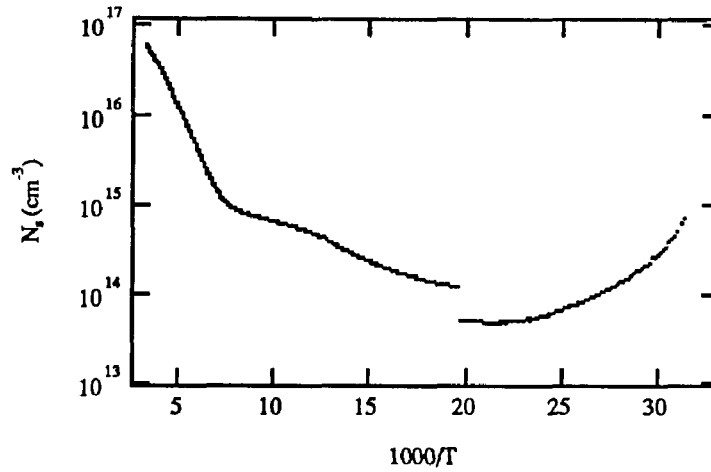
(b)

Fig.(2.9) (a) I-V curve for the contacts V_H^B and V_R shown in Fig.(2.7b).
 (b) The I-V curve for the contacts V_H^B and V_H^T for large bias voltages showing a slight deviation from ohmic conduction.

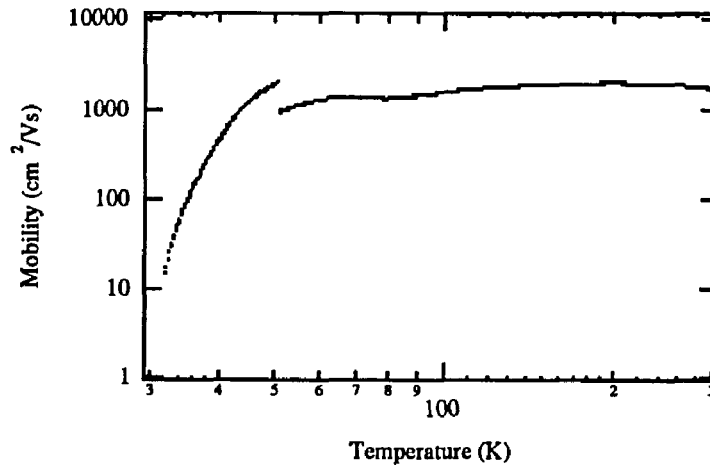
and the FEL. The mesas were about 10mm long leaving about 7mm between ohmic contacts. The reason for choosing such a long mesa was to avoid illuminating the contacts with intense FIR of the focused beam.

The contact and mesa geometry used for the photo-hall measurements in an $Al_{0.3}Ga_{0.7}As:Si$ epilayer is shown in Fig.(2.7b). All seven contact tabs were

73



(a)



(b)

Fig.(2.10) (a) Hall electron concentration as a function of $1000/T$. Two glitches are seen at $1000/T = 19.8$ ($T=50.5\text{K}$) and $1000/T = 12.9$ ($T=77.5\text{K}$). (b) Hall mobility as a function of temperature. Two glitches are seen at the temperature 50.5K and 77.5K

metalized with 1000\AA of AuGe then 200\AA of Ni followed by 1000\AA of Au. The sample was annealed for 4 minutes at about 410 to 430°C .

Quality of the ohmic contacts of the Hall bar

At room temperature, all seven contacts were ohmic. Not all the contacts

were used. The contacts marked with I_0^1 and I_0^2 in Fig.(2.7b) were used to supply the bias current. These two contacts were Schottky at temperatures below about 50K and started to deviate from being ohmic at around 100K. The I-V curve taken around 40K for the two current contacts (I_0^1, I_0^2) is shown in Fig.(2.8a).

The Hall voltage was measured between the V_H^B and V_H^T contacts shown in Fig.(2.7b). The I-V curve taken at about 40K for the contacts used to measure the Hall voltage (V_H^B, V_H^T) is shown in Fig.(2.8b). The I-V curve shows that the Hall voltage tabs were ohmic at 40K.

The sample conductivity or resistance was measured from the IR voltage drop between contacts V_H^B and V_{IR} as shown in Fig.(2.7b). The I-V curve for the contacts used to measure the conductivity is shown in Fig.(2.9a). The contacts are seen to deviate slightly from being ohmic. This deviation is more pronounced than the deviation from ohmic conduction shown in Fig.(2.9b) which shows the I-V curve between V_H^B and V_H^T at large bias voltages.

It is important to be aware of these deviations in ohmic conduction (nonlinear) because they lead to glitches in Hall electron concentration, N_H , and Hall mobility, μ_H , data as shown in Fig.(2.10). The glitches occur when changing the constant current through the Hall bar. The glitch at 50K corresponds to decreasing I_0 from $5\mu A$ to $1\mu A$. The glitch at 77K corresponds to decreasing I_0 from $10\mu A$ to $5\mu A$ - i.e. not linearly dependent on current.

Part II, Equipment used

Equipment to be discussed will be the usual list of cryostat, sources of FIR, and electronics. The discussion will also include a specially built apparatus for the photo-Hall measurements. The apparatus was a small permanent magnet assembly that fit over the sample holder and bolted onto the cold finger of the cryostat. The experimental techniques section will include discussions of how the FIR was coupled to the sample and a discussion of how the photovoltaic, photoconductivity, and photo-Hall measurements were done.

§D Cryostats

The primary cryostat used was a variable temperature cold finger with four windows for optical access (Andonian model #MHD-31-30N). The other optical access cryostat used was a continuous flow cryostat with a strip line or horn geometry for coupling the FIR into the sample. This cryostat and coupling geometry will not be discussed here since a description is given by C. L. Felix [2.14]. Some other cryostats were used for transport measurements done in collaboration with the U.C.S.B. Material Science Department. These cryostats were setup for standard Hall and Shubnikov de Haas transport measurements and will not be discussed further. Both M. Sundaram and P. F. Hopkins of the U.C.S.B. Material Science Department did transport measurements using the above mentioned cryostats on some of the samples studied in this thesis.

Polypropylene windows were used so as to minimize FIR loss. The windows are porous to He₂ gas so He₂ exhaust gas should be carefully vented to avoid developing a poor vacuum over time. Heater tape was used around the large o-ring seal at the top of the cryostat to keep it from freezing and hence losing the vacuum.

The temperature could be regulated between 8K and 300K by means of a needle valve, high resistance heater wire, and a Lake Shore Cryotronics DRC 82C temperature controller with a Lake Shore temperature diode (DT-470 standard). The heater wire was wrapped around the base of the sample holder near the Lake Shore temperature sensing diode. The lower the temperature the faster liquid helium was used. Operating below 10K seemed to be wasteful. Regulating at 12K could be maintained for about 6 to 8 hours. If longer times were needed the cryostat could be refilled without moving the cryostat or any of the experimental setup.

The cryostat had many wires running from the feed throughs on top of the cryostat down to the sample holder at the end of the cold finger. All the wires were heat sunk at the cold finger running to the liquid He bath. Two twisted pairs were used for the temperature sensing diode. All other wires were Lake Shore coax (model #C1). The coax were used for powering the IR LED, measuring photovoltaic signals, Hall bar current biasing, and measuring Hall voltages and photoconductivity signals.

§E FIR sources

TEA laser

The primary FIR source used was the TEA laser operating at either 9R14 or 9R30 pumping a methylfluoride gas producing FIR lines at 29.5cm^{-1} and 43.3cm^{-1} respectively (two very strong lines). The typical spot size was about 3mm in diameter. The vertical axis was about 0.5mm larger than the other. The total pulse energy for the 29.5cm^{-1} line was typically 3 to 6mJ and for the 43.3cm^{-1} line typically 8 to 10 mJ, but occasionally as high as 15 to 18mJ. Both the 29.5cm^{-1} line (9R14) and the 43.3cm^{-1} line (9R30) were single frequency lines.

The time structure of the FIR pulse from the TEA laser is very complicated [2.12]. The pulse length is about 50nsec with fine structure easily seen on the 5nsec scale. The “jaggedness” of the pulse structure can be controlled some what by the helium gas going to the CO_2 pump laser.

Free-electron laser

The U.C.S.B. Free-Electron Laser was also used. The frequency was typically around 50cm^{-1} . The spot size varied from 3mm to 1.5mm in diameter. The pulse shape was a very regular rectangular pulse shape and could be varied from $0.5\mu\text{sec}$ to $15\mu\text{sec}$. With the original beam line, pulse lengths could not be obtained much longer than $2\mu\text{sec}$. With the cavity dump coupler, pulses as short as 30nsec could be obtained. Typically for pulse lengths of $1\mu\text{sec}$, a total pulse energy of 1 to 2kWatts could be obtained around 50cm^{-1} . Using the cavity dump coupler, powers of up to about 10kWatts was available at 50cm^{-1} . The FEL was found to have

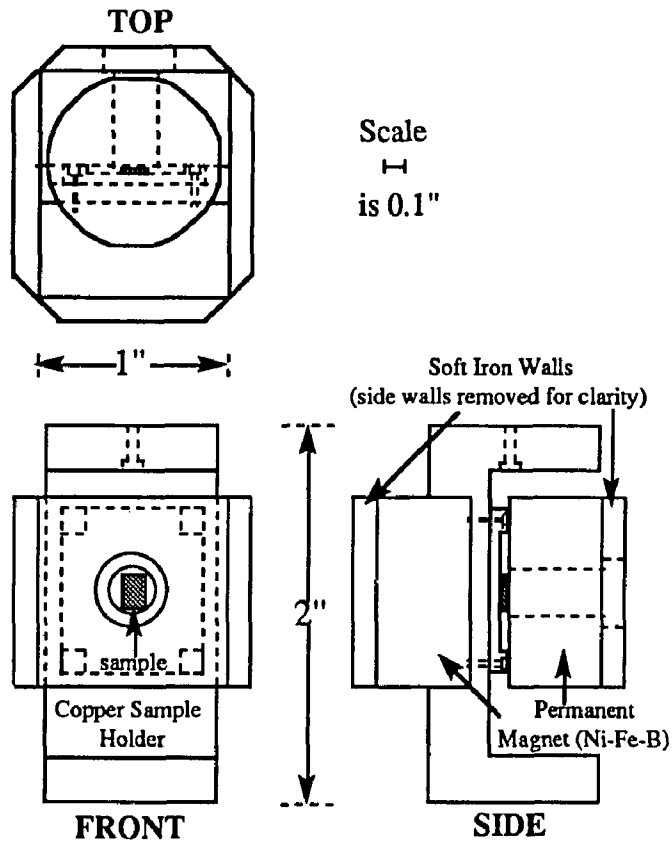


Fig.(2.11) Permanent magnet assembly with sample holder and sample shown.

harmonics but they are of such lower power they are not of concern for measurements reported here.

§F Electronics

The standard collection of electronic instruments were commonly used. The instruments used were: a Hewlett Packard 54200A Digitizing Oscilloscope, Fluke 8840A (with GPIB interface) and 77 DVM, Hewlett Packard 7004B chart recorder, Lambda LG-412 0 to 40 Volt regulated power supplies, Keithley 236 Source

Measurement Unit used as a constant current source, Lake Shore Cryotronics DRC 82C Temperature Controller, and FIR power meters and detectors. The Fluke 8840A and the temperature controller were interfaced to a Macintosh II computer using Labview version 2.0 software.

Very little electronic fabrication was done for the measurements reported here. IR and red LEDs were used to illuminate the sample with light. No special circuitry besides a current limiting resistor were used for the LEDs. The LEDs were simply switched on and off by hand. No circuitry was used to control how long the LED was on. A resistance bridge circuit along with a battery and the Ithaco 1201 low noise preamplifier were used to null the resistance of the sample for the photoconductivity measurements.

§G Hall magnet assembly

One special apparatus was constructed for the photo-Hall measurements. It consisted of two pieces of very strong permanent magnetic material. The material was nickel iron boron. The two magnet pieces were rectangular solids of dimensions 1"x1"x1/2". One of the pieces had a 1/4" (5mm) hole drilled in it to allow FIR to irradiate the sample. The 1/4" hole was very difficult to drill since the material was so hard and brittle. It was drilled without using a pilot hole. The first try used a pilot hole but attempting to drill the next larger hole only ruined the drill bit by wearing away the sides of the bit cutting the material. A standard drill press and bits were used. The 1/2" deep hole took 45 minutes to drill. Even going this slowly the bit chipped the material as it broke through the other side. The magnets were held in

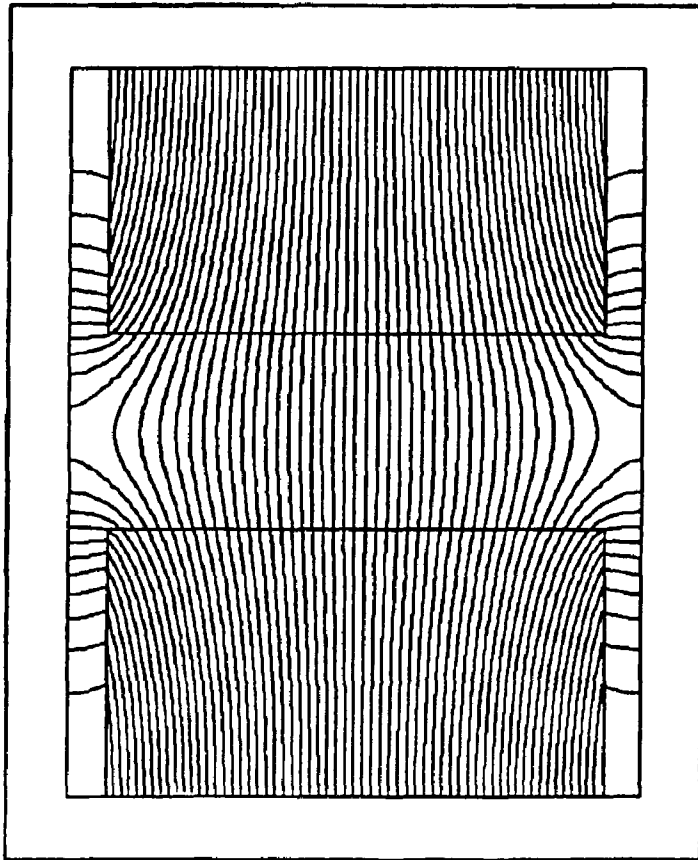


Fig.(2.12) Magnet field lines for the permanent magnet assembly with a 1.0cm gap and residual field of 12.5kG for a nickel-iron-boron permanent magnet. This arrangement produces a field of 8kG between the magnets. The soft walls for this calculation were 1/4" thick.

place primarily by their own attractive forces. The copper sample holder was machined so as to help hold the magnets in place. Soft iron walls of 1/8" thickness surrounded the magnets and sample holder were used to further stiffen the entire assembly. The soft iron plates also helped to confine the magnetic field and concentrate the field within the gap between the magnets. A drawing of the assembly is shown in Fig.(2.11). The sample is mounted on a stand off so the permanent magnets do not crush the sample from their strong mutual attraction. One of the soft

iron walls also has a 3/8" hole drilled in it and it aligns with the 1/4" hole in the permanent magnet.

The magnet arrangement shown in Fig.(2.12) produces a calculated field within the gap of the magnets to be 8kG. This arrangement uses a 1.0cm gap and 1/4" thick soft iron walls with a 1/8" gap between the soft iron and the sides of the permanent magnets. This arrangement was too large to fit within the cryostat with liquid nitrogen shields in place. It was modified by: reducing the thickness of soft iron walls to 1/8", leaving no gap between the soft iron and the sides of the magnet, and the gap was reduced to 8mm. The calculated fields shown in Fig.(2.12) did not assume a 1/4" hole drilled into one of the soft iron plates and one of the magnets. The magnetic field of the final assembly was measured to be about 4kG at the sample position shown in Fig.(2.11). The field was measured with a Bell Digital Gaussmeter model 660R. The presence of the 1/4" hole in the assembly produces a nonuniform field near the sample. Measurements with the gauss meter showed variations in the field of about 0.2kG.

There is probably some temperature dependence of the magnetic field from the permanent magnets as they cool from 300K down to 10K. The fields probably tend to increase a bit as the magnets cool. The permanent magnets survived many temperature cyclings. The assembly was always cooled at a rate of about a few kelvin per minute. Most of the contraction probably takes place from 300K to 77K so rapid temperature rises or falls at cold temperatures probably does not hurt the assembly much.

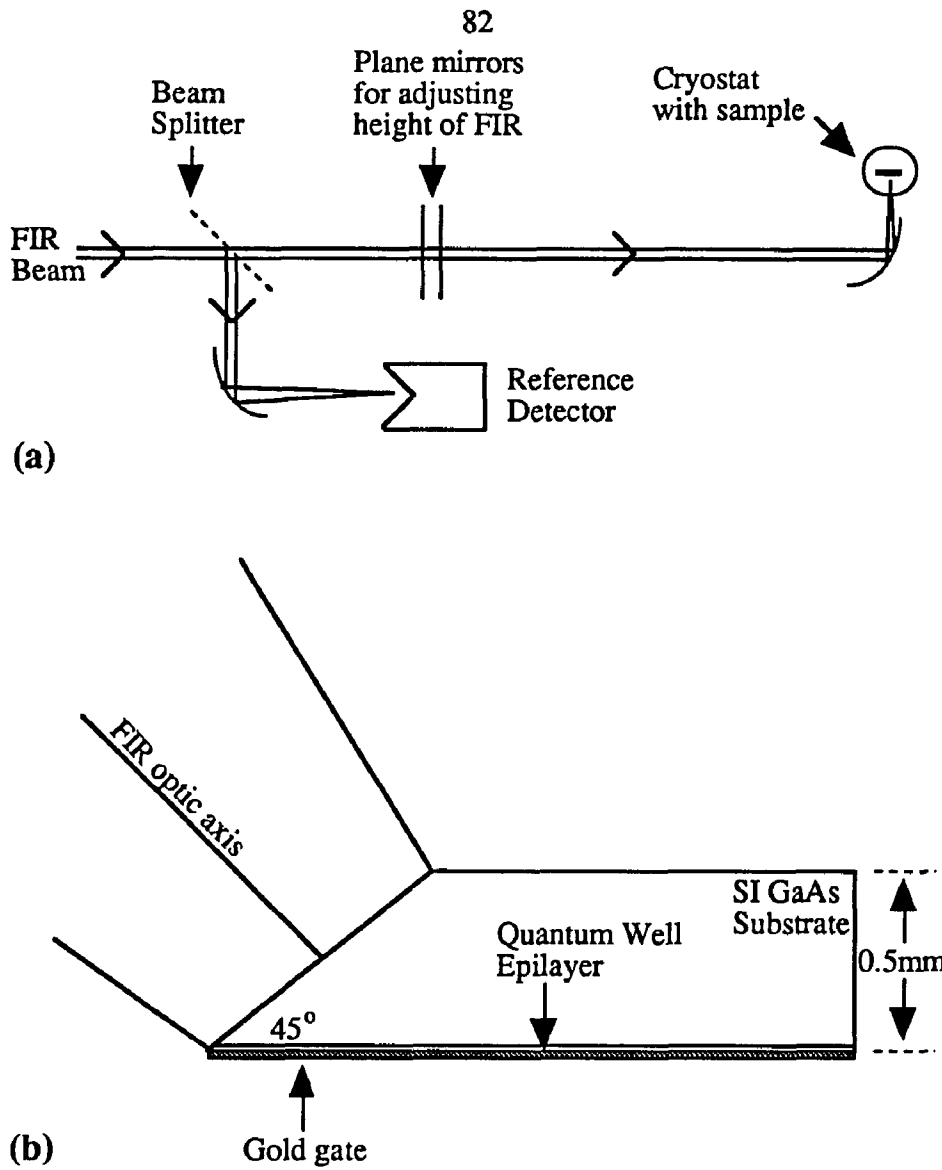


Fig.(2.13) (a) Typical optics layout for all FIR experiments reported within. (b) Coupling of FIR normal to the 45° lapped plane on the edge of the sample.

§H Optics and coupling of FIR into the sample

All optical setups used were very similar to the one shown in Fig.(2.13a). The

only thing that changed from one measurement to another was the coupling of the focused FIR beam. For all the photoconductivity and photo-Hall measurements, the FIR was coupled at normal incidence (perpendicular to the plane of the sample). For most of the photovoltaic studies, the edge of the sample was lapped at 45° and the FIR beam was coupled at normal incidence to the surface of the lapped 45° surface as shown in Fig.(2.13b). See C. L. Felix [2.14] for a discussion of edge coupling efficiency.

The percentage of reflected FIR from normal incidence coupling is given by the formula:

$$R = (n-1)^2/(n+1)^2,$$

where n is the index of refraction and is about 3.5 for GaAs. So the maximum fraction of the free field that could get coupled into the sample is $1-R = 0.69$ for GaAs. Therefore all the measurements done with normal incidence only 69% of the free-space intensity gets coupled into the sample.

The tricky thing in the optics layout shown in Fig.(2.3a) is not having the cryostat stand interfering with the optics path or focusing mirror. The focusing mirror used was a Mells Groit off-axis parabola with a focal length of 119mm. This was about the shortest focal length mirror that could be used with the Andonian cryostat that was used for the measurements.

Another important point about the optics setup was that the cryostat window assembly could be removed and replaced without moving the cryostat itself. This allowed all the optics to be setup and the HeNe alignment beam could be focused onto the sample without the window assembly on the cryostat. This greatly helped in setting up the optics. In order to do this the height of the FIR beam above the optics

bench had to be adjusted to the height of the sample. This was done with two plane mirrors. This proved to be an easier scheme than adjusting the height of the cryostat to match the height of the FIR beam above the optics table. The cryostat is a very heavy object and it is difficult to adjust the height of the sample accurately.

A special cryostat mount was constructed which allowed the cold finger of the cryostat to be held about 14 inches above the optics table. This was sufficiently high to remove the window assembly without disturbing the cryostats position. The tabel which the cryostat sat on was made large enough so that the legs of the stand where well away from the optics path required by a 5 inch focusing mirror to illuminate the sample.

Part III, Experimental Technique

§I The measurements

The three measurements that will be described are photovoltaic, photoconductivity, and photo-Hall. None of the measurements required any special electronic equipment. It was nice to have a fast digitizing oscilloscope for the photovoltaic transients. Some photovoltaic transients were very fast being on the order of 50nsec (20Mhz). The photoconductive and photo-Hall transients were very slow typically ranging from 0.1 seconds to hours.

Photovoltaic

The photovoltaic measurements were particularly simple. The sample usually had two ohmic contacts to the channel (2DEG) and a Schottky gate as shown

in Fig.(6.2b or 6.2c) of Chapter 6. One of the ohmic contacts (drain) was grounded to the cryostat cold finger to reduce noise pickup. Then one of the other contacts, either the gate or the other ohmic contact (source), was connected to the input of an oscilloscope whose ground was connected to the cryostat ground (or drain contact). The oscilloscope was then triggered by the laser (TEA or FEL) trigger pulse. The photovoltaic response was then stored on the digitizing oscilloscope. Hard copies were made by hooking up a Hewlett Packard 74704 plotter to the HP digitizing oscilloscope. Sometimes a negative gate bias (with respect to the channel) was applied to the gate in order to deplete the channel of electrons. This was done using a Lambda variable regulated power supply directly to the gate and channel contacts.

Photoconductivity

The photoconductivity measurements were only slightly more complicated in that they required a constant current source and an LED to expose the sample to IR or visible light. The sample had only two contacts as shown in Fig.(2.7a). The current source was either a battery in series with a resistor or the Keithley 236 SMU used as a constant current source. The series resistor varied from $100\text{k}\Omega$ to $20\text{M}\Omega$ depending on the resistance of the sample. Since the transients that were studied were so slow, a chart recorder was initially used to record the transient responses to irradiation of the sample by intense FIR and light from the LED. Eventually the chart recorder was replaced by a Fluke 8840A DVM with a GPIB interface that was read using a Macintosh II computer running Labview version 2.0 software. Depending on what measurement was done, the computer would read the DVM once every few seconds to once every 0.05 seconds. The digitization rate was an adjustable

parameter of the Labview application. The digitized data proved to be extremely useful even though it took a few weeks to a month to analyze the data collected in just one evening. Only one quantity was needed to be measured and that was the voltage drop across the sample, V_{IR} . From $V_{IR} = I_0 R$ the sample resistance, R , could be calculated since the constant current, I_0 , was known. The conductivity, σ , of the sample could be calculated from the sample geometry and resistance,

$$\sigma = 1/\rho = L/RA,$$

where A is the cross-sectional area of the sample and L is the length of the sample.

The photo-Hall measurements were very similar to the photoconductivity measurements except that an additional quantity, the Hall voltage, was measured as a function of time. The constant current is supplied through contacts marked I_0^1 and I_0^2 , the Hall voltage is measured between contacts marked V_H^B and V_H^T , and the conductivity is measured between contacts marked V_H^B and V_{IR} in Fig.(2.7b). The Hall contacts used were the pair that showed the least misalignment voltage (see Chapter 3, §C). The misalignment voltage was measured using a constant current with and without a magnetic field applied to the sample at room temperature. The misalignment voltage is the voltage from the IR voltage drop between the misalignment of a pair of Hall contacts. The misalignment voltage is given by

$$V_{\text{misal.}} = V_{\text{Hall,B=B}_0} - V_{\text{Hall,B=0}}$$

The difference in Hall voltage with, $V_{\text{Hall,B=B}_0}$, and without, $V_{\text{Hall,B=0}}$, a magnetic field applied. The data collection program written for the photoconductivity data was modified to read and store the voltage from two Fluke 8840A DVMs. The conductivity was calculated as described above using the geometry of the sample shown in Fig.(2.7b). From the measured Hall voltage the Hall electron concentration,

N_H , can be calculated from:

$$N_H = -I_0 B_0 / (V_{Hall} e t),$$

where B_0 is the magnetic field, t is the epilayer thickness, I_0 is the constant current, and e is the magnitude of the electron charge (assuming the charge carriers are electrons). The thickness used for the calculation of N_H was the Si doped epilayer thickness which was $2\mu\text{m}$ (neglecting surface depletion of about $150\text{\AA} \ll 20,000\text{\AA}$). The magnetic field used for calculating N_H was calculated from room temperature measurement of V_H assuming that $N_H = 1/2(\# \text{ of Si donors}) = 1/2(1.5 \times 10^{17} \text{cm}^{-3}) = 7.5 \times 10^{16} \text{cm}^{-3}$. This gave a value of $B_0 = 4.1 \text{kG}$ which is consistent with that measured at room temperature with the field of $4 \pm 0.5 \text{kG}$ measured using a hand held gauss meter probe held at the position of the sample. The absolute value of the Hall electron concentration is not as important as the relative changes in N_H observed in response to intense FIR. The absolute value of N_H reported here is probably accurate within a factor of two of the actual electron concentration $N_s = r_H N_H$ where r_H is the Hall factor discussed below in Chapter 2, §J.

The FIR was attenuated using clear plexiglass and green colored plastic sheets (see [6.1a] Fig.(3.7)). The diameter of the attenuators was 4 inches which easily covered the 2 inch diameter of the unfocused FIR. Varying degrees of attenuation were achieved by changing the thickness of the attenuators. The set of clear plexiglass attenuators were 0.025 to 0.200 of an inch thick with 0.025 of an inch increments (8 attenuators in all). The 0.025 attenuator transmitted about 53% of the incident radiation at 29.5cm^{-1} and attenuated by larger amounts as the frequency of the radiation increased. Only one thickness (3mm) of the green plastic was available. This thickness transmitted about 75% of the incident radiation at 29.5cm^{-1} .

§J The importance of measuring both Hall electron concentration and mobility

Resistance changes imply that the electron concentration changes if the mobility is constant. But in many cases the mobility changes so resistance changes do not imply that the electron concentration is changing. In order to conclude that the carrier concentration is changing, the electron concentration must be measured directly with a Hall measurement.

Epilayer resistance

The resistance of an epilayer of an $\text{Al}_x\text{Ga}_{1-x}\text{As}:\text{Si}$ of length L , width w , and thickness t , is given by:

$$R = L\rho/(wt) = L/(wt\sigma) = L/(wtN_s e\mu),$$

where N_s is the 3 dimensional electron concentration (assuming the contribution from the holes is very small), e the fundamental electronic charge, μ the mobility of the electrons in the epilayer, and ρ the resistivity of the sample. If the mobility remains constant throughout a measurement, the epilayer resistance will be a measure of the electron concentration N_s .

The first measurements of the N_s for this thesis were done by monitoring changes in resistance. Conversations with T. N. Theis made us aware of the fact that the mobility of the electrons in $\text{Al}_x\text{Ga}_{1-x}\text{As}$ epilayers could be a complicated function of carrier concentration N_s . For example, it could be a multivalued function of N_s . If the resistance changes, it could be because of changes in the mobility and not reflect the true changes in the carrier concentration. Conversations with A.

Kastalsky during the same meeting made us aware of the possibility that the mobility could change without the carrier concentration changing.

Mobility changes from population of an unintentional 2DEG

Large mobility changes can occur if the 2DEG at the substrate interface is easily populated with electrons. An $\text{Al}_x\text{Ga}_{1-x}\text{As}$ epilayer grown by Molecular Beam Epitaxy (MBE) is grown on a GaAs semi-insulating (SI) or n^+ -GaAs substrate (see Chapter 2, §B and §C, for a discussion of sample and sample growth details). At the interface between the $\text{Al}_x\text{Ga}_{1-x}\text{As}$ and GaAs is a band offset and electrons from the epilayer can be transferred easily to the GaAs substrate (lower energy state) until enough of epilayer is depleted to cause a sufficiently large amount of band bending (a built in electric field) to prevent further transfer. If the epilayer is doped to the GaAs substrate, this charge transfer will happen and the sample will have electrons at the GaAs interface (an unintentional two-dimensional electron gas (2DEG) [2.16]). These electrons are removed from their donor Si atoms which are positively charged and they have a higher mobility since the ionized impurity scattering is reduced [2.17, 2.11]. So the resistance can go up and down if electrons are being transferred back and forth between the epilayer and the GaAs substrate. In this case, changes in resistance are arising from changes in the mobility and the assumption that this means the carrier concentration is changing is wrong.

Since the electron mobility in $\text{Al}_x\text{Ga}_{1-x}\text{As}$ epilayers for x near 0.3 as a function of temperature is known [2.18, 2.16, 2.19] and is much smaller than that in $\text{Al}_x\text{Ga}_{1-x}\text{As}/\text{GaAs}$ 2DEGs, the value of the Hall mobility, μ_H , is a good indication of whether or not a 2DEG is populated. If it is populated μ_H will be an order of

magnitude higher than the $\text{Al}_x\text{Ga}_{1-x}\text{As}$ epilayer value. So the precise details of the theory of the two-layer Hall technique (deducing Hall concentration and mobility of each layer of a two layered system [2.20,2.21]) do not need to be known to determine whether or not a 2DEG is populated. Knowing that the Hall mobility is sort of an average of the different mobilities in the two layers is sufficient in this case.

In the first epilayer studied, this unintentional 2DEG was present and we were wrongly concluding that the carrier concentration was changing. After speaking with Kastalsky, we started studying epilayers with a buffer layer between the doped $\text{Al}_x\text{Ga}_{1-x}\text{As}$ and the GaAs substrate so as to prevent the forming of this unintentional 2DEG. Shown in Fig.(2.14) is the band bending that occurs when a buffer layer is grown that prevents electron transfer to the GaAs substrate. N. Chand et al. [2.19] argue that a $2,000\text{\AA}$ buffer layer thickness is sufficient to prevent the 2DEG from forming. We studied $\text{Al}_{0.3}\text{Ga}_{0.7}\text{As:Si}$ epilayers with a $10,000\text{\AA}$ ($1\mu\text{m}$) buffer layer (see Fig.(2.4)).

Other causes of mobility changes

Electron mobility can also change if different conduction band valleys are occupied i.e. transferring electrons from the Γ band to the X band or L band (see Chapter 1, §B for a discussion of the GaAs band structure.). Mobility can change with the lattice temperature. If some sort of lattice heating were taking place, the resistance change observed could be from mobility changes (N_s also depends on lattice temperature). So once again, in these situations, changes in resistance do not reflect changes in carrier concentration only.

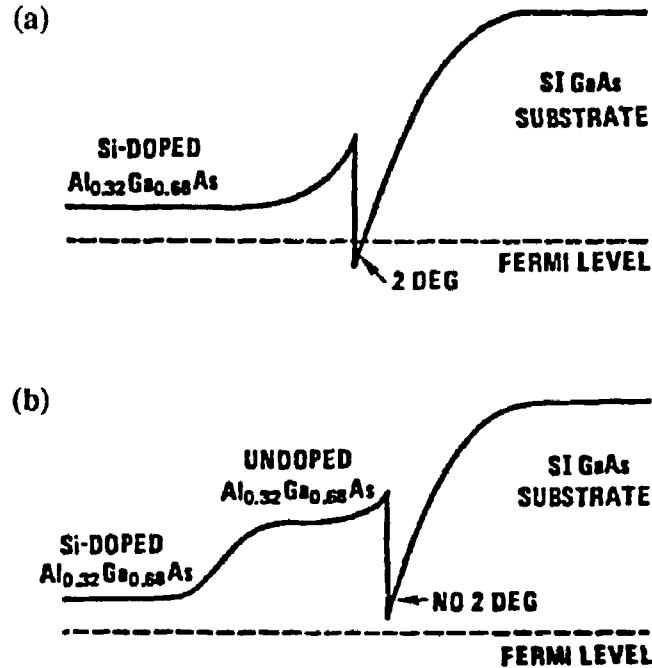


Fig.(2.14) Schematic representation of the conduction band minima near the $\text{Al}_x\text{Ga}_{1-x}\text{As}/\text{GaAs}$ interface for (a) the case without a buffer layer and (b) the case with an undoped $\text{Al}_x\text{Ga}_{1-x}\text{As}$ buffer layer between the doped $\text{Al}_x\text{Ga}_{1-x}\text{As}$ and the GaAs substrate. With the undoped $\text{Al}_x\text{Ga}_{1-x}\text{As}$ buffer layer present, the bottom of the 2DEG in the GaAs substrate lies above the Fermi level and the 2DEG is not populated [2.16].

The Hall electron concentration

The Hall electron concentration, N_H , (the electron concentration measured by the Hall effect) is determined from the Hall voltage, V_H , that develops across the sample as a current, I_0 , is maintained through the epilayer that has its face (plane of the epilayer) perpendicular to a magnetic field B_0 as shown in Fig.(2.15). The Hall voltage is given by:

$$V_H = -I_0 B_0 r_H / (N_H e t) = R_H I_0 B_0 / t, \text{ with } R_H = -r_H / (N_H e);$$

where r_H is the Hall factor and R_H the Hall constant [2.22]. There are theoretical expressions for the Hall factor which depends on which scattering mechanism is

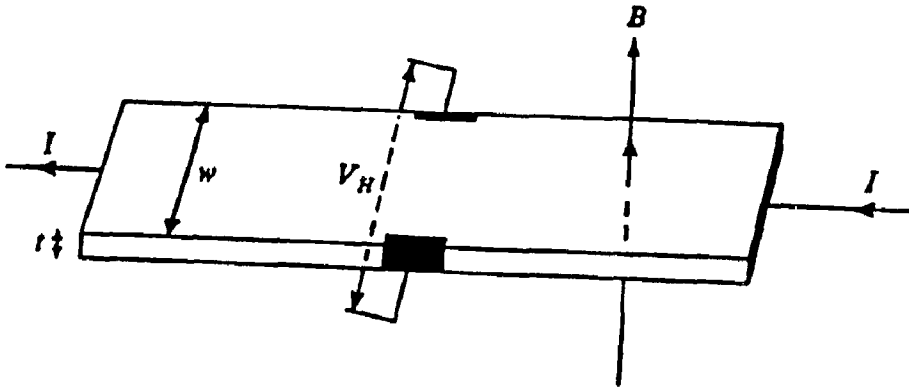


Fig.(2.15) The orientation of the magnetic field with respect to the sample and contacts for the Hall effect measurement [2.22].

dominant i.e. $r_H = +3/2$ for ionized impurity scattering and $r = -1/2$ for acoustic deformation potential scattering, but can be taken as an order of magnitude of 1 [2.23]. In this thesis, N_H will be discussed most of the time with the understanding that $N_s = N_H/r_H$ with $r \approx 1$ where N_s is the actual electron concentration. For absolute measurements of the electron concentration, the value for r_H is important. For relative changes in electron concentration at a constant temperature its exact value is not important.

Errors involved in measuring the Hall concentration

Errors in the absolute carrier concentration can be made if the effect of surface and interface depletion are not considered [2.32]. Carrier concentrations in epilayers studied for this thesis (10^{16} to 10^{17} cm^{-3}) have surface and interface depletion lengths are of the order of 100 \AA and epilayer thickness of $2 \mu\text{m}$ ($20,000 \text{ \AA}$) so depletion effects are small.

Since scattering mechanism which is dominant depends on temperature, r_H will be dependent upon temperature. When comparing relative changes in N_H at

different temperatures it is important to take the different values of r_H into account. Temperature dependent Hall electron concentration is an important part of this thesis since E_d for the DX center is determined from this type of measurement.

As with any semiconductor system there are always impurities that act as acceptors (compensated semiconductors). In some cases if compensation is not taken into account, large errors can result in analysis of the Hall data. It is not uncommon for authors to not indicate whether or not their samples are compensated and this can lead to an error of a factor of 2 in their analysis for E_d (See [1.38] page R7.).

The Hall mobility

Hall mobility of the electrons in an $Al_xGa_{1-x}As$ epilayer is given by

$$\mu_H = \sigma_0 |R_H| = r_H \sigma_0 / N_H e,$$

so if the electron concentration, N_H , of the epilayer is measured along with the D.C. conductivity, σ_0 , the Hall mobility, μ_H , can be calculated with the above equation.

The conductivity can be determined from the geometry of the sample by the relation

$$\sigma_0 = 1/\rho = L/RA = L/Rwt,$$

where R is the resistance, A is the cross-sectional area, L is the length, w is the width, and t is the thickness of the epilayer. With a Hall and resistance measurement, both the electron concentration and mobility of the epilayer can be determined. This enables one to unravel the coupled effects of electron concentration and mobility changes.

The drift mobility

The drift mobility, μ_d , is given by

$$v_e = \mu_d E,$$

where v_e is the velocity the electron gains from the application of an electric field E .

The drift mobility is related to the Hall mobility by

$$\mu_H = \sigma_0 |R_H| = r_H \sigma_0 / N_H e = (r_H / N_H e) N_H \mu_d = r_H \mu_d$$

where r_H is the Hall factor. So the Hall mobility differs from the drift mobility by the Hall factor.

Some models for the mobility

The most commonly discussed model for electron mobility in $Al_xGa_{1-x}As$ epilayers at cold temperatures is ionized impurity scattering process. This gives $\mu_d \approx (T)^{3/2}$ with a weak but complicated dependence on carrier concentration. Ionized impurity scattering is sometimes referred to as the Brooks-Herring model [2.24] describing how the mobility depends on temperature and carrier concentration within the temperature range of 30K to 80K. The main physical idea of the model is that the donor atom gets screened by the surrounding electron gas. An approximate finite analytic result can be obtained by considering a screened coulomb potential in the quantum mechanical calculation of the scattering cross-section which give the results described above about the temperature and carrier concentration dependence of the mobility [2.24].

Detailed models of standard scattering processes have been developed over the years and in many instances a good agreement between theoretical and experimental mobility has been achieved [2.25, 2.26, 2.27]. An unresolved issue involves the

contribution of charged defect scattering to the electron mobility [2.28]. A related question involves the predicted mobility dependence of the different possible charge states of the DX center. The DX^0 and DX^- states give different predictions for the dependence of electron mobility in GaAs under pressure. Measuring the pressure dependence of mobility in such systems should reveal the charge state of the ground state of the DX center. A definite conclusion is not clear at this date but the data seems to be favoring a DX^- ground state [2.29, 2.30, 2.31].

Conduction band electron concentration

The number of electrons in the conduction band is measured by a temperature dependent Hall effect and can be thought of in terms of the following relation

$$N_H \approx N_D^+ - N_A^- - N_{DT}^-$$

where N_D^+ is the number of ionized donors (Si atoms for the epilayers studied in this thesis with $N_D \approx 1.5 \times 10^{17} \text{cm}^{-3}$), N_A^- is the number of acceptors taking electrons from the conduction band ($N_A \approx 10^{15} \text{cm}^{-3}$ mainly from carbon impurities in MBE grown samples), and N_{DT}^- is the number of electrons trapped from the conduction band by deep levels.

All three terms on the right hand side of the above equation are temperature dependent. The first two terms, $N_D^+ - N_A^-$, give rise to what is called compensation in semiconductors. That is, the number of electrons provided by the donor atoms is reduced by the presence of acceptor atoms (intentionally or unintentionally doped) since for typical electron concentrations the Fermi level is well above the acceptor level. The acceptors are usually from back ground impurities (the unintentionally doped case) as in MBE grown samples. The term N_{DT}^- is strongly temperature

dependent. This term is believed to be related to N_D^+ by the notion of the bistability of donors mentioned in the discussion of persistent photoconductivity (PPC) (Chapter 1, §F). For temperature dependent Hall measurements of N_H below 100K, N_{DT}^- can be regarded as constant while the sample remains in the dark. For Hall measurements above 150K, the capture and emission barriers are ineffective and all deep states (including DX related states) participate in the electron concentration (see Fig(1.9) of Chapter 1, §F). So interpretations of the temperature dependent Hall data in terms of physical quantities such as the concentration of donor atoms, impurity atoms, and deep electron traps is difficult and is an on going area of research.

DX center ground state

The ground state of the DX center can in principle be determined by temperature dependent Hall data but the donor and acceptor concentrations need to be determined from other experiments. To date, temperature dependent Hall measurements have been inconclusive as to the ground state of the DX center primarily because of the large number of impurities that participate in compensation of the sample [1.35, 1.40].

Chapter 2 references

1. C. Weisbuch, **Semiconductors and Semimetals 24**, Chapter 1 (1987).
2. Herman and Sitter, **Molecular Beam Epitaxy** (Springer-Verlag, Berlin, Heidelberg, New York, 1989).
3. P. M. Petroff, R. C. Miller, A. C. Gossard, and W. Wiegmann, *Appl. Phys. Lett.* **44**, 217 (1984).
4. H. C. Casey, Jr. and M. B. Panish, **Heterostructure Lasers** (Academic, New York, 1978), Parts A and B.
5. R. L. Anderson, *Solid-State Electron.* **5**, 341 (1962).
6. K. von Klitzing, G. Dorda, and M. Pepper, *Phys. Rev. Lett.* **45**, 494 (1980).
7. M. Sundaram, A. C. Gossard, J. H. English, and R. M. Westervelt, *Superlattices and Microstructures* **4**, 683 (1983).
8. A. Wixforth, M. Sundaram, D. Donnelly, J. H. English, and A. C. Gossard, (to be published in *Surface Science*).
9. B. I. Halperin, *Jpn. J. Appl. Phys.* **26** Suppl. **26-3**, 1913 (1987).
10. R. C. Miller, A. C. Gossard, D. A. Kleinmann, and O. Munteanu, *Phys. Rev.* **B29**, 3740 (1984); E. G. Gwinn, R. M. Westervelt, P. F. Hopkins, A. J. Rimberg, M. Sundaram, and A. C. Gossard, *Phys. Rev.* **B39**, 6260 (1989).
11. R. Dingle, H. L. Stormer, A. C. Gossard, and W. Wiegmann, *Appl. Phys. Lett.* **33**, 665 (1978).
12. Greg Snider of the U.C.S.B. Material Science Department wrote, in 1990, a user oriented program that calculates the band structure, electron distribution, electron wavefunctions, and electron energy levels for an $\text{Al}_x\text{Ga}_{1-x}\text{As}/\text{GaAs}$ semiconductor quantum well or heterostructure. This program was used every time a self-consistent calculation is mentioned within this chapter.
13. Private communication from A. Kastalsky.

14. C. L. Felix, Ph. D. Thesis, U.C.S.B. Department of Physics, 1992.
15. C. T. Gross, J. Kiess, A. Meyer, and F. Keilmann, *IEEE J. Quan Elec* **QE-23**, 377 (1987).
16. D. M. Collins, D. E. Mars, B. Fisher, and C. Kocot, *J. Appl. Phys.* **54**, 857 (1983).
17. L.L. Chang and K. Ploog, **Molecular Beam Epitaxy and Heterostructures**, Proc. Eric 1983 Summer School, Martimus Nijhoff, The Hague, 1985.
18. R. J. Nelson, *Appl. Phys. Lett.* **31**, 351 (1977).
19. N. Chand, T. Henderson, J. Klem, T. Masselink, R. Fischer, Y. C. Chang, and H. Morkoc, *Phys. Rev.* **B30**, 4481 (1984).
20. R.D. Larrabee and W. R. Thurber, *IEEE Trans. Elec. Dev.* **ED-27**, 32 (1980).
21. M. Kever, T. J. Drummond, H. Morkoc, K. Hess, B. G. Streetman, and M. Ludowise, *J. Appl. Phys.* **53**, 1034 (1982).
22. R. A. Smith: **Semiconductors**, 2nd ed. (Cambridge University Press 1978) p. 106.
23. K. Seeger: **Semiconductor Physics**, 4th ed. (Springer-Verlag Berlin Heidelberg New York 1989) pps.52 to 58.
24. K. Seeger, 4th ed., **Semiconductor Physics**, (Springer-Verlag, Berlin, Heidelberg, New York, 1989) p.162.
25. D. L. Rode, **Semiconductors and Semimetals**, edited by R. K. Willardson and A. C. Beer (Academic, New York, 1982) **10**, Ch. 1.
26. W. Zawadzki, **Handbook of Semiconductors**, edited by W. Paul (North-Holland, New York, 1982) **1**, p.713.
27. J. R. Meyer and F. J. Bartoli, *Phys. Rev. Lett.* **57**, 2568 (1986).
28. W. Walukiewicz, *Phys. Rev.* **B41**, 10218 (1990).

29. D. K. Maude, L. Eaves, T. J. Foster, and J. C. Portal, *Phys. Rev. Lett.* **62**, 1922 (1989).
30. D. J. Chadi, K. J. Chang, and W. Walukiewicz, *Phys. Rev. Lett.* **62**, 1923 (1989).
31. E. D. O'Reilly, *Appl. Phys. Lett.* **55**, 1409 (1989).
32. A. Chandra, C. E. C. Wood, D. W. Woodard, and L. F. Eastman, *Solid State Elec.* **22**, 645 (1979).

Chapter 3

Hall Electron Transport Data for an $\text{Al}_{0.3}\text{Ga}_{0.7}\text{As}:\text{Si}$ Epilayer

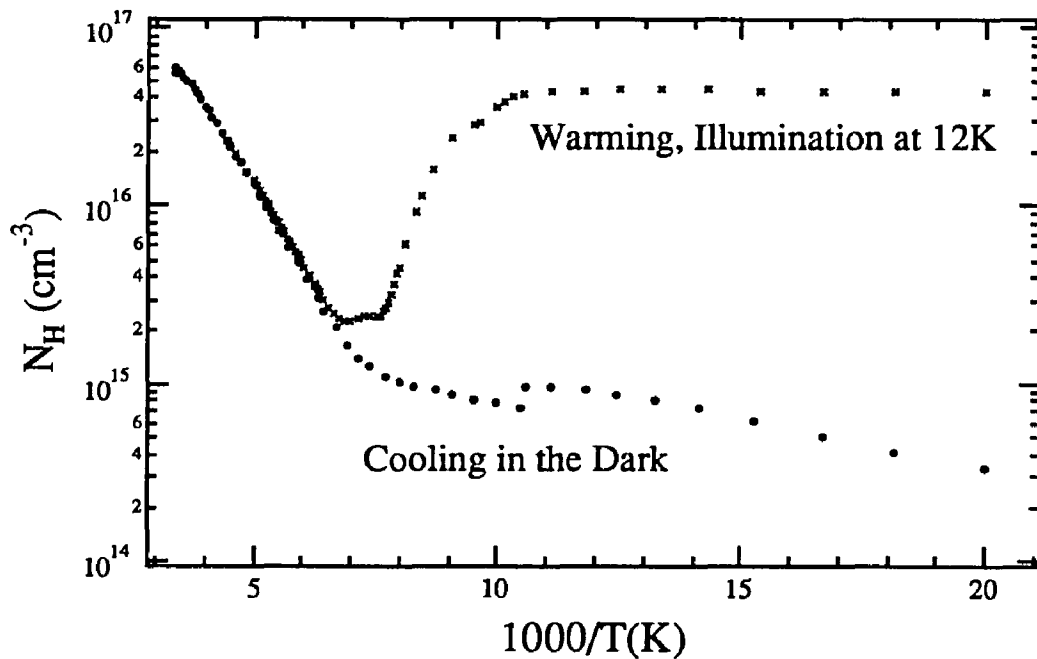
§A Introduction

In this chapter, all the electron transport data for the $\text{Al}_{0.3}\text{Ga}_{0.7}\text{As}:\text{Si}$ epilayer are presented. The most important data are that of the effect of intense FIR on the electron transport properties of the epilayer. Before the FIR effect is discussed, the well established temperature and IR LED flash effects on the transport properties are presented so as to provide a framework to think about the FIR effect data. The chapter ends with a discussion of the power and frequency dependence of the intense FIR effect on electron transport properties of the epilayer.

Only the data are presented in this chapter. In Chapter 4, a discussion is presented that relates the observed FIR effect to the DX center.

§B Temperature dependent Hall electron concentration

The temperature dependent Hall concentration, $N_{\text{H}}(T)$, in $\text{Al}_x\text{Ga}_{1-x}\text{As}$ epilayers has been extensively studied so a measurement of $N_{\text{H}}(T)$ can be compared



Fig(3.1) Persistent photoconductivity (PPC) in an $\text{Al}_{0.3}\text{Ga}_{0.7}\text{As}:\text{Si}$, $2\mu\text{m}$ thick, epilayer. The PPC is apparent by the large difference in the carrier concentration, N_H , between the dark cooled sample and when the sample is illuminated cold. The persistent effect is observed for temperatures as high as 140K . The magnitude of the effect starts to sharply drop at about 100K . The sample was cooled and warmed at a rate of about $2\text{K}/\text{min}$.

with the published data to serve as a test of the measurement apparatus. A measurement of $N_H(T)$ for the $\text{Al}_{0.3}\text{Ga}_{0.7}\text{As}:\text{Si}$ epilayer studied in this thesis is shown in Fig.(3.1). These data look almost identical to Fig.(1.9) of Chapter 1, §F which are taken from Theis et al. [1.36]. This strongly supports the fact that the temperature dependent Hall measurement done with the apparatus described in Chapter 2, §I accurately measures relative changes in electron carrier concentration in an $\text{Al}_{0.3}\text{Ga}_{0.7}\text{As}:\text{Si}$ epilayer. See Chapter 2 §I and §H for a discussion of the measurement of the absolute carrier concentration.

The data, $N_H(T)$, are interpreted within the model of the bistability of Si

donors in $\text{Al}_x\text{Ga}_{1-x}\text{As}:\text{Si}$ epilayers by Theis et al. [1.36] as discussed in Chapter 1, §F. The data obtained while cooling the sample in the dark show the effect of freeze out of free electrons to DX centers around 150K ($1000/T \approx 6.5$). The PPC effect is seen after illuminating the sample with an AlGaAs IR LED and continues to persist up to the temperature of 150K when the DX centers begin to equilibrate with the conduction band electrons within the time scale of the measurement (2K/min.). The signature of this equilibrating is the change in slope at 150K of the curve corresponding to warming the sample after illuminating at 12K shown in Fig.(3.1).

There are two regions of differing slope corresponding to the points before $1000/T \approx 6.5$ and between the points $1000/T \approx 6.5$ and $1000/T \approx 7.75$ of the warming from 12K curve in Fig.(3.1). These two different temperature regions are believed to be a signature of two of the four alloy perturbed DX levels [1.48]. The high and low temperature region of the dark cooling data curve give the thermal ionization energy, E_d , for the DX center and shallow substitutional donor energy, E_{1s} , respectively. The glitch seen in the dark cooling data curve at $1000/T$ is not reproducible. It does not correspond to changing the constant current through the Hall bar as was described in Chapter 2, §C Fig.(2.10). The E_d from a fit to the high temperature data of Fig.(3.1) is 40.9meV. Theis et al. [1.36] finds $E_d \approx 73\text{meV}$ for the DX center and $E_{1s} \approx 14\text{meV}$ for the shallow donor. Theis et al. [1.36] is very vague about how the above fits to find E_d and E_{1s} were done. Dmochowski et al. [1.41] is a much better reference for a discussion of how the $N_H(T)$ versus $1000/T$ is fitted to find E_d and E_{1s} .

How accurately the measured Hall electron concentration, N_H , represents the actual electron concentration, N_s , depends on how well the Hall factor, r_H , is known. Recall from Chapter 2 §J that the actual electron concentration $N_s(T)$ is related to the

Hall electron concentration $N_H(T)$ by the Hall factor r_H and the relation is $N_S(T) = N_H(T)/r_H$. The Hall factor also depends on temperature since it depends on the dominant scattering mechanism [2.21]. The measured Hall factor reported in Ref.(2.21) for an AlGaAs/GaAs heterostructure (2DEG) was between 1 and 3/2 for temperatures between 77K and 400K. This means that the measured values for $N_H(T)$ are within a factor of 2 of the actual electron concentration $N_S(T)$.

§C Temperature dependent Hall mobility

The Temperature dependent Hall mobility of $Al_xGa_{1-x}As$ epilayers is also well known and a measure of it can serve as a crude diagnostic of where the electrons are and which scattering mechanism is dominant. If the D.C. conductivity, σ_0 , of the sample is measured along with the Hall concentration, N_H , the Hall mobility, μ_H , can be calculated from the equation

$$\mu_H = |R_H| \sigma_0 = \sigma_0 / N_H e.$$

Polar optical phonon scattering is the dominant scattering mechanism at high temperatures. As these optical phonons get frozen out, ionized impurity scattering becomes the dominant mechanism. From the Brooks-Herring model, Chapter 2 §J, the mobility has a $T^{3/2}$ temperature dependence.

The temperature dependent mobility of an $Al_{0.3}Ga_{0.7}As$ epilayer is shown in Fig.(3.2). The mobility measured while warming the sample after illumination cold is seen to have a $T^{3/2}$ dependence below 100K. The range of temperature, around 60K, in which the dark-cool mobility follows $T^{3/2}$, is smaller because of the set in of carrier freeze out. Such small ranges of $T^{3/2}$ dependence near this temperature

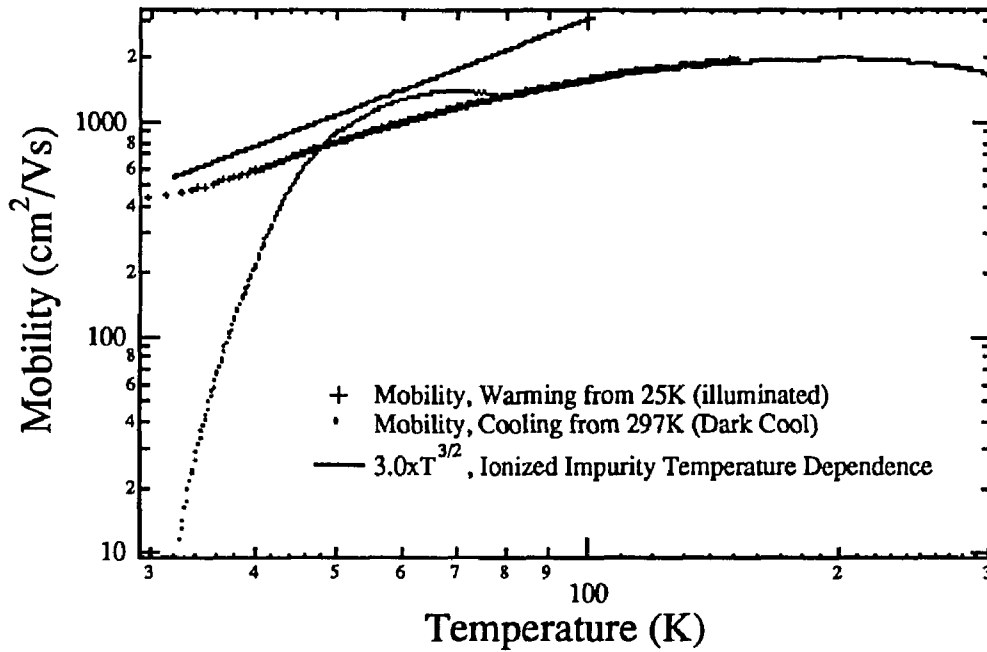


Fig.(3.2) Comparison of dark cooled mobility and mobility measured while warming the sample after being illuminated cold with a $T^{3/2}$ dependence given by the Brooks-Herring model for ionized impurity scattering. The sample was an $\text{Al}_{0.3}\text{Ga}_{0.7}\text{As}:\text{Si}$ epilayer with an undoped $\text{Al}_{0.3}\text{Ga}_{0.7}\text{As}$ epilayer.

are commonly seen in systems with ionized impurity scattering [3.1]. For high temperatures where polar optical phonon scattering is dominant, the mobility has a roughly constant dependence on temperature. Also characteristic of $\text{Al}_x\text{Ga}_{1-x}\text{As}$ epilayers is the rapid drop in mobility at low temperature which is a signature of large carrier freeze out.

At low temperatures $\mu_H \approx 100\text{cm}^2/\text{Vs}$ which is indicative of the fact that the 2DEG of the $\text{Al}_{0.3}\text{Ga}_{0.7}\text{As}/\text{GaAs}$ substrate interface is not populated [Chapter 2, §J Ref.(2.16)]. If mobilities are on the order of $10,000\text{cm}^2/\text{Vs}$ in an $\text{Al}_x\text{Ga}_{1-x}\text{As}$ epilayer, then this is probably a signature of the population of the 2DEG at the epilayer interface. Mobility on the order of $1000\text{cm}^2/\text{Vs}$ at cold temperatures is the intermediate regime where it is difficult to be sure that the 2DEG at the substrate interface is not

populated. References 2.16 and 2.19 of Chapter 2, §J present two slightly different arguments of where the electrons are when the mobility is in this intermediate regime. Most likely with $\mu_H \approx 1000 \text{cm}^2/\text{Vs}$ most of the electrons are in the epilayer and only a small fraction in the 2DEG at the interface. See Fig(2.3b) and Fig(2.4b) for a qualitative picture of an occupied and unoccupied substrate interface 2DEG respectively.

For temperatures below 40K, the Hall voltage, V_{Hall} , starts to have significant contributions from the IR voltage drop resulting from the misalignment of the contacts along the Hall bar used to measure V_{Hall} . Below 40K, $V_{\text{Hall}} \propto V_{\text{IR}}$ and is dominated by the IR drop from the misalignment of the contacts for the particular sample studied in this thesis. As more electrons are frozen out at cold temperatures, the electron mobility decreases hence increasing the resistance contributing to the misalignment voltage drop given by $V'_{\text{IR}} = I_0 R_{\text{misalign}}$. Then V'_{Hall} , which is given by

$$V'_{\text{Hall}} = V_{\text{Hall}} + V'_{\text{IR}} = -r_H I_0 B / (N_s e t) + V'_{\text{IR}}$$

(See Chapter 2 §J for an explanation of the expression for V_{Hall}) is eventually dominated by V'_{IR} to the extent that

$$V'_{\text{Hall}} \approx V'_{\text{IR}} \propto R_{\text{misalign}}.$$

For all the measurements made on the $\text{Al}_{0.3}\text{Ga}_{0.7}\text{As}:\text{Si}$ epilayer studied in this thesis, when $V_{\text{Hall}} \approx V'_{\text{IR}}$ then $V_{\text{Hall}} > 0$. The Hall voltage was typically seen to go positive below 35K when the sample was cooled in the dark. So the dark cooled low temperature ($T < 40\text{K}$) Hall electron concentration and mobility are not accurate measures of the electron concentration and mobility.

Once the sample is illuminated after cooling in the dark to low temperature

(10K to 30K), then there are again enough electrons in the conduction band and mobility high enough so the misalignment voltage is only a few percent of the measured Hall voltage, V_{Hall} . The lowest Hall electron concentration measured after illuminating the sample cold (with intense FIR or small IR LED flashes) has been on the order of 10^{14} cm^{-3} with mobilities on the order of $1000 \text{ cm}^2/\text{Vs}$.

It is seen from Fig.(3.2) that the mobility tracks the $T^{3/2}$ temperature dependence more closely and for a larger temperature range after warming from illumination cold than the mobility corresponding to cooling in the dark. The dark-cool mobility data do not follow as well because of carrier freeze out. The change in slope seen in the region around 75K is a result of slightly non-ohmic contacts used to measure the Hall voltage. An I-V curve for the contacts, V_{H}^{B} and V_{H}^{T} shown in Fig.(2.7b), that were used to measure the Hall voltage is shown in Fig.(2.9a). At the temperature of about 80K where the dark-cool mobility rises above the mobility measured while warming the sample is a result of decreasing the constant current being applied through the Hall bar from $5 \mu\text{A}$ to $1 \mu\text{A}$. This was done to keep the current source from operating near the limits of its compliance range. The reason this happened was because of the Schottky nature of current contacts, I_0^1 and I_0^2 shown in Fig.(2.7b), at the end of the Hall bar which leads to very large voltage drop over the bar. The I-V curve for the current contacts, I_0^1 and I_0^2 , is shown in Fig.(2.8a).

§D IR LED flash effect on Hall electron concentration and epilayer resistance

Low temperature regime ($T < 50\text{K}$)

The effect of cooling the sample in the dark is to have most all of the electrons trapped by DX centers. This carrier freeze out may be reversed by either warming up the sample to temperature above 150K or illuminating the sample with photons of energy greater than 0.8eV. The LED used for the measurements was an AlGaAs IR light emitting diode (TRW OP290 and OP295) having spectral emissions of $875 \pm 20\text{ nm}$ (photon energies of $1.42 \pm 0.03\text{ eV}$) [3-2]. These IR LEDs produce light well above the optical ionization threshold observed for DX centers. Hence, these IR LEDs may be used to ionize electrons trapped by DX centers at low temperatures. The IR LEDs perform very well at cryogenic temperatures. Red light LEDs could also be used but seem to fail more often at cryogenic temperatures. Another nice feature of the AlGaAs IR LEDs is that light from them can penetrate the GaAs semi-insulating substrates that quantum wells and epilayers are grown on whereas light from red LEDs is absorbed strongly by the GaAs substrates.

The effect of ionizing electrons from DX centers using an IR LED is shown in Fig.(3.3). Ionizing electrons from the DX center increases the Hall electron concentration, Fig.(3.3b), and decreases the epilayer resistance, Fig.(3.3c), after the IR LED flash. Note that while the IR LED is on (from 19 to 25 seconds into the data file) the values of the Hall electron concentration, N_H , and epilayer resistance, R , are complicated by photovoltages most likely resulting from the AuGe/Ni/Au contacts to the Hall bar mesa.

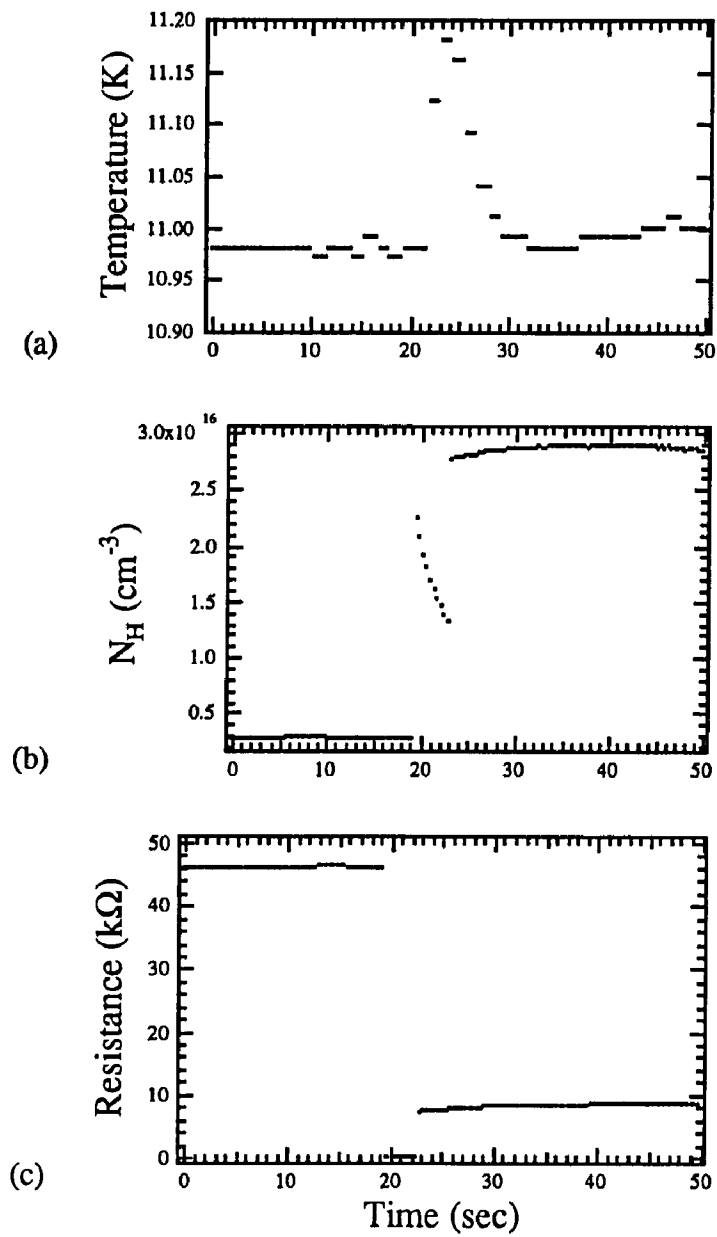


Fig.(3.3) The response of (a) temperature, (b) Hall electron concentration, and (c) epilayer resistance of an $\text{Al}_{0.3}\text{Ga}_{0.7}\text{As}:\text{Si}$ epilayer to an IR LED flash at a temperature of 11K.

Sample heating by the IR LED

Another interesting effect is that the LED flash heated up the sample and

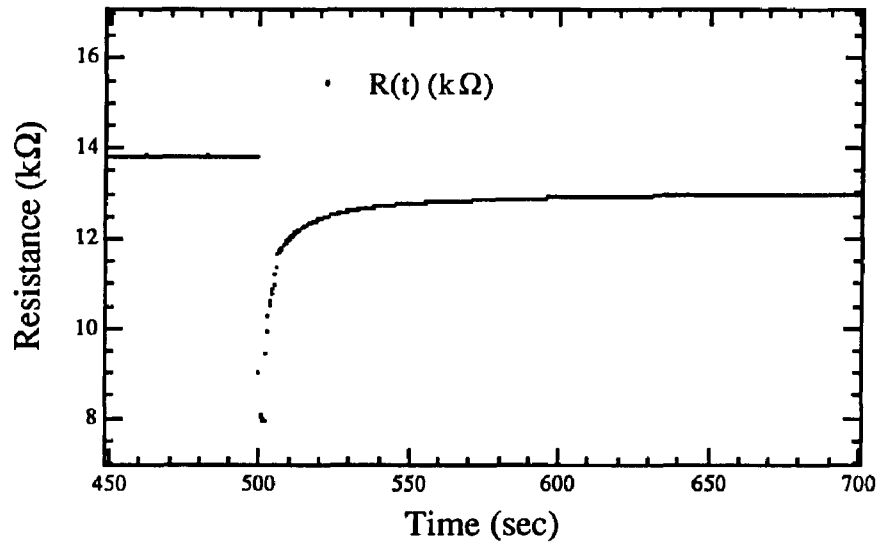
copper sample holder by 0.2K. This heating effect and subsequent cooling from the cold finger reservoir shows up as drifts in N_H and R after the LED is turned off. The drift in these quantities from the heat pulse stabilizes about 10 seconds after the IR LED flash. The heat pulse seems to come from the Joule heating resulting from putting 300mA through the LED for 5 seconds. The IR LED is in physical contact with the copper sample holder block. The amount of heat transferred to the sample holder can be estimated by

$$\Delta Q = \Delta T m C,$$

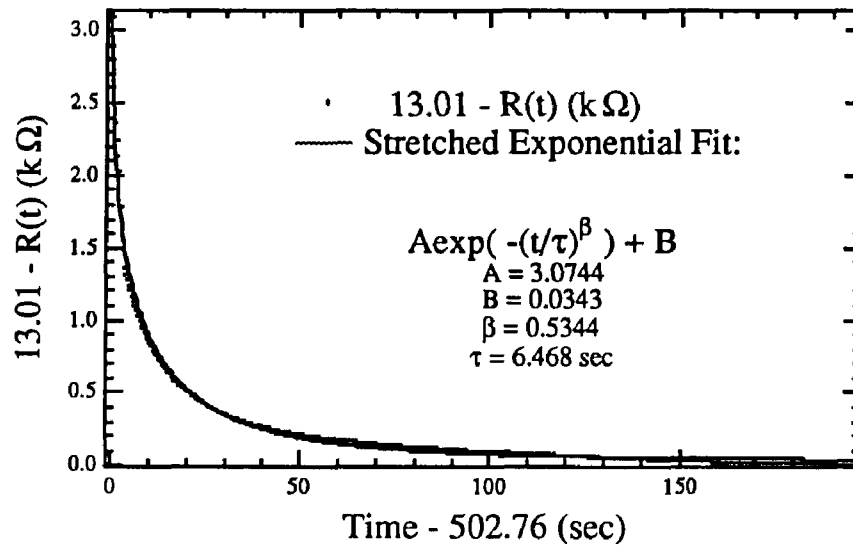
where ΔQ is the amount of heat absorbed by the copper sample holder, ΔT is the change in the temperature of the sample holder, m is the mass of the sample holder, and $C_{11K} = 0.0727 \text{ J/degmol}$ [3.3] is the heat capacity of copper at 11K. The mass of the copper sample holder is about 90 grams (1.4 moles of copper). The temperature change, $\Delta T = 0.2K$, is inferred from Fig.(3.3a). Substituting these numbers into the expression for ΔQ we get $\Delta Q \approx 0.02$ Joules. Putting a current, I_0 , of 300mA through the LED for 5 seconds and assuming the LED turns on at 4V and is biased at 5V implies that the voltage drop across the LED contributing to Joule heating is about 1V. This gives $(I_0 V) \times (\text{time}) \approx 1.5$ Joules of heat given off to the LED surroundings. So it is quite reasonable that the sample holder absorbed some of this heat and this was the effect observed in Fig(3.3a). The effect of Joule heating by the IR LED is hardly measurable at 25K. This is because the heat capacity of copper at 25K is more than an order of magnitude higher than it is at 11K ($C_{25K} = 0.937 \text{ J/degmol}$ [3.3]).

Intermediate temperature regime ($T > 100K$)

The effect of IR LED flashes at intermediate temperatures (100K to 300K)



(a)



(b)

Fig.(3.4) (a) The response of an $Al_{0.3}Ga_{0.7}As:Si$ epilayer resistance to an IR LED flash at a temperature of 160K. (b) A stretched exponential curve fit to the above resistance relaxation. The time constant extracted from the curve fit is $\tau = 6.468\text{sec}$.

no longer lead to persistent changes in N_H and R but lead to changes with relaxation times that are temperature dependent. Shown in Fig.(3.4) is the effect of an IR LED

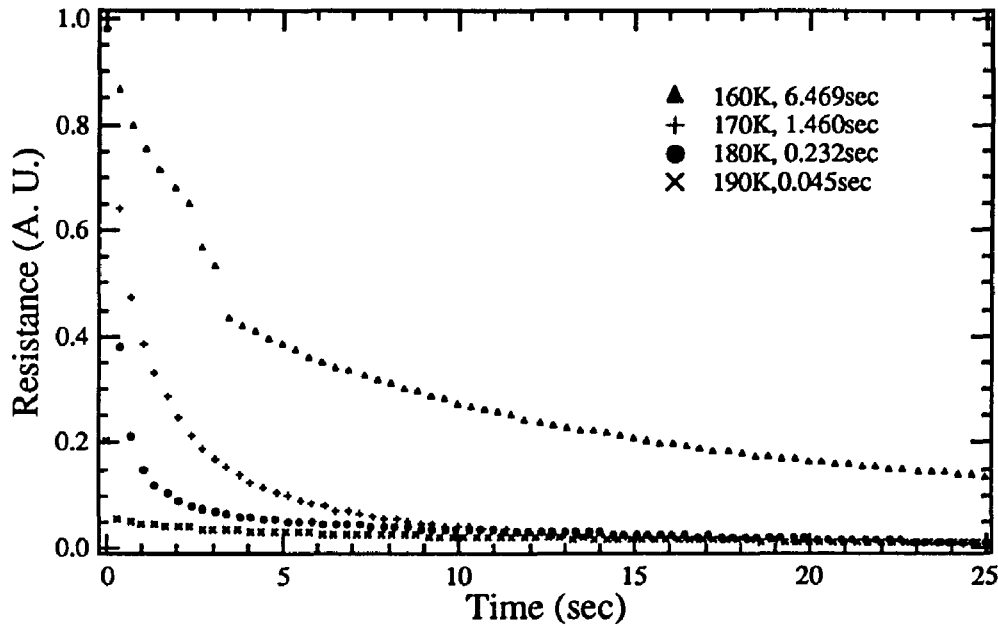


Fig.(3.5) Non-exponential relaxation of the $\text{Al}_{0.3}\text{Ga}_{0.7}\text{As}:\text{Si}$ epilayer at four different temperatures from 160K to 190K. The time constants extracted from the stretched exponential curve fits are also shown in the legend next to its corresponding temperature.

flash on the epilayer resistance at a temperature of 160K. The most important point to note about the IR LED flash at an intermediate temperature is that it induces changes that have non-exponential relaxation rates. The relaxation rates are well fitted by a stretched exponential. Stretched exponentials have the following functional form

$$A \exp\left(-\left(t/\tau\right)^\beta\right),$$

where the prefactor A and β are constants and τ is the time constant extracted from the fit. Non-exponential relaxations are not uncommon in semiconductor systems. Queisser [3.4] discusses a variety of functional forms for the non-exponential relaxation where as Jiang and Lin [3.5] use the more common stretched exponential form given above to fit relaxations in the resistance of an $\text{Al}_{0.3}\text{Ga}_{0.7}\text{As}$ epilayer induced

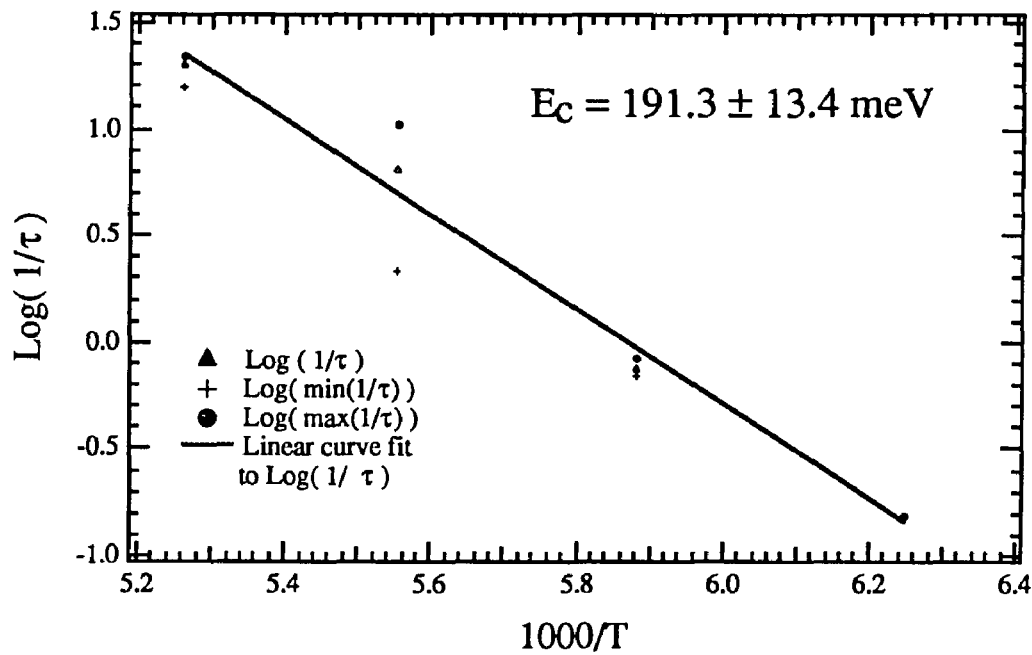


Fig.(3.6) The Arrhenius plot for the non-exponential relaxations of the epilayer resistance for temperatures between 160K and 190K in response to IR LED flashes. The thermal capture barrier, E_C , of the DX center deduced from this plot is $191.3 \pm 13.4 \text{ meV}$.

by 436 to 546 nm radiation from a mercury lamp.

A comparison of relaxations of the epilayer resistance after an IR LED flash for temperatures from 160K to 190K is shown in Fig.(3.5). It is seen that the time constants decrease as the temperature is raised. The β 's in the exponent for the stretched exponential $\exp(-(t/\tau)^\beta)$ also decrease with increasing temperature. There does not seem to be any physical interpretation for β in $\text{Al}_x\text{Ga}_{1-x}\text{As}$ semiconductor systems. Queisser [3.4] gives a more physical basis for other functional forms for the relaxation whereas Palmer et al. [3.6] present a physical model for the stretched exponential relaxation in glassy systems. The time constant, τ , that is extracted from the stretched exponential is used only as a parameter to characterize a resistance relaxation at a given temperature.

The temperature dependent time constants for the epilayer resistance relaxations implies that the electrons are thermalizing over a barrier. The functional form for the time for the electron to thermalize over a barrier of height E_c is given by

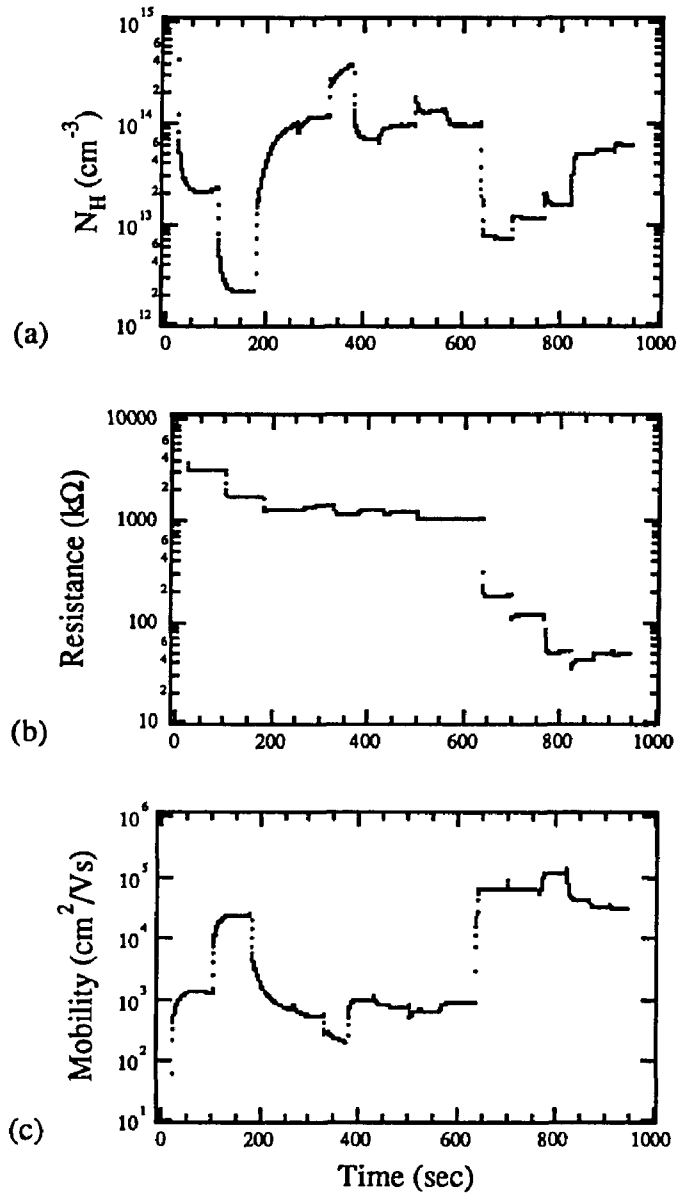
$$\tau \propto \exp(E_c/kT).$$

This barrier, E_c , is the thermal capture barrier of the DX center. See Chapter 4, §B for a discussion of the capture barrier, E_c . By measuring the time constant, τ , at a variety of temperatures and plotting $\log(1/\tau)$ versus $1000/T$, the slope of the line fitted to this plot multiplied by Boltzmann's constant, $k = 86.2 \times 10^{-3} \text{meV/K}$, gives the barrier height, E_c , in the units of meV. Such a plot is called an Arrhenius plot. Shown in Fig.(3.6) is an Arrhenius plot of the resistance relaxation τ 's for the $\text{Al}_{0.3}\text{Ga}_{0.7}\text{As}:\text{Si}$ epilayer. The barrier height deduced from Fig.(3.6) is 191.3 ± 13.4 meV. Similar measurements of $\text{Al}_x\text{Ga}_{1-x}\text{As}$ epilayers have been presented in the literature and have reported E_c 's as follows: 160meV [3.5], 180meV [1.28], and 260meV [3.7]. Lang and Logan [3.7] interpret E_c to be the thermal capture barrier of the DX center. The barrier height measured here agrees with previous published results and serves as a test of the measurement and curve fitting procedure (see Chapter 4, §B for further discussion i.e. dependence of thermal capture barrier on Al mole fraction and electron concentration.).

§E The effect of intense FIR on N_H , R, and μ_H at 10K to 200K

Low temperature regime ($T < 50\text{K}$), dark cooled with no IR LED flashes

Dark-cooling prepares the $\text{Al}_{0.3}\text{Ga}_{0.7}\text{As}:\text{Si}$ epilayer in a state where almost



Fig(3.7) The effect of intense FIR on an $\text{Al}_{0.3}\text{Ga}_{0.7}\text{As}:\text{Si}$ epilayer dark cooled to 25K. The FIR is seen to cause persistent changes in (a) The Hall electron concentration, (b) epilayer resistance, and (c) the Hall mobility. The TEA laser was operated at 29.5cm^{-1} with a total pulse energy of 4 to 6mJ in 50nsec.

all of the electrons are trapped in DX centers. Illuminating a dark-cooled sample with intense FIR ionizes electrons trapped at some centers, possibly DX centers, as

shown in Fig.(3.7a). Initially the Hall electron concentration, N_H , is unmeasurably small. The first pulse of FIR to the dark-cooled sample is around 20 seconds into the data file shown in Fig.(3.7). The signature of an FIR pulse is to produce persistent changes in the Hall electron concentration, N_H , epilayer resistance, R , and Hall mobility, μ_H .

Typically the TEA laser is being blocked from the sample with an aluminum shutter. To expose the sample to FIR, the shutter is opened until the TEA laser is triggered and then it is quickly closed before another laser trigger. A period of 5 seconds between triggering of the TEA laser is plenty of time to safely open and close the shutter before the laser is triggered again.

As can be seen in Fig.(3.7), the typical time between FIR exposures is around 50 seconds. This is usually enough time to allow transients to die out. Transients from photovoltages are typically on the order of 1 second. Note the drifts in N_H and μ_H for times before 400 seconds into the data file in Figs.(3.7a and 3.7c). These drifts are not understood and may be due to the extremely low carrier concentration ($\approx 10^{13}$ to $\approx 10^{14} \text{ cm}^{-3}$) achieved when exposing a dark cooled sample to intense FIR. There is some question of how reliable these Hall measurements are at such low carrier concentrations (2 to 3 orders of magnitude below room temperature concentrations of $7.5 \times 10^{16} \text{ cm}^{-3}$). These observed Hall electron concentrations are on the order of the background impurity level of 10^{14} cm^{-3} in GaAs/AlGaAs MBE grown epilayers (See Chapter 2, §A for a discussion of background impurities in MBE grown samples.).

The resistance measurements of a dark cooled sample shown in Fig.(3.7b) (i.e. $V_{IR} = I_0 R$ with I_0 the constant current through the Hall bar and V_{IR} the voltage

drop between two adjacent Hall tabs and R the epilayer resistance) seem to be more reliable than the measurements of Hall electron concentration shown in Fig.(3.7a). Typically the resistance is on the order of $1\text{M}\Omega$ for the dark cooled $\text{Al}_{0.3}\text{Ga}_{0.7}\text{As}:\text{Si}$ epilayer. Illuminating the sample with intense FIR steadily decreases the resistance to around 50 to $100\text{K}\Omega$ after about 10 to 20 pulses of FIR. The variation in the size of the persistent changes is most likely a reflection of the large fluctuations of pulse to pulse power in the TEA laser. Another factor in the variation of peak power is the variation of the fine time structure within a given TEA laser pulse (see Chapter 2, §E for a discussion of the fluctuations in TEA laser power.). Within the resistance data set, Fig.(3.7b), there are three cases (at times around 270sec, 370sec, and 860sec into the data file) where the resistance does not decrease after an FIR pulse but increases. In all three cases, these increases are small with respect to the decreases. Note that this is not the case with the persistent changes in N_{H} and μ_{H} . For N_{H} and μ_{H} , the persistent increases can be as large as the persistent decreases.

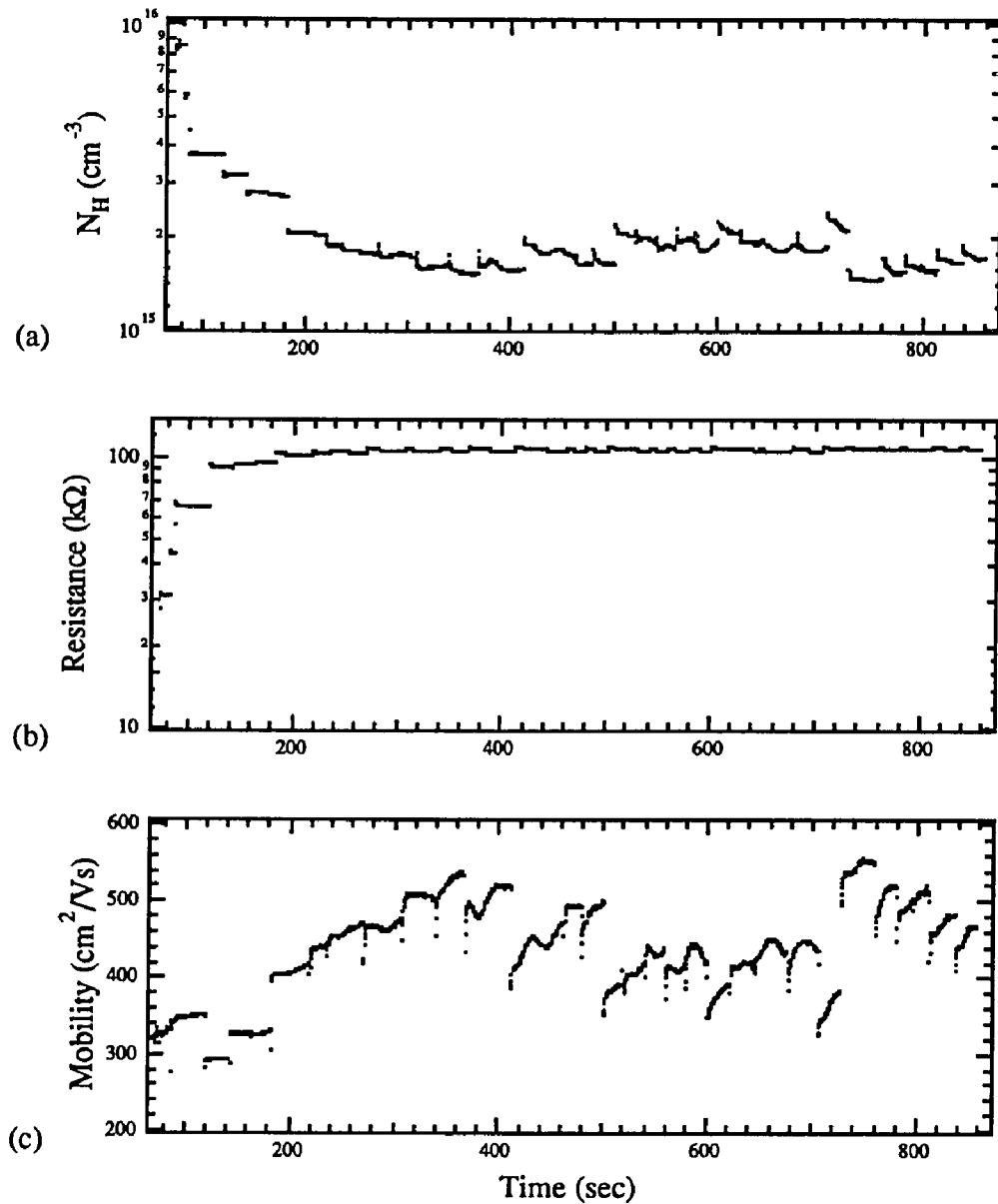
At times the mobility is much larger than $1000\text{cm}^2/\text{Vs}$. Whereas at other times the mobility is less than or equal to $1000\text{cm}^2/\text{Vs}$. When $\mu_{\text{H}} \gg 1000\text{cm}^2/\text{Vs}$, this would seem to indicate that the small population of electrons in the 2DEG at the AlGaAs/GaAs substrate interface is significant. For the time between 100sec and 180sec, μ_{H} is around $3 \times 10^4\text{cm}^2/\text{Vs}$ and N_{H} is around $2 \times 10^{12}\text{cm}^{-3}$. This is a very small concentration of electrons; most of which are probably populating the 2DEG at the substrate interface. For times greater than about 630sec into the data file, the mobility is about $5 \times 10^4\text{cm}^2/\text{Vs}$ and $N_{\text{H}} < 6 \times 10^{13}\text{cm}^{-3}$. It would seem that again there is a significant fraction of the free electron concentration in the substrate interface 2DEG. When $\mu_{\text{H}} < 10^3\text{cm}^2/\text{Vs}$, then N_{H} is greater than or equal to 10^{14}cm^{-3} .

3. This would seem to indicate that the free electron concentration at the substrate interface 2DEG is no longer a significant enough percentage to produce unreasonably large mobilities for the $\text{Al}_{0.3}\text{Ga}_{0.7}\text{As}:\text{Si}$ epilayer. With $\mu_{\text{H}} \approx 1000\text{cm}^2/\text{Vs}$, this is somewhat large for an $\text{AlGaAs}:\text{Si}$ epilayer at low temperatures implying that there is still a small percentage of free electron concentration at the substrate interface 2DEG.

Low temperature regime ($T < 50\text{K}$) with IR LED flashes

An IR LED flash of about 5 seconds with a current of about 300mA through the LED after dark cooling the sample usually prepares the sample with $N_{\text{H}} \approx 10^{16}\text{cm}^{-3}$, $R \approx 50\text{K}\Omega$, and $\mu_{\text{H}} \approx 300\text{cm}^2/\text{Vs}$ as shown in Fig.(3.8) (for times before 80sec into the data file). The first 5 to 10 FIR pulses steadily decrease N_{H} from 1×10^{16} to $2 \times 10^{15}\text{cm}^{-3}$, steadily increase R from $50\text{K}\Omega$ to $100\text{K}\Omega$, and do not change μ_{H} much from its original value of $300\text{cm}^2/\text{Vs}$. The initial effect of the FIR is the opposite of that of an IR LED flash. That is, the intense FIR induces electron capture to DX centers after an IR LED flash has ionized electrons from DX centers.

The effect of FIR pulses asymptotically (i.e. when the sample has been exposed to many FIR pulses) after an IR LED flash is more complicated. In Fig.(3.8b), the resistance changes very little from its value around $100\text{K}\Omega$. The Hall mobility, Fig.(3.8c), varies around the value of $400\text{cm}^2/\text{Vs}$ and the Hall electron concentration, Fig.(3.8a), varies around $2 \times 10^{15}\text{cm}^{-3}$. Note that N_{H} and μ_{H} can have persistent changes that either increase or decrease in the asymptotic region. So initially the effect of the FIR, after the IR LED flash, is to induce electron capture to DX centers and asymptotically induce capture to and emission from some electron



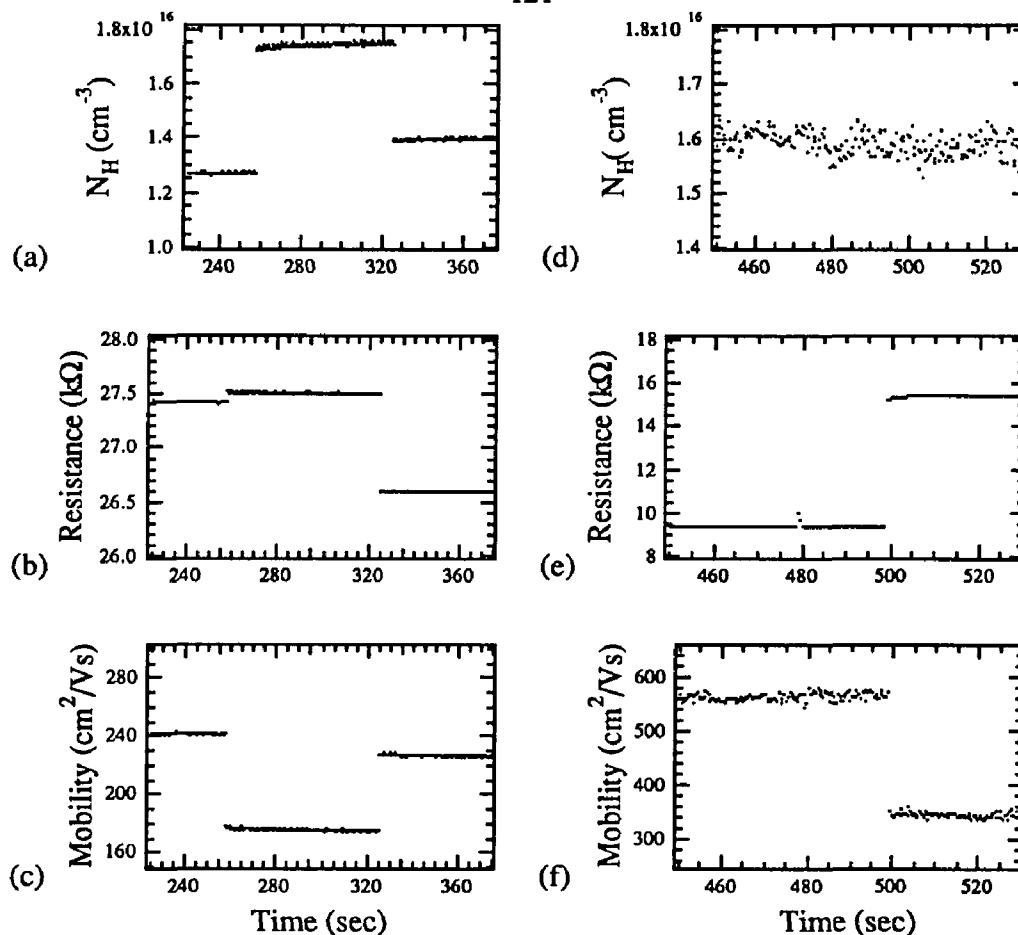
Fig(3.8) The effect of intense FIR on an $\text{Al}_{0.3}\text{Ga}_{0.7}\text{As}:\text{Si}$ epilayer after an IR LED flash. Previous to the IR LED flash, the sample had been exposed to intense FIR as in Fig.(3.7). The Hall concentration is shown in (a), the epilayer resistance in (b), and the Hall mobility in (c). The TEA laser was operated at 29.5cm^{-1} with a total pulse energy of 2 to 4mJ in 50nsec. The sample temperature was 11.0K

trap which could possibly be the DX center. Qualitatively this is what is seen every time this measurement is done just so long the carrier concentration is not too high, that is $N_H < 10^{17} \text{cm}^{-3}$. Quantitatively the values at which N_H , R , and μ_H asymptotically tend to are different for similar measurements done on different days.

This gets right to the difficulty of doing these photo-Hall measurements. That is, preparing the sample with the same *initial conditions* before exposing it to intense FIR. The parameters N_H , R , μ_H , and temperature should be the same before illuminating the sample with FIR. This alone does not seem to uniquely define the *state of the sample*. To illustrate what is meant by this statement, the state of the sample depends on whether or not the sample was prepared with a given N_H by either exposing it to an IR LED flash or by illuminating it with successive intense FIR pulses. The sample's initial condition probably even depends upon how quickly the sample was cooled and how the sample's temperature was regulated. See Chapter 3, §G, Chapter 4, §D and Chapter 7 (Conclusions and Future Experiments) for more discussion of this very important point.

As can be seen from Fig.(3.9), intense FIR can induce a variety of changes in the quantities N_H , R , and μ_H . Two examples of FIR effects that cannot be understood from the resistance and Hall electron concentration changes only are shown in Fig.(3.9a,b,c). Here the changes in μ_H are significant enough to make predictions from $R \propto 1/N_H$ wrong. Knowing that $R \propto 1/\mu_H N_H$, then the observed changes make sense.

An example of an FIR effect where the Hall electron concentration does not change at all but there is a large change in the resistance is shown in Fig.(3.9d,e,f). This dramatic example illustrates the importance of simultaneously measuring the



Fig(3.9) (a), (b), and (c) are an examples of an FIR effects that induce an increase and decrease in N_H , a small increase and decrease in resistance, and a decrease and increase in μ_H respectively. (d), (e), and (f) is an example of an FIR effect that induces (a) no change in N_H , a large increase in resistance, and a large decrease in μ_H respectively. The TEA laser was operated at 29.5cm^{-1} with a total pulse energy of 2 to 4mJ in 50nsec. The sample was an $\text{Al}_{0.3}\text{Ga}_{0.7}\text{As}:\text{Si}$ epilayer at a temperature of 11.0K

Hall electron concentration and the epilayer resistance. It would seem that the electric field from the intense FIR has redistributed the electrons within the $\text{Al}_{0.3}\text{Ga}_{0.7}\text{As}$ epilayer without changing the free electron concentration. It is possible that electrons were transferred in real space from the substrate 2DEG to the

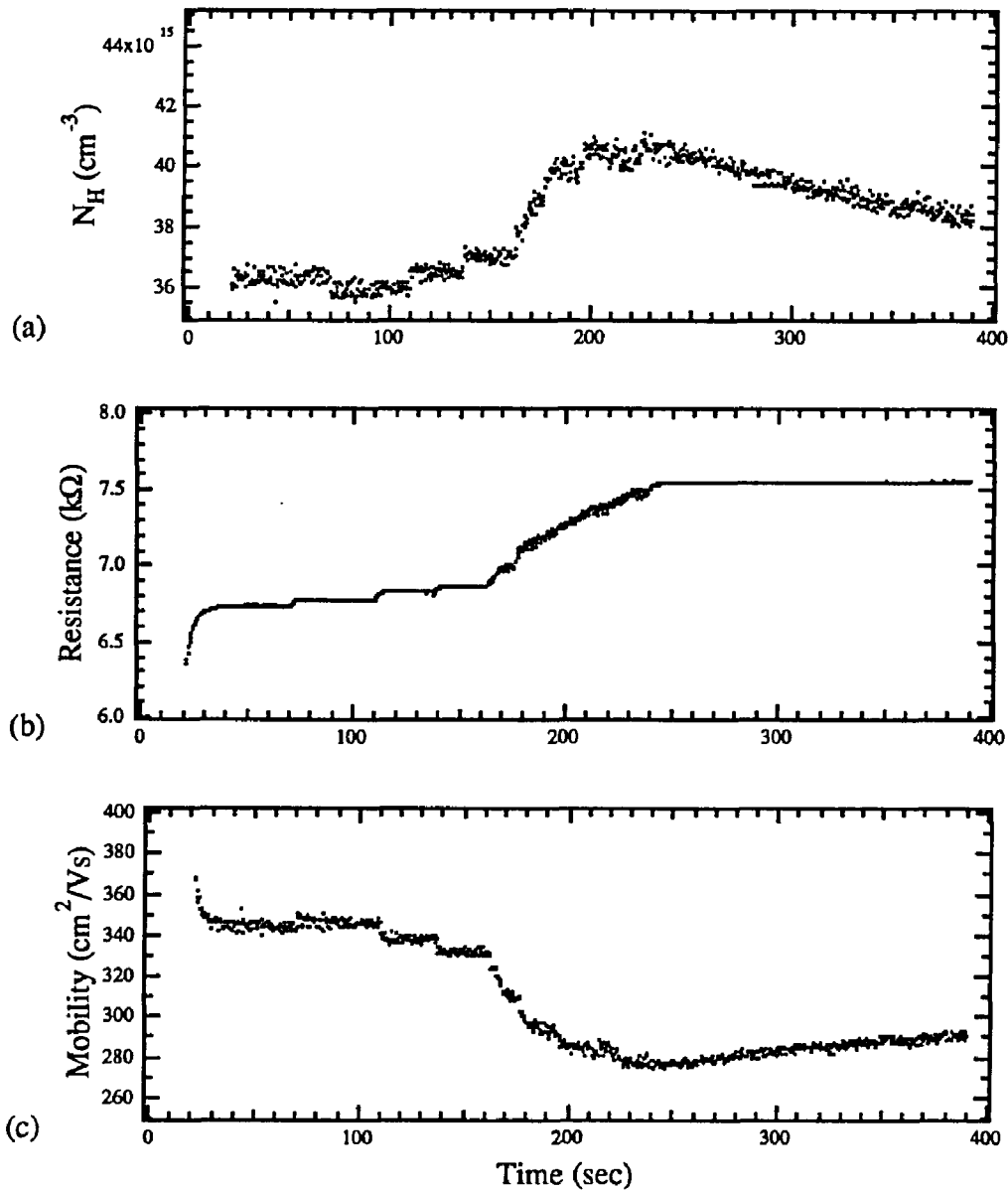
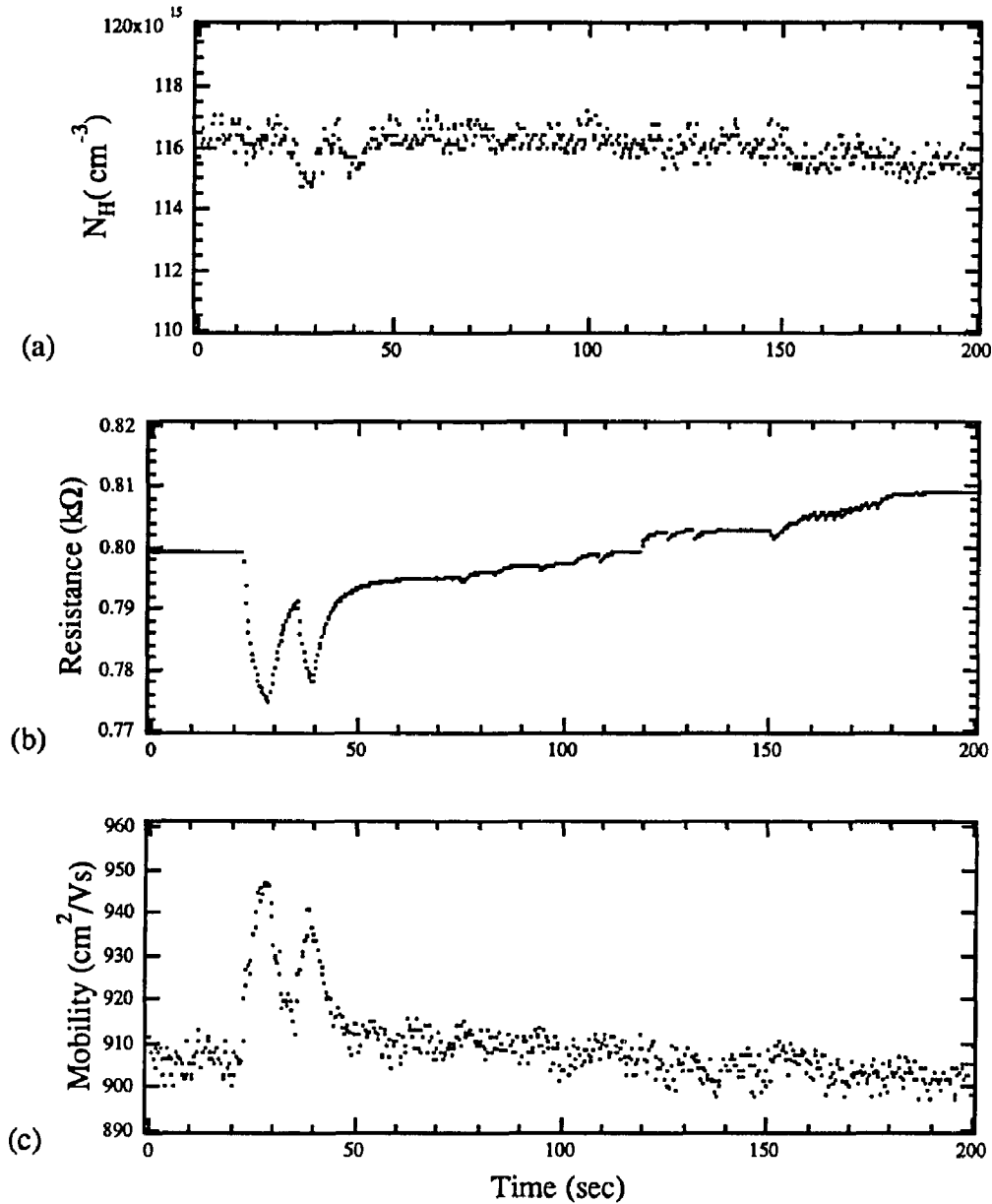


Fig.(3.10) Shown here from 170 to 230 seconds into the data file is the effect of FIR at 1/2Hz repetition rate on (a) the Hall electron concentration, (b) epilayer resistance, and (c) the Hall mobility of an $\text{Al}_{0.3}\text{Ga}_{0.7}\text{As}:\text{Si}$ epilayer. From 270 seconds into the data file, the sample was not exposed to any FIR shots. The TEA laser was operated at 43.3cm^{-1} with a total pulse energy of 17 to 18mJ in 50nsec. The sample temperature was 9.0K.

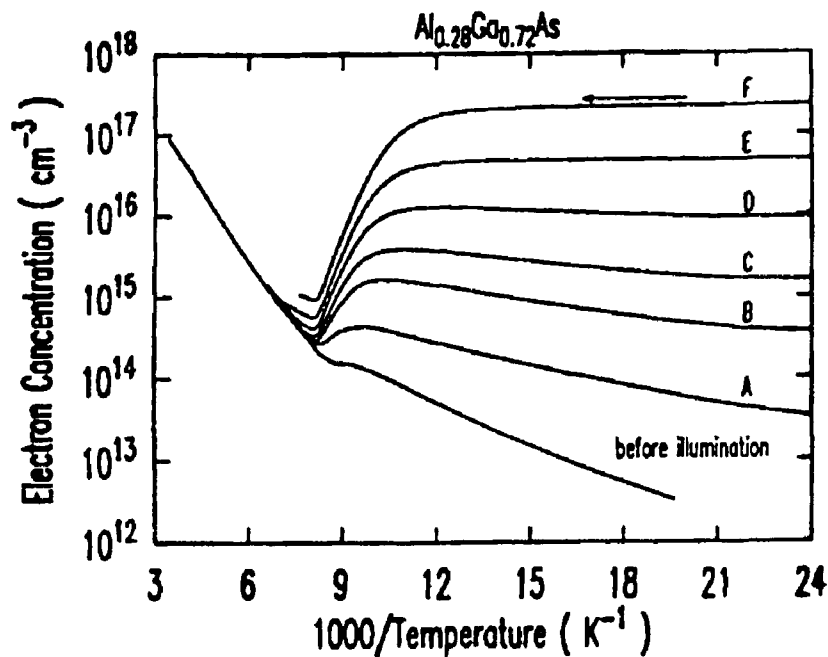


Fig(3.11) The effect of FIR on an $\text{Al}_{0.3}\text{Ga}_{0.7}\text{As}:\text{Si}$ epilayer when the Hall electron concentration is very high ($N_H \approx 10^{17} \text{cm}^{-3}$). The changes in (a) Hall electron concentration (b) sample resistance, and (c) Hall mobility are quite small. The two large spike like features at 28 and 39 seconds into the data file are the effects of two IR LED flashes. The TEA laser was operated at 29.5cm^{-1} with a total pulse energy of 7 to 8mJ in 50nsec. The sample temperature was 25K.

$\text{Al}_{0.3}\text{Ga}_{0.7}\text{As}$ epilayer even though the sample has a large undoped $\text{Al}_{0.3}\text{Ga}_{0.7}\text{As}$ buffer layer between the doped $\text{Al}_{0.3}\text{Ga}_{0.7}\text{As}$ and the substrate interface as shown in Fig.(2.4). See Chapter 5 for discussions of FIR induce hot electron real space transfer and Chapter 4, §D.

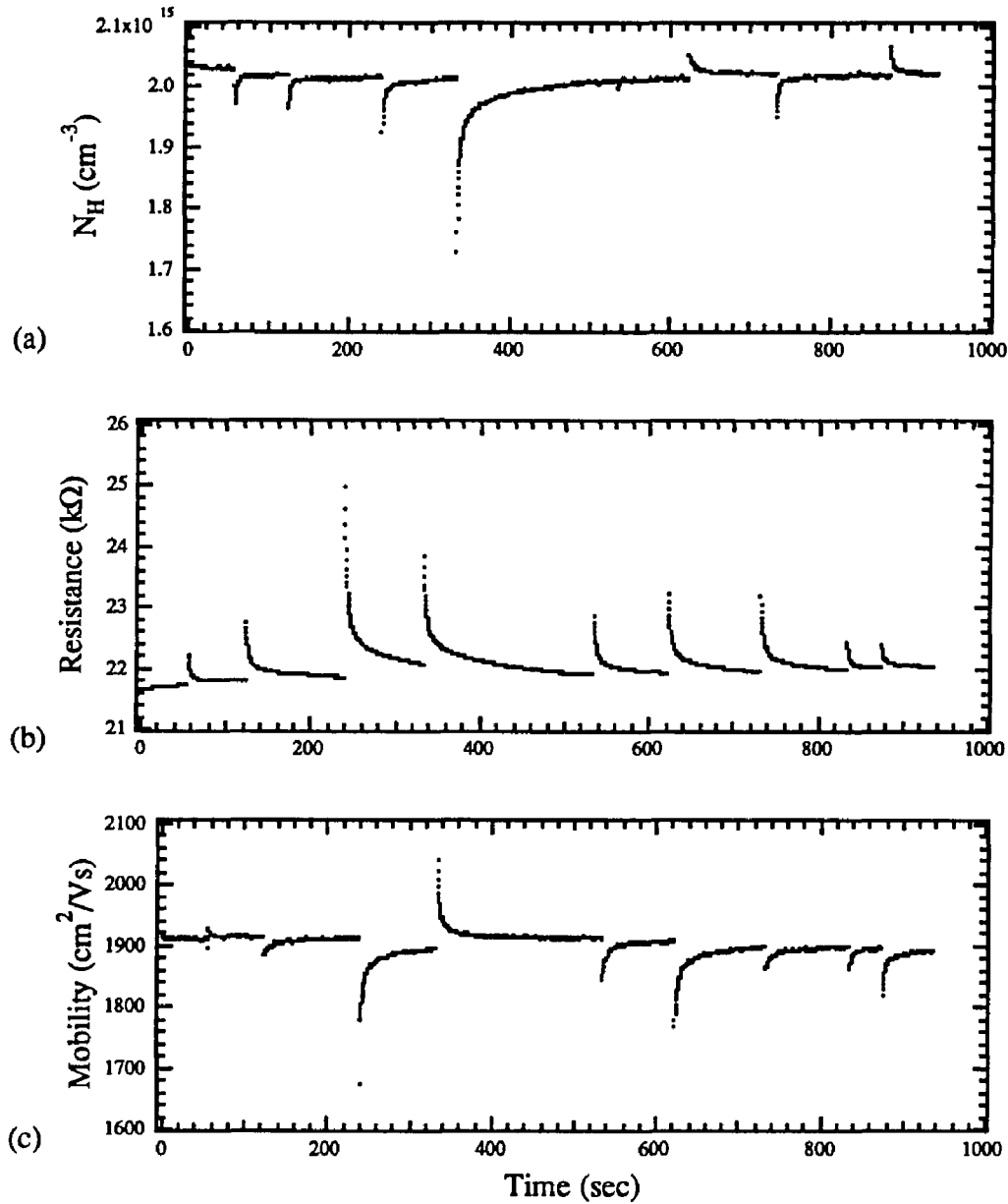
Shown in Fig.(3.10), from 170 to 230 seconds into the data file, is the effect of allowing the FIR to illuminate the sample with a repetition rate of 1/2Hz for 60 seconds. It is seen in Fig.(3.10a) that N_H steadily increases and then, after the FIR is blocked, relaxes back towards its value before the 1/2Hz repetition rate of FIR pulses. In Fig.(3.10b), the resistance steadily increases and persists at its value obtained after the last pulse of FIR. The mobility in Fig.(3.10c) is seen to steadily decrease and then, after the FIR is blocked, relaxes back towards its value before the repetition of FIR pulses. It would seem that the relaxation in N_H and μ_H , after the beam is blocked, are close enough to each other in value that the resistance, R , does not change. The information drawn from these data is that if N_H is less than or equal to 10^{16}cm^{-3} , then it would seem that the effect of continuous pulses of FIR is for N_H , R , and μ_H not to attain any asymptotic values but to steadily and slowly increase or decrease depending on which quantity was being investigated. For most every measurement done, the effect was to steadily increase the sample resistance. The exception was when $N_H > 10^{17}\text{cm}^{-3}$.

When the Hall electron concentration becomes very large, $N_H > 10^{17}\text{cm}^{-3}$, and the sample temperature is less than 80K, the effect of intense FIR and IR LED flashes becomes quite small. Such a situation is shown in Fig.(3.11). With $N_H > 10^{17}\text{cm}^{-3}$ the free electron concentration is larger than it is at room temperature. The reason why the electron concentration can get so high is because of the effect of



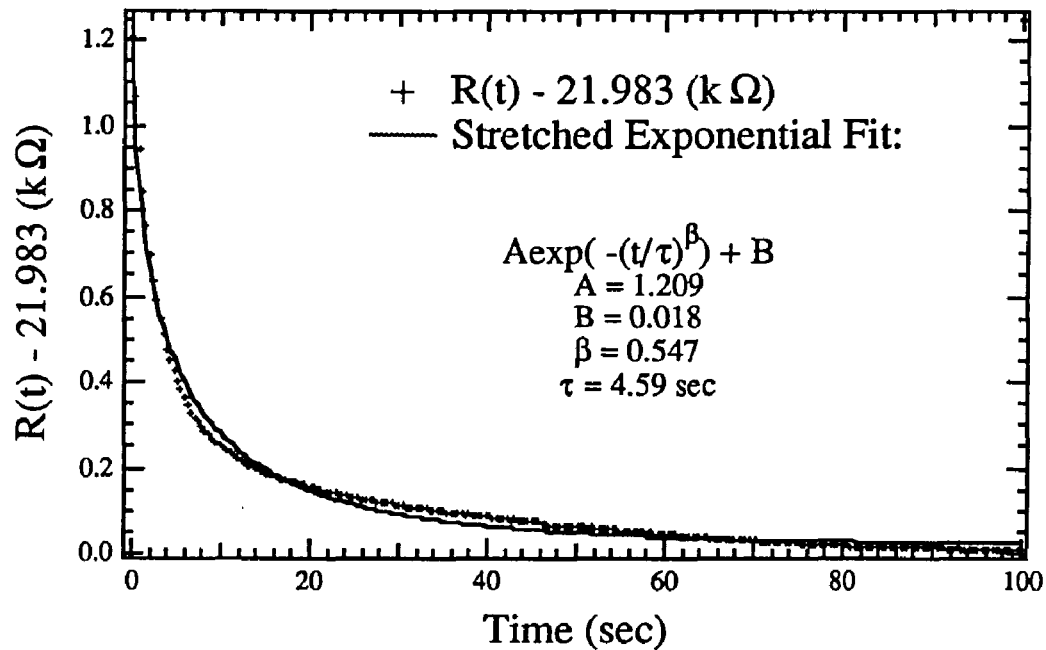
Fig(3.12) Van der Pauw Hall measurements of the free electron carrier concentration as a function of reciprocal temperature in a sample of Si-doped $\text{Al}_{0.28}\text{Ga}_{0.72}\text{As}$. Successive curves from A through F correspond to successively longer low-temperature illuminations of the sample (Ref. 3.4).

persistent photoconductivity, PPC, seen in $\text{Al}_x\text{Ga}_{1-x}\text{As}$ epilayers for $x > 0.22$. Shown in Fig.(3.12) is the effect of PPC for successively longer illumination of the sample at low temperatures. It is seen from curve F in Fig.(3.12) that the electron concentration can become larger than its value at room temperature if the sample is exposed to enough radiation with photon energy greater than 0.8eV (i.e. IR LED flashes for measurements made for this thesis). The FIR effect on N_H observed in Fig.(3.11a) only induces an overall decrease in N_H . The changes induced from one pulse of FIR is too small to be observed and only a drift in N_H can be detected as a possible signature of an FIR effect on N_H . Whereas changes in N_H shown in Fig.(3.10a) from individual FIR pulses are still clearly resolved and above the noise level. The



Fig(3.13) The effect of intense FIR at an intermediate temperature of 150.0K on (a) the Hall electron concentration, (b) the epilayer resistance, and (c) the Hall electron mobility of an $\text{Al}_{0.3}\text{Ga}_{0.7}\text{As}:\text{Si}$ epilayer. The TEA laser was operated at 29.5cm^{-1} with a total pulse energy of 2 to 4mJ.

Hall mobility data shown in Fig.(3.11c) are similar to the N_H data in the sense that the effect from individual FIR pulses are difficult to resolve from the noise and only



Fig(3.14) Stretched exponential curve fit to a FIR induced relaxation in the epilayer resistance at 150.0K of an $\text{Al}_{0.3}\text{Ga}_{0.7}\text{As:Si}$ epilayer. The relaxation is fit to a stretched exponential of the form: $R(t) = A \exp(-(t/\tau)^\beta) + B$ where τ is the parameter that is of interest in the curve fit.

an over all trend downward can be detected as a signature of an effect of illuminating the sample with FIR.

Intermediate temperature regime ($T > 150\text{K}$)

At intermediate temperatures, 150 to 300K, the effect of intense FIR illumination is no longer persistent as shown in Fig.(3.13). Most of the changes in N_H , Fig.(3.13a), and μ_H , Fig.(3.13c), decrease with only a few that increase. All of the observed changes in the epilayer resistance increase. So the majority of FIR effects at intermediate temperatures is to induce capture of electrons by DX centers. Note that the few increasing changes in N_H and μ_H do not occur at the same times. That is, μ_H goes positive at about 60sec and 315sec into the data file and N_H goes

positive at about 615sec and 860sec into the data file.

The non-exponential relaxations can be fit to a stretched exponential of the form: $A \exp(-(t/\tau)^\beta) + B$, as shown in Fig.(3.14). In Fig.(3.14), τ is a parameter of the curve fit that is of interest in constructing an Arrhenius plot for the temperature dependent relaxations. The constant, τ , is used only to parameterize a relaxation at a given temperature. The Arrhenius plot for the FIR induced relaxations will be presented in Chapter 4 along with an interpretation of the barrier height deduced from the plot. See Chapter 3, §D for references to the literature about non-exponential relaxations in semiconductor systems [3.4,3.5,3.6].

Introduction to §F and §G

The next two sections discuss the effects of attenuation and frequency (comparing two TEA laser lines: 29.5 and 43.3cm⁻¹) on changes in epilayer resistance, ΔR . These are presented here only to get a qualitative feel for possible power and frequency dependent effects. The measurements need to be improved further. Chapter 7 discusses such improvements and future experiments.

The reason the resistance changes are studied instead of the Hall electron concentration is that the resistance data are not as noisy as the Hall data so smaller effects can be observed. This is a very risky thing to do since it could be only changes in mobility that are leading to the observed changes in the resistance. Since the resistance changes are so small, perhaps the intense FIR is only transferring the electrons back and forth between the substrate interface 2DEG and the Al_{0.3}Ga_{0.7}As epilayer. The reader should keep this in mind while reading the next two sections.

The observed changes in N_H corresponding to the resistance changes will be discussed qualitatively to try and support the claim that N_H is changing with R . However the Hall concentration data are quite noisy and are therefore not convincing.

§F Power dependence of changes in epilayer resistance

Attenuation measurements are difficult to do at low temperatures (below 100K) because the largest persistent effects observed in N_H and R occur within the first few FIR pulses immediately after an IR LED flash. Typically, the first FIR pulse after an IR LED flash leads to the largest persistent change observed until the sample is again illuminated with an IR LED flash. This behavior is shown in Fig.(3.8). The largest change in resistance and Hall electron concentration are observed within the first five FIR pulses (note the log scale for N_H and R). The measurements are further complicated by the pulse to pulse fluctuations of the TEA laser's power (see Chapter 2 §F).

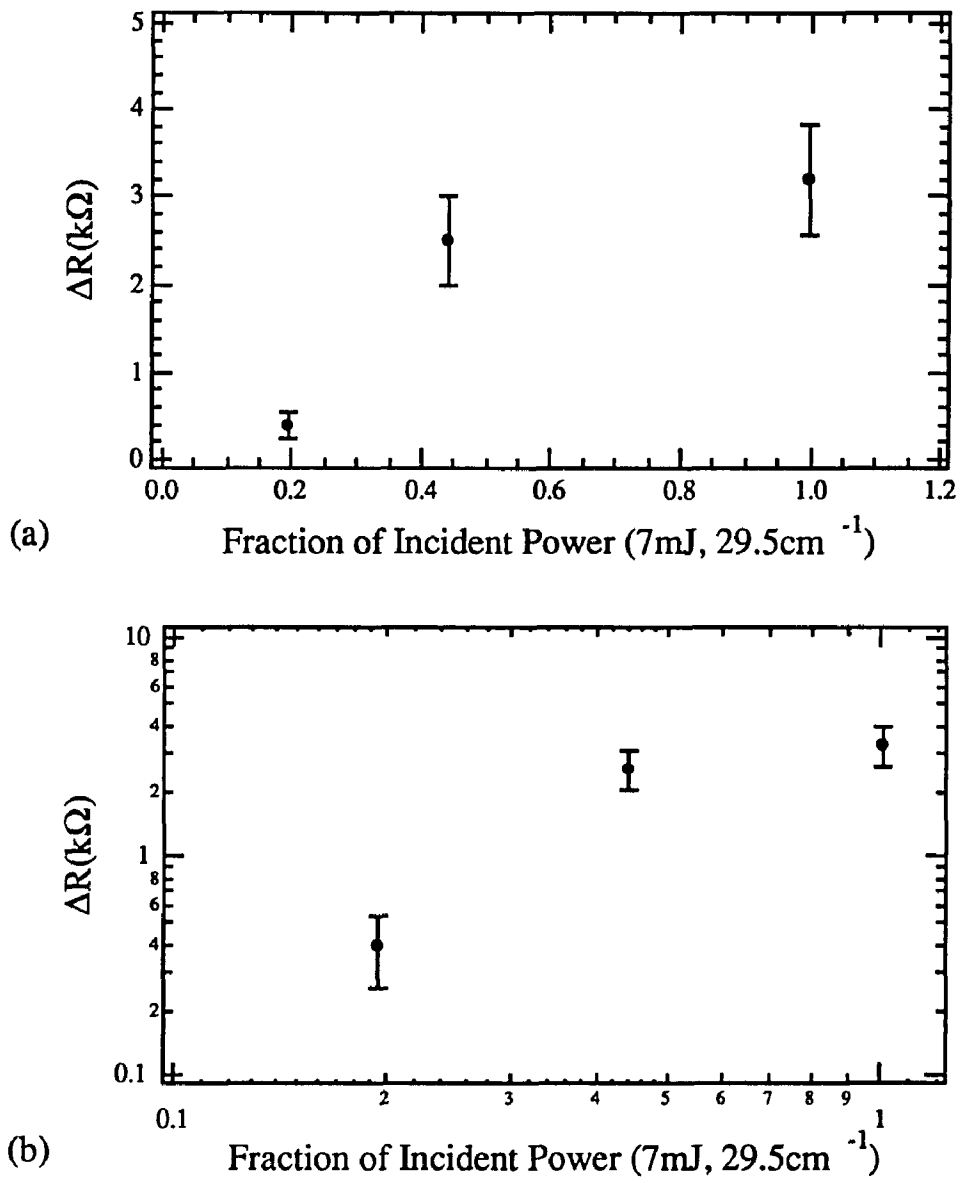
A possible way to reproducibly prepare the sample in a unique initial state would be to warm the sample up above 150K, slowly cool (2K/min.) the sample to a low temperature say 20K, and illuminate the sample with an IR LED for a precisely known time. This should prepare the sample in a known initial condition, i.e. one that can be reproduced. The problem with this procedure is that it would take far too long to do the measurement. For a good statistical measurement, it is necessary to have 10 to 20 pulses at 4 or 5 different attenuations. This would equate into 50 to 100 warming and cooling of the sample; about 100 hours of work. Ideally this is what should be done for an attenuation measurement or any other measurement that

requires the sample to be in a known reproducible initial state.

There are two alternatives that are not as time consuming but of a questionable nature. One possibility is that the measurement could be done at an intermediate temperature where the FIR effects are no longer persistent but relax within a few minutes. The other possibility is at low temperature after the large changes from the intense FIR have taken place. It is seen in Fig.(3.8) that after the first five or six FIR pulses the changes are seen to be similar in size with N_H going up and down and R steadily increasing by small amounts in response to the FIR. It was this particular data file and two subsequent data files (no IR flashes in these two files) from which the attenuation data presented in this section were taken.

The three groups of points shown in Fig.(3.15) correspond to three different amounts of attenuation. The point corresponding to 1.0 unit on the incident power axis represents full power so an attenuator was not used. The two following points at fractional powers of 0.44 and 0.19 were taken with two plastic attenuators of different thickness, 25 and 50 thousandths of an inch respectively (calibrated at 29.5cm^{-1}). The attenuators are circular with a four inch diameter which easily cover the one to two inch diameter unfocused FIR beam when carefully centered on the optic axis of the FIR beam. The attenuators were placed a few inches in front of the mirror used to focus the FIR onto the sample.

The peak power of a laser pulse is unknown because of the TEA lasers complicated time structure (see Chapter 2, §F). The fine time structure within a pulse is known to be as short as 5 to 10 nsec if not shorter with the pulse itself as long as 50 to 100 nsec. The total pulse energy for the attenuation data presented in Fig.(3.15) was 7mJ averaged over 10 pulses with pulse to pulse total energy ranging from 5 to 8mJ.



Fig(3.15) The power dependence of intense FIR on the change of resistance, ΔR , of an $\text{Al}_{0.3}\text{Ga}_{0.7}\text{As}:\text{Si}$ epilayer. The sample temperature was 11.0K and the TEA laser was operated at 29.5cm^{-1} with a total pulse energy of 7mJ. A linear plot is shown in (a) and a log-log plot is shown in (b).

The points in Fig.(3.15) are the average of 20 to 25 laser pulses at the given attenuation. The large error bars in the data are believed to be in part caused by the

large pulse to pulse fluctuations of the TEA laser power.

Even with such large scatter in the data, it is clear that the power dependence is nonlinear. By examining Fig.(3.15b), it is seen that there is not a power law dependence to the attenuation data. The data even seem to suggest some sort of threshold in the power dependence. This suggests doing an FEL measurement to try and find the threshold if it indeed exists.

Measurements were done with the FEL on an $\text{Al}_{0.3}\text{Ga}_{0.7}\text{As}:\text{Si}$ (Si concentration $1.5 \times 10^{17} \text{cm}^{-3}$) epilayer sample that was fabricated for only two point resistance measurements. The sample was not grown with a buffer layer of undoped $\text{Al}_{0.3}\text{Ga}_{0.7}\text{As}$ so it had a large population of electrons at the substrate interface 2DEG. So it was effectively a 2DEG with very poor mobility ($10^4 \text{cm}^2/\text{Vs}$). Nonetheless, the measurements were done and its epilayer resistance changes showed a linear dependence on power. This linear dependence on power was observed for both the large changes immediately after an IR LED flash and the subsequent smaller changes after a few FIR pulses following the IR LED flash. It would be nice to be able to match up the power dependence of the FEL data and the TEA laser data but this has proven to be impossible so far.

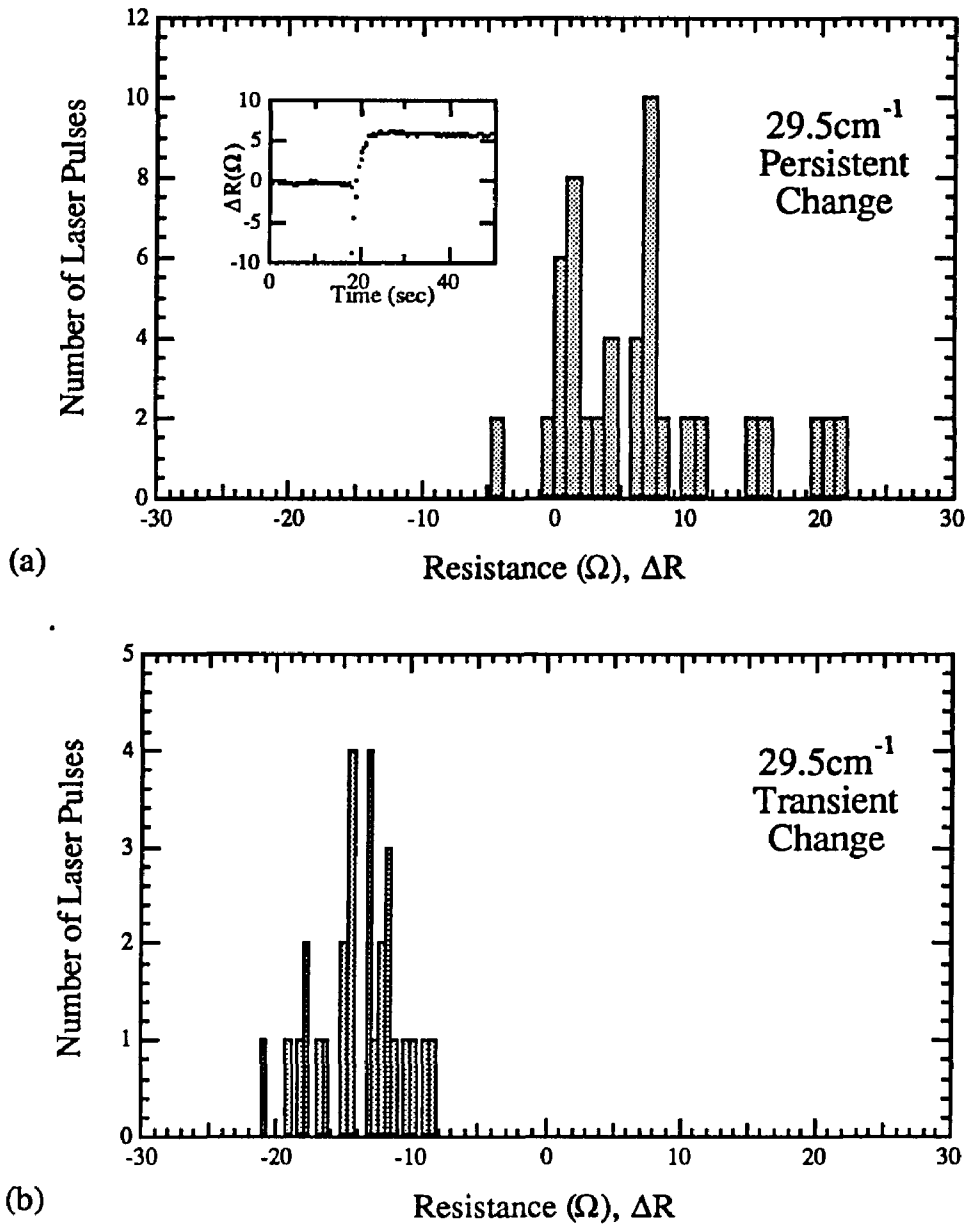
As an aside, attenuation measurements on a 2DEG (intentional) resistance changes have been done with the TEA laser and the data were very nonlinear. The presence of a lower power linear dependence was not clear. So once again, matching up this data with the FEL data discussed above is difficult. These facts will be discussed at much greater length in Chapter 5 which discusses the measurements that have been done with the TEA laser on quantum wells (both a 2DEG and a wide (1000\AA) half-parabolic well).

§G Frequency dependence of changes in epilayer resistance

Frequency dependence measurements are difficult for the same reasons attenuation measurements are because of the importance of preparing the sample in the same initial state prior to each FIR pulse. Once again the data presented in this section are meant only as a motivation of a possible frequency dependence of the changes in $\text{Al}_x\text{Ga}_{1-x}\text{As}$ epilayer resistance. No firm conclusions should be drawn from the data. It is included here only to motivate more careful future measurements of the frequency dependence of the persistent changes seen in N_H , R , and μ_H under the influence of intense FIR at low temperatures. A detailed discussion of such experiments will be presented in Chapter 7.

Only epilayer resistance changes were tabulated for the different frequencies presented here since the corresponding Hall electron concentration were very close to the noise level. This case is illustrated in Fig.(3.11). By examining Fig.(3.11), it can be seen that the resistance steadily increases by small amounts with an overall downward trend in the Hall electron concentration. Notice that even the IR LED flashes early on in the data file have a very small effect on the Hall electron concentration. The resistance changes are not large but are clearly measurable. The Hall electron concentration changes seem to be overwhelmed by the noise. This has been the general behavior observed when N_H rises above around $7.5 \times 10^{16} \text{cm}^{-3}$ (the value of N_H at room temperature). Only after many intense FIR pulses can any noticeable change be observed. But could still only be the result of a temperature drift since the N_H changes are so small.

The measurements presented in Fig.(3.16) and Fig.(3.17) were done using



Fig(3.16) A histogram of (a) persistent changes and (b) transient changes in the resistance, ΔR , of an $\text{Al}_{0.3}\text{Ga}_{0.7}\text{As}:\text{Si}$ epilayer. The sample temperature was 12K and the TEA laser was operated at 29.5cm^{-1} with total pulse energy of 8mJ. The inset of (a) shows the time structure of a persistent resistance change.

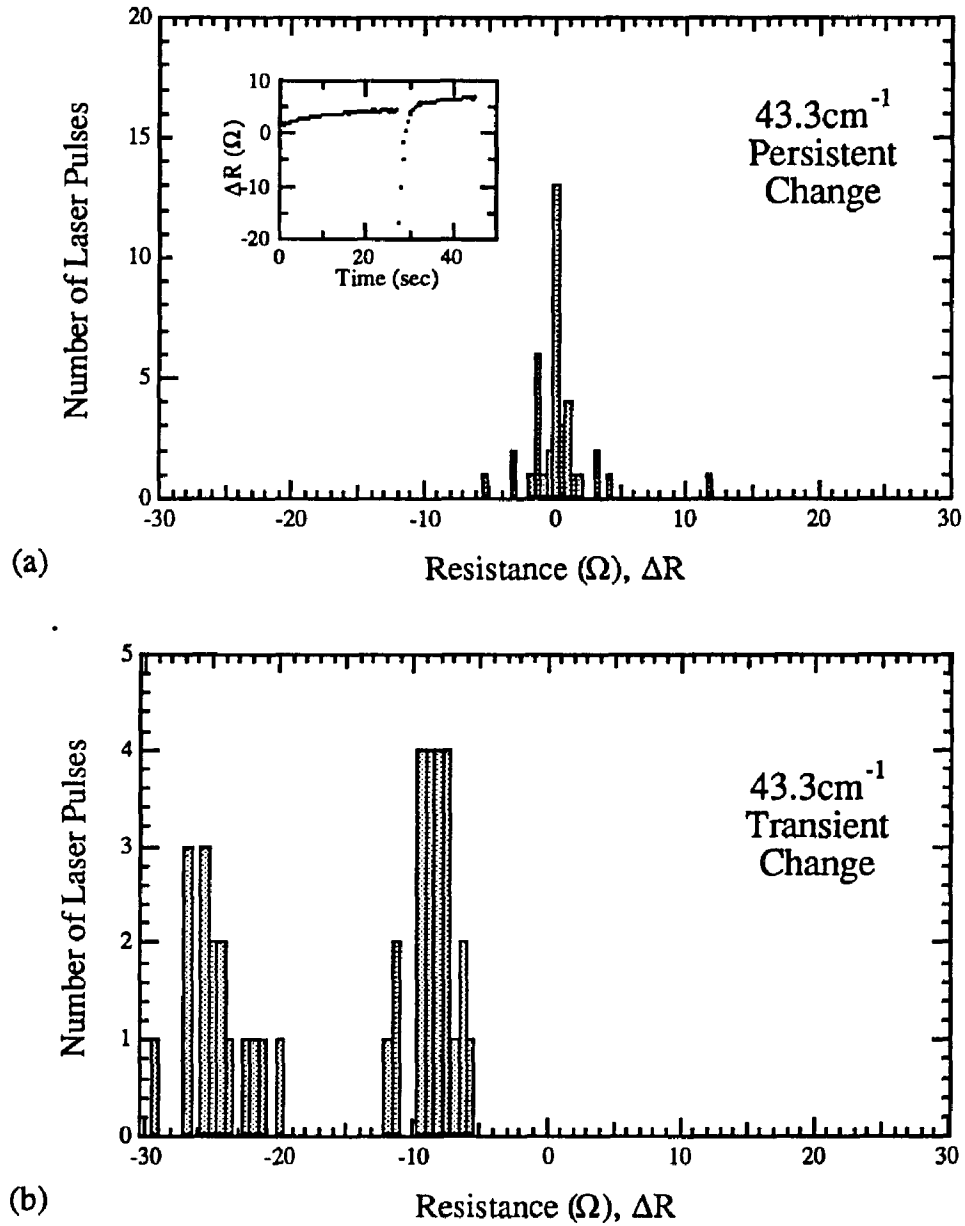


Fig.(3.17) A histogram of (a) persistent changes and (b) transient changes in the resistance, ΔR , of an $\text{Al}_{0.3}\text{Ga}_{0.7}\text{As}:\text{Si}$ epilayer. The sample temperature was 12K and the TEA laser was operated at 43.3cm^{-1} with total pulse energy of 15mJ. The inset of (a) shows the time structure of a persistent change.

two different TEA laser lines. One line was 29.5cm^{-1} , Fig.(3.16), with total pulse energy averaged over 10 pulses of 8mJ with pulse to pulse total energy ranging from 6 to 9mJ. The other line was 43.3cm^{-1} with an average total pulse energy of 15mJ with pulse to pulse total energy ranging from 12 to 17mJ.

For a given line, the sample was at a temperature of 12K and flashed with an IR LED then exposed to 10 to 20 FIR pulses at a rate of one pulse every 10 to 20 seconds. This makes up the data within one computer file as shown in Fig.(3.11). After the completion of the measurement at the given line, the TEA laser was adjusted to the other line and a new computer data file was started with the sample relaxing from the FIR irradiation from the previous file. Always when a new file was begun, the sample was exposed to an IR LED flash and then irradiated with 10 to 20 pulses of FIR at a rate of one pulse every 20 to 30 seconds. The data compiled for Fig.(3.16) are made up of two data files and the data compiled for Fig.(3.17) are comprised of 3 data files. The two files for Fig.(3.16) were taken sequentially. Two of the three data files used in compiling Fig.(3.17) were taken before the data files used to make Fig.(3.16) and one taken after the two data files used in compiling Fig.(3.16).

From the above discussion of how the different data files were compiled, it is clear that the sample is prepared in a different initial condition each time a new file is begun. The main difference between successive data files is that the sample gets exposed to an additional IR LED flash in the later file. This means that the Hall electron concentration will be a little higher at the start of each data file compared with the previous data file. This is illustrated in Fig.(3.12) showing how the Hall electron concentration at low temperatures increases with increasing illumination

from a source with photon energies greater than 0.8eV.

So once again these conditions are far from ideal for doing a frequency dependent measurement. The sample should be warmed to above 150K, cooled slowly in the dark to a known stable temperature, illuminated with an IR LED flash for a precise amount of time, and exposed to an intense FIR pulse. This procedure of warming, cooling, and IR flash should be repeated before the next FIR pulse.

The histograms were compiled by tabulating all the effects from intense FIR pulses observed in the epilayer resistance versus time data files. The data in Fig.(3.16) correspond to the two files taken at 29.5cm^{-1} and the data in Fig.(3.17) correspond to the three files taken at 43.3cm^{-1} . More data files were collected at each line but they represent the same effect shown in Figs.(3.16 and 3.17). The files were grouped as they were in order to compare the data taken as near as possible to the same initial conditions. That is, files were compared only if they had close to the same Hall electron concentration. If N_H differs by an order of magnitude between two files, then comparing the two data files is useless because the file corresponding to the lower N_H will show a much larger change in epilayer resistance.

For each TEA laser line, two histograms are shown. Shown in Fig.(3.16a) and Fig.(3.17a) are the histograms of persistent changes observed after the FIR pulses. This is the change in resistance measured, either positive or negative, well after the observed negative going transients have relaxed (see the insets in Figs.(3.16a and 3.17a)). The histograms of transient changes are shown in Fig.(3.16b) and Fig.(3.17b). The transient is measured with respect to the point where the persistent change first settles in. All the transients are negative. In some instances for the 29.5cm^{-1} line, the persistent change is larger than the transient change. In that case, the transient changes and persistent changes both rise above the resistance measured

before irradiating with intense FIR.

There were two pulses, for the 29.5cm^{-1} data, that were not included in the histogram of Fig.(3.16a) because they were too large for the range of ΔR 's presented in Figs.(3.16 and 3.17). One pulse had a $\Delta R = 154\Omega$ and the other had a $\Delta R = 37\Omega$. The 154Ω change was immediately after an IR LED flash. All observed changes in the files corresponding to 43.3cm^{-1} were included. The one point with $\Delta R = 11.7\Omega$ in Fig.(3.17a) corresponds to an FIR pulse immediately after an IR LED flash.

What Figs.(3.16 and 3.17) suggest is that the effect of intense FIR on persistent resistance changes at 29.5cm^{-1} is larger (by a factor of 2 or so) than the persistent changes at 43.3cm^{-1} . Even though the total pulse energy for the 43.3cm^{-1} line was about a factor of 2 larger than the total pulse energy for 29.5cm^{-1} . It is interesting to note that the transient changes are roughly comparable, that is, the 43.3cm^{-1} transients are a little larger than the 29.5cm^{-1} transients. The transients are typically about 5 seconds long and most likely are photovoltaic transients from the AuGe/Ni/Au contacts on the Hall bar (There are 7 contacts on the Hall bar as shown in Fig.(2.7b).). Also note that the persistent changes for the 43.3cm^{-1} are both positive and negative, i.e. symmetrical about zero, and the persistent change for the 29.5cm^{-1} line are all positive except for two pulses.

It has been observed that different lines of the TEA laser used for these measurements have different large scale time structure which could lead to different total pulse energies but the same peak power.

The high pulse energy reported here, 15mJ for 43.3cm^{-1} and 8mJ for 29.5cm^{-1} , was only observed with a methylfluoride (CH_3F) gas bottle that has since been used up. Newly purchased bottles of methylfluoride only give total pulse energies of 2

to 4 mJ at 29.5cm^{-1} and 4 to 7mJ for 43.3cm^{-1} .

This has been stated here to alert the reader that TEA lasers are very unstable machines and vary widely in performance from machine to machine. Fielding Brown from Williams College in Massachusetts has an older TEA laser at his lab that has a much more smooth large scale time structure than the one in the U.C.S.B. Free-Electron Laser Lab. It cannot be stressed enough here that different lines (and different machines) can have widely different time structures especially if different gases are used. The time structure can usually be improved if the laser is not operated with higher than needed He gas pressures. The He gas pressure is sometimes increased to get higher total pulse energies which most likely correspond to more irregular fine time structure and less smooth long time structure.

Chapter 3 references

1. K. Seeger, 4th ed., *Semiconductor Physics*, (Springer-Verlag, Berlin, Heidelberg, New York, 1989) p.177
2. TRW Optoelectronics Division, TRW Electronic Components Group, *Product Bulletin 5069*, January 1985, p. 32-35.
3. *Handbook of Chemistry and Physics*, 52nd ed., R. C. Weaton editor, (The Chemical Rubber Company, Cleveland, Ohio, 1971).
4. Hans J. Queisser, *Phys. Rev. Lett.* **39**, 635 (1977); H. J. Queisser and D. E. Theodorou, *Phys. Rev.* **B33**, 4027 (1986).
5. H. X. Jiang and J. Y. Lin, *Phys. Rev. Lett.* **64**, 2547 (1990).
6. R. G. Palmer, D. L. Stein, E. Abrahams, and P. W. Anderson, *Phys. Rev.* **B53**, 958 (1984).
7. D. V. Lang and R. A. Logan, *Phys. Rev. Lett.* **39**, 635 (1977).

Chapter 4

Hot Electron Capture of Electrons by DX Centers

§A Introduction

Some of the observed FIR induced carrier concentration changes can be explained in terms of DX center phenomenology. The first part of this chapter will be concerned with drawing this connection with the DX center.

The fact that the FIR induces persistent changes in N_H at low temperatures ($T < 50K$) can be explained in terms of capture of hot electrons by DX centers. The size of the changes in electron concentration implies that the electrons are captured by DX centers since they are the only trap of sufficient concentration to produce such large changes.

At low temperatures when electrons are trapped by DX centers they remain trapped for times as long as hours to days. The persistency observed in FIR induced changes is consistent with the persistency observed with electron transport in the presence of DX centers at low temperatures.

Associated with the DX center is a thermal barrier to both capture and emission of electrons. Electrons may thermalize over the barrier via multiphonon

emission and capture processes. At intermediate temperatures ($T > 150\text{K}$), the DX center is in equilibrium with the conduction band states. The electrons will no longer remain trapped by DX centers for long times but will equilibrate with the conduction band on the order of seconds to minutes. The FIR induced changes at intermediate temperatures relax within seconds to minutes and are no longer persistent as they were at low temperature. This observation is also consistent with electron capture by DX centers.

From the temperature dependent FIR induced relaxations, a barrier height, E_b , for the thermalizing electrons can be extracted from an Arrhenius plot. This barrier height can then be compared with barriers associated with the DX center in an attempt to verify that the electrons are in fact captured by the DX center.

The first part of this chapter will discuss how the barrier height, E_b , is found from the FIR measurements and what it means in terms of DX center phenomenology will be the main point of this chapter and will be discussed first.

The second part of this chapter will estimate the amount of electron heating by intense FIR, discuss the possible observed frequency dependence reported in Chapter 3, §G, and summarize the many interesting observations reported in Chapter 3 of the FIR induced changes in the Hall electron concentration. The purpose of discussing of the unusual FIR effects in this part of the chapter is to draw attention to data discussed in Chapter 3 that are interesting and not understood.

§B The barrier height, E_b , associated with the FIR induced relaxations

FIR induced changes in N_H , R , and μ_H at intermediate temperatures ($T > 150K$)

The FIR induced relaxations of N_H , R , and μ_H at intermediate temperatures are nonexponential and temperature dependent. Some typical FIR induced relaxations at 150K are shown in Fig.(3.13) of Chapter 3, §E. The temperature dependence of such FIR induced relaxations is illustrated in Fig.(4.1) along with an example of a stretched exponential fit to the data corresponding to 160K. The purpose of the stretched exponential fit is to parameterize each relaxation with a time constant, τ . No information about the physics of how the electrons are relaxing is intended from the functional form of the fit. See Chapter 3, §D for a discussion of the stretched exponential curve fit.

Relaxations in the epilayer resistance, R , are fitted instead of the relaxations in the Hall electron concentration, N_H , since the resistance data is less noisy. All the fitted resistance relaxations correspond to changes in N_H which were above the noise. This ensures that the FIR effect induced a change in the Hall electron concentration. All the resistance changes were observed to increase after the FIR pulse and then relax back to within 10% of its initial value. Most all the corresponding Hall electron concentration, N_H , changes were observed to decrease initially with the FIR pulse and then relax back to within 10% of its initial value.

The barrier height, E_b

The temperature dependence of the time constants, τ , extracted from the stretched exponential fits, can be fit to an exponential,

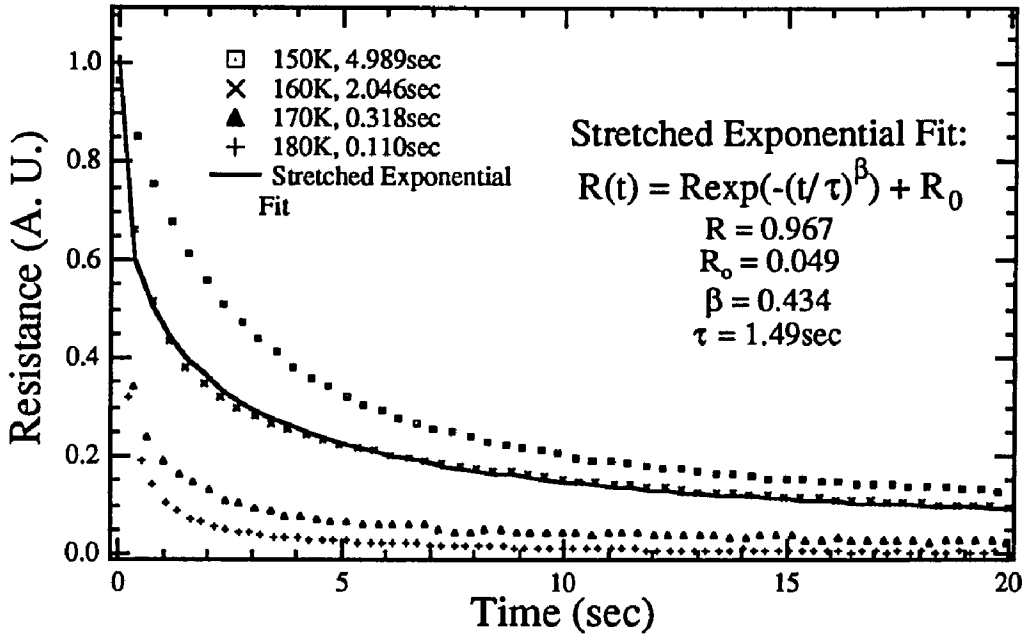


Fig.(4.1) The temperature dependence of the intense FIR effect on an $\text{Al}_{0.3}\text{Ga}_{0.7}\text{As}:\text{Si}$ epilayer resistance. The solid line is a stretched exponential fit of the form: $R(t) = R \exp(-(t/\tau)^\beta) + R_0$. All four relaxations have been normalized to 1.0.

$$\tau = \tau_0 \exp(E_b/kT),$$

as shown in Fig.(4.2). In Fig.(4.2), $\log(\tau)$ is plotted versus $1000/T$ with a least squares fit line drawn through the scatter of data points. From the slope, m_0 , of the linear least squares fit, the barrier height, E_b , corresponding to the temperature dependent FIR relaxations, can be found. Since Boltzmann's constant is $8.62 \times 10^{-5} \text{eV/K}$ and $\log(\tau)$ is plotted versus $1000/T$, E_b is given by

$$E_b = (8.62 \times 10^{-5} \text{eV/K})(1000\text{K})m_0 = (86.2 \text{meV})m_0,$$

where m_0 is the slope of the Arrhenius plot. From the fit done to the data in Fig.(4.2), a barrier height, E_b , of $132 \pm 12 \text{ meV}$ is found.

Doing such a fit assumes that E_b is independent of temperature. Barriers associated with the DX center have been found to have a very small temperature

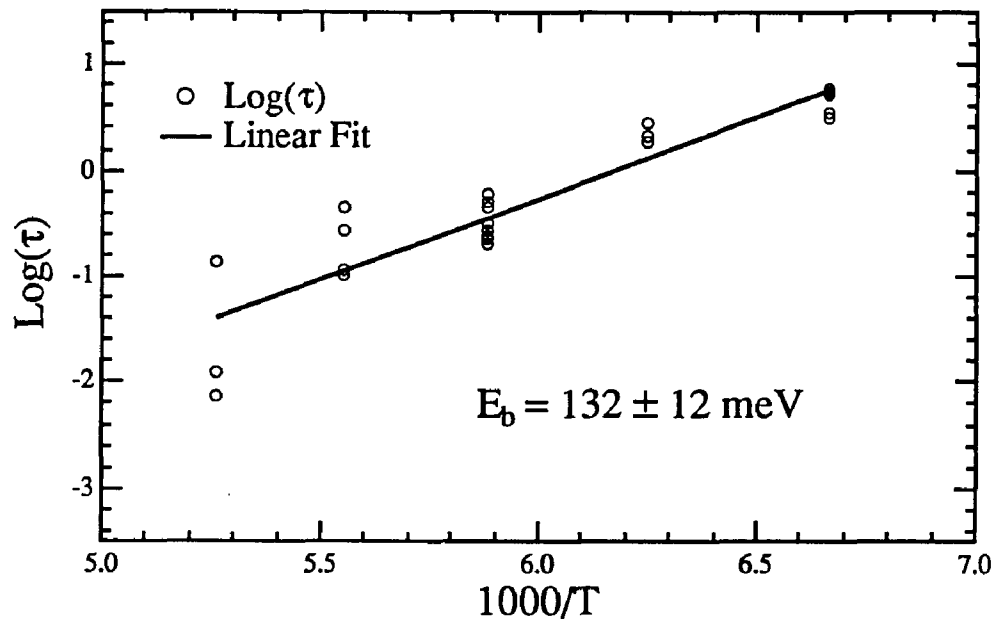


Fig.(4.2) An Arrhenius plot of the temperature dependent resistance relaxations of an $\text{Al}_{0.3}\text{Ga}_{0.7}\text{As}:\text{Si}$ epilayer. The solid line is a least squares linear fit to the logarithm of the time constants extracted from the stretched exponential curve fits to relaxations in the epilayer resistance.

dependence, on the order of 0.1 meV/K [1.8]. A corresponding temperature effect might exist for E_b but would most likely lead to corrections much smaller than the experimental error of $\pm 12 \text{ meV}$ found for E_b .

The barrier of 132 meV measured from the FIR relaxations discussed above is smaller than the barrier measured from IR LED induced relaxations in the epilayer resistance. The barrier corresponding to temperature dependent IR LED relaxations was found to be $191 \pm 13 \text{ meV}$ in Chapter 3, §D. It is known from the literature [4.5, 3.5, 3.7, 1.8] that such IR LED induced relaxations measure the thermal capture barrier, E_c , of the DX center (See Fig.(1.12b) Chapter 1, §C). The open question is what barrier is measured from the temperature dependence of the intense FIR relaxations.

Interpretations of E_b

When thinking about which barrier height associated with the DX center is measured with the intense FIR effect at intermediate temperatures, it helps to visualize where the electrons were before the FIR pulse and where they were immediately after the FIR pulse. Before the FIR pulse, it is assumed that the electrons in the conduction band are in thermal equilibrium with the electrons localized at the DX centers (see Fig.(3.1) of Chapter 3, §B). Immediately after the FIR pulse the Hall electron concentration goes down and the epilayer resistance goes up. This implies that the new nonequilibrium distribution of electrons has more electrons localized at the DX center and fewer electrons in the conduction band as compared with the equilibrium distribution before the FIR pulse. The nonequilibrium distribution starts to relax immediately after the end of the intense FIR laser pulse. So the electrons thermalize over the DX center's thermal emission barrier, E_e , during the relaxation of the nonequilibrium distribution (See Fig.(1.12b) of Chapter 1, §C). This argument suggests that the barrier measured by the temperature dependence of the intense FIR relaxations correspond to the thermal emission barrier, E_e , of the DX center.

The thermal emission barrier, E_e , for the DX center is typically around 400meV and is independent of aluminum mole fraction and electron concentration as is shown in Fig.(1.11a) of Chapter 1, §F. So the thermal emission barrier of the DX center is a factor of 3 larger than the barrier, E_b , measured from the intense FIR data. The barrier, E_b , is even lower than the thermal capture barrier of the DX center which has been measured to be 191 ± 13 meV from the IR LED flashes for the sample studied in this thesis (see Fig(3.6) Chapter 3, §D).

Mechanisms for FIR induced electron capture

The reason why E_b is smaller than either E_e or E_c for the DX center is unknown. However, the values for E_c and E_e of the DX center quoted in the literature are for multiphonon capture and emission processes. We believe that since E_b is less than the values of E_e or E_c this is indirect evidence that the mechanism for intense FIR induced changes in N_H and R is not a multiphonon capture process (i.e. not from simple lattice heating). One possible mechanism is that the electric field of the intense FIR induces hot electron capture via an intermediate state of the DX center which is believed to have a smaller capture and emission barrier ($\approx 100\text{meV}$, see Ref(1.52)) than the thermal capture, E_c , and emission, E_e , barrier of the DX center. It is also possible that the FIR excites a local vibrational mode (LVM) of the Si atom which is responsible for the capture of electrons by the DX center. The model of Chadi and Chang [1.29] predicts that when the silicon atom shifts by about 1\AA , moving from its substitutional site to an interstitial site (see Fig.(1.7) of Chapter 1, §F), it traps two electrons and becomes a negatively charged center, DX^- . Exciting a LVM of the Si atom with intense FIR could move the Si atom enough to induce capture and emission of electrons onto and from DX centers. A LVM has been measured at 395cm^{-1} [4.1]; however, the detector in Ref.(4.1) was not sensitive to frequencies below 200cm^{-1} [4.2]. So the existence of a low frequency (30cm^{-1} to 50cm^{-1}) LVM of the Si atom at the FIR frequencies used in this thesis cannot be ruled out on the basis of the results of Ref.(4.1).

There are two distinct physical processes discussed in the literature about how electron capture by DX centers occurs. One is by a multiphonon capture process

and the other is by a hot electron capture process. This leads to two physically distinct ways to measure the electron capture barrier of the DX center. One technique, which probes multiphonon capture process, uses what is called deep level transient spectroscopy (DLTS) [4.3]. The other technique, which probes hot electron capture, is done by monitoring conductance transients, in a short channel MODFET, in response to brief, $5\mu\text{s}$ to 5ms , (larger than 1.0V) source-drain voltage, V_{SD} , pulses [4.4, 4.5, 4.6, 1.39]. This technique probes the dynamics of a capture process since, upon repeated application of V_{SD} , free electrons can enter the depleted region of the $\text{Al}_x\text{Ga}_{1-x}\text{As}$ and then get captured by the DX centers during each pulse. The electron capture barriers, E_c , measured by these two methods turn out to be quite different. For $x = 0.35$, the DLTS technique gives values of about 300meV for E_c [4.7, 4.8] and the hot electron induced capture gives a value of 103meV for E_c [4.4].

An important point about the electron capture barrier of the DX center is that it depends on aluminum mole fraction and free electron concentration. Shown in Fig.(1.12b) of Chapter 1, §F is how E_c (measured with respect to the conduction band) depends on aluminum mole fraction when the occupied DX center concentration is 50% for Si doped $\text{Al}_x\text{Ga}_{1-x}\text{As}$ epilayers. The capture barrier has a minimum at $x = 0.35$ of about 210meV , near the crossover from direct to indirect gap materials. The capture experiments suggest a distribution of capture barriers which is partially explained by the decreasing electron concentration in the conduction band as capture occurs. This alone does not account for all of the observed distribution in capture barriers so an analysis of the data includes a distribution of capture barriers with a full width at half maximum (FWHM) of 45meV for $x = 0.35$ [1.39].

For the hot electron capture between 77 and 90K [4.4], the capture rate

changed very little. This suggests the onset of a purely athermal (not assisted by phonons) capture process. The hot electron capture is reconciled with the thermal capture data by assuming that capture occurs not only by a multiphonon process but that it is assisted by the athermal (hot electron) population of an intermediate state of the DX center [4.9, 1.48] - i.e. a possibility for this intermediate state is the A_1 symmetry, D^0 state discussed in Chapter 1, §E.

In summary, the energy barrier, E_b , found from the temperature dependent intense FIR changes in epilayer resistance of 132 ± 12 meV is closest to the hot electron capture barrier of 103meV. But E_b is believed to be an emission barrier not a capture barrier. Hot electron capture can be used to fill the DX centers and then the emission transients can then be measured to assure that the DX center is the trap responsible for the hot electron capture. Such emission transients observed from hot electron capture by Theis et al. [4.6] were found to be about 300meV [4.10] which corresponds reasonably well with the emission transients measures by DLTS. So even though there is a discrepancy of 100meV between hot electron capture and the thermal capture barrier observed by Theis et al. [4.6], the emission barriers observed after hot electron capture or with DLTS are virtually the same. This is not surprising since, in both cases of hot electron capture and thermal capture, the emission occurs via multiphonon processes. With all of this in mind, it seems that the barrier, E_b , corresponds to the emission of electrons from an intermediate state of the DX center - i.e. an intermediate state with an emission barrier of about 100meV.

§C Generation of hot electrons by intense FIR

The DC and AC Gunn effect

The transfer of electrons from the Γ valley (conduction band valley) to the L valley in bulk GaAs is observed at room temperature when electrons are heated by a DC electric field of around 3.5kV/cm or higher. This transfer of electrons from the Γ valley to the L valley in GaAs is known as the DC Gunn effect [4.11]. The Γ and L valleys are separated by about 300meV (see Chapter 1 §B) so the DC Gunn effect represents significant heating of electrons by a DC electric field. The Gunn effect has also been seen at large AC fields of 35GHz microwave radiation [4.12]. The intervalley transfer of electrons was observed at peak AC fields of about 4kV/cm at 300K in bulk GaAs for these microwave experiments. Since the peak AC field for the intense FIR (1 to 2THz) used for the experiments reported in this thesis is up to 15kV/cm (TEA laser total pulse energy of 4mJ in 50nsec focused to 3mm spot size), the electrons could be heated considerably by comparison with the microwave studies of the AC Gunn effect.

Energy and momentum relaxation times

When thinking about simple estimates of how much an AC field heats electrons two time scales are important: the momentum relaxation time, τ_m , and the energy relaxation time, τ_e . The momentum relaxation time is related to the drift mobility by

$$\mu_d = e\tau_m/m^*.$$

This time can be thought of as the time it takes for the electron to scatter. The drift

mobility or τ_m determines how much kinetic energy is absorbed by the electrons from the AC field before the electron scatters. With frequencies of the AC field such that $\omega\tau \ll 1$, the electric field does not change much before the electron is scattered (for $\mu_d = 100\text{cm}^2/\text{Vs}$ and $\omega = 29.5\text{cm}^{-1}$, $\omega\tau \approx 0.02$). This means that the electron would adiabatically follow the electric field if the electron also lost energy to the lattice in time τ_m . However, this is not the case. The rate at which electrons lose energy to the crystal lattice is determined by the energy relaxation time, τ_e . The electron loses energy to the lattice by emitting phonons. So τ_e is a measure of how quickly the electrons give off phonons to equilibrate with the lattice. The heating of electrons means that the electrons acquire more energy than their surrounding lattice.

Electron-temperature model

A model used to quantitatively describe how much more hot the electrons are than the lattice is called the electron-temperature model [4.13]. The electron-temperature model assumes that the excited hot electrons are in thermal equilibrium with each other and their distribution is thermal. A thermal distribution of electrons is a distribution of electrons that are in equilibrium with each other and hence are described by an effective electron temperature, T_e , that is higher than the lattice temperature, T_L . There is strong experimental evidence (see references within [4.13]) in favor of the electron-temperature model described above.

The relaxation process by which the excited electrons lose their energy to the surrounding crystal lattice is characterized by the energy relaxation time τ_e . The amount by which T_e is greater than T_L determines whether acoustic phonons or polar optical phonons are emitted as the electrons lose energy to the lattice. For a hot

electron gas with kT_e greater than the longitudinal optical (LO) phonon energy, $\hbar\omega_{LO}$ ($\approx 36\text{meV}$ for GaAs), the electron gas cools by emitting LO phonons. When kT_e for the hot electron gas is less than $\hbar\omega_{LO}$, the energy relaxation slows down and electrons lose energy by emitting acoustic phonons only. The LO-phonon emission relaxation times for a single electron in bulk GaAs is calculated to be 0.13psec [4.13]. The relaxation time for acoustic-phonon emission is much longer and typically on the order of 100psec.

In order for the energy to be taken out of the electron lattice system, the LO phonon must decay into acoustic phonons which thermalize with the lattice very quickly. The decay of an LO phonon into two acoustic phonons takes about 5 to 10 psec. This long lifetime of the LO phonon can lead to a nonequilibrium LO phonon population and the hot electrons can reabsorb these nonequilibrium phonons and slow down the relaxation of the hot electron gas. This *phonon bottle neck* is referred to as the hot-phonon effect in the literature. So the energy relaxation time for bulk GaAs is then determined by the LO phonon lifetime. A τ_e of 7psec is typically quoted in the literature as the measured LO phonon lifetime for bulk GaAs [4.14].

This energy relaxation rate of $7 \times 10^{-12}\text{sec}$ is very long compared with the momentum relaxation times of $\tau_m(\mu_d=1000\text{cm}^2/\text{Vs}) = 3.8 \times 10^{-14}\text{sec}$ typical for the $\text{Al}_{0.3}\text{Ga}_{0.7}\text{As}$ epilayer studied in this thesis. This can lead to large electron heating by the intense FIR.

The amount of energy gained by the electrons can be estimated by a calculation based upon the balance of energy gain and loss processes for the electron gas in the illuminated $\text{Al}_{0.3}\text{Ga}_{0.7}\text{As}:\text{Si}$ epilayer. The following two equations used

in [4.15] form the basis of a simple phenomenological analysis:

$$dE/dt = evE_0 - [E(T_e) - E(T_L)]/\tau_e, \quad (1)$$

$$v + \tau_m dv/dt = \mu_d E_0, \quad (2)$$

where the effects of energy loss to the lattice and intervalley scattering have been included in τ_e which is taken as the energy relaxation time discussed above ($\tau_e \approx 5$ psec). In the above equation, $E(T_e)$ is the kinetic energy of the electrons at a temperature of T_e , $E(T_L)$ is the kinetic energy of the electrons at the lattice temperature T_L , e is the fundamental electron charge, v is the drift velocity, E is the kinetic energy, μ_d is the drift mobility, E_0 is the applied electric field (assumed to be a DC field in [4.15]), and τ_e is the energy relaxation time. So in the steady state, $dE/dt = 0$, the average electron energy is related to the electric field by:

$$E(T_e) - E(T_L) = e\tau_e\mu_d E_0^2.$$

For the estimate described here, E_0 is taken as the root mean square of the AC field corresponding to the intense FIR ($E_{\text{peak}} = 15$ kV/cm, for the TEA laser with 4 mJ total pulse energy in 50 nsec focused to a 3 mm spot size), $\mu_d = 1000$ cm²/Vs, $\tau_e = 5 \times 10^{-12}$ sec (assuming $E(T_e) - E(T_L) > \hbar\omega_{LO}$). Using these values in the above equation gives $E(T_e) - E(T_L) \approx 0.5$ eV. This corresponds to an enormous amount of electron heating which is well above the difference in energy between the Γ and L minima in bulk GaAs, $\Delta E_{\Gamma L} = 0.3$ eV.

Once electrons are heated sufficiently to be scattered into the L valley, the electron distribution no longer satisfies the assumption of the electron-temperature model. The reason for this is that the electrons that are scattered in the L valley are quite close to the lattice temperature T_L while the electrons in the conduction band (Γ valley) are at a temperature T_e much larger than T_L [4.16]. So all that can be

concluded from the above estimate is that there is sufficient electron heating to populate the L valley. It would be incorrect to assume that the electrons are heated significantly above $\Delta E_{\Gamma L}$ ($=0.3\text{eV}$) even though the estimate gives a value larger than 0.3eV . Incidentally, the above two equations were derived with the assumption that the contribution to the kinetic energy, E , from satellite valleys (i.e. L and X valleys) is small. This assumes that all the heating takes place in the Γ (or central) valley.

So it seems possible that there is sufficient electron heating to populate an intermediate state of the DX center around 100meV above the conduction band (hot electron capture) which could then be captured by the DX center by phonon assisted processes (i.e. an FIR induced LVM). Note as the electrons relax and give off LO phonons, these LO phonons could supply the needed lattice energy (see the LLR model of the DX center, Chapter 1, §F [1.32, 1.33]) for an electron to be captured by a DX center. This lattice energy is required since the hot electron capture is believed to be thermally assisted by phonons at intermediate temperatures [4.4]. The lattice energy could also be supplied by FIR excited local vibrational modes of the Si atom associated with the DX center [4.1] or by intense FIR excited bulk acoustic phonons of the $\text{Al}_{0.3}\text{Ga}_{0.7}\text{As}$ lattice.

For cold temperatures, the hot electron capture by DX centers is believed to be athermal [4.4] (not assisted by phonons). It is possible that the electrons are metastably captured at an intermediate state of the DX center at these cold temperatures. However, the intermediate state of the DX center is believed not to exhibit persistent photoconductivity. The FIR effect at cold temperatures is persistent which seems to imply that the electrons do not remain at the intermediate

state after being athermally captured but do become trapped at the DX center.

§D Summary of Interesting FIR induced effects

Frequency dependence of the FIR induced effect

One of the most interesting FIR effects reported in Chapter 3 but not discussed yet was the possible frequency dependence of the intense FIR induced changes in the $\text{Al}_{0.3}\text{Ga}_{0.7}\text{As}:\text{Si}$ epilayer resistance. Recall that the FIR effect at 29.5cm^{-1} , Fig.(3.16), was at least a factor of 2 larger than the effect at 43.3cm^{-1} , Fig.(3.17), even though the total pulse energy for the 43.3cm^{-1} line was twice that of the 29.5cm^{-1} . For simple lattice heating of the electrons from FIR excited acoustic phonons, the phonon density of states predicts that the 29.5cm^{-1} line should have a smaller effect than the 43.3cm^{-1} line. This is the case since the density of states of phonons at 43.3cm^{-1} (note momentum does not need to be conserved with LVM so only one phonon is created by one photon i.e. the photon does not split its energy in two when creating phonons as would be required if momentum was conserved [4.17]) is significantly larger than the density of states of phonons at 29.5cm^{-1} (see Fig.(1.7) for a phonon density of states in GaAs). This means that there are many more 43.3cm^{-1} phonons than the 29.5cm^{-1} phonons and simple lattice heating should be greater with a larger number of phonons available to heat the lattice. So this observed frequency dependence is evidence against simple lattice heating since the effect at 29.5cm^{-1} is larger than the effect at 43.3cm^{-1} .

The other possibility is that the frequency effect observed could be due to local vibrational modes (LVM) of the silicon atom corresponding to the DX center.

(See the discussion earlier in Chapter 4, §B of the LVM and the model of Chadi and Chang.) This certainly motivates a careful frequency dependence study of the FIR induced changes in N_H and R to see what sort of structure could be seen and how it might relate to LVMs of the Si atom in $Al_xGa_{1-x}As:Si$ epilayer.

Power dependence of the FIR induced effect

The attenuation data of Fig.(3.15) of Chapter 3 §F seems to suggest some sort of power threshold for the TEA laser FIR effect. While at the same time the FEL measurements seem to indicate a linear dependence on power. These data are not consistent and motivate a careful attenuation study to figure out how to match up the two different power regimes of the FEL and TEA laser, and more importantly, find out what details of the attenuation data presented in Chapter 3 are reproducible. At this stage the two sets of data seem to contradict each other and hence suggest that they are somehow in error.

FIR induced electron capture by the DX center

Close examination of Fig.(3.8) of Chapter 3, §E raises many interesting unanswered questions. The only aspect of Fig.(3.8) that is thought to be understood is that the first five FIR pulses induce electron capture by DX centers. The next tempting thing to say about the data is that the persistent increases and decreases of N_H implies that the FIR induces electron capture by DX centers and emission of electrons from DX centers. However, it seems that the mobility changes observed imply that the resistance is not changing as it should if the FIR were indeed inducing both ionization and capture. This makes it difficult to conclude that electrons

involved are originating from only DX centers. The persistent changes could be coming from some other persistent effect associated with the unintentional 2DEG at the AlGaAs/GaAs interface substrate [4.5].

Large effect of the FIR after an IR LED flash

Another feature of Fig.(3.8) is that the largest effect observed seems to be within the first few FIR pulses immediately following the IR LED flash. The effect is particularly striking in the resistance data where the asymptotic pulses (the pulses well after the IR LED flash) are quite small. The asymptotic value of N_H and R are not reproducible and seem to depend on mobility and whether or not the sample was exposed to an IR LED flash after dark cooling. Nonetheless, the first few FIR pulses after the IR LED flash are consistently the largest and seem to be independent of the specific details of how the initial values of N_H , R , and μ_H were obtained. It should be stated that the data of Fig.(3.8) is difficult to reproduce and is an exceptional case. Similar data collected at different times does not show such clear asymptotic behavior and initial trends in N_H and R .

FIR effect on a dark cooled sample

The FIR induced effects in N_H , R , and μ_H of a dark cooled $Al_{0.3}Ga_{0.7}As:Si$ epilayer also show very rich structure as shown in Fig.(3.7). The most regular feature of such data is that the epilayer resistance starts out on the order of $4M\Omega$ (typical of a sample that is frozen out) and after 10 to 20 FIR pulses is reduced to around $50k\Omega$. However, the Hall electron concentration is never larger than $10^{14}cm^{-3}$ and quite often is as low as $5 \times 10^{12}cm^{-3}$. It is well known that the background impurities in

MBE grown samples are 10^{14} to 10^{15}cm^{-3} . So it is difficult to say where the electrons, observed after intense FIR pulses on a dark cooled epilayer, come from. They could be from some unknown shallow donor impurity. It is possible that the intense FIR is inducing electron capture by DX centers and ionization of electrons from DX centers.

FIR induced Hall electron mobility changes

There are many examples of FIR effects that induce increases in both Hall electron concentration, N_H , and epilayer resistance, R , or decreases in both N_H and R . Two such effects are shown in Fig.(3.9a,b,c). These data show that the mobility does not remain constant during the FIR induced changes in N_H and R but changes by large amounts. This is a very strange effect and is not uncommon. It could be the result of transferring electrons between two different mobility regions of the sample.

It is quite possible that the electrons are hot enough to be transferred in real space between the $\text{Al}_{0.3}\text{Ga}_{0.7}\text{As}:\text{Si}$ epilayer and the unintentional 2DEG (see Fig.(2.4) and Chapter 5 for a discussion of hot electron real space transfer). This real space transfer can lead to large mobility changes since the mobility of the electrons at the unintentional 2DEG is around $10,000\text{cm}^2/\text{Vs}$ and that of the $\text{Al}_{0.3}\text{Ga}_{0.7}\text{As}:\text{Si}$ epilayer is around $100\text{cm}^2/\text{Vs}$. So even a small amount of charge transfer from the $\text{Al}_{0.3}\text{Ga}_{0.7}\text{As}:\text{Si}$ to the unintentional 2DEG can lead to measurable increases in the mobility. The reverse process of transferring a small number of electrons in the 2DEG to the $\text{Al}_{0.3}\text{Ga}_{0.7}\text{As}:\text{Si}$ epilayer can lead to measurable decreases in mobility.

Examining Fig.(2.4b), reveals that the electrons need to gain 700meV in order to be transferred to the 2DEG at the substrate interface. From the discussion

presented in §C of this chapter, it seems unlikely that electrons can get heated much more than 300meV by intense FIR. So it is not too plausible that electrons are being transferred back and forth between the substrate interface 2DEG and the $\text{Al}_{0.3}\text{Ga}_{0.7}\text{As}:\text{Si}$ epilayer given the $1\mu\text{m}$ undoped $\text{Al}_{0.3}\text{Ga}_{0.7}\text{As}$ buffer layer shown in Fig.(2.4a). See Ref.(4.5) for a discussion of other mechanisms for persistent changes in mobility.

Chapter 4 References

1. J. A. Wolk, M. B. Kruger, J. N. Neyman, W. Walakiewicz, R. Jeanloz, and E. E. Haller, *Phys. Rev. Lett.* **66**, 774 (1991).
2. N. M. Haegel, E. E. Haller, and P. N. Luke, *Int. J. Infrared Millimeter Waves* **4**, 945 (1983).
3. G. L. Miller, D. V. Lang, and L. C. Kimerling, *Ann. Rev. Mater. Sci.* **7**, 377 (1977).
4. T. N. Theis, *Inst. Phys. Conf. Ser.* **91**, 1 (1988).
5. A. Kastalsky and R. A. Kiehl, *IEEE Trans. Electron Devices* **ED-33**, 414 (1986).
6. T. N. Theis, B. D. Parker, P. M. Solomon, and S. L. Wright, *Appl. Phys. Lett.* **49**, 1542 (1986).
7. M. O. Watanabe, K. Morizuka, M. Mashita, Y. Ashizawa, and Y. Zota, *Jpn. J. Appl. Phys.* **23**, L103 (1984).
8. B. L. Zhou, K. Ploog, E. Gemlin, X. O. Zheng, and M. Schultz, *Appl. Phys.* **A28**, 223 (1982).
9. Private communication with T. N. Theis.
10. The emission transients of Ref.(4.6), Fig(3), were scanned into a computer and fit to stretched exponentials. A barrier height was deduced from an Arrhenius plot and found to be 295 ± 24 meV.
11. K. Seeger, *Semiconductor Physics*, 4th edition (Springer-Verlag, New York, Berlin, Heidelberg, 1989) p.234.
12. W. T. Masselink, N. Braslau, D. La Tulipe, W. I. Wang, and S. L. Wright,

Solid-State Electron. **31**, 337 (1988).

13. S. Das Sarma, in **Hot Carriers in Semiconductor Nanostructures: Physics and Applications**, (academic Press, 1992), p.53.
14. D. vanderLinde, J. Kuhl, and H. Klingenberg, Phys. Rev. Lett. **44**, 1505 (1980).
15. G. H. Glover, J. Appl. Phys. **44**, 1295 (1972).
16. P. N. Butcher and W. Fawcett, Proc. Phys. Soc. **86**, 1205 (1965).
17. Private communication with E. Haller.

Chapter 5

FIR Induced Hot Electron Real-Space Transfer in an $\text{Al}_{0.3}\text{Ga}_{0.7}\text{As}/\text{GaAs}$ Heterostructure

§A Introduction

In this chapter, the effect of intense FIR on electron transport in an $\text{Al}_x\text{Ga}_{1-x}\text{As}/\text{GaAs}$ heterostructures (2DEG) and half parabolic quantum wells are discussed (see Chapter 2, §A and §B for details of these two quantum well structures). The measurements reported in this chapter were actually the first observations of the effect of intense FIR on electron transport in $\text{Al}_x\text{Ga}_{1-x}\text{As}/\text{GaAs}$ quantum wells and epilayers that are discussed in this thesis. After these preliminary measurements, the system under study was simplified to an $\text{Al}_{0.3}\text{Ga}_{0.7}\text{As}:\text{Si}$ epilayer, discussed in Chapters 3 and 4, in an effort to understand the effect of the FIR in the 2DEG systems.

For the initial measurements of electron transport in quantum wells, only the channel (2DEG) resistance was measured as a function of time while the sample was periodically (1/3 Hz) exposed to intense FIR. Photo-Hall measurements were not done since these preliminary measurements were investigating optical properties of quantum wells in the FIR (namely, second harmonic generation [5.1]).

The effect of intense FIR on the transport of electrons in these structures was an accidental discovery [5.2]. It was only after W. W. Bewley, C. L. Felix, and M. S. Sherwin had discussions with many people [5.3] at the March 1991 APS meeting that we learned the importance of doing photo-Hall measurements to enable us to unravel the dependence of the epilayer resistance (channel resistance for a 2DEG) on electron concentration and mobility. In addition, we learned about the importance of having a large ($1\mu\text{m}$) buffer layer between the Si doped $\text{Al}_x\text{Ga}_{1-x}\text{As}$ and the GaAs buffer and substrate to prevent the population of a 2DEG at the substrate interface. It is regrettable that all the measurements done to date on the quantum wells do not include any Hall electron concentration data but only channel resistance data. Time, money, and ignorance have prevented us from having photo-Hall data for the effect of FIR on electron transport in quantum wells.

In light of the fact that data presented in this chapter do not include photo-Hall transport data, there is a very strong possibility that many of the conclusions drawn in this chapter are wrong! The hope is that what was learned from the photo-Hall transport in the $\text{Al}_{0.3}\text{Ga}_{0.7}\text{As}:\text{Si}$ epilayer discussed in Chapters 3 and 4 can help strengthen the arguments presented in this chapter.

In §B of this chapter, background information on real-space transfer of electrons in quantum wells will be presented.

In §C, the data will be discussed. The data are complicated by different quantum well structures and FIR coupling schemes used in the transport measurements. The polarization data presented are of marginal quality; its purpose is only to show that the FIR effect is observed for both electric field polarizations (electric field vector of the FIR polarized parallel and perpendicular to the growth direction of the

quantum well). The calculation of the electric field within the sample for the different coupling schemes is also discussed in §C.

The data are analyzed in §D within the context of hot electron real-space transfer in quantum wells.

The chapter is concluded with transport data for an $\text{Al}_{0.3}\text{Ga}_{0.7}\text{As}:\text{Si}$ epilayer with the unintentional 2DEG of the substrate interface populated. Because of this 2DEG, it is likely that real-space transfer is a relevant mechanism for the observed FIR effect.

§B Real-space transfer of electrons in quantum wells

Introduction

Intervalley transfer of electrons (e.g. Γ valley to L valley) in bulk GaAs (the Gunn effect) was discussed in Chapter 4. In quantum wells, electrons can be transferred from the 2DEG of the $\text{Al}_x\text{Ga}_{1-x}\text{As}/\text{GaAs}$ interface to the $\text{Al}_x\text{Ga}_{1-x}\text{As}:\text{Si}$ region of a heterostructure. This transfer of electrons is referred to as real-space transfer of electrons in heterostructures and is the real-space analogy of the k-space transfer of the Gunn effect. Real-space transfer involves electron transfer from the Γ valley of the GaAs to the Γ valley of the $\text{Al}_x\text{Ga}_{1-x}\text{As}$ but could also occur via the L or X valleys of the $\text{Al}_x\text{Ga}_{1-x}\text{As}$. Such real-space transfer of electrons is used to explain hot electron mobility data in a 2DEG heterostructure using 35GHz microwave radiation with peak AC field of 3.5kV/cm to generate the hot electrons [4.12]. Hot electron mobility data interpreted in the context of real-space transfer has also been reported for DC fields around 3kV/cm [5.4].

To make sure that the mechanism for real-space transfer is distinct from that of k-space transfer (the RWH mechanism [5.6]), Keever et al. [5.4] made measurements with a heterostructure having $x=0.17$ so that the conduction band offset is smaller than the energy separation from the Γ valley to the L valley. Their Monte Carlo simulations show that for x less than or equal to 0.17 the electrons move out of the GaAs long before they can populate higher valleys. They observed the threshold field to be between 2 and 3 kV/cm for $x = 0.17$.

Time scale for real-space transfer

The time for real-space transfer to occur in $\text{Al}_x\text{Ga}_{1-x}\text{As}/\text{GaAs}$ heterostructures has been calculated by Monte Carlo methods and the transfer time was estimated to be of the order of 10^{-11} seconds [5.5]. Measurement of this time was not possible with the experimental arrangement in Ref.(5.4). All that can be inferred is that the effect is faster than 1 nsec [5.4].

Models for real-space transfer

Real-space electron transfer can be modeled by thermionic emission of hot electrons from the high-mobility GaAs layers into the neighboring low-mobility $\text{Al}_x\text{Ga}_{1-x}\text{As}$ layer [5.7]. Within the context of real-space transfer, the electron temperature in the GaAs layer is assumed constant and the electron temperature in the $\text{Al}_x\text{Ga}_{1-x}\text{As}$ layer is assumed to be position dependent along with the quasi-Fermi level. The reverse process of cool electrons in the $\text{Al}_x\text{Ga}_{1-x}\text{As}$ layer transferring into the GaAs is also included in the thermionic emission model of Ref.(5.7). Band bending by ionized donors in the $\text{Al}_x\text{Ga}_{1-x}\text{As}$ layer was not included in the analysis

in Ref.(5.7) but should aid in the transfer of electrons into the low mobility $\text{Al}_x\text{Ga}_{1-x}\text{As}$ layers. This is the case since the built-in electric field will attract electrons from the GaAs layer and the barrier will impede transfer back into the GaAs.

An application of a DC electric field parallel to the 2DEG layer interface results in heating of the high-mobility electrons in the GaAs layer. When the average kinetic energy of the electrons in the GaAs becomes comparable to the potential barrier height of the conduction band offset, ΔE_c , they can be thermionically emitted into the $\text{Al}_x\text{Ga}_{1-x}\text{As}$ layer.

The Boltzmann equation is solved assuming a Maxwellian distribution for the isotropic part of the electron distribution function with a position-dependent electron temperature. This assumption is justified since electron-electron collisions will randomize the energy gained in the electric field direction and hence establish a Maxwellian distribution. The use of the Boltzmann equation is allowed for layer widths large enough to avoid the complications arising from size quantization effects and other two-dimensional effects. For this reason, the calculations in Ref.(5.7) choose layer widths larger than 400\AA .

Monte Carlo simulations [5.8] were also done in collaboration with the authors of Ref.(5.7). The Monte Carlo simulations were in good agreement with the thermionic calculations. The simulations did not include electron temperature gradients in the $\text{Al}_x\text{Ga}_{1-x}\text{As}$ layer but did consider the L valley conduction band for the GaAs layer. The thermionic calculations of Ref.(5.7) did not consider the effects of the L valley.

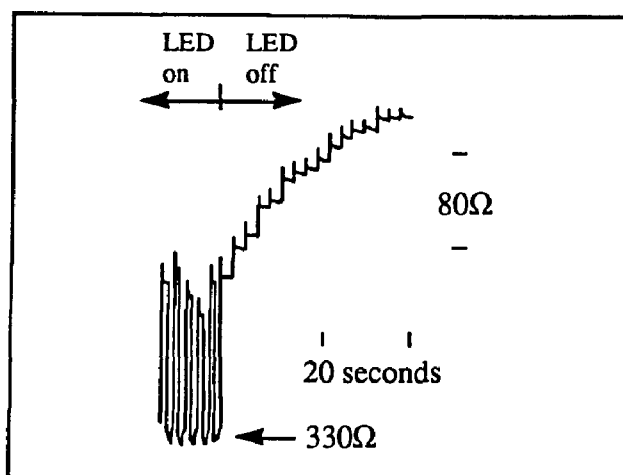
Since the threshold fields, 2 to 3kV/cm, for real-space transfer in heterostructures is so close to the threshold field, 3.5kV/cm, for intervalley transfer

in bulk GaAs, an attempt was made to assess the importance of intervalley scattering in the GaAs and $\text{Al}_x\text{Ga}_{1-x}\text{As}$ of the heterostructure in the Monte Carlo simulations [5.8]. The result of the simulation was that the average kinetic energy of an electron in the $\text{Al}_x\text{Ga}_{1-x}\text{As}$ was less than 100meV for field strengths of 2 to 4kV/cm. This average kinetic energy of the electrons is well below the intervalley Γ -L energy separation of 300meV in the $\text{Al}_x\text{Ga}_{1-x}\text{As}$. The conclusion drawn was that the mechanism of electrons leaving the high-mobility GaAs layer by thermionic emission and transferred in real space to the low-mobility $\text{Al}_x\text{Ga}_{1-x}\text{As}$ layer is from the Γ or L valley of the GaAs to the Γ valley of the $\text{Al}_x\text{Ga}_{1-x}\text{As}$.

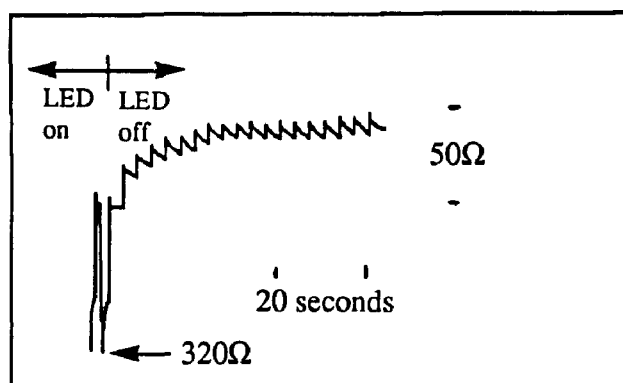
§C The electron transport data for the FIR effect in an $\text{Al}_x\text{Ga}_{1-x}\text{As}/\text{GaAs}$ heterostructure and quantum well

10 Half parabolic well data

The data shown in Fig.(5.1a) correspond to having the electric field polarized parallel to the growth direction of the quantum well. As marked on Fig.(5.1), the LED (red light emitting diode) was kept on for the first few FIR pulses and then turned off with the FIR still firing at about 1/3Hz repetition rate. The data shown in Fig.(5.1b) correspond to having the electric field polarized perpendicular to the growth direction. The sample studied in Fig.(5.1) was made up of 10 half parabolic quantum wells (See Chapter 2, §A and §B for a sample description.). Different cryostats were used for the two different polarizations. For the case with the electric field polarized parallel to the z-direction, Fig.(5.1a), the sample was mounted in a strip line (horn) geometry and cooled with a continuous flow cryostat [5.9]. For the



(a)



(b)

Fig.(5.1) The FIR induced resistance changes in a 10 half parabolic quantum well sample with the electric field of the TEA laser polarized: (a) parallel to the growth direction of the well with the TEA laser operating at 29.5cm^{-1} and total average pulse energy of 4mJ and (b) perpendicular to the growth direction with the TEA laser operating at 43.3cm^{-1} and total pulse energy of 5mJ .

case with the electric field polarized perpendicular to the z-direction, Fig.(5.1b), a top loading cryostat was used which allowed the sample to be rotated so as to achieve the proper coupling of the electric field polarization (see Chapter 2, §D and §H for a discussion of cryostats and FIR coupling schemes used for measurements reported

in this thesis). The strip line geometry was also used for the data presented in Figs.(5.2 and 5.3) of this chapter.

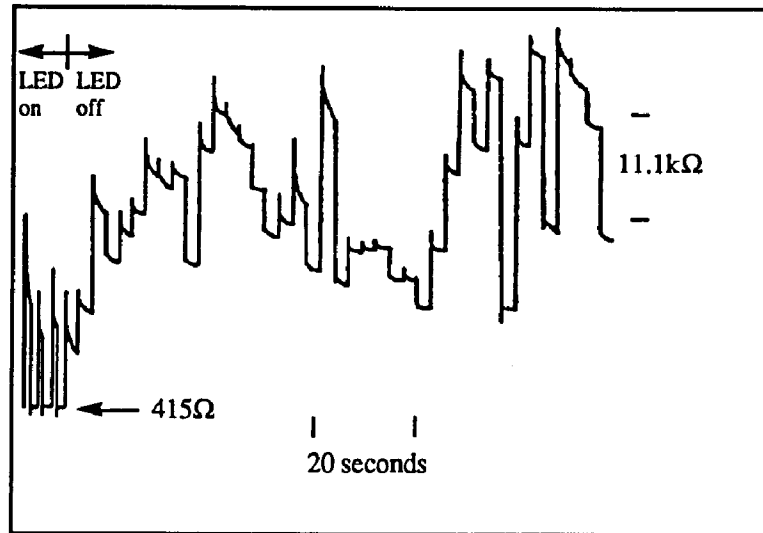
Heterostructure data

The effect of intense FIR on the epilayer resistance of an $\text{Al}_{0.3}\text{Ga}_{0.7}\text{As}/\text{GaAs}$ heterostructure (2DEG) is shown in Fig.(5.2) (see Chapter 2, §B for a description of the sample). The electric field vector of the FIR is polarized parallel to the growth direction of the quantum well and was coupled to the sample using the horn geometry of Ref.(5.9). As in Fig.(5.1), the LED was kept on for the first few FIR pulses and then turned off with the FIR still firing at about a 1/3 Hz repetition rate. The resistance remains above 415Ω after each FIR pulse with the LED off in both Figs.(5.2a and 5.2b). The FIR induced changes in resistance shown in Fig.(5.2a) are always increasing with the LED on. Once the LED is turned off, the resistance changes are seen to both increase and decrease except for the FIR pulse immediately after turning the LED off. The first FIR pulse immediately after turning off the LED always induces an increase in the epilayer resistance.

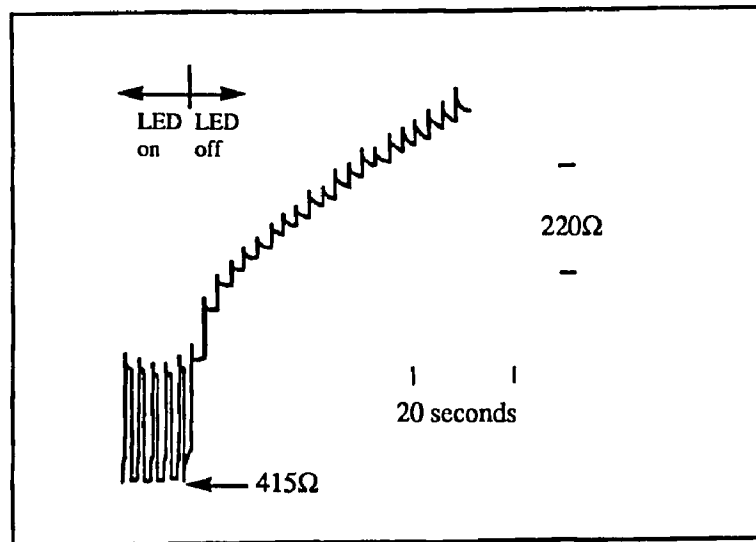
Estimates of the electric field in the sample

The two coupling schemes described above require different analyses to estimate the electric field within the sample. The estimates of the electric field are probably within a factor of two of the actual fields achieved.

The electric field estimates are averages of pulse to pulse fluctuations in the TEA laser. The peak electric fields are higher than the average estimates presented in this thesis. See Chapter 2, §E for a discussion of the time structure and pulse to



(a)



(b)

Fig.(5.2) The effect of intense FIR on the epilayer resistance of an $\text{Al}_{0.3}\text{Ga}_{0.7}\text{As}/\text{GaAs}$ heterostructure (2DEG) at two different powers. The TEA laser was operated at 29.5cm^{-1} with an average total pulse energy of (a) 3.3mJ ($220\text{kW}/\text{cm}^2$ or an electric field of $6.8\text{kV}/\text{cm}$) at the sample and (b) 0.8mJ ($49\text{kW}/\text{cm}^2$ or an electric field of $3.2\text{kV}/\text{cm}$) at the sample.

pulse fluctuations of the TEA laser pulses.

For the horn geometry of Ref.(5.9), the assumption is that 5% of the free field intensity, S_f , outside the horn gets coupled into the sample, S_s , and the electric field within the sample is found from the expression

$$S_s = (0.05)S_f = (c/8\pi)n^{1/2}E_0^2,$$

where n is the index of refraction of GaAs ($n=3.6$) and E_0 is the estimated electric field within the sample. The free field intensity, S_f , is the average total energy of the FIR pulse divided by the FIR pulse length and the spot size of the FIR on the edge of the sample within the horn. This spot size is taken as the thickness of the sample, 0.5mm, times the diameter of 3mm for the focused FIR beam. This gives 1.5mm^2 for the spot size within the horn. The horn couples the FIR onto the edge of the sample which is 0.5mm thick so the thickness of the sample determines one of the dimensions in the area of the focused spot size. As an example, an average total pulse energy of 3.3mJ in 50nsec pulse of the TEA laser focused to a spot size of 1.5mm^2 using the horn coupling scheme gives 220kW/cm^2 for the field intensity within the sample, S_s , and 6.8kV/cm for E_0 as is the case in Fig.(5.2a).

The assumption that 5% of the free field intensity, S_f , is coupled into the sample is based on transmission measurements of the horn with a sample mounted in it using the TEA laser operating at 29.5cm^{-1} and an average total pulse energy of around 3 to 4mJ.

The corresponding calculation for the top loading cryostat is simpler since the FIR is coupled with the electric field parallel to the surface of the sample (The propagation direction is at normal incidence to the sample.). The assumption here is that around 32% of the free field intensity is reflected, $R = (n-1)^2/(n+1)^2 = 0.32$

for $n= 3.6$, by the sample at normal incidence. So 68% of the free field intensity is coupled into the sample. Since the top loading cryostat has z-cut quartz windows, another 50% of the free field intensity is absorbed by the quartz. With the FIR beam from the TEA laser focused to a 3mm diameter spot and an average total pulse energy of 5mJ, the free field intensity within the sample is $480\text{kW}/\text{cm}^2$ which implies an E_0 of 10kV/cm as is the case in Fig.(5.2b).

§D Analyzing the FIR induced ΔR 's in terms of real-space transfer

Electric field polarization data

The main point of Fig.(5.1) is that the FIR induce ΔR 's are observed for both polarizations of the electric field. However it must be noted that the sample in Fig.(5.1a) is exposed to other polarizations beside the electric field component parallel to the growth direction of the quantum well (see Ref.(5.9) for a discussion of the transmission of the FIR in the strip line (horn) geometry). In conclusion, the electric field of the laser need not be polarized only in the growth direction of the quantum well in order to observe the FIR-induced resistance changes. Note that all calculations of real-space electron transfer in $\text{Al}_x\text{Ga}_{1-x}\text{As}/\text{GaAs}$ heterostructures assume that the electric field is polarized in the plane of the wafer which is perpendicular to the growth direction.

Power dependence data

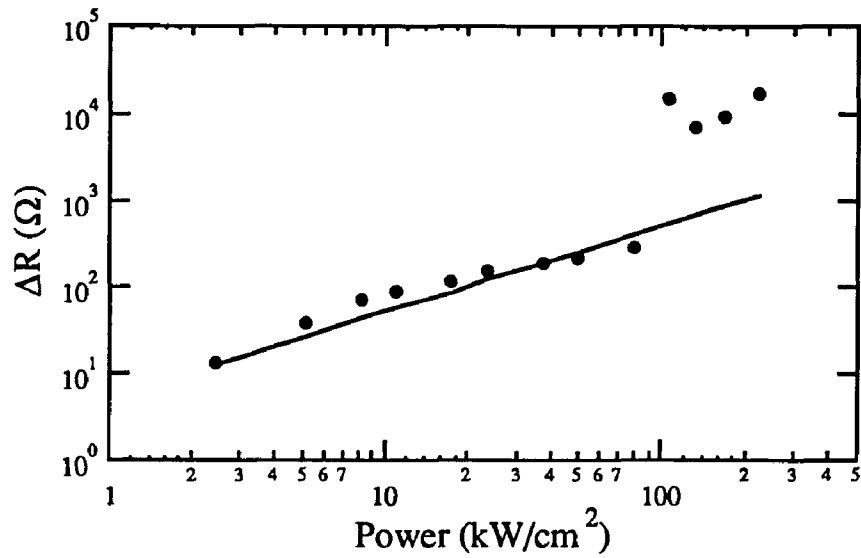
The FIR induced resistance changes at full power, Fig.(5.2a), are on the order of 10k Ω . While the FIR induced resistance changes at about 22% full power,

Fig.(5.2b), are on the order of 10 to 100 Ω and are steadily increasing. These two figures suggest some sort of power threshold between the steadily increasing resistance changes of Fig.(5.2b) and the increasing and decreasing FIR induced resistance changes of Fig.(5.2a).

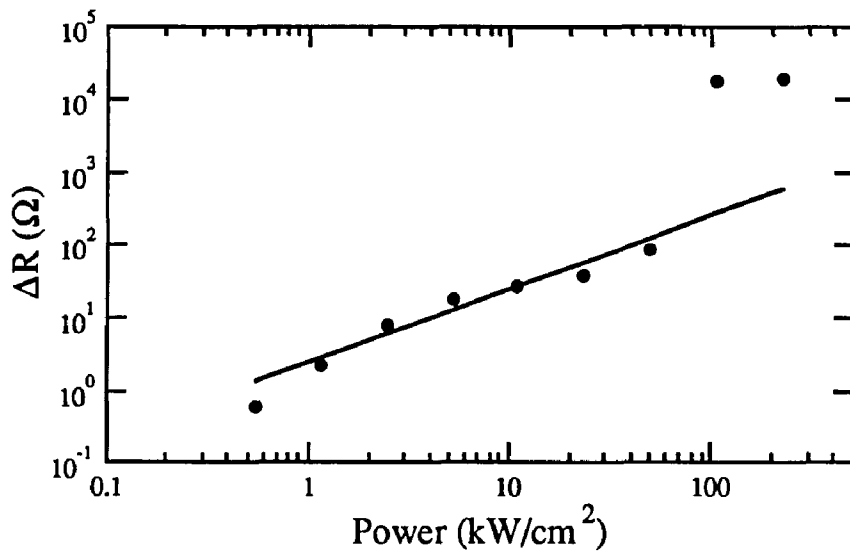
The power dependence of the resistance changes is shown in Fig.(5.3). The data shown in Fig.(5.3a) were compiled from having the LED *on* while the sample was exposed to intense FIR at a repetition rate of 1/3 Hz. Each point in Fig.(5.3a) corresponds to the average of 3 to 5 FIR induced resistance changes at a given attenuation of the FIR beam. The data shown in Fig.(5.3b) were compiled from having the LED *off* while the sample was exposed to FIR. Each point in Fig.(5.3b) corresponds to the average of the first three FIR induced resistance changes immediately after the LED was turned off.

The two graphs shown in Fig.(5.3) are qualitatively very similar even though they were compiled from quite different circumstances. The points in Fig.(5.3b) have a smaller resistance change, ΔR , than the corresponding points in Fig.(5.3a). This is because after the LED is turned off each successive FIR induced ΔR is smaller than the preceding one so the average of 3 successive pulses results in a ΔR smaller than that measured while the LED is on as in Fig.(5.3a).

For powers below 78kW/cm² (35% of full power or electric fields below 4.0kV/cm) the power dependence of ΔR is linear. The lines drawn in Fig.(5.3) have a slope of one and are not fit to the data but are only drawn in to guide the eye. This is different from the power dependence of FIR induced ΔR 's observed in an Al_{0.3}Ga_{0.7}As:Si epilayer (see Fig.(3.15)).



(a)



(b)

Fig.(5.3) Power dependence of the FIR induced channel resistance changes in an $\text{Al}_{0.3}\text{Ga}_{0.7}\text{As}/\text{GaAs}$ heterostructure. The data in (a) were taken with the LED on and the data in (b) correspond to the first 3 FIR effects immediately after the LED is turned off. The TEA laser was operated at 29.5cm^{-1} with an average total pulse energy of 3.3mJ . The sample temperature was 8.0K . The line drawn has a slope of one.

Threshold electric field for real-space transfer

The jump discontinuity seen in the data of Fig.(5.3) corresponds to an electric field between 4.0kV/cm and 4.7kV/cm (There is probably about a 30% error in the electric field estimates.). The corresponding ΔR 's for electric fields above 4.7kV/cm are on the order of 10k Ω and for electric fields below 4.0kV/cm are on the order of 100 Ω . It is interesting to note that the threshold electric field for real-space transfer in $Al_xGa_{1-x}As/GaAs$ heterostructures is about 3.0 to 3.5kV/cm at DC electric fields [5.4] and 3.5kV/cm at 35GHz electric fields [4.12]. It then seems plausible that the jump discontinuity seen in Fig.(5.3) corresponds to a large fraction of electrons transferred out of the GaAs (2DEG interface) to the $Al_{0.3}Ga_{0.7}As$ region for electric fields above about 4.0kV/cm.

To achieve a $\Delta R \approx 10k\Omega$ with the FIR, requires that about 98% of the electrons in the 2DEG ($\mu_{GaAs} = 320,000cm^2/Vs$) be transferred to the $Al_{0.3}Ga_{0.7}As:Si$ ($\mu_{AlGaAs} = 100$ to $500 cm^2/Vs$) region with the resistance of the epilayer at about 415 Ω before the FIR pulse. To achieve a $\Delta R \approx 100\Omega$ with the FIR, requires that about 20% of the electrons be transferred from the GaAs to the $Al_{0.3}Ga_{0.7}As:Si$ region. The data of Fig.(5.3) seem to imply that the intense FIR is inducing real-space transfer of electrons from the GaAs to the $Al_{0.3}Ga_{0.7}As:Si$ region of a 2DEG heterostructure. It is interesting to note that Monte Carlo simulations of real-space transfer in $Al_xGa_{1-x}As$ heterostructures predict that 60% of the electrons can be transferred out of a 2DEG for DC electric fields above 4kV/cm [see Fig.(3) of Ref.(5.8)] with electron transfer starting at electric fields around 2kV/cm.

The increasing and decreasing of ΔR in Fig.(5.2a) after the first FIR pulse with the LED turned off seems to be either from electron capture and emission of

electrons onto and from DX centers in the $\text{Al}_{0.3}\text{Ga}_{0.7}\text{As}:\text{Si}$ region or from a small amount of electron transfer back and forth between the $\text{Al}_{0.3}\text{Ga}_{0.7}\text{As}:\text{Si}$ and GaAs. It is difficult to quantify this any further since only resistance measurements were done for the quantum wells and 2DEG.

To resolve which of the above two models produce the increases and decreases in ΔR , measurements of both the electron concentration in the GaAs, n_s , and the electron concentration in the $\text{Al}_{0.3}\text{Ga}_{0.7}\text{As}$, n_o , would be needed. This in principle can be done since Shubnikov de Haas oscillations measure n_s [5.10] and a Hall measurement gives $n_H = n_o + n_s$, the total electron concentration in the two layers. Then n_o can be calculated since $n_o = n_H - n_s$. This is a purposed future experiment (see Chapter 7 for a discussion of future measurements).

The data presented in Chapter 3 (see Fig.(3.8)) on FIR induced ΔR 's in an $\text{Al}_{0.3}\text{Ga}_{0.7}\text{As}:\text{Si}$ epilayer show that the ΔR 's tend to asymptote to some value of the epilayer resistance, R_o , and do not exhibit the large continued increasing and decreasing as shown in Fig.(5.2a) of this chapter. This would seem to suggest that the increasing and decreasing ΔR 's seen in Fig.(5.2a) are from the transfer of a small amount of charge back and forth between the low-mobility $\text{Al}_{0.3}\text{Ga}_{0.7}\text{As}:\text{Si}$ region and the high-mobility GaAs region.

FIR induced ΔR 's as seen in the 2DEG discussed above were also seen in a half parabolic quantum well made by digital alloying Aluminum in an $\text{Al}_x\text{Ga}_{1-x}\text{As}/\text{GaAs}$ quantum well (see Chapter 2, §A and §B for sample description). Increases and decreases in ΔR at high power were observed in the half parabolic well. A similar threshold was observed for the large increases and decreases in ΔR as was observed for the 2DEG.

The 10 half parabolic well sample never exhibited the large increases and decreases in ΔR as did the 2DEG (Fig.(5.2a)) and the single half parabolic well samples. Presumably the electrons were transferred from one well to the other and the case of fully ionizing all wells was never realized. That is, never did all 10 wells become sufficiently (98%) ionized in order to observe large $\Delta R \approx 10K\Omega$.

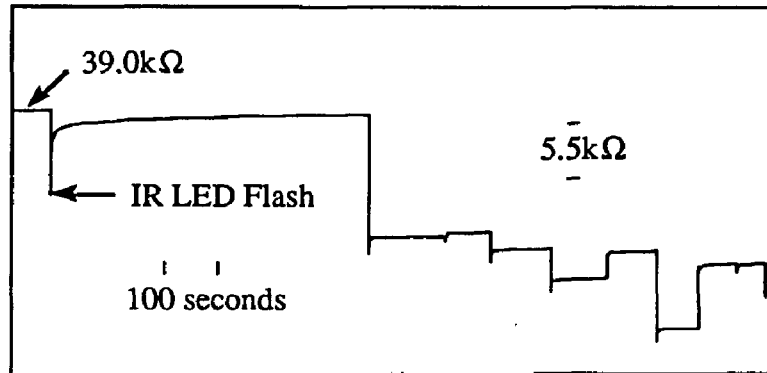
§E Resistance changes of an $Al_{0.3}Ga_{0.7}As:Si$ epilayer with an unintentional 2DEG populated

Introduction

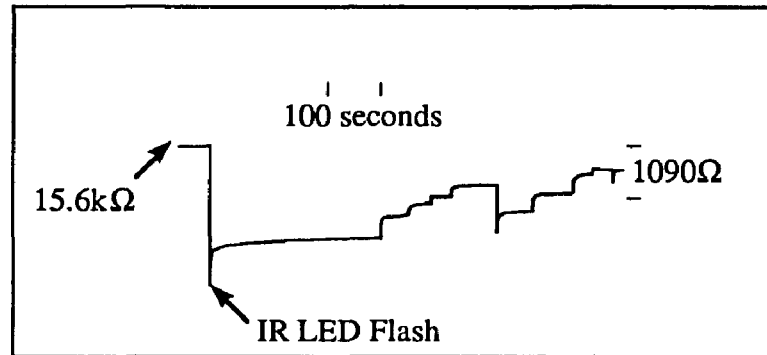
Because of the complications in interpreting the resistance data of the quantum wells, we decided to study the resistance changes in an $Al_{0.3}Ga_{0.7}As:Si$, $2\mu m$ thick, epilayer. The FIR induce resistance changes of an $Al_{0.3}Ga_{0.7}As:Si$ epilayer was presented in Chapter 3. Before that sample was studied, much time was spent studying an $Al_{0.3}Ga_{0.7}As:Si$ epilayer with an unintentional 2DEG populated at the substrate interface. In this section, data are presented on that sample. It is not the intention of this section to draw any conclusions from these data but only to see how it compares with the data corresponding to a 2DEG heterostructure and an $Al_{0.3}Ga_{0.7}As:Si$ epilayer without an unintentional 2DEG populated.

Data from an unintentionally populated 2DEG

Shown in Fig.(5.4), are resistance changes, increasing and decreasing, induced by intense FIR from the TEA laser operating at $29.5cm^{-1}$ with an average total pulse energy of 4mJ. The electric field vector of the FIR was coupled parallel



(a)



(b)

Fig.(5.4) Resistance changes induced by intense FIR in an $\text{Al}_{0.3}\text{Ga}_{0.7}\text{As}:\text{Si}$, $2\mu\text{m}$ thick, epilayer with the population of an unintentional 2DEG of the substrate interface at two different TEA laser powers. The TEA laser was operated at 29.5cm^{-1} with a total average pulse energy of 4mJ . The data in (a) were taken at full TEA laser field intensity within the sample of $690\text{kW}/\text{cm}^2$ and in (b) were taken at 11% of full field intensity within the sample or $76\text{kW}/\text{cm}^2$.

to the plane of the sample using a cold finger cryostat at 12K. This gives a field intensity of $690\text{kW}/\text{cm}^2$ within the sample assuming a spot size of 3mm diameter, a reflection of 32% of the free field intensity, and a 90% transmission of the free field intensity through the polypropylene windows of the cryostat. With these data, the

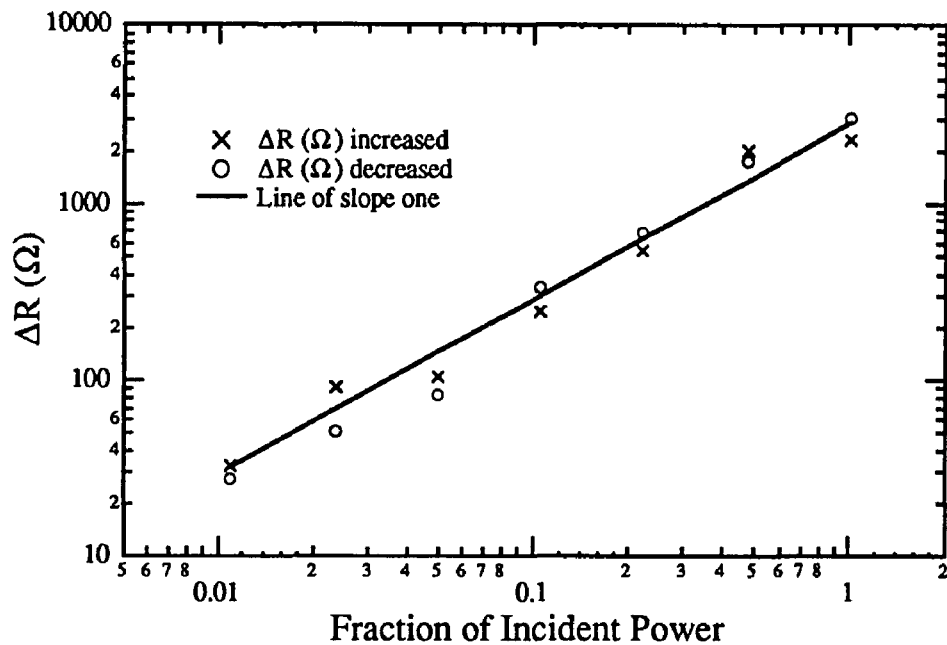


Fig.(5.5) Power dependence of the FIR induced increases and decreases in epilayer resistance of an $\text{Al}_{0.3}\text{Ga}_{0.7}\text{As}:\text{Si}$ epilayer with an unintentional 2DEG populated. The TEA laser was operated at 29.5cm^{-1} with a total average pulse energy of 4mJ. The line drawn has a slope of one.

IR LED flash occurs before any FIR pulses as was the case for the data presented in Chapter 3. The main point about these data is that the FIR induced resistance changes have $\Delta R \approx 10\text{k}\Omega$. This is similar to the resistance changes observed in conjunction with real-space electron transfer in a 2DEG heterostructure. This implies it is likely that the FIR is transferring electrons back and forth between the $\text{Al}_{0.3}\text{Ga}_{0.7}\text{As}:\text{Si}$ epilayer and the unintentional 2DEG.

Power dependence of the FIR induced changes

The power dependence of the increases and decreases in ΔR is shown in Fig.(5.5). The increasing or decreasing ΔR was the average of all FIR induced

changes, increasing or decreasing, observed at a given TEA laser power. The line drawn in Fig.(5.5) has a slope of one and is not fit to the data but just drawn to guide the eye. It is interesting to note that the increases and decreases of ΔR is seen for the entire power range of Fig.(5.5). That is, a threshold for large resistance changes is not seen as in Fig.(5.2). This might be because the mobility of the unintentional 2DEG is probably only on the order of $10,000\text{cm}^2/\text{Vs}$ as opposed to $320,000\text{cm}^2/\text{Vs}$ for the sample used to collect the data in Fig.(5.2) (see Chapter 2, §B for a discussion of sample parameters). With such a low mobility for the 2DEG, the sample resistance can never get down to around 400Ω as was the case for the 2DEG with the mobility of $320,000\text{cm}^2/\text{Vs}$. The increases and decreases observed for all powers in Fig.(5.5) could still be the result of ionizing electrons from DX centers or capturing electrons by DX centers of the $\text{Al}_{0.3}\text{Ga}_{0.7}\text{As}:\text{Si}$ epilayer.

The linear power dependence of the FIR induced ΔR 's of Fig.(5.5) is different from the nonlinear power dependence observed in Fig.(3.15). The sample studied for the data presented in Fig.(3.15) was an $\text{Al}_{0.3}\text{Ga}_{0.7}\text{As}:\text{Si}$ epilayer with a $2\mu\text{m}$ undoped $\text{Al}_{0.3}\text{Ga}_{0.7}\text{As}$ buffer layer which prevented the population of the unintentional 2DEG. It is possible that the linear dependence at low powers in Fig.(5.3) and all powers in Fig.(5.5) is a signature of real-space transfer where as the nonlinear dependence on power in Fig.(3.15) is a signature of FIR induced capture of electrons by DX centers.

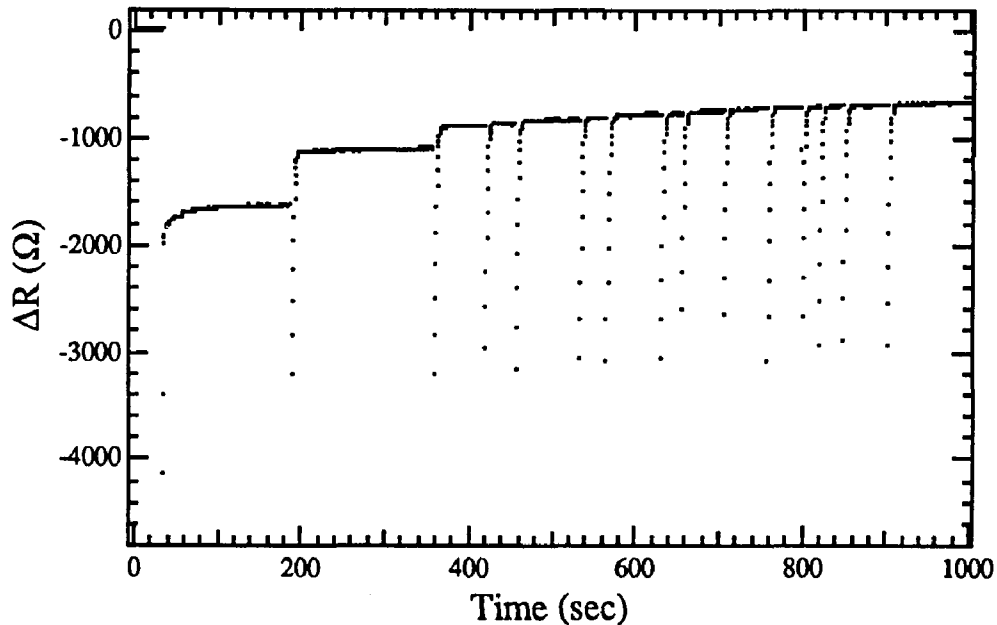


Fig.(5.6) Resistance changes induced by FIR from the free-electron laser operating at 50cm^{-1} with a total average pulse energy of 13.2mJ in $12\mu\text{sec}$ (1.1kW or a free field intensity of 3.9kW/cm^2 with the beam focused to 3mm spot size). The sample was an $\text{Al}_{0.3}\text{Ga}_{0.7}\text{As}:\text{Si}$ epilayer with the population of an unintentional 2DEG at the substrate interface.

FIR induced changes from the free-electron laser (FEL)

The resistance changes shown in Fig.(5.6) are induced by FIR from the free-electron laser operating at 50cm^{-1} with a total pulse energy of 13.2mJ in $12\mu\text{sec}$ (1.1kW or a free field intensity of 3.9kW/cm^2 with the beam focused to a 3mm spot size). The main point to be drawn from Fig.(5.6) is that $\Delta R \approx 100\Omega$ and the ΔR are always increasing. The field intensity within the sample, S_s , for the FEL data was about 2.7kW/cm^2 and S_s for the TEA laser data was about 290kW/cm^2 . So it could be that the FEL field intensity was too low to see the decreases in ΔR . With the TEA laser attenuated to approximately the power of the FEL, not as many decreasing as increasing ΔR 's were observed, although the ΔR 's were close to the noise levels.

The large negative going non-persistent resistance transients seen in Fig.(5.6) might result from a frequency of 50cm^{-1} used for the FEL measurements as opposed to 29.5cm^{-1} for the TEA laser measurements. The negative going transients could be a signature of ionization of the shallow Si donors in the $\text{Al}_{0.3}\text{Ga}_{0.7}\text{As}:\text{Si}$ epilayer. Negative transients are observed in the TEA laser data of Fig.(5.4) but are quite small. The negative resistance transients at the 43.3cm^{-1} TEA laser line are somewhat larger than the 29.5cm^{-1} transients but are still not as large as the 50cm^{-1} transients. The shallow silicon donor in $\text{Al}_{0.3}\text{Ga}_{0.7}\text{As}:\text{Si}$ has a binding energy of around 8meV which corresponds to about 65cm^{-1} . In GaAs the shallow donor has a binding energy of 5.6meV which corresponds to 45cm^{-1} (see Chapter 6, §E for a discussion of the photovoltages arising from the negative going resistance transients).

Chapter 5 References

1. W. W. Bewley, Ph.D. Thesis, University of California Santa Barbara 1991.
2. W. W. Bewley and C. L. Felix were conducting a second harmonic generation experiment on an digitally alloyed $\text{Al}_x\text{Ga}_{1-x}\text{As}/\text{GaAs}$ 10 half parabolic well the night of October 5, 1990. They observed that the 2nd harmonic signal would disappear after 3 or more TEA laser shots. This implies that the electrons were being ionized from the well or transferred in real space from the GaAs to the $\text{Al}_x\text{Ga}_{1-x}\text{As}$ and remaining there after being localized at the DX center in the Si doped $\text{Al}_x\text{Ga}_{1-x}\text{As}$ (temperature < 10K). The epilayer resistance was also being monitored while the sample was illuminated with the intense FIR from the TEA laser. The epilayer resistance was observed to jump from around 330Ω to 600Ω or 700Ω after 3 or more shots of the TEA laser (see Chapter 5, §D).
3. They had conversations with T. N. Theis, P. M. Mooney, and A. Kastalsky about DX centers and the epilayer resistance measurements. Kastalsky pointed out the possibility of populating an unintentional 2DEG at the epilayer substrate. L. Y. Lin gave us information about stretched exponential fits to the epilayer resistance relaxations. We were initially under the impression that such relaxations did not exist and our observations were somewhat strange.
4. M. Keever, H. Shichijo, K. Hess, S. Banerjee, L. Witkowski, H. Morkoc, and B. G. Streetman, *Appl. Phys. Lett.* **38**, 36 (1981).
5. K. Hess, H. Morkoc, H. Shichijo, and B. G. Streetman, *Appl. Phys. Lett.* **35**,

469 (1979).

6. C. Hilsum, *Proc. Inst. Radio Engr.* **50**, 185 (1962); B. K. Ridley and T. B. Watkins, *Proc. Phys. Soc.* **78**, 293 (1961).
7. H. Shichijo, K. Hess, and B. G. Streetman, *Solid-State Electron.* **23**, 817 (1980).
8. T. H. Glisson, J. R. Hauser, and M. A. Littlejohn, K. Hess, B. G. Streetman, and H. Shichijo, *J. Appl. Phys.* **51**, 5445 (1980).
9. C. L. Felix, Ph. D. thesis, University of California Santa Barbara, 1992.
10. J. P. Harrang, R. J. Higgins, R. K. Goodall, P. R. Jay, M. Laviron, and P. Delescluse, *Phys. Rev.* **B32**, 8126 (1985).

Chapter 6

Photovoltaic Responses of $\text{Al}_x\text{Ga}_{1-x}\text{As}/\text{GaAs}$ Semiconductors to Intense FIR.

§A Introduction

The initial experiment undertaken for this thesis project was to study the conductivity of a quantum well while illuminated by intense FIR from the FEL. The hope was that the intense FIR would ionize electrons from the quantum well and hence decrease the conductivity of the sample. These photoconductivity measurements were complicated by photovoltages associated with the sample contacts. This chapter discusses these photovoltages and some believed to be associated with the electrons in the quantum well.

Transient photovoltaic response to intense FIR illumination are reported in a wide variety of $\text{Al}_x\text{Ga}_{1-x}\text{As}$ and GaAs samples with various contact and gate geometries. The photovoltages are observed at all temperatures from 4K to 300K. The photovoltaic responses can be quite varied. They have been observed to be positive, negative, and bipolar (i.e. changing from positive to negative) within the duration of the FIR pulse. Some photovoltaic responses are very fast and follow the

FIR pulse while others exhibit long decay times on the order of a 100 μ sec (The FIR pulse is typically on the order of 1 μ sec long.). Photovoltages from the FIR produced by the FEL have been observed to be as large as 30 to 40mV while some photovoltages from the FIR of the TEA laser have been seen to be on the order of 10 volts.

The photovoltages reported in this thesis were not the first observation of photovoltages from $\text{Al}_x\text{Ga}_{1-x}\text{As}/\text{GaAs}$ heterostructures under illumination of intense FIR using the U.C.S.B. FEL. The Ph.D. thesis of Jann Kaminsky [6.1a] and [6.1b] reports the observation of photovoltages from $\text{Al}_x\text{Ga}_{1-x}\text{As}/\text{GaAs}$ heterostructures with gratings or periodic surface structures at a sample temperature of 4.2K. The discussion in Ref.(6.1a) of the origin of the photovoltaic signals is in terms of changes in 2DEG electron concentration (equivalently changes in the chemical potential of the 2DEG electrons). The discussion in this chapter will differ from Ref.(6.1a) in that most of the signals reported here are believed to be associated with the Schottky barriers of the contacts. In addition, the photovoltaic signals are observed at all temperatures from 4K to 300K. Some of the photovoltaic data presented are correlated with the temperature dependence of the channel electron mobility in a 2DEG $\text{Al}_{0.3}\text{Ga}_{0.7}\text{As}/\text{GaAs}$ heterostructure. The photovoltaic signals that are believed to be artifacts of the contacts were observed from: $\text{Al}_{0.3}\text{Ga}_{0.7}\text{As}/\text{GaAs}$ heterostructures or quantum wells, bulk n^+ -type GaAs, and semi-insulating GaAs.

The photovoltaic data can be summarized as wild. The photovoltages reported in this thesis are not understood. This chapter has been included in order to document some of what has been observed and to give future researchers a place

to look when faced with mysterious photovoltaic data. It will also try to provide information on how one might avoid photovoltaic signals and on when they might occur.

No theoretical model is presented for the photovoltaic effects reported in this chapter. Some possible explanations will be presented and references cited so as to give the reader a place to look within the literature for further study. A discussion of the semiconductor-metal contact will be presented which will introduce the Schottky barrier and how such a contact can lead to “rectification of the FIR”. The thermoelectric effect (or Seebeck voltage) of hot electrons will be discussed and given as a possible mechanism for the negative photovoltages observed.

The data discussed so far (Chapters 3, 4, and 5) has not been concerned with transient photovoltages since the effects discussed within those chapters have been persistent or having relaxation times on the order of 0.1 to 1.0 seconds or longer. The photovoltaic transients are typically a few microseconds long with some as long as 100 microseconds. These photovoltaic transient times are much shorter than any relaxation times observed in resistance or photo-Hall data so they were neglected in the analysis of that data.

§B The metal-semiconductor contact

Since many of the photovoltages observed seem to be associated with metal contacts to semiconductor surfaces, a discussion of the metal-semiconductor contact is presented here. It is important to realize that all contacts whether they are ohmic or Schottky have a Schottky barrier (see below) associated with them. The width of

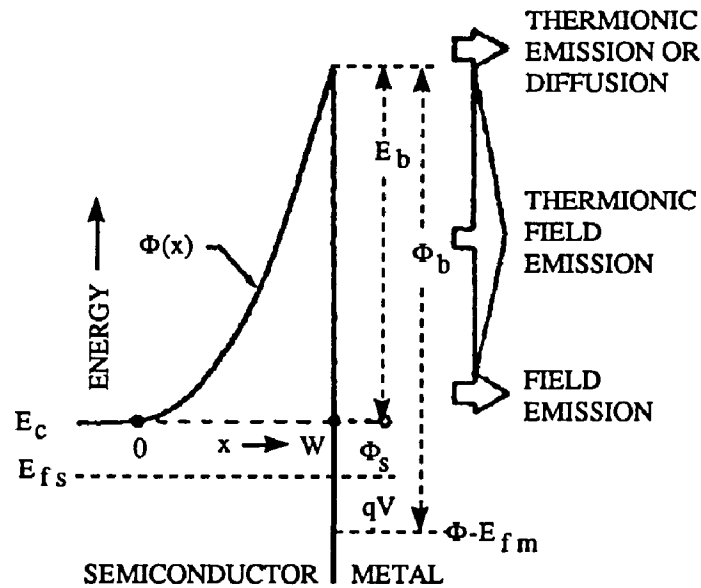
this barrier determines the contact type. If the barrier is sufficiently thin, electrons can easily tunnel through it and the contact will be ohmic.

The Schottky barrier formed at a metal-semiconductor interface is shown in Fig.(6.1a). For a good review of Schottky barriers and the theory and application of metal-semiconductor rectifiers see Rideout [6.2].

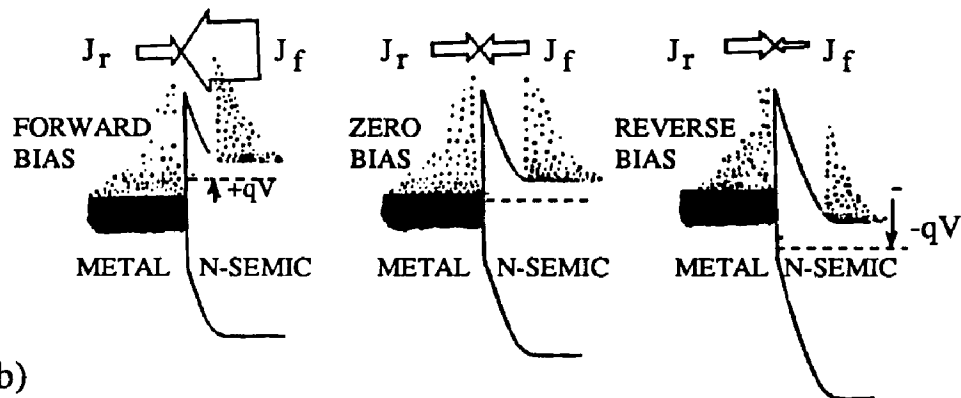
The conduction band curvature near the surface of the semiconductor is from the uniform distribution of positive charge resulting from charge depletion of this layer. As shown in Fig.(6.1a), the surface depletion length is W . The charge from the depletion region is transferred to the surface of the semiconductor where the electrons are trapped (highly localized) by surface states [6.3]. This localizing of electrons at the surface states pins the Fermi level at the interface (mid gap [6.4]) and hence fixes the barrier height Φ_b . This barrier height, Φ_b , has been observed to be independent of the metal (the metal work function) at the metal-semiconductor interface for Si, Ge, GaAs and other highly covalent semiconductors [6.2].

Dependence of surface depletion depth on doping

An important aspect of the modeling of the metal-semiconductor interface in Fig.(6.1a) is the fact that the depletion length, W , is smaller for larger charge doping levels. The barrier acts like a rectifier for doping levels below 10^{17}cm^{-3} where thermionic emission [6.5] over the barrier is the primary charge transfer mechanism. Shown in Fig.(6.1b) is a schematic representation of rectification due to thermionic emission. As the doping concentration is increased, the width of the depletion layer is decreased. For doping levels between 10^{18}cm^{-3} and 10^{19}cm^{-3} the barrier becomes thin enough that thermally excited carriers can tunnel through near the top of the



(a)



(b)

Fig.(6.1) (a) The Schottky barrier of a metal-semiconductor interface (Ref.6.2). (b) Rectification due to thermionic emission at a Schottky barrier (Ref.6.2).

barrier (thermionic field emission). As the doping level is increased above 10^{19}cm^{-3} the barrier becomes so thin that a significant number of electrons can tunnel through at the base of the Schottky barrier [6.6] (field emission tunneling). This is the case

for an ohmic contact. Note that in Fig.(6.1a) the above three different emission regimes are indicated by large arrows at the right of the figure. Also keep in mind that the metastable DX center in GaAs limits the doping concentration in GaAs to around 10^{19}cm^{-3} [6.7] and most of the samples that are n^+ -GaAs (n^+ means high n-type doping) are only doped to around 5 to $7 \times 10^{18}\text{cm}^{-3}$ [6.7]. So it seems that only thermionic and thermionic field emission are of importance for that samples studied in this thesis.

Temperature dependence of the thermionic emission current

As the temperature of the sample decreases there is a large decrease in the magnitude of the thermionic emission current. The temperature dependence of the thermionic emission current is given by $T^2\exp(-q\Phi_b/kT)$ when the barrier height is large compared to kT which is the most common case for metal-semiconductor contacts (with N_d between 10^{15} to 10^{19}cm^{-3}) [6.6]. So the large decrease in the magnitude of the current with decreasing temperature is primarily due to the reduction of kT in the exponent rather than the barrier height increase. The Schottky barrier height, Φ_b , for GaAs is around 0.8 to 0.9eV [6.8] and this increases by about 50meV as the temperature is decreased from 300K to 30K .

Electric field effects

There are three electric field effects that lead to an effectively lower barrier height Φ_b [6.2]. One of the effects is that of an image charge in the metal. A carrier in the semiconductor will induce an image charge of opposite sign in the metal. The image charge produces an attractive force on the carrier in the semiconductor. The

attractive force reduces the electric field and hence lowers the barrier height. The second effect is due to the presence of a charge dipole at the metal-semiconductor interface. The dipole causes the electrons from the metal to penetrate into the semiconductor. It also causes the electric field from the semiconductor to extend into the metal. The result is that the barrier height is lowered in proportion to the electric field [6.2]. A third predicted effect is appreciable tunneling can occur for electric fields in excess of 9kV/cm for n-type Au-GaAs Schottky barriers [6.9].

§C Thermoelectric effect of hot electrons

The Seebeck or thermoelectric voltage arises from a spatial variation of the electron distribution due to a gradient in lattice temperature [6.10]. Spatial variation of the electron distribution due to a gradient in the electric field has also given rise to a voltage [6.11]. This voltage is sometimes called the “thermoelectric voltage of hot electrons” because of the analogy with the Seebeck effect. This thermoelectric voltage has also been observed by using microwave (2.85 GHz) radiation to heat the electrons [6.12].

Homogeneous material

Conwell and Zucker [6.12] show that within a homogeneous material the thermoelectric voltage is zero since the temperature rise and fall take place within the same homogeneous material. What happens is that the field in two different regions cancel each other. This cancellation need not take place when one of the regions is inhomogeneous.

Inhomogeneous material

A typical inhomogeneous region is that of a metal-semiconductor contact as discussed in §B. In a semiconductor system like silicon where a p-n junction can be fabricated within the bulk material and an ohmic contact fabricated on the surface, the contributions to an observed voltage can be separated into that produced by rectification at the p-n junction and that produced by the thermoelectric effect. The reason this can be done is because rectification by the p-n junction involves minority carrier current and the hot electron thermoelectric effect involves majority carrier current so the two effects will have opposite sign. Such behavior has been observed by Harrison and Zucker [13] in p-type Ge and n-type epitaxial Si. Hot electron thermoelectric voltages have been observed from ohmic contacts with rectification from the contact being ruled out since it gives a contribution of the opposite sign.

Thermoelectric power

The thermoelectric voltage is usually modeled in terms of the thermoelectric power of the hot electrons [6.14]. If an electron temperature difference dT_e causes a voltage difference dV , then the thermoelectric power of the hot electrons is defined as $\mathcal{P} = dV/dT_e$. So the thermoelectric voltage is obtained by integrating the thermoelectric power \mathcal{P} with respect to the temperature. The thermopower for metals and semiconductors are typically in the range of $\mathcal{P} \approx 1\mu\text{V}/\text{deg}$ for a metal and $\mathcal{P} \approx 1\text{mV}/\text{deg}$ for a semiconductor. For a n-type (lightly doped) semiconductor the sign of the thermoelectric voltage (V_{th}) is negative and for a p-type (lightly doped) semiconductor V_{th} is positive. Room temperature hot electron thermoelectric

voltages have been observed in the range of 1mV to 1000mV in semiconductor systems [6.14]. (An interesting aside is that a measurement of the thermoelectric power of hot carriers can provide a measurement of the energy relaxation time of the hot carriers in semiconductor systems [6.14].)

The ordinary thermoelectric effect gives a thermoelectric power that varies inversely to the carrier concentration [6.10]. Then, by analogy, the hot electron thermoelectric effect is smaller in a material with a substantial portion of the change from hot electrons to thermally distributed electrons (the metal contact) taking place in a portion of the material with high carrier concentration. Which means that a temperature gradient in such a material would result in a much smaller voltage than a similar gradient in a lightly doped (small carrier concentration) material.

§D Photovoltaic response of $\text{Al}_x\text{Ga}_{1-x}\text{As}/\text{GaAs}$ quantum wells and n^+ -GaAs to intense FIR

Photovoltaic signal from a half parabolic well

A typical photovoltage observed from a half-parabolic quantum well at room temperature illuminated by intense FIR from the free-electron laser (FEL) is shown in Fig.(6.3). The contact geometry that was used is shown in Fig.(6.2a). The photovoltage was measured between the two contacts shown in Fig.(6.2a). The FIR was focused onto the edge of the sample. The sample was about 8mm square. With the FEL focused to a 3mm diameter spot (spot size of 3mm), it was difficult not to illuminate the contacts. It was not uncommon to see the photovoltaic signal change sign within the time of the FIR pulse as shown in Fig.(6.3b). The photovoltaic

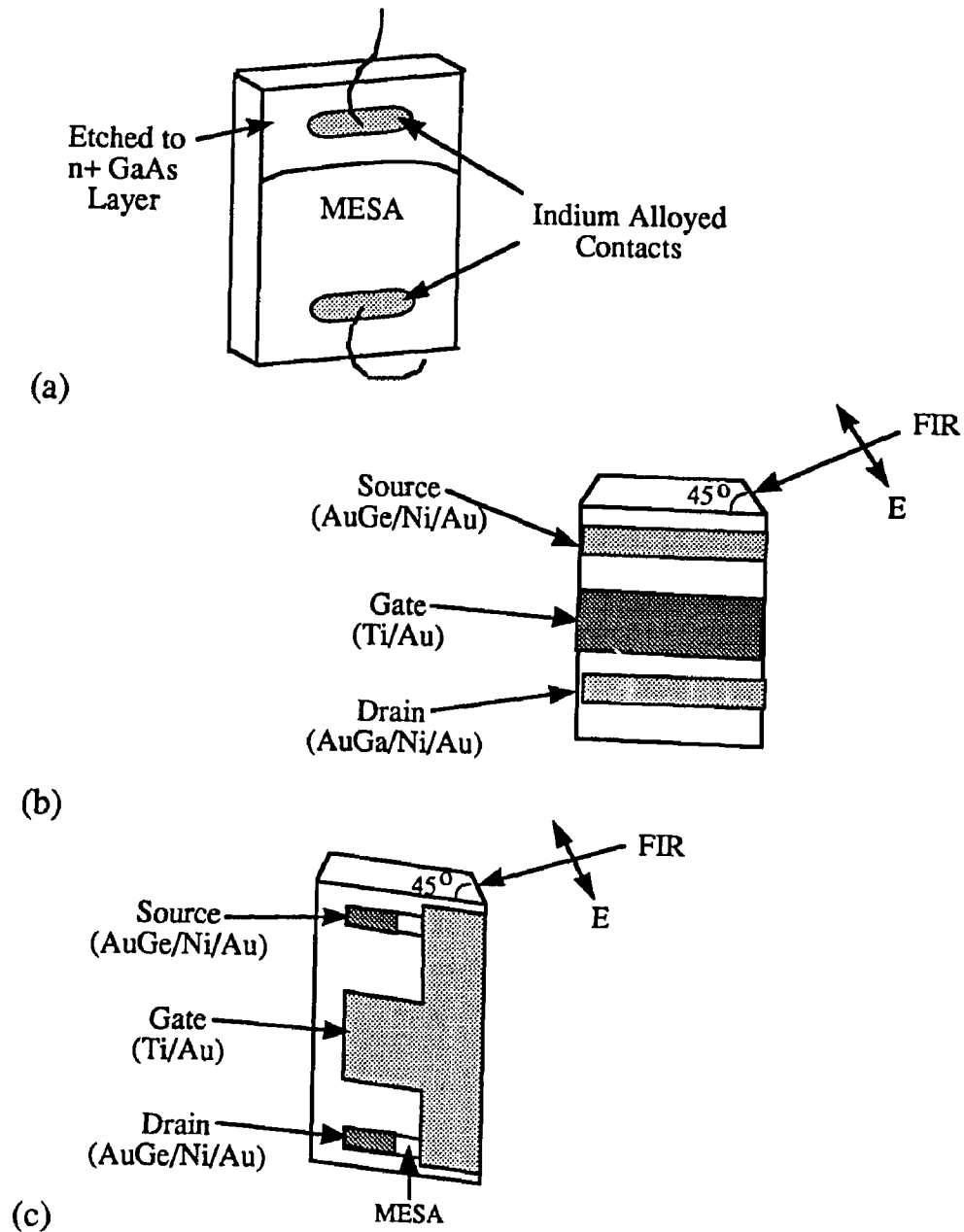
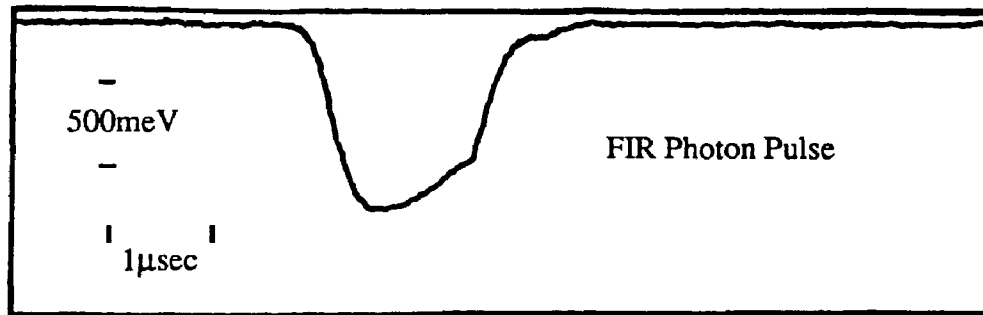
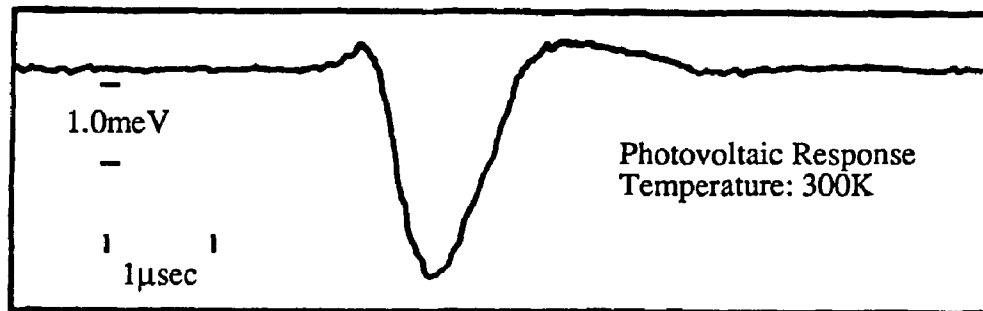


Fig.(6.2) Different contact geometries from which photovoltaic signals were observed from intense FIR. In (a), the FIR was focused onto the face and edge of the part of the sample with the mesa. In (b) and (c), the FIR was focused onto the 45° lapped edge of the sample



(a)



(b)

Fig.(6.3) A typical photovoltaic response to a pulse of intense FIR. The FIR photon pulse is shown in (a) and the response to the FIR is shown in (b). The sample was an $\text{Al}_x\text{Ga}_{1-x}\text{As}/\text{GaAs}$ half parabolic quantum well. The free-electron laser (FEL) was operated at 50cm^{-1} with a peak power between 3 to 5 kW/cm^2 (spot size of 3mm diameter). The sample temperature was 300K.

response was commonly seen to be fast enough to follow the FIR photon pulse rise time. The decay of the photovoltage signal was between $1\mu\text{sec}$ and $100\mu\text{sec}$ depending on the temperature of the sample and impedance the photovoltage was driving. The decay time and pulse shape was seen to change with temperature. Whenever the sample was loaded with a small parallel resistor (small with respect to the input

impedance of $1\text{M}\Omega$ of the digitizing oscilloscope used to measure the photovoltaic response), say around $10\text{k}\Omega$, the decay was seen to be no longer than $1\ \mu\text{sec}$ (see Chapter 2, §F, for a discussion of the electronics used to measure the photovoltaic response). So the decay time depends on the impedance the signal drives. The photovoltaic pulse shape also changed with position of the FIR with respect to the sample's contact geometry.

Photovoltaic signal from an n^+ GaAs substrate

Such peculiar behavior suggested that a control sample with ohmic contacts to an n^+ -GaAs substrate be studied to see if it would show any photovoltaic responses. A collection of typical photovoltaic responses observed from the n^+ -GaAs substrate is shown in Fig.(6.4). The contact geometry that was used is that shown in Fig.(6.2a) but without a mesa etched on the surface of the sample. The different shapes of the photovoltaic responses in Fig.(6.4) correspond to different positions of the FIR with respect to a given ohmic contact.

With these data from an n^+ ohmic contact, it was difficult to conclude whether or not the signals observed from the half-parabolic quantum well were from the contacts or the electrons in the well. Most likely, many of the photovoltages observed were artifacts of the ohmic or Schottky contacts. Schottky contacts were observed to yield much larger photovoltaic signals than the ohmic contacts.

The photovoltaic responses from ohmic contacts might be from the thermoelectric hot electron effect but the changes in sign of the photovoltage can not be understood within this model. The thermoelectric effect for n-type dopants predicts a negative thermoelectric voltage on the order of 1mV or larger [6.14].

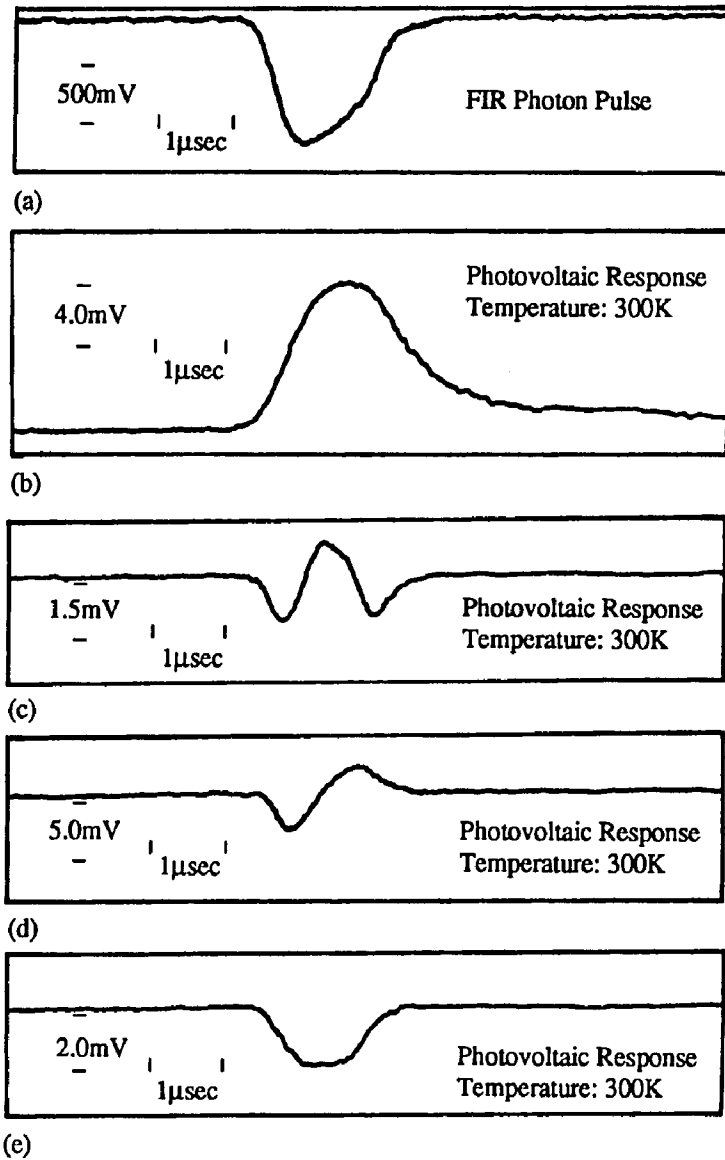


Fig.(6.4) Photovoltaic responses from a highly doped n^+ -GaAs substrate. The FIR beam is moved from the source contact in (b) and towards the drain contact in (c) to (e). The electron concentration is around 10^{18}cm^{-3} . The FEL was operated at 50cm^{-1} with peak powers between 3 to 5kW/cm^2 . The sample temperature was 300K.

Rectification at the Schottky barrier should also produce a negative signal since it involves thermionic emission of majority carrier current (electrons for a n-type doped semiconductor). This rules out the possibility that the positive signal is produced by thermionic emission over a Schottky barrier. In conclusion, the positive signal is not understood. The most important information known about it is that it is very dependent on the position of the focused FIR spot.

Photovoltaic signal from a heterostructure (2DEG)

Even with the contacts exhibiting such complex photovoltages a correlation of the photovoltaic response with channel electron mobilities of a 2DEG heterostructure, was observed, as a function of temperature as shown in Fig.(6.5). The contact geometry used for the measurement of the data presented in Fig.(6.5) is shown in Fig.(6.2b). The photovoltaic response was measured between the gate and drain. The drain was grounded to the dewar. The FIR was coupled at normal incidence to the 45° lapped edge of the sample. The FIR was positioned just above the top edge of the gate. This position corresponded to the largest photovoltaic signal observed while scanning the FIR beam up and down the edge of the sample. As the sample cooled, the FIR beam was moved in response to the contraction of the sample and cold finger of the cryostat. Most of the contraction takes place from 77K to 300K. The contraction observed was about 1.8 to 2.0mm. The mobility was scaled to the photovoltage at 80K. The mobility measurements were done by Mani Sundaram of the materials science department at U.C.S.B. A separate cryostat with a permanent magnet and computer data acquisition system was used for the Hall mobility measurements. A portion of the wafer that the sample, used for the

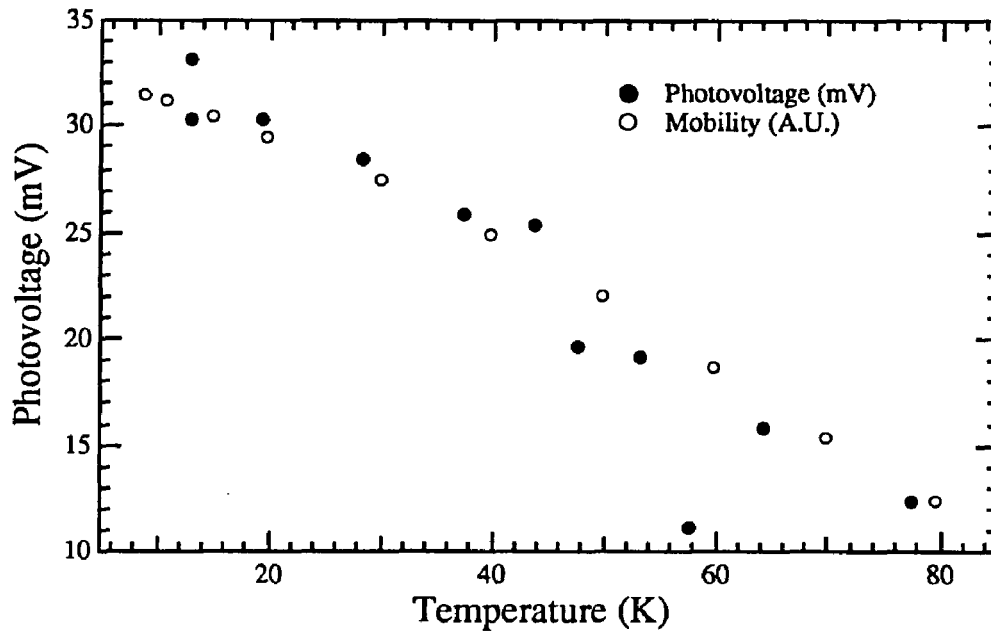


Fig.(6.5) Correlation of the photovoltaic response to channel mobility in an $\text{Al}_{0.3}\text{Ga}_{0.7}\text{As}/\text{GaAs}$ heterostructure (2DEG) as a function of temperature. The FEL was operated at 50cm^{-1} with peak powers between 3 to $5\text{ kW}/\text{cm}^2$. The mobility was normalized to the photovoltage at 80K.

collection of data shown in Fig.(6.5), came from was fabricated with a van der Pauw geometry [6.16] for the mobility measurements.

Shown in Fig.(6.6a) is a plot of the photovoltaic response versus FIR beam position along the edge of a 2DEG sample different from that studied in Fig.(6.5). The photovoltaic response was measured between the gate and drain. The top of the gate corresponds to about 23mm micrometer position in Fig.(6.6a). The micrometer positions for the middle of the ohmic contacts were about 24mm for the source and about 20mm for the drain. The sample was about 6mm square. A problem with the contact geometry shown in Fig.(6.2b) is that the edges of the contacts correspond to the largest photovoltaic responses. This suggest that the edges of the contacts tend to enhance the electric field of the laser radiation in some uncontrollable fashion.

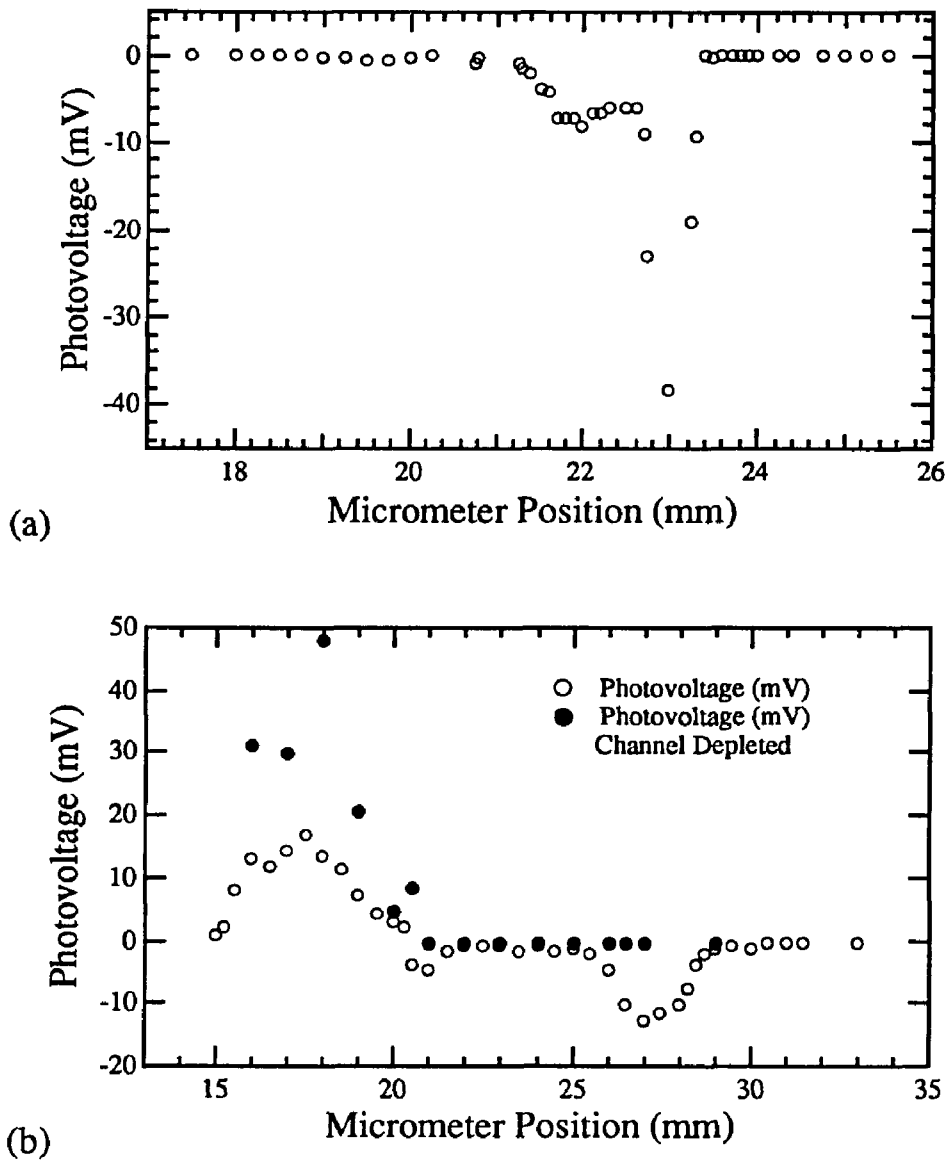
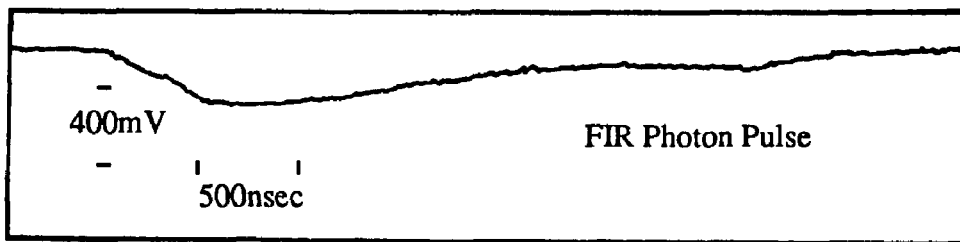


Fig.(6.6) (a) The positional dependence of the photovoltaic response for the contact geometry shown in Fig.(6.2b). The sample temperature was 300K. (b) The positional dependence of the photovoltaic response for the contact geometry shown in Fig.(6.2c). Sample temperature was 10K. For both (a) and (b) the FEL was operated at 50cm^{-1} with peak powers between 3 to 5 kW/cm^2 .

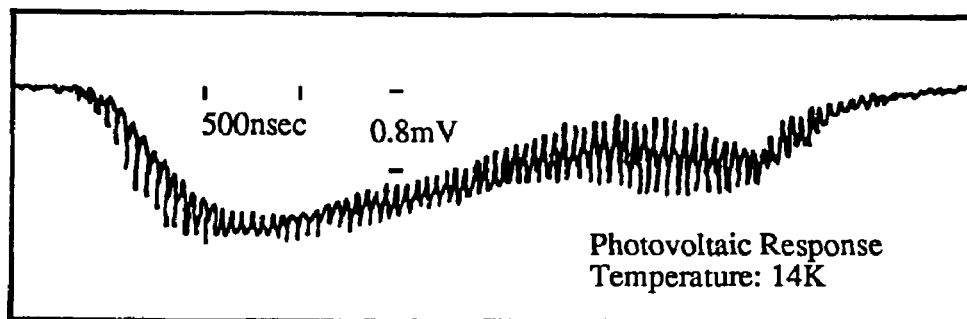
The contact geometry shown in Fig.(6.2c) is an example of an attempt to eliminate the contact edge effect described above. In this geometry, the ohmic contacts are removed to the back of the wafer by means of a mesa etch. The ohmic contact tabs were 1.0mm wide and 4.0mm from the sample edge where the FIR was coupled. The gate extended over the entire mesa including the sample's edge. With this geometry, there are not any ohmic/Schottky contact interfaces where the FIR is coupled to the sample as in Fig.(6.2b). The only two edges where the FIR is coupled are the top and bottom ends of the etched mesa. The gate serves two purposes: one is to provide enhancement of the electric field parallel to the growth direction [6.17] and the other is to enable the channel to be depleted with a negative gate bias of a few volts.

The photovoltaic response to intense FIR as the FIR beam is moved up and down the sample edge of the contact geometry of Fig.(6.2c) is shown in Fig.(6.6b). The two bumps, one positive and one negative, shown in Fig.(6.6b) seem to be correlated with the ends of the mesa. A small photovoltage of around 0.5mV was observed between the channel and the gate when the beam was centered on the middle of the gate region. The drain contact in Fig.(6.2c) was grounded to the dewar. The micrometer position of around 29mm corresponds to the bottom of the sample (drain end) and the position of around 18mm corresponds to the top of the sample (the source end). It is interesting to note that the negative photovoltages were substantially reduced when the channel was depleted of electrons by a negative (-3V) bias on the gate with respect to the channel.

The contact geometry of Fig.(6.2c) was some what successful in reducing the variety of signals seen from the contact geometry of Fig.(6.2b). However, the



(a)



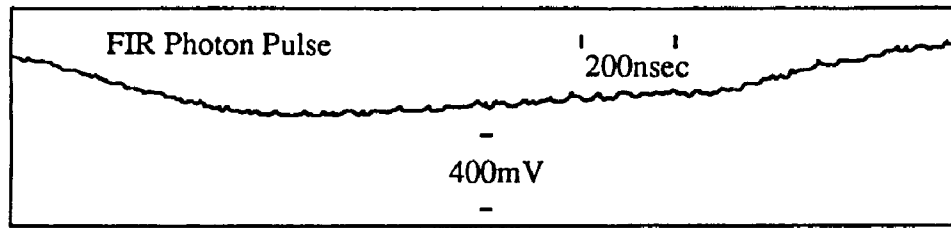
(b)

Fig(6.7) Photovoltaic response from an $\text{Al}_{0.3}\text{Ga}_{0.7}\text{As}/\text{GaAs}$ heterostructure 2DEG resolving longitudinal mode beating within the FEL photon pulse. The FEL reference photon pulse is shown in (a) and the photovoltaic response is shown in (b). The FEL was operated at 50cm^{-1} with peak powers between 3 to 5 kW/cm^2 .

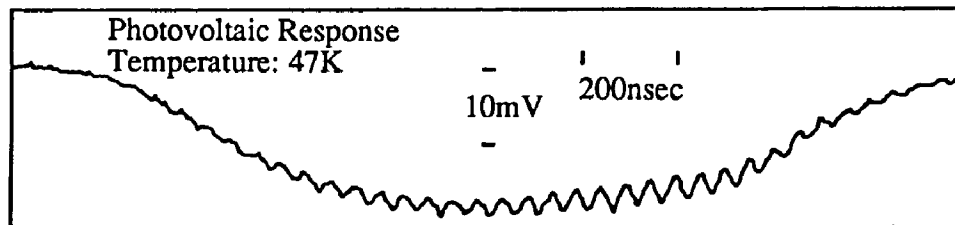
contact geometry of Fig.(6.2c) still exhibited some puzzling positive photovoltages and photovoltages changing sign within the time of the FIR pulse. The most important advantage of the contact geometry of Fig.(6.2c) over that of Fig.(6.2b) is that the channel can be entirely depleted (no ungated mesa regions).

Fast photovoltaic responses of Schottky contacts

Some of the samples studied performed well as fast detectors as shown in



(a)



(b)

Fig.(6.8) Photovoltaic response from an n^+ -GaAs substrate resolving the longitudinal mode beating within the FEL pulse. The FEL photon reference pulse is shown in (a) and the photovoltaic response is shown in (b). The FEL was operated at 50cm^{-1} with peak power between 3 to 5 kW/cm^2 .

Figs.(6.7 and 6.8). In both figures, the 19.4MHz longitudinal mode beating [6.18] of the FEL was resolved at low temperatures. The sample used for the data shown in Fig.(6.7) was an $\text{Al}_{0.3}\text{Ga}_{0.7}\text{As}/\text{GaAs}$ 2DEG heterostructure and that used for the data in Fig.(6.8) was a highly doped n^+ -GaAs substrate. The photovoltaic responses were measured between the gate and drain with the contact geometry of Fig.(6.2b). The ratio of the fast modulation amplitude to the amplitude of the negative photovoltaic pulse is larger for the 2DEG sample which probably is correlated with the large electron mobility (more electron heating) in the 2DEG as compared with electron mobility in a n^+ -GaAs substrate. The sample used for the data of Fig.(6.8)

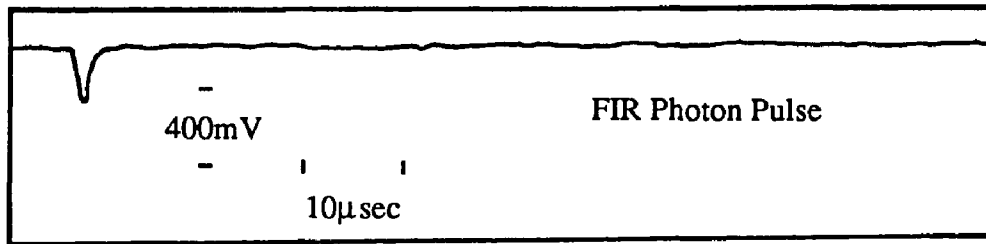
is almost identical to a sample geometry used in commercially available Schottky diode detectors used for FIR detection at room temperature [6.19]. A major difference is that the commercial diodes have a much smaller sample area and use a corner cube coupling scheme for getting the FIR focused onto the Schottky diode. The mechanism for rectification at a Schottky diode is that of thermionic emission of electrons over the Schottky barrier as shown in Fig.(6.1b). Commercial Schottky diodes are operated at room temperature and forward biased to enhance the rectification. The data shown in Figs.(6.7 and 6.8) are without a forward bias voltage applied.

Photovoltaic response of a semi-insulating substrate

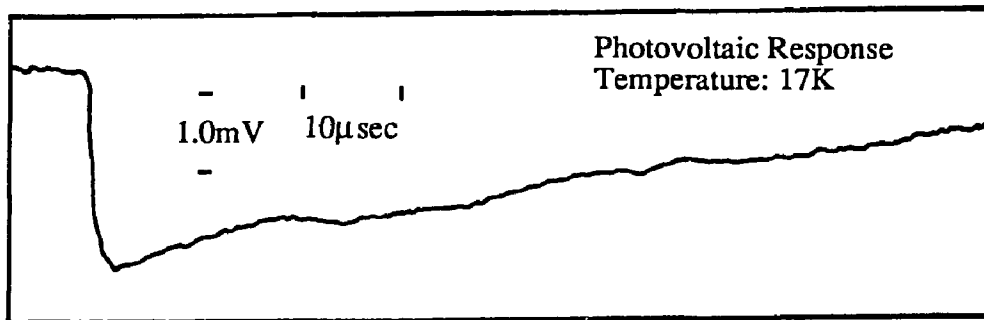
Photovoltages were also seen from semi-insulating GaAs substrate with a contact geometry of Fig.(6.2b). Such a photovoltaic response is shown in Fig.(6.9). The signals seen from semi-insulating GaAs substrates were always very small and all contacts fabricated to them are Schottky (rectifying) contacts. The two “ohmic” contacts were AuGe/Ni/Au and annealed as usual to maintain consistency throughout the different samples studied. The long decay time is characteristic of the large impedance of the semi-insulating substrate which leads to large intrinsic RC time constants for the decay of the photovoltage.

§E Photovoltaic response of an $\text{Al}_{0.3}\text{Ga}_{0.7}\text{As}/2\text{DEG}$ epilayer

The large negative resistance transients discussed in Chapter 5, Fig.(5.6), correspond to a photovoltaic response of the sample to the intense FIR when the bias



(a)



(b)

Fig.(6.9) Photovoltaic response from a semi-insulating GaAs substrate at 17K. The FEL photon reference pulse is shown in (a) and the photovoltaic response is shown in (b). The FEL was operated at 50cm^{-1} with peak powers between 3 to 5kW/cm^2 . The sample temperature was 17K.

current was removed. The photovoltages observed from the sample were quite large and regular. They were always the same shape, never changed sign, and were fast and followed the FEL photon pulse shape. They were seen to follow a square-root power dependence over three orders of magnitude as shown in Fig.(6.10). It is believed that this photovoltage arises from the shallow Si donors of the $\text{Al}_{0.3}\text{Ga}_{0.7}\text{As}$ epilayer (see Chapter 1 §C and §D for a discussion of the bistability of the Si atom). The square-root power dependence (i.e. the effect is linear in the electric field) is not

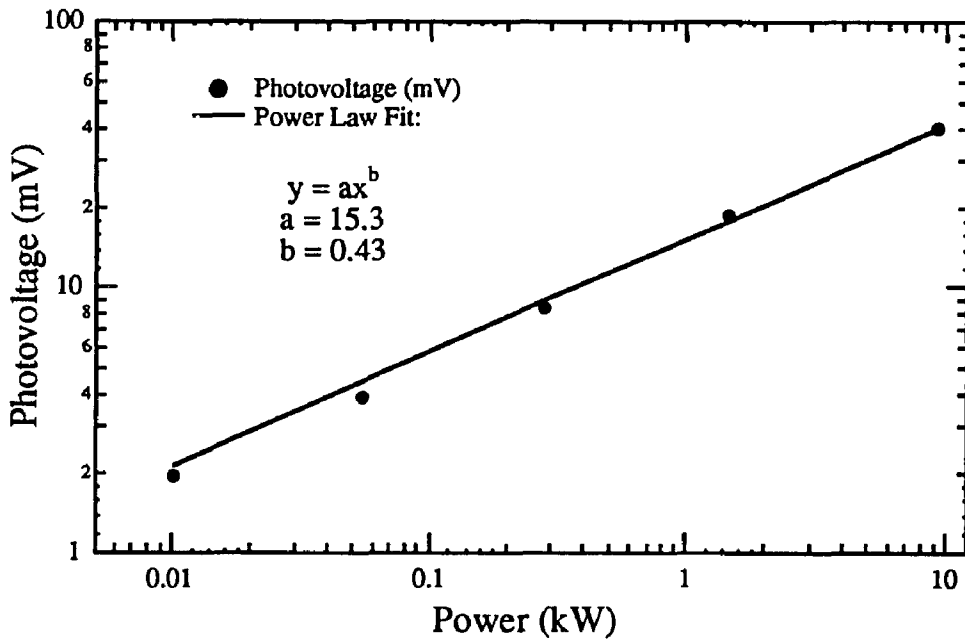


Fig.(6.10) Power dependence of a photovoltaic response observed from an $\text{Al}_{0.3}\text{Ga}_{0.7}\text{As}:\text{Si}$ epilayer with an unintentional substrate interface 2DEG populated. The FEL was being cavity dumped at 50cm^{-1} with peak power of $32\text{kW}/\text{cm}^2$.

understood. F. Keilmann [6.20] has observed a similar power dependence in the FIR in GaAs semiconductor samples.

§F Very large photovoltages from intense FIR of the TEA laser

Very large, on the order of 10 volts, photovoltaic signals were seen from an $\text{Al}_{0.3}\text{Ga}_{0.7}\text{As}/\text{GaAs}$ heterostructure (2DEG) and 10 half parabolic quantum well using intense FIR from the TEA laser. At low temperatures (8K), signals of 1 to 2 volts were very common with the largest observed being about 40 volts. At room temperature the signals were on the order of 100meV. The low temperature studies were done using the strip-line horn geometry [2.14] mounted in a continuous flow

cryostat to couple the FIR parallel to the growth direction of the sample (see Chapter 2, §D for a discussion of the cryostat used.). The room temperature studies had the sample mounted on the copper sample holder which was bolted onto rotation and translation stages. The sample was in the atmospheric environment of the lab. Having the sample at atmospheric pressure is a bad practice since the large electric field of the TEA laser can break down the air at the sample which produces an arc that can damage the sample.

Chapter 6 References

1. J. P. Kaminski, Ph. D. Thesis, University of California Santa Barbara 1989, Chapter 5, Section 6.
2. V. L. Rideout, *Thin Solid Films* **48**, 261 (1978).
3. J. Bardeen, *Phys. Rev.* **71**, 717 (1947).
4. W. E. Spicer, I. Lindau, P. Sheath, C. Y. Su, and P. Chye, *Phys. Rev. Lett.* **44**, 420 (1980).
5. G. Salardi, B. Pellegrini, and T. D. Leo, *Solid-State Electron.* **22**, 435 (1979).
6. V. L. Rideout, *Solid-State Electron.* **18**, 541 (1975).
7. T. N. Theis, P. M. Mooney, and S. L. Wright, *Phys. Rev. Lett.* **60**, 361, (1988).
8. I. Bahl and P. Bhartia, **Microwave Solid State Circuit Design** (John Wiley & Sons, New York, 1980), page 390.
9. C. R. Crowell, S. M. Sze, *Solid-State Electron.* **9**, 1035 (1966).
10. D. K. C. MacDonald, *thermoelectricity: an Introduction to the Principles* (John Wiley & Sons, Inc., New York, 1962), Chapter 1.
11. S. H. Koenig, *J. Phys. Chem. Solids* **8**, 227 (1963).
12. E. M. Conwell and J. Zucker, *J. Appl. Phys.* **36**, 2192 (1965).
13. R. I. Harrison and J. Zucker, *Appl. Phys. Lett.* **3**, 153 (1963).
14. J. Zucker, *J. Appl. Phys.* **35**, 618 (1964); R. A. Smith, **Semiconductors**, 2nd edition (Cambridge University Press, Cambridge, England, 1978), Chapter 6.
15. R. A. Smith, **Semiconductors**, 2nd edition (Cambridge University Press, Cambridge, England, 1978), p. 157.

16. K. Seeger, **Semiconductor Physics**, 4th edition (Springer-Verlag Berlin Heidelberg New York London Paris Tokyo) pages 61-63.
17. The frequency of the longitudinal mode beating is given by the difference in two longitudinal mode frequencies. A longitudinal mode is determined by the integral number of half wave lengths that can be fit within the resonating cavity of the FEL. The lowest such frequency is the case with only a half wavelength difference between modes. This gives $\nu_{\text{beating}} = \nu_{n+1} - \nu_n = (n+1)c/2L - nc/2L = c/2L$, where c is the speed of light and L is the length of the FEL cavity. For the undulator used in the measurements reported in Figs.(7 & 8) the cavity length was 7.74 meters (including the cavity dump extension). This gives $\nu_{\text{beating}} = 19.4\text{MHz}$.
18. Farran Technology Limited, Ballin Collig, Cork, Ireland, data sheet 87/1-AN12.
19. Private discussion with Fielding Brown.

Chapter 7

Conclusions and Future Experiments

§A Introduction

This chapter is divided into three sections. The first section summarizes what is understood about the effect of intense FIR perturbations on electron transport in GaAs/Al_xGa_{1-x}As quantum wells and Al_xGa_{1-x}As:Si epilayers. The second section discusses the necessary conditions for observing the effect of intense FIR in GaAs/Al_xGa_{1-x}As semiconductor systems. The third section discusses future experiments that would help in understanding the FIR effect observed in these semiconductor systems.

§B Conclusions drawn from measurements presented in this thesis

A question asked early on in the measurements of intense FIR perturbations on electron transport in a 2DEG and quantum well (see Chapter 5, §C Figs.(5.1 and

5.2)) was: “Where are the electrons going after a pulse of intense FIR?”. The answer to this question is the primary conclusion of this thesis. The FIR is inducing capture of electrons by the DX center in the Si doped $\text{Al}_x\text{Ga}_{1-x}\text{As}$ layer of a heterostructure, quantum well, or epilayer. The mechanism for the effect in the $\text{Al}_x\text{Ga}_{1-x}\text{As}:\text{Si}$ is believed to be hot electron capture by the DX center (Chapter 4, §B). And the mechanism for the effect in the heterostructure or quantum well is hot electron real-space transfer (Chapter 5, §D).

Hot electron capture by DX centers in an $\text{Al}_{0.3}\text{Ga}_{0.7}\text{As}:\text{Si}$ epilayer

The evidence for hot electron capture by DX centers in the Si-doped $\text{Al}_{0.3}\text{Ga}_{0.7}\text{As}$ epilayer is presented in chapter 3 §E Fig.(3.8) and chapter 4 §B Fig.(4.2). In chapter 4, an emission barrier of height, E_b , for the hot electron capture is deduced from an Arrhenius plot of intense FIR resistance and Hall electron concentration relaxations. The barrier height, E_b , was found to be $132\pm 12\text{meV}$ and is believed to be an emission barrier of an intermediate state of the DX center (see the discussion of E_b in Chapter 4, §B).

Hot electron real-space transfer in a heterostructure 2DEG

The evidence for FIR induced hot electron real-space transfer in a heterostructure and half-parabolic quantum well is not as clear as the FIR induced capture of electrons by the DX center since the electron concentration was not measured. The strongest support for the conclusion drawn is from the rough agreement of the estimated FIR threshold electric field (Chapter 5, §B and §D) with the threshold electric field reported for transport measurements done at 35GHz and DC in

Refs.(4.12, 5.4). In §D below, an experiment will be discussed that could provide stronger support for the conclusion that the FIR is inducing hot electron real-space transfer in heterostructures and quantum wells.

§C The conditions necessary to observe FIR induced hot electron effects

Tea laser measurements

The FIR effect discussed above is easily seen in an epilayer or heterostructure with the TEA laser operating at 29.5cm^{-1} and total pulse energy of about 2mJ. The higher the laser pulse energy the larger the effect of the FIR. With higher electron mobility in the heterostructure 2DEG or quantum well, the observed channel resistance changes will be larger (Chapter 5, §C and §E). The frequency dependence of the effect is not known but preliminary measurements of the epilayer seem to indicate a larger effect at $29.\text{cm}^{-1}$ than 43.3cm^{-1} (see Chapter 3, §G and Chapter 4, §D for a discussion of the frequency dependence of the FIR effect in an epilayer). Frequency dependent effects observed from the TEA laser are very unreliable because of the large pulse to pulse variations in laser power and pulse time structure variations for different TEA laser lines. The free-electron laser (FEL) is a much better laser to use for a frequency dependence study of the FIR effect on electron transport in epilayers.

Free-electron laser measurements

The effect is more difficult to observe with the FEL because the peak powers are about 100 times lower than the TEA laser. The effect has a linear dependence on pulse length and is readily seen with long, 10 to 20 μ sec, pulses of the FEL. If the typical 1 to 2 μ sec long FEL pulse is used, the effect could go unnoticed unless care is taken to try and see it. The effect has been seen with the 31nsec long cavity dump FEL pulses but was not easily detected.

Dark cooling and IR LED flashes

The size of the FIR effect also depends on the amount of radiation the sample has been exposed to after dark cooling. The FIR effect is largest with a few IR LED flashes after dark cooling the sample. If the sample is exposed to too much IR LED light then the electron carrier concentration becomes too high (above $5 \times 10^{16} \text{cm}^{-3}$) and the FIR effect is no longer easily observed. The FIR effect also becomes smaller after a few consecutive FIR pulses.

§D Future Experiments

Reproducibility of an initial state of a sample

Fundamental to all future electron transport measurements with intense FIR perturbations is being able to prepare the sample in a reproducible state or initial condition. The following parameters or procedures determine the state of the sample: the rate at which the sample was cooled, sample temperature, free electron concentration, electron mobility, amount of light the sample is exposed to at low

temperatures ($\hbar\omega > 0.8\text{eV}$), and the number and intensity of FIR pulses the sample is exposed to.

If the sample is at temperatures below 150K, then an IR LED flash or intense FIR pulse will change the state of the sample. In order to get the sample back to its initial condition before the perturbation, it is necessary to heat the sample to a temperature above 150K and then cool the sample to its initial temperature. This heating and cooling of the sample is a very time consuming process and is necessary after each FIR perturbation. The best solution to this problem is to keep the sample temperature above 150K were all FIR perturbations relax within a few minutes so a series of FIR exposures can be done in a short period of time. Another solution is to keep the IR LED on while exposing the sample to intense FIR at low temperatures (below 100K). In this case, the persistent changes immediately relax back to the state before the FIR pulse since the sample is being constantly exposed to the IR LED. It only takes a few seconds for the sample to relax to its initial state with the IR LED on continuously. This method leads to very fast data collection. The only draw back is that the initial state of the sample is with an IR LED on (which means a constant back ground of electron and hole pairs within the sample) and this is highly unconventional. The conventional technique is to repeatedly warm and cool the sample. The data in Fig(5.3a) were collected by keeping the IR LED on continually and it agreed well with the data of Fig.(5.3b) which were compiled from continuous FIR shots after the IR LED was turned off.

Frequency dependence of the FIR effect

One of the more important measurement that has not been done is determining

the frequency dependence of the FIR induced hot electron capture by DX centers in an $\text{Al}_x\text{Ga}_{1-x}\text{As}:\text{Si}$ epilayer. The frequency dependence of the FIR effect is interesting since it could be related to local vibrational modes (LVM) of the Si atom in an $\text{Al}_x\text{Ga}_{1-x}\text{As}$ lattice. It is not known if the Si atom has any LVM's below 200cm^{-1} (See chapter 4 §B).

Photo-Shubnikov de Haas and Photo-Hall measurements of quantum wells and 2DEGs

There are a number of interesting experiments to try with quantum wells or 2DEG heterostructures. One of primary importance is to verify that intense FIR does induce hot electron real-space transfer in these systems. The transfer of electrons from the 2DEG interface or quantum well to the Si-doped $\text{Al}_x\text{Ga}_{1-x}\text{As}$ region of the heterostructure or quantum well needs to be measured. This can be done by measuring both the electron concentration at the 2DEG interface and the electron concentration in the $\text{Al}_x\text{Ga}_{1-x}\text{As}$ region. The concentration of high mobility electrons in the quantum well or 2DEG, N_S , can be deduced from Shubnikov de Haas oscillations. A Hall measurement provides a measure of the electron concentration, N_H , in the entire sample. The $\text{Al}_x\text{Ga}_{1-x}\text{As}:\text{Si}$ electron concentration, N_O , can then be deduced from N_S and N_H since $N_O = N_H - N_S$. The effect predicted by intense FIR induced hot electron real-space transfer is that N_S will decrease with N_O increasing after an FIR pulse. This measurement is complicated by the FIR inducing electron capture by the DX center in the Si-doped $\text{Al}_x\text{Ga}_{1-x}\text{As}$. In this case, the observed effect might be that both N_S and N_O decrease. In either case, the electron concentration in the 2DEG or quantum well should decrease.

If the FIR does induce real-space transfer of electrons in 2DEG heterostructures, it would be interesting to look for the effect in a wide, 2000Å to 4000Å, parabolic quantum well. Some preliminary saturation spectroscopy measurements done by C. L. Felix using the TEA laser seem to indicate a smaller FIR effect in these parabolic wells. The changes in channel resistance of the parabolic well are not nearly as large as in the 2DEG sample. The experiment to try would be to measure electron concentrations, N_0 and N_s as described above, in the parabolic well with FIR perturbations and compare them with the heterostructure data.

Dependence of the FIR effect on aluminum mole fraction in an $\text{Al}_x\text{Ga}_{1-x}\text{As}:\text{Si}$ epilayer

It would be interesting to study the mole fraction dependence of the emission barrier, E_b , deduced from FIR perturbations of the Hall electron concentration. It is well known that the emission barrier of the DX center does not depend on aluminum mole fraction. T. N. Theis et al. [4.6] used this fact to verify that the hot electron capture they observed was independent of aluminum mole fraction, x , by measuring the temperature dependence of the emission time constants for different values of x . They found that the time constants (hence emission barrier) were independent of x . They were able to observe the emission from a sample with $x = 0.14$ which corresponds to a DX center that is resonant with the conduction band states - i.e. a metastable state of the DX center.

It would be very interesting to see if the FIR effect reported in this thesis could induce electron capture for an $\text{Al}_x\text{Ga}_{1-x}\text{As}:\text{Si}$ epilayer with $x < 0.22$ where the DX center is a resonant state.

Knowing the aluminum mole fraction dependence of the emission barrier, E_b , for the FIR induced electron capture would provide important information about this FIR induced capture state. It would help in identifying it as an intermediate state of the DX center.